Drug Eluting Electrospun Scaffolds for Tissue Regeneration

Willem Johannes Wian van den Bergh

Submitted for the degree: MSc (Med) Biomedical Engineering

University of Cape Town

February 2018

Department of Human Biology: Division of Biomedical Engineering

in association with

Cardiovascular Research Unit: Chris Barnard Division of Cardiothoracic Surgery

Supervisor: Assoc. Prof Deon Bezuidenhout

Co-Supervisor: Prof Thomas Franz

To the fathers who nurtured my scientific curiosity, W.A. Stegmann (1931-2009) & J.S. van den Bergh

Declaration

I, **Wian van den Bergh**, declare this document as my original work and that neither the substance nor any part of it (unless rightfully acknowledged) has been in the past, or is being, or is to be submitted for a degree at this or any other institution. Furthermore, I hereby grant the University of Cape Town a free licence to reproduce this thesis, in whole or in part, for the purposes of open access research and development.

Signed: Signed by candidate

Date: 08/02/2018

Abstract

The desired healing response to electrospun scaffolds in tissue engineering is often limited by poor ingrowth due to insufficient porosity, thrombogenicity, lack of vascularisation and/or excessive inflammation. This study aimed at increasing structural porosity and incorporating/delivering anti-thrombotic/angiogenic (heparin) and anti-inflammatory (dexamethasone) agents.

Porosity enhancement techniques were explored using two different approaches i) electrospinning of biostable polymer (Pellethane®, Pel) with concomitant electrospraying of soluble microparticles, which were subsequently removed to increase scaffold interconnectivity and ii) electrospinning of biodegradable polymer (DegraPol®, DP) at low collecting temperatures. Dexamethasone (Dex) was incorporated by simple admixture, while heparin (Hep) required chemical modification (heparin tributyl-ammonium, HepTBA) to achieve solubility. Release rates were determined *in vitro*, followed by thrombogenicity (thromboelastography) and cytotoxicity (cell viability) assessments of modified/unmodified heparin prior to incorporation and after elution. Finally, *in vivo* responses were evaluated in a subcutaneous model (24 rats) for up to 12 weeks.

Porosity was enhanced ($P<0.001$) for both Pel (79 to 90%) and DP (50 to 83%) scaffolds. Incorporated drugs showed a burst release (Dex 36%, HepTBA 47%, 7 days) followed by a sustained delivery (78%, 48%, 90 days). Heparin, post modification, retained its anti-thrombotic properties and showed no difference in cytotoxicity ($P>0.1$). At 12 weeks of implantation, high-porosity Pel scaffolds allowed for full tissue ingrowth (>98%) while conventional scaffolds were limited (<42%). The localised delivery of HepTBA resulted in additional blood vessel formation ($P<0.01$), while Dex did not significantly suppress scaffold inflammation ($P>0.3$).

High-porosity scaffolds produced by combined electrospinning/spraying have the potential to enhance healing. Dex or HepTBA can be incorporated and eluted from degradable electrospun scaffolds, and localised delivery of HepTBA improves implant vascularisation. This study may contribute towards tissue engineered vascular graft development where anti-thrombogenicity and increased vascularisation are desired.

Graphical Abstract

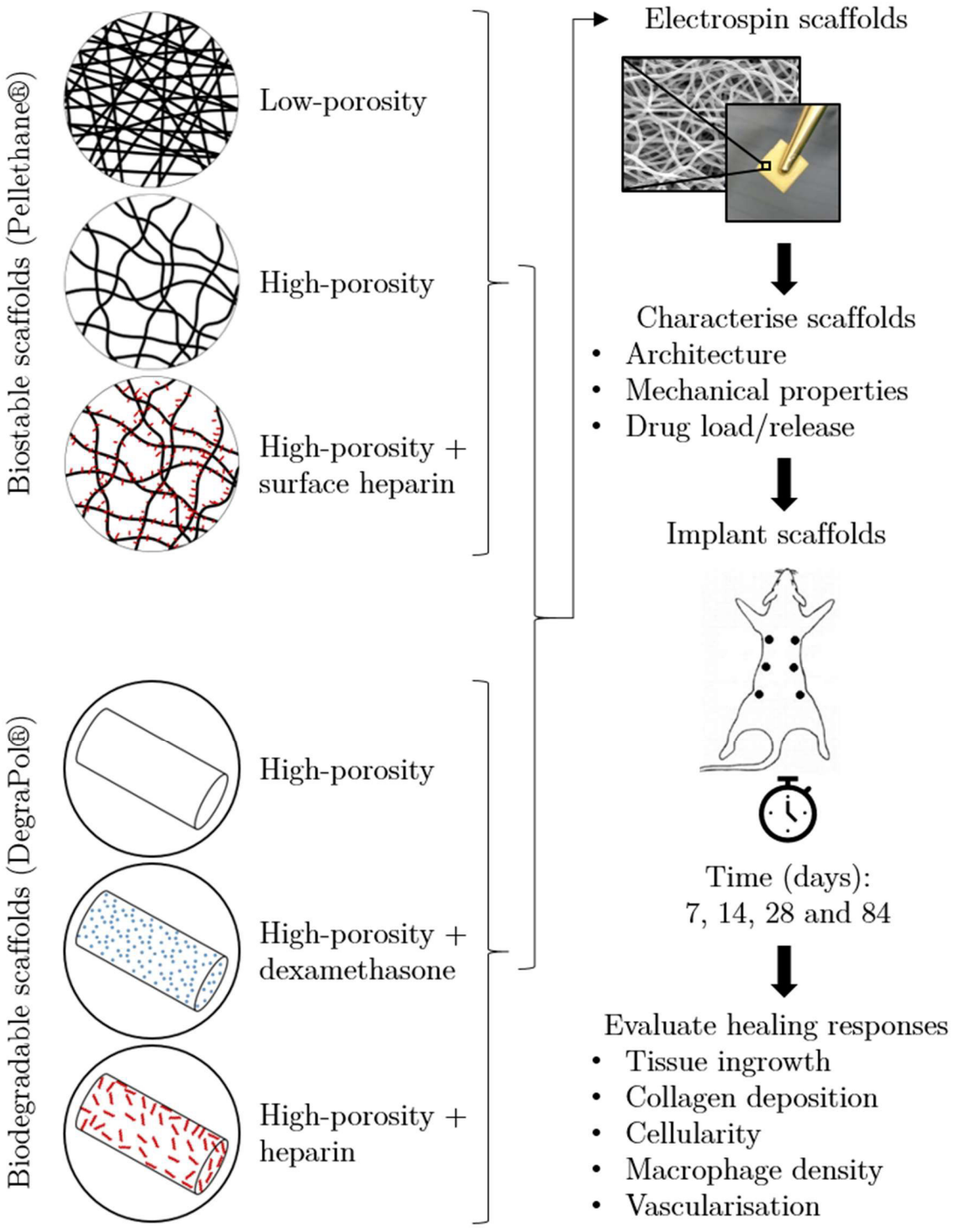

Acknowledgements

I would like to thank my supervisor, Assoc. Prof Deon Bezuidenhout, for his hands-on contributions, continuous mentorship and enthusiasm throughout the course of this project. He's a valuable asset towards the health science community and I'm grateful for his generous investment in my development.

The completion of this project would not have been possible without the help from a group of incredible individuals. Whether their inputs were in the form of assistance, mentorship, consultations or merely emotional support - I thank you all from the bottom of my heart: Aliza Janse van Rensburg (mentorship), Anel Oosthuysen (heparin and experimental consultations), Carla Gustafsson (biology consultations), Claudia de Sousa (lab assistance), Damita Zireva (lab assistance), David Conradie (polymer consultations), Emma Doubell (project support), Helen Ilsley (histological preparations), Jandre de Villiers (polymer consultations), Janet McCallum (animal welfare), Jason Voorneveld (mentorship), Joel Du Toit (technical lab support), Johan Coetzee (polymer consultations), Kim Tutt (surgical procedures), Kyle Goetsch (biology consultations), Lizel Loo (blood analysis), Miranda Waldron (SEM preparations), Nikolaus Thierfelder (clinical/biology consultations), Pete Roberts (NMR analysis), Rodney Lucas (technical animal support), Rudy Cozett (chemistry consultations) and Waled Hadasha (polymer consultations).

A deep appreciation for the financial support is expressed to the following organisations: University of Cape Town (UCT) and the postgraduate funding office, Medical Research Council (MRC), National Research Foundation (NRF) of South Africa and the International Centre for Mechanical Sciences (CISM) in Italy.

I would also like to thank ab medica s.p.a. (exclusive licensee) for providing the DegraPol® biomaterial (owners: ETH Zürich and the University of Zürich) and

Integrated Engineering software (Dr Prasad) for the evaluation and assistance of their simulation environment: Coulomb3D.

A great deal of appreciation is given to my family and friends, and especially to my parents, Jaco and Anet, for their encouragement over the years. To my beloved Caren, thank you for your love and support - you have inspired me in more ways than you realise. Finally, I praise the Creator for leading me down this blessed journey.

RESEARCH OUTPUTS

List of conference appearances

W. van den Bergh, A. Oosthuysen, T. Franz, P. Zilla, D. Bezuidenhout. ***Improved healing of electrospun tissue engineered scaffolds by increased porosity and drug delivery.*** 5th International Conference on Electrospinning, 16-18 January 2018, Stellenbosch, SA. ORAL PRESENTATION

W. van den Bergh, A. Oosthuysen, T. Franz, P. Zilla, D. Bezuidenhout. ***In vivo response to tissue engineered electrospun scaffolds with drug delivery and enhanced porosity*** . 14th annual UNESCO/IUPAC workshop & conference on Macromolecules & Materials, 11-13 April 2017, Stellenbosch, SA. ORAL PRESENTATION

W. van den Bergh, A. Oosthuysen, T. Franz, P. Zilla, D. Bezuidenhout. ***Drug eluting electrospun scaffolds for tissue regeneration*** . 10th Leiden International (bio)-Medical Student Conference (LIMSC), 15-19th March 2017, Leiden, NL. POSTER PRESENTATION

W. van den Bergh, A. Oosthuysen, T. Franz, P. Zilla, D. Bezuidenhout. ***Combined electrospinning/spraying for high porosity tissue regenerative scaffolds with concurrent drug delivery***. 2nd South African Biomedical Engineering Conference, 22-24 March 2016, Stellenbosch, SA. ORAL PRESENTATION

Publication in progress (2018)

Preliminary title (article): ***Improved healing of electrospun tissue engineered scaffolds by increased porosity and drug delivery.***

Contents

List of Tables

List of Figures

List of Appendices

List of Abbreviations

Ac	Acetyl
AR	Aspect ratio
AT-III	Antithrombin-III
AV	Arteriovenous
BDO	Butanediol
BE	Blend electrospinning
bFGF	Basic fibroblast growth factor
BP	Boiling point
C	Circumferential
CAD	Coronary artery disease
CD31	Cluster of differentiation 31
CD68	Cluster of differentiation 68
$CDCl_3$	Deuterated chloroform
CF	Coulombic fission
$CHCl_3$	Chloroform
CRU	Cardiovascular research unit
CVD	Cardiovascular disease
Da	Dalton
DAPI	Diamidino phenylindole
DCE	Dichloroethane
DCM	Dichloromethane
Dex	Dexamethasone
DI	Deionised water
DMAC	Dimethylacetamide
DMF	Dimethylformamide
DMSO	Dimethyl sulfoxide
DP	DegraPol®
EC	Endothelial cell
ECM	Extracellular matrix
EDA	Ethylene diamine
EDC	Ethyl dimethyl aminopopyl carbodiimide
EHD	Electrohydrodynamics
ePTFE	Expanded polytetrafluoroethylene
ESRD	End stage renal disease
FBR	Foreign body response
FDA	Food and drug administration
FGF-2	Fibroblast growth factor
GaGs	Glycosaminoglycans
GF	Growth factor
GlcA	Glucuronic acid
GlcNAc	Acetyl-glucosamine

GlcNS	Sulfo-glucosamine
H&E	Hematoxylin and Eosin
HCl	Hydrochloric acid
Hep	Heparin
HepH	Heparin acid
HepNa	Heparin sodium
HepTBA	Heparin-tributylammonium
HF	Heart failure
HFIP	Hexafluoro-iso-propanol
HP	High-porosity
IdoA	Iduronic acid
KCl	Potassium chloride
L	Longitudinal
LBe	Large base electrode
LMWH	Low molecular weight heparin
LP	Low-porosity
LTE	Low temperature electrospinning
M1	Macrophage phenotype 1
M2	Macrophage phenotype 2
MA	Maximum amplitude
MBe	Medium base electrode
MBTH	Methyl benzothiazolinehydrazone hydrochloride
MCP	Monocyte chemoattractant protein
MDI	Methylene-di-phenyldiisocyanate
MeOH	Methanol
MES	Morpholino ethanesulfonic acid
MS	Microsoft
NaCl	Sodium chloride
NaOH	Sodium hydroxide
NMP	Methyl pyrrolidone
NMR	Nuclear magnetic resonance
OI	Orientation index
PAD	Peripheral artery disease
PAN	Polyacrylonitrile
PBS	Phosphate-buffered saline
PCL	Polycaprolactone
PDGF	Platelet-derived growth factor
PEG	Polyethylene glycol
Pel	Pellethane®
PEO	Polyethylene oxide
PGA	Polyglycolic acid
PGS	Polyglycerol sebacate
PHB	Polyhydroxybuterate
PLA	Polylactic acid
PLCL	Poly(lactide-co-caprolactone)
PLGA	Poly(lactic-co-glycolic acid)

PLLA	Poly-L-lactic acid
PS	Polystyrene
PSR	Picroserius Red
PSU	Polysulfone
PTMO	Polytetramethylene oxide
PU	Polyurethane
RGB	Red, green and blue
RH	Relative humidity
RHD	Rheumatic heart disease
ROI	Region of interest
RSA	Republic of South Africa
RT	Room temperature
RTE	Room temperature electrospinning
SANS	South African national standard
SAVC	South African veterinary council
SBe	Small base electrode
SEM	Scanning electron microscope
SM	Surface modification
SMC	Smooth muscle cell
TA	Transanastomotic
TB	Toluidine blue
TBA	Tributylamine
TE	Tissue engineering
TEG	Thromboelastography
TFA	Trifluoro acetic acid
TFE	Trifluoroethanol
TGF-b	Transforming growth factor-b
THF	Tetrahydrofuran
TM	Transmural endothelialisation
UCT	University of Cape Town
UTS	Ultimate tensile strength
VAD	Ventricular assist device
VEGF	Vascular endothelial growth factor
VG	Vascular graft
VHD	Valvular heart disease
wt%	Weight percentage

List of Symbols

A	Area
ϑ	Bulk volume
α	Clot strength
K	Conductivity
r^2	Correlation coefficient square
ρ	Density
D	Diameter of fibre/particle/pore
ε	Dielectric constant
k	Drug release constant
ω	Drug release exponent
Em	Electric field intensity
n_e	Entanglement number
Q	Flow rate
l	Length
m	Mass
ε_{max}	Maximum elongation
Λ	NMR proton signal
n	Number
OI	Orientation index
AR	Particle aspect ratio
C	Particle circularity
φ	Polymer concentration
M_w	Polymer molecular weight
P	Porosity
U	Quantity of drug released
r	Radius
n	Sample size
M_e	Solution entanglement molecular weight
P	Statistical P value
ρ_s	Surface charge density
γ	Surface tension
v_c	Tangential collector velocity
K	TEG clot formation time
MA	TEG maximum amplitude
R	TEG reaction time
t	Thickness
T	Time
V	Voltage
w	Width
E	Young's modulus

Glossary

ablumen	Outside surface
adhesion	A process by which a cell attaches to a surface/device/other cells
adverse effects	Device or drug inducing undesirable/cytotoxic side effects
amphiphilic	Polymer or salt with both hydrophobic and hydrophilic properties
angiogenesis	The formation of new blood vessels from pre-existing vessels
arrhythmia	Abnormal cardiac rhythms
arteriosclerosis	Thickening of the arterial wall due to cholesterol build-up
atomisation	The formation of small particles by electrospraying
avascularised	A scaffold without a vasculature
binary	Image containing only two pixel intensity values - black and white
calcification	Abnormal calcium depositions causing the tissue/surface to harden
cellularisation	The formation/infiltration of cells within a scaffold
circumferential	Direction going around the circumference of a rotating collector
coherency	Image processing measurement of fibre alignment from SEM images
compliance	Mechanical responsiveness of vessel to an internal pulsating force
decellularised	A scaffold made from tissue that were striped from all cells
differentiation	A process by which a cell develops into a more complex type
electrohydrodynamics	Interdisciplinary study of fluid dynamics and electrostatics
explant	Implant retrieved from animal model at a selected time point
femoral	Refers to the main artery that supplies blood to the leg
haemodialysis	Artificial blood purification for poorly functioning kidneys
hydrophilic	A polymer or salt soluble in water/polar solvents
hydrophobic	A polymer or salt not soluble in water/polar solvents
hypertension	High blood pressure
in situ	Investigations performed in its natural/original context
in vitro	Investigations performed outside of its biological context
in vivo	Investigations performed on living organisms
longitudinal	Direction going along the length of a rotating collector
lumen	Inside surface
off-the-shelf	Medical devices that are readily available
popliteal	Refers to the artery found in the fossa behind the knee
porogen	A particle acting as a space holder to create additional pores
proliferation	The process by which cells are growing in numbers
restenosis	The narrowing of a blood vessel
semi-dilute	Polymer solutions with a certain degree of macromolecular overlap
Taylor cone	Cone-shaped droplet at a critical charge during electrospinning
thrombogenicity	Tendency of a material in contact with blood to form a clot
thrombosis	Blood clot formation that is blocking the device from the inside
vascular graft	Device to replace or repair arteries/veins - vascular prostheses
vascularisation	The formation of new blood vessels within a scaffold

1 Introduction

This chapter provides background information on the need for medical devices aimed at cardiovascular disease treatment. The subsections to follow covers a literature review on topics related to the development of tissue regenerative scaffolds using synthetic biomaterials and bioactive molecules. Thereafter, a research proposal is framed in the form of a problem statement and project objectives.

1.1 Background

1.1.1 The burden of cardiovascular diseases

Cardiovascular disease (CVD) is the number one killer of humankind since the 1990's. Globally, one out of every three deaths (~16 million human lives per annum) is caused by heart related diseases [1]. The mortality rate of CVD among developing economies (which accounts for 80-85% of the global population) is on the rise [1, 2]. Estimates show that Sub-Saharan African countries, such as South Africa, could see a 41% increase in the number of deaths (ages 35-65 years) due to CVD within the period of 2000 to 2030 [3]. It is believed that the cumulative adoption of a western life style (smoking, physical inactivity, poor nutrition and obesity) that lead to hypertension, high blood cholesterol, diabetes mellitus, metabolic syndrome and chronic kidney disease could be at the root of the expected incline of CVD fatalities [4]. Nevertheless, these trends are likely to result in higher patient numbers and may set fragile economies under immense pressure. An urgent need for next generation cardiovascular treatments and devices are therefore highlighted. New solutions should be focused on therapies that would reduce hospitalisation and recovery times, minimise re-admissions, lower cost and improve the patient's overall quality of life [5].

1.1.2 Medical devices for cardiovascular therapies

Clinicians turn to implantable medical devices when conventional, lower risk therapies (like corrective surgery) have failed or is insufficient to treat end-stage CVD patients [6]. Arteriovenous (AV) access shunts, bypass grafts, heart valves, pacemakers, stents and ventricular assist devices are principle medical devices for invasive CVD treatments (two examples of such devices shown in Figure 1.1).

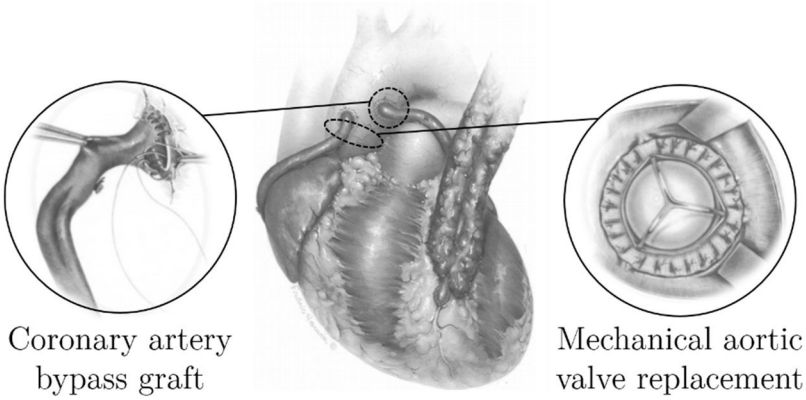

Figure 1.1: Examples of implantable medical devices for the heart. On the left, a vascular graft (great saphenous vein) and on the right, a mechanical heart valve (Starr-Edwards caged ball valve). Illustrations were adapted from [7].

Prosthetic heart valves (mechanical or bioprosthetic) are used to replace diseased valves of patients that have valvular heart disease (VHD). Severe stenosis (narrowing of the valve orifice and stiffening of the leaflets) in high pressure sites like the mitral or aortic valve, or less often tricuspid/pulmonary valves, of patients with VHD disorders may require valve replacements. Rheumatic heart disease (RHD) is a VHD that mainly occurs in developing countries, with numbers on the rise, and may lead to the need for mitral/aortic valve replacement [8, 9]. A ventricular assist device (VAD) is an electromechanical pump designed to aid poor performing chamber(s) of the heart with blood circulation to the rest of the body. Patients that experienced heart failure (HF) may require the implantation of a VAD (commonly aiding the main pumping chamber of the heart, i.e. the left ventricle) to accommodate for weak cardiac outputs [10]. Implantable pacemakers provide external electrical stimuli to strategically excite heart tissues of patients with cardiac arrhythmia-related symptoms (abnormal heart beats).

Patients with arrhythmia could have insufficient blood supply to heart muscles due to arteriosclerosis (thickening of the arterial wall), called coronary artery disease (CAD) [11]. Besides the narrowing of arteries around the heart, arteriosclerosis can also occur in lower limb regions (e.g. femoral/popliteal arteries) which is referred to as peripheral artery disease (PAD). Vascular stents (cylindrical wire-framed structures) are catheter deployable implants that forcefully open, and retain, the lumen of constricted arteries of CAD/PAD patients [12]. Individuals suffering from end stage renal disease (ESRD) undergo regular haemodialysis (external blood purification) due to kidney failure. Dialysis is often performed through vascular access provided by an arteriovenous (AV) access shunt. AV shunts are implantable tubes that connects arterial and venous blood flow, sutured to deep veins and arteries in the fore/upper arm, to generate a higher flow rate required by the artificial kidney machine (i.e. the dialyser) [13]. Bypass grafts, also tubular devices, are used to replace or re-direct blood flow (bypass) of restricted/occluded blood vessels in CAD/PAD patients [14]. Although, bypass surgery could be considered as a last resort procedure after lower risk therapies (such as vascular stenting) have reached its threshold of repetition or were unable to allow sufficient blood flow. The related CVD, estimated annual need and therapy cost for each of these devices are summarised in Table 1.1.

Table 1.1: The global need for principle CVD medical devices. End stage renal disease (ESRD), coronary artery disease (CAD), peripheral artery disease (PAD), valvular heart disease (VHD), rheumatic heart disease (RHD) and heart failure (HF). Adapted from [15, 16].

Implantable device	Related CVD	Annual need	Cost (bil.USD/yr.)
Arteriovenous shunts	ESRD	1 028 000	59.4
Bypass grafts	CAD/PAD	750 000	24.0
Heart valves	VHD/RHD	244 000	14.6
Pacemakers	CAD	669 000	16.7
Stents	CAD/PAD	1 750 000	36.8
Ventricular assist devices	HF	250 000	49.3
Total		4 691 000	200

Accounting for 40% of the total annual need and therapy costs (1.8 million and 85 billion US dollars respectively), vascular prostheses (AV shunts plus bypass grafts)

have the highest demand and financial burden of the principle devices listed in Table 1.1. Medical advances on vascular grafts (VG) could play a significant role in the fight against CVD. Therefore, it is important to investigate technologies that have the potential to improve VG in ways that would align with the challenges set out in section 1.1.1.

1.1.3 The challenges of implantable devices

Despite the overall success of implantable medical devices, there are a vast number of reports submitted to regulatory affairs of complications or adverse outcomes each year. More than 900 000 of such cases were reported to the United States Food and Drug Administration (FDA) in 2015 alone [17]. Although many other factors could lead to device failure (such as inadequate sterilisation [18, 19], compliance mismatch [20, 21], mechanical fatigue [22], restenosis [23, 24] or thrombosis and calcification [9, 25, 26] in cases of VG), many of the complications can be attributed to poor healing due to fibrotic encapsulation (associated with the human's foreign body response -FBR) [27–32]. The underlying complication involves an avascularised fibrous layer that isolates the implant from the surrounding tissue. After merely 2 weeks of implantation, fibrous encapsulation may wall off biosensors/pacemakers leads, shut down drug delivery systems, occlude and inhibit endothelialisation of vascular grafts or cause an acute inflammatory response. This is troubling due to complicated revision surgeries that may follow which could compromise the patient's life. It is of even greater concern that biocompatible materials (FDA approved biomaterials) were used in the construction of these failed medical devices. However, it is known that one biomaterial could be compatible in a particular application and may present adverse effects in another [33]. Therefore, leading experts (DF.Williams [34], R.Langer [35], P.Zilla [29, 36] and B.Ratner [37]) have suggested that healthy biological integration between a medical device and its host is achievable when significant emphasis is carried out on biomaterial microarchitecture and its surface chemistry at the implant/tissue interface. Tissue

engineering is a discipline dedicated to provide solutions to overcome biocompatibility issues and eventually improve the long-term performances of the already millions of implantable CVD devices.

1.1.4 The tissue engineering concept

Tissue engineering (TE), as defined by DF.William [34], is the creation of new tissue for the therapeutic reconstruction of the human body, by the deliberate and controlled stimulation of selected target cells through a systematic combination of molecular and mechanical signals. Or, as explained by R.Langer [35], newly functional living tissue fabricated using living cells, which usually associated, in one way or another, with a matrix or scaffolding to guide tissue development. Regardless of the official definition, current day TE can conveniently be subdivided into two main approaches: i) classic *in vitro* TE or ii) *in situ* TE [38, 39]. The main differences are summarised in Table 1.2.

Table 1.2: A comparison of tissue engineering approaches. Adopted from [39]

	In vitro TE	*In situ* TE
Off-the-shelf availability	Possible	More likely
Scalability	Difficult	Easier
Clinical translation	Complex	More likely
Biomaterials	Extensively used	Extensively used
Bioreactors	Yes	Not commonly used
Chemical factors	Yes	Yes
Cells (pre-seeding)	Yes	Not commonly used
Cost	High	More affordable

Classic *in vitro* tissue engineering entails a 3D biomaterial (with or without bioactive molecules) that is seeded with targeted cells, usually harvested from the eventual host, and cultured in a bioreactor until a desired bulk of living tissue is developed before implantation. On the other hand, *in situ* tissue engineering typically involves a cell-free 3D biomaterial (with or without bioactive molecules) that is immediately implanted into the host (as is) and uses its own body as the cell source and natural bioreactor to populate the structure and grow into functional native-like organ tissue (the latter approach may also be considered as a form of regenerative medicine [32, 40, 41]). This

idea is more practical in a clinical setting, especially in developing countries, as it would require less time and resources (skills, equipment and funds) to generate an implant-ready device compared to *in vitro* TE. A graphical representation of the two TE strategies are displayed in Figure 1.2 (blue and red arrows are for *in vitro* and *in situ* TE respectively).

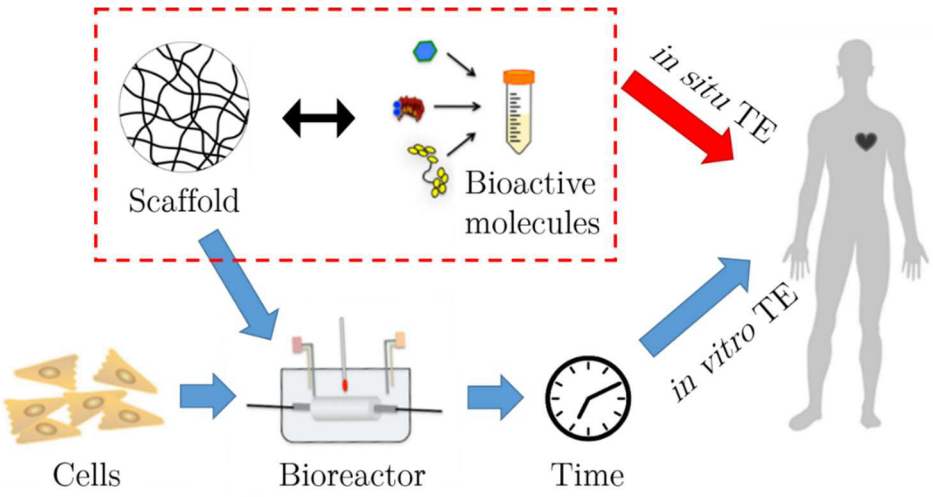

Figure 1.2: Graphical representation of tissue engineering approaches. Blue arrows indicate *in vitro* TE and the red arrow *in situ* TE respectively. Altered from the original sketch [39].

Although simplified *in vitro* TE approaches have already gained some clinical success (e.g. heart valve [42–45] and vascular prostheses [46, 47]), it will be advantageous to develop 'off-the-shelf' products that can be implanted with immediate effect along with the embedded signals (mechanical and chemical) that would allow for complete *in vivo* tissue regeneration over time.

1.1.5 Design parameters for tissue engineered scaffolds

Despite the different approaches towards TE, the reconstruction, repair or replacement of tissue constructs (e.g., nerve, tendon, cartilage, bone or cardiac/smooth/skeletal muscle) require a porous three-dimensional structure that would ultimately house the cells either permanently (non-degradable) or preferably, only temporarily allow cells and then disappears (degradable biomaterials). Researchers have widely reported [29, 34, 36, 37, 48–50] that the microenvironment of these scaffolds plays a substantial role in stimulating the desired cellular response for the intended tissue remodelling. Ideally,

scaffold microarchitecture should be designed to closely match that of the natural extracellular matrix (ECM) of the targeted tissue. The ECM act as a media that accommodates intercellular communication. It is enriched with cell surface receptors (e.g., integrins, laminin, and syndecans) and structural proteins (e.g., collagens, laminins, fibronectin, vitronectin, and elastin) which allow cellular adhesion, migration, proliferation and differentiation [51]. The natural ECM can be observed and studied when tissue constructs are decelullarised. A porous network of fibres (wave-like strings made up of collagen/elastin) can be seen in Figure 1.3 for a decellularised a) canine aorta and b) the leaflet of a porcine aortic valve.

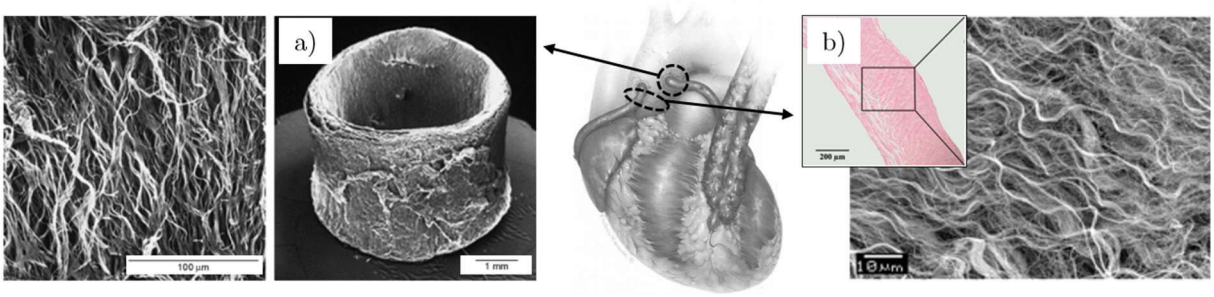

Figure 1.3: The fibrous network of natural extracellular matrices. Decellularised tissue: a) longitudinal fibres (canine aorta [52]); b) wave-like fibres of a heart valve leaflet (porcine aortic valve [53]).

While mimicking the architecture of the targeted tissue's ECM, tissue engineers should also consider the following parameters for developing a TE scaffold [54]:

- Biocompatibility - appropriate biomaterial selection (either natural or synthetic origins, but should be non-toxic with minimal induced immunogenic responses).
- Porosity and pore size - sufficient interconnectivity and void spaces to allow for the desired cells to infiltrate/migrate with additional spaces to also accommodate waste/nutrient transportation.
- Surface area - a high surface area to volume ratio is desirable for optimising cellular attachment sites and has the additive advantage of optimising drug delivery.
- Surface properties - suitable surface chemistry and morphology that would promote protein absorption and cellular adhesion, growth and proliferation.

- Bioactivity - ideally, the scaffold should provide bioactive cues to residing cells with beneficial effects towards tissue generation.
- Mechanical properties - the structure should be able to support the cells and have a mechanical performance that matches that of the native tissue.
- Biodegradability - preferably, the scaffold should be completely resorbed after it has full fill its mechanical responsibilities.
- Cost - the manufacturing process should have a viable translatable cost involved.

Among the techniques developed to manufacture porous TE scaffolds (e.g., phase inversion/porogen extraction [55], phase separation [56], self-assembly [57], gas foaming [58], salt leaching [59], freeze drying [60] and 3D printing [61]), electrospinning is a versatile process that produces fibrous scaffolds and has the potential to accommodate most of the design parameters set out in the above list. An electrospun vascular graft [62] and heart valve [63] along with representative images of their respective nano-and-micro-fibrous networks are on displayed in Figure 1.4.

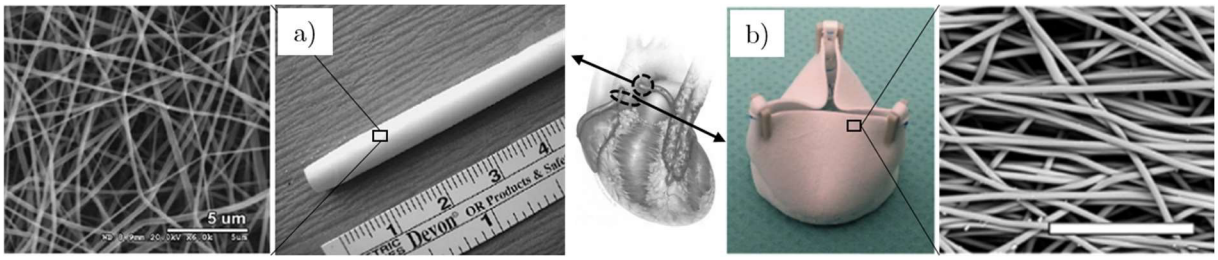

Figure 1.4: Tissue engineered electrospun scaffolds for implantable medical devices. a) small diameter vascular graft [62] and b) pulmonary prosthetic heart valve [63]. SEM scale bars are 5 and 50 µm.

Although significant advances have been made in the field of TE scaffolds as medical devices (using electrospinning and other methods), the following are key scientific challenges that remain unsolved [64]:

- Minimise immune response,
- Control inflammatory reaction,
- Reduce thrombogenicity, and ultimately,
- Favour cellular infiltration, remodelling and growth.

1.2 Applied electrohydrodynamics for tissue engineering

This section introduces electrohydrodynamics and how it can be applied as an additive manufacturing process for producing micro to nano-scaled particles and fibres towards the development of 3D tissue engineered scaffolds. Furthermore, the challenges and latest advances of electrospun TE scaffolds are reviewed.

1.2.1 Introduction to electrohydrodynamics

In the year 1600, William Gilbert (Figure 1.5.a) published a book on his observations of static drops of water deforming into cone shapes when approached by a rubbed (charged) piece of amber [65, 66]. Lord Rayleigh, in 1882, was the first to describe the relationship between the surface tension of a droplet and the electrostatic forces acting on it within an electric field [67]. He referred to the cone shaped droplet as being in a 'critical' state when the electrostatic forces attempt to overcome the surface tension of the liquid at a certain charge. More than three centuries after Gilbert's observation, John Zeleny [68] and Sir Geoffrey Taylor [69, 70] re-investigated the critical sate of water/glycerine droplets fed through a small capillary and subjected to an electric field (Figure 1.5.b). Taylor in particular [69] derived theoretical models and experimentally confirmed that the critical cone shape of a water droplet was angled at 49.3° (now known as the Taylor cone). Furthermore, they found that a high enough potential created an above critical charge that caused a thin jet of fluid to shoot from the apex of the Taylor cone towards the counter electrode (Figure 1.5.c) [70].

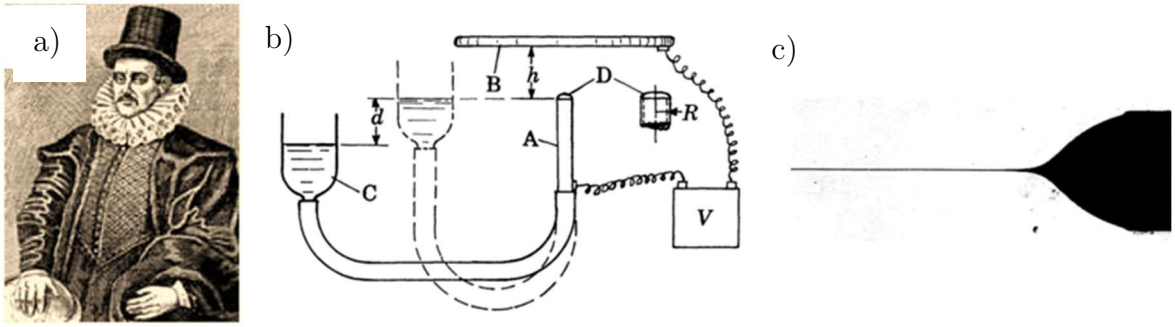

Figure 1.5: A brief history of electrohydrodynamics. The English medical doctor a) William Gilbert (1544-1603)[66]; b) a typical electrospinning setup used by Sir G. Taylor and c) a Taylor cone published by Taylor himself in 1969 [71].

During flight, the authors observed that the straight jet rapidly became unstable (in a fashion that resembles pushing instead of pulling on a piece of string) and eventually, dissipated into a cascade of droplets. These early discoveries laid the foundations of electrohydrodynamics (EHD), the study of electrically charged fluids in motion [72]. Following the work of Taylor and peers, researchers such as L. Larrondo *et al.*[73–75], D.H. Reneker *et al.*[76–82], A.L. Yarin *et al.*[78, 79, 81–84] published influential studies that started in 1980, 1990 and 2000 (respectively) which brought a new light to EHD. Their focus was on exploiting a process that applied EHD to semi-dilute polymer solutions with a sufficient degree of macromolecular entanglement that would resist jet break-up during the instability phase. Under the right conditions, such experiments produced continuous polymeric nanofibers - a phenomenon we now refer to as electrospinning. Soon, electrospinning became widely adopted in research areas such as microfiltration for air [85] or water systems [86], composite materials for structural reinforcement [87], sound attenuation [88], energy generation from solar [89] or mechanical sources [90], energy storage [71], high intensity heat exchangers [91], biosensors [92] and tissue engineering [93]. Electrospinning is attractive to these applications due to its relatively low manufacturing cost, upscaling potential and in particular, its ability to produce structures with a high surface area to mass ratio [82].

1.2.2 Electrospinning of polymeric fibres

Current electrospinning systems are fundamentally unchanged since their discovery (e.g. Figure 1.5.b). A basic experimental setup for producing polymeric fibres include a semi-dilute solution that is supplied (e.g. 0.1-10 ml/h) through a highly charged (e.g. 30-500 kV/m) capillary with a grounded collector situated at some distance away (e.g. 50-350 cm) [94, 95]. Applying enough voltage causes solution from the tip of the capillary to form an above critical Taylor cone. An initial jet accelerates from the cone and follows a unidirectional path while becoming narrower as it travels towards the counter electrode. Consequently, surface charge density escalates and induces

axisymmetrical instabilities (wave formed) to occur down the length of the jet [78, 96, 97]. Statistical variance of surface charge modulation causes same charges to repel one another, thereby inducing radial forces. The lateral movements amplify the repelling effect which evolves into a spiral with an increasing radius, while jet radius continuous to decrease, towards the counter electrode (a flat, rotating or custom-made collector [98]). This process could repeat itself by developing secondary, tertiary [82] or even a fourth series [78] of coils (depending on solution properties) before the solvent evaporates and the jet solidifies into polymeric fibres. It was estimated that the initial jet could experience velocities and strain rates in the range of 1-15 m/s [99–101] and 10^5/s [82] respectively, resulting in solid fibres after ~25 ms that are less than 500 nm in diameter [82, 102, 103]. The fibre formation processes is summarised in Figure 1.6.

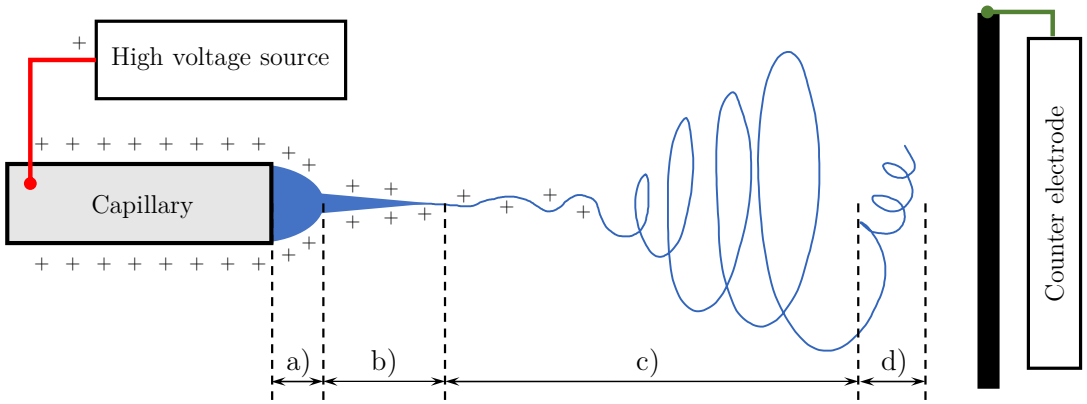

Figure 1.6: Fibre formation during electrospinning. a) Taylor cone, b) straight jet region; and unstable region of c) primary d) secondary coil formation.

In contrast to the simplistic experimental design, controlling the outcome of the electrospinning process is complex. Numerous factors could affect the fibre formation process. Thus, it is important to identify and understand the existing control parameters for the development of application specific electrospun structures (e.g. control over porosity, inter-fibre pore sizes, average fibre diameter and/or fibre alignment). Due to polymer-solvent specific properties and complex inter parametric relationships, theoretical models are not yet capable of predicting the outcome of the electrospinning process [102]. Therefore, the following subsections explored a few parameters from literature to provide an empirical overview of their influences. Table

1.3 is a list of parameters identified according to the following sub-categories: solution, climate or processing parameters.

Table 1.3: Controllable electrospinning parameters

Solution	Climate	Processing
Viscosity	Ambient temperature	Collecting distance
Polymer concentration	Relative humidity (RH)	Needle diameter
Polymer molecular weight		Applied voltage
Conductivity		Flow rate
Surface tension		Collecting speed
Temperature		
Solvent viscosity		
Solvent surface tension		
Solvent dielectric constant		
Solvent vapour pressure		

1.2.2.1 Electrospinning solution

Solution viscosity is one of the main controllable parameters for influencing the resultant electrospun fibre diameter [93, 94, 98, 102, 104, 105]. In general terms, a higher viscosity is known for producing thicker fibres. Polymer concentration and molecular weight are two common properties used for solution viscosity adjustment, and thereby controlling fibre diameter. Several studies have reported that fibres with larger diameters were produced at higher polymer concentrations [106–109]. For example, Yang *et al.* showed that fibre diameters increased from 0.7 µm to 3.5 µm when the concentration of PLLA (300kDa), dissolved in DCM:DMF at 70:30, was increased from 2 to 5wt% [109]. At a constant concentration, changing the molecular weight of the polymer is known for inducing/reducing the degree of beading and altering the diameter of electrospun fibres due to its strong influence on solution viscosity [110–113]. Tao *et al.* doubled the thickness of electrospun fibres (200 to 400 nm) when the molecular weight was increased from 10 to 18 kDa at 30wt% concentration of PVA in distilled water [112]. This effect was also confirmed by others [111, 114]. Despite the ease of controlling fibre diameter by varying solution viscosity (a power-law relationship [107]), it should be noted that such effects only exist within a certain range. Viscosities

that are too high (e.g. >4000 cPoise) might resist the formation of a Taylor cone and are physically unspinnable. On the other hand, a viscosity below a certain point (e.g. <800 cPoise) might not have sufficient polymer chain entanglements (due to concentration and/or the molecular weight being too low) to resist jet break-up after Taylor cone formation [98]. In such a case, beads or beaded fibre are formed instead of smooth cylindrical fibres. An ideal concentration (φ_{fibres}) at which smooth fibres are formed is unique to each electrospinning solution.

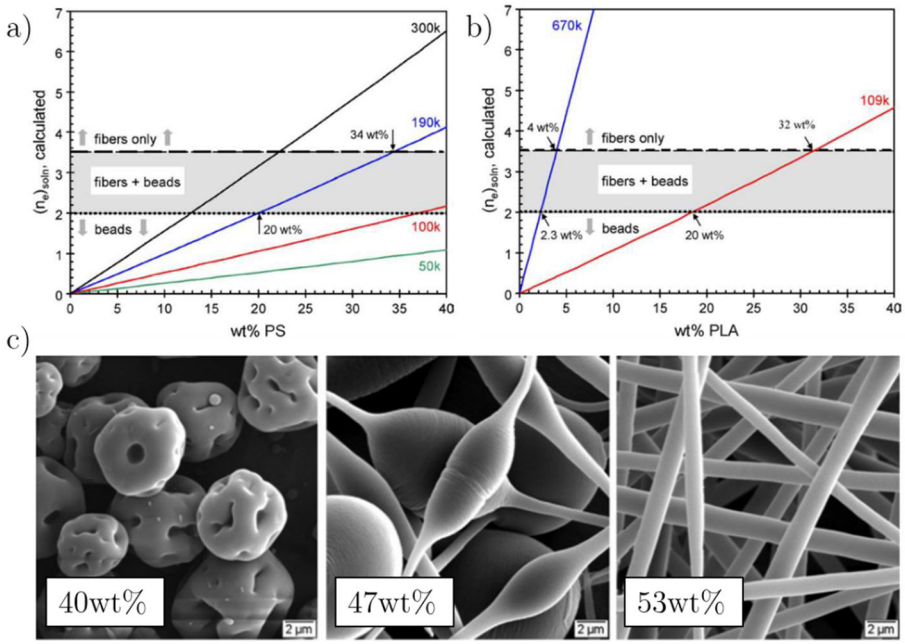

Figure 1.7: Chain entanglement as a function of concentration and molecular weight. Critical concentrations for a) PS/THF and b) PLA(DMF:DCM) [115]. The lines represent different molecular weights and fibre formation is indicated by the dashed line at $(n_e)_{solution}$= 3.5 and higher. c) SEM images of PS(19 kDa) electrospun at different concentration (40-53%) from DMF [116].

Molecular weight and polymer-solvent interactions (e.g. solubility) are the main factors determining φ_{fibres} [115]. An entanglement number, $(n_e)_{solution}$: equation (1-1) from [117], is often used to describe the concentration region for fibre formation $\varphi > \varphi_{fibres}$ of a particular electrospinning solution; where M_w is the molecular weight of the polymer and M_e the solution entanglement molecular weight:

$$(n_e)_{solution} = \frac{\varphi M_w}{M_e} \quad (1\text{-}1)$$

Shenoy *et al.* [115] and later Eda *et al.* [116], investigated the morphological influence

of chain entanglement on electrospun PS and PLA of different molecular weights at various concentrations (examples shown in Figure 1.7). Their semi-empirical model predicted that smooth fibres are formed when $(n_e)_{solution} > 3.5$ [115], unless M_w<100 kDa and/or φ >30wt% [116]. Although molecular weight does influence fibre morphology and governs at which point φ_{fibres} would be, concentration is a more practical parameter for fine tuning fibre diameter.

A solution with a higher conductivity (K) has a greater charge carrying capacity and would experience more elongation during the fibre formation process resulting in thinner fibres [93, 95, 98, 107, 118]. Solution conductivity can be controlled by strategic selection of solvent(s) and/or by salt additives. Solvents with a higher dielectric constant (ε) are associated with a higher conductivity $K \propto e^{-\frac{1}{\varepsilon}}$, (also known as the Nernst-Thomson rule) [119]. Young *et al.* showed that the inclusion of 2wt% salt (benzyl triethylammonium chloride) reduced the average fibre diameter of electrospun PLGA/chloroform from 760 to 450 nm [120]. Moreover, the authors showed that fibres electrospun from PLGA/HFIP (ε = 17.8) produced thinner fibres (270nm) compared to the fibres spun from chloroform (ε = 4.8). Increasing solution conductivity shifts the minimum concentration for producing smooth fibres (φ_{fibres}) to a lower point, as shown by Young *et al.* [120]. This explains why many observed reduced beading when fibres were spun from more conducting solutions [121–124]. Solution conductivity could also be used to control the fibre orientation of electrospun fibres on a rotating collector. Sun *et al.* demonstrated that a high degree of fibre orientation was obtainable by electrospinning PEO from a poorly conductive solution (prepared by solvent selection, chloroform, ε = 4.8) when compared to the collecting patterns of a more conductive PEO solution (water, ε = 79.7) [125].

The surface tension of an electrospinning solution can be altered by strategic solvent selection and/or adding surfactants [104, 111, 116, 126–128]. After the Taylor cone is formed, a solution with a higher surface tension (an elastic force attempting to

shapeshift the jet back into a droplet) dominates the electrostatic forces that are trying to elongate the solution, resulting in spherical/elongated beads or beaded fibres (depending on polymer entanglement) [123, 129, 130]. Heating the electrospinning solution reduces its viscosity and increases the electrical conductivity (assuming semi-conductor behaviour). As expected, several authors have observed thinner fibres when electrospinning solutions at higher temperatures compared to those processed as room temperature [107, 131–133]. Wang *et al.* controlled the solution temperature by circulating heated silicon oil through a custom-made double walled syringe [132]. The average diameter of the fibres they captured while electrospinning a solution of PDLLA (20wt%, DMF) at 45°C were nearly 60% reduced (503 to 318 nm) compared to those spun from a room temperature (25°C) solution.

Solvent selection can be a powerful tool in electrospinning control. Ideally, all available solvents should be identified that dissolves the selected polymer at room temperature. Thereafter, properties such as viscosity, surface tension, dielectric constant, boiling point/vapour pressure etc. should be taken into consideration before making the final selection. For comparison, properties of twenty-four common organic solvents are summarised in Figure 1.8 (ranked according to an increasing dielectric constant). A solvent with a higher viscosity will automatically increase the overall solution viscosity and therefore, would produce thicker fibres when compared to a same concentration solution prepared using a less viscous solvent [106, 123]. In the same fashion, a solvent with a lower dielectric constant will result in a less conductive spinning solution and thereby produce thicker fibres [125]. A solvent's surface tension may influence the overall surface tension of the solution and, as mentioned before, could result in fibre beading [123]. The volatility (in terms of boiling point/vapour pressure) of the electrospinning solvent system could induce significant morphological alterations. Solvents with a higher boiling point (lower vapour pressure) have a greater difficulty to evaporate during the instability phases compared to a more volatile solvent system. If the boiling point is too high, insufficient evaporation may result in 'wet' or fused

fibres instead of smooth cylindrical fibres [107, 134–136]. Matsuda [135] and Kidaoki *et al.* [134] showed that increasing the content of DMF of a DMF:THF co-solvent system (with boiling points of 153 and 66°C for DMF and THF respectively), resulted in more fusion of segmented polyurethane electrospun fibres due to an overall increase in solvent boiling point.

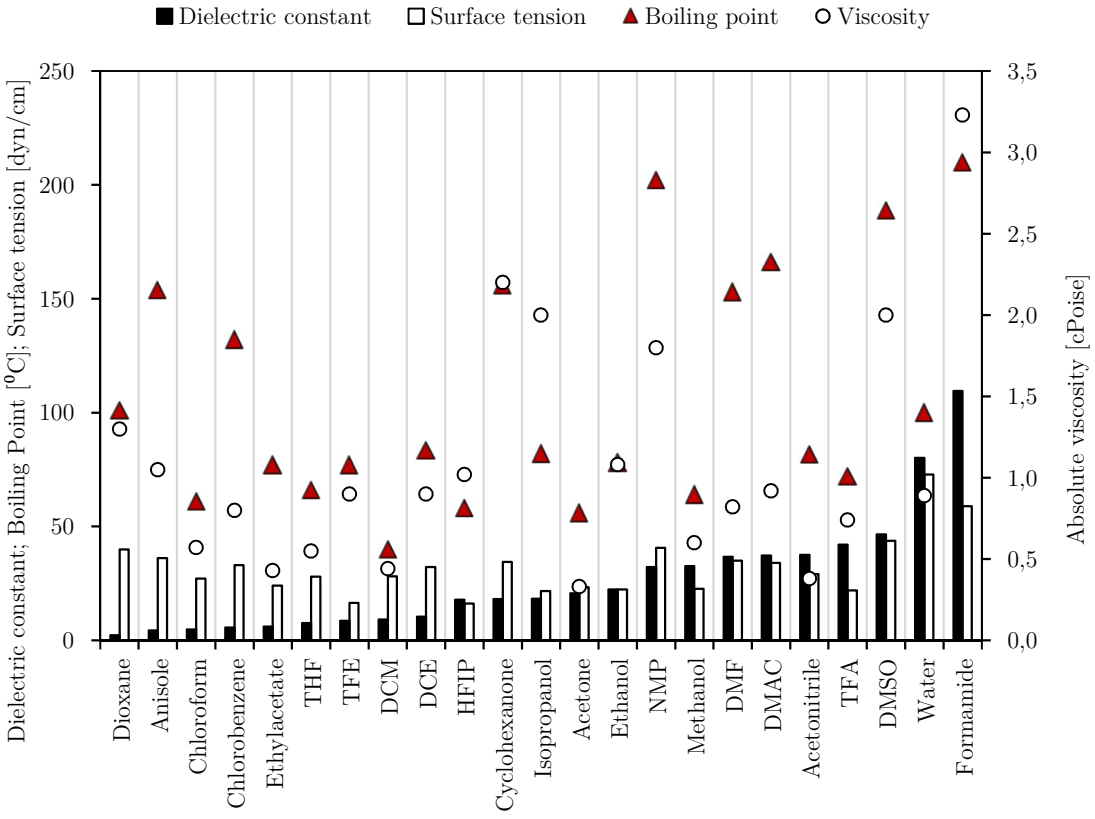

Figure 1.8: Organic solvent properties: a selection for experimental electrospinning. Abbreviations: tetrahydrofuran (THF), trifluoro acetic acid (TFA), trifluoroethanol (TFE), dichloromethane (DCM), dichloroethane (DCE), hexafluoro isopropanol (HFIP), methyl pyrrolidone (NMP), dimethylformamide (DMF), dimethylacetamide (DMAC) and dimethyl sulfoxide (DMSO). Numerical data [137] can be found in Appendix A1.

Considering the multitude of solvent specific effects, and their mutual dependencies, solvent selection is vital for achieving a desired outcome. The fluorinated alcohol 1,1,1,3,3,3-Hexafluoro-2-propanol (HFIP) is known for being one of the most popular electrospinning solvents [93, 94, 138, 139], and was used for many synthetic (e.g. Pellethane® [140], PHB [141], PLCL [142], PGA [120], PLA [143], PLGA [144], PGS [145] and PCL [104]) and natural (e.g. collagen [146], fibrinogen [147], silk fibroin [148] and chitin [149]) polymers towards development of TE scaffolds. Reasons for its

popularity as a fibre producing solvent may include: its ability to dissolve a wide array of polymers/drugs, mid-range dielectric constant (ideal for producing nanofibers), relatively low boiling point (a fast evaporation rate), low surface tension (less likely to form beads) and being versatile as a co-solvent with almost any other organic solvent (miscible with polar-opposites, e.g. water and chloroform). It is therefore not surprising to use co-solvent systems made up of those from different ends of the spectra to balance each other's short comings. For example, combining low and high dielectric constant or boiling point solvents such as DMF:$CHCl_3$ [150], MeOH:$CHCl_3$ [151, 152] or DMF:THF [134, 142, 153].

1.2.2.2 Electrospinning climate

The ambient conditions (temperature and humidity) are known to affect solvent evaporation rates and filament flow dynamics [104]. Electrospinning in a warmer environment decreases solution viscosity and enhances solvent evaporation rate, thereby producing thinner fibres. Zhang *et al.* produced fibres with 50% reduced diameters by increasing the ambient temperature from 35 to 50°C while electrospinning aqueous gelatin solutions [154]. Thinner fibres due to higher ambient temperatures were also reported by others [155, 156]. Conversely, increasing the relative humidity (RH) of the electrospinning environment has been observed to produce thicker fibres [157–159]. Huang *et al.* showed that increasing the RH of 0 to 50/60% while electrospinning polyacrylonitrile (PAN) or polysulfone (PSU) dissolved in DMF resulted in thicker fibres [158]. The average diameter was increased from 150 to 630 nm and 1.15 to 3.58 µm for PAN and PSU fibres respectively. Such an effect could be explained by less whipping of the filaments before solidification. The higher moisture content (available water molecules at a high RH) between the needle and the collector caused more electrostatic discharge to occur on the surfaces of incoming filaments [159], thereby reducing the degree of stretching (whipping) when compared to observations at a lower RH. Moreover, it was found that electrospinning at higher RH may also alter fibre surface roughness [157–159]. Casper *et al.* found that electrospinning of polystyrene

(PS) at >30% RH induced surface nanopores that increased in size and frequency as RH was further increased [157]. It should be noted that RH's influence on the outcome of electrospun structures strongly depends on polymer hydrophobicity and solvent properties (vapour pressure and its miscibility with water) [105]. Therefore, an appropriate solvent system and constant awareness/control of ambient conditions should be considered when designing and reproducing eletrospinning experiments.

1.2.2.3 Processing parameters

Processing parameters for electrospinning control can be categorised into pre-processing (constant during the process) and real-time adjustable parameters. Depending on the experimental setup, pre-processing parameters could include collecting distance and needle diameter while examples of real-time control parameters are the applied voltage, flow rate and colleting speed. The air gap between the needle and the collector has a direct influence on the time for solvent to evaporate and the strength of the electric field. At short distances, solvent might not have sufficient time to evaporate completely and could result in 'wet' or fused fibres [160]. Moreover, fibre beading has also been associated with a collecting distance being too close to the collector [161]. Increasing the working distance creates space for additional instabilities to occur and therefore could produce thinner fibres [106, 162]. Although, many have observed an increase in the average fibre diameter attributed to significant less fibre stretching/whipping due to a weaker electric field at distances further as appose to closer from the Taylor cone [160, 163–165]. Needle diameter is yet another control parameter with contradicting observations. Predominantly, fibre diameter was found to be directly proportional to the needle diameter [166–169] while a minority suggested an inverse relationship [170] or that no correlation exist [171]. According to the electrospinning model developed by Thompson *et al.*, a needle with a larger diameter will produce a Taylor cone with a larger initial jet radius and, essentially, would produce thicker fibres compared to those spun from a smaller orifice [169]. This assumption was experimentally confirmed [166–168]. The applied voltage has multiple influences on the electrospinning process, and

again, not without associated contradictions. In general, it was found that a higher applied voltage reduced electrospun fibre diameters [106, 111, 160, 172]. This trend is expected as greater electrostatic forces, caused by a higher electric field, would promote more solution stretching and thus, produce thinner fibres. Increasing the electric field could also induce fibre beading [114, 130, 173]. Ki *et al.* observed beaded fibres and an increase in their frequency when gelatin-formic acid was electrospun at >20 kV while smooth fibres were found at a lower voltage (7.5 kV) [173]. In such cases, fibre beading is said to be the result of an unstable Taylor cone [114], which usually forms on the edges of the needle and not in the centre as it would for a stable cone. It is therefore necessary to find the optimal voltage (specific to each electrospinning solution) for producing smooth cylindrical fibres. A minimum flow rate exist that would sufficiently replace the volume of solution that gets drawn from the needle at a set of constant electrospinning conditions (e.g. working distance, voltage, needle diameter etc.) [174]. Such a flow rate is required to maintain a stable Taylor cone and therefore, for the production of uniform (bead free) fibres [175]. Although small adjustments to the flow rate may not have a significant effect on the outcome (e.g. electrospinning PCL at 0.6-1.5 ml/h [176]), increasing the solution feed rate has been observed to increase the average fibre diameter [132, 169, 177, 178]. Milleret *et al.* showed that DegraPol® fibres of 4 µm could be produced at a flow rate of 4 ml/h while thicker fibres (10 µm) were obtainable at 12 ml/h [178]. This is mainly due to a larger initial jet radius caused by an increase of solution volume at the tip of the needle which lead to a thicker fibre formation [169]. A further increase in flow rate might result in ribbon like or fused fibres due to insufficient solvent evaporation [105, 179]. In the case of a rotating collector, collecting speed can be used to alter the orientation of deposited fibres and thus, tailor the mechanical/architectural properties of electrospun scaffolds. Fibre alignment is directly proportional to collector face velocity [178, 180–183]. Moreover, collecting speed was also shown to influence the average fibre diameter (higher speeds resulted in thinner fibres) [125, 178]. Sun *et al.* found that the average diameter of

electrospun fibres (PEO/$CHCl_3$) decreased with increasing collector face velocity (0.6-16 m/s) until it reached a point where diameter remained constant despite a faster speed (1.6 µm and reaching a plateau of 658 nm at 12 m/s) [125]. Considering all mentioned factors, Table 1.4 is a summary for electrospinning parametric control.

Table 1.4: Parametric control of electrospun scaffold morphology.

Desired outcome	Parameter(s) to upregulate	References
Reduce fibre diameter 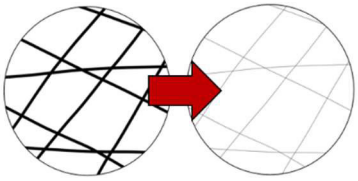	Solution conductivity	[93, 95, 98, 107, 118]
	Solution temperature	[107, 131–133]
	Ambient temperature	[154–156]
	Applied voltage	[106, 111, 160, 172]
	Collecting speed	[125, 178]
	Collecting distance	[106, 162]
Increase fibre diameter 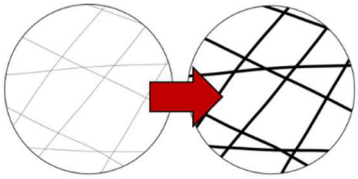	Flow rate	[132, 169, 177, 178]
	Polymer concentration	[106–109]
	Polymer molecular weight	[111, 112, 114]
	Needle diameter	[166–169]
	Ambient humidity	[157–159]
	Collecting distance	[160, 163–165]
Reduce fibre fusion 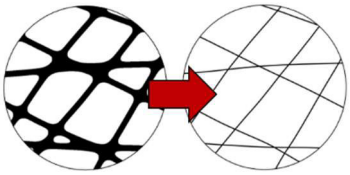	Collecting distance	[160, 179]
	Solvent vapour pressure	[107, 134–136]
Induce fibre fusion 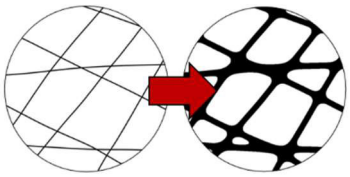	Flow rate	[105, 179]
	Solvent boiling point	[107, 134–136]
Reduce fibre beading 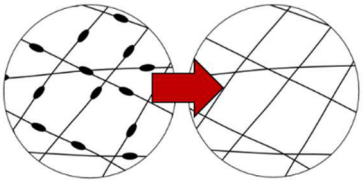	Solution conductivity	[121–124]
	Polymer concentration	[106–109]
	Polymer molecular weight	[110–113]
	Surfactant concentration	[104, 116, 126–128]
	Collecting distance	[160, 161]
Enhance fibre allignment 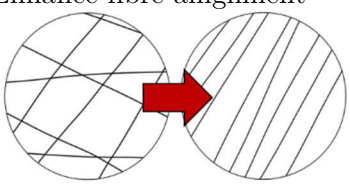	Collecting speed	[178, 180–183]
	Solution resistivity	[125]

1.2.3 Electrospraying of polymeric particles

Electrospraying is fundamentally the same process as electrospinning. While electrospinning produces polymeric fibres, electrosraying is a process for creating nano or micro particles. The main distinguishing variable between electrospraying and electrospinning is the molecular entanglement number of the processing solution. At a constant molecular weight, reducing the polymer concentration below a certain point would produce beads ($\varphi < \varphi_{beads}$) instead of fibres (Figure 1.9) [184].

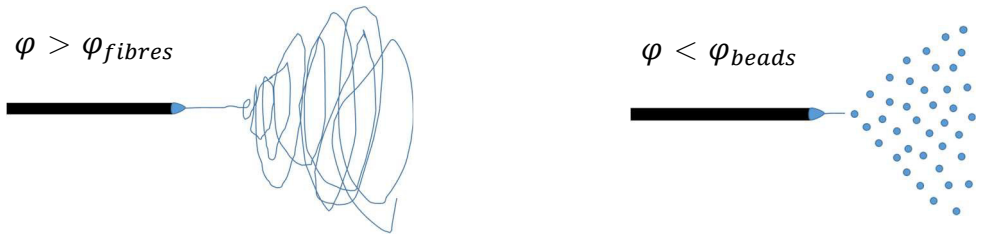

Figure 1.9: The difference between electrospinning and electrospraying

The same processing parameters that govern the electrospinning process also control the outcome of electrosprayed particles. Therefore, principal parameters such as flow rate, solution conductivity and polymer concentration can be used to manipulate the size of the particles. Several authors have developed empirical scaling laws to describe the relationship between the principal parameters and the resulting particle diameter [184–191]. Analogous to the electrospinning relationships (Table 1.4), the diameter of electrosprayed particles can be expected to increase with increasing flow rate (Q) and polymer concentration (φ) while smaller beads would be produced when sprayed from a more conductive solution (K). These relationships are demonstrated in Figure 1.10.

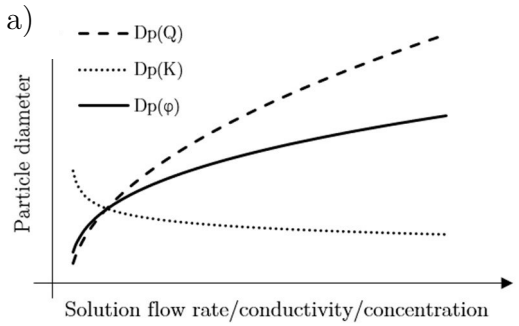

b)

Scaling laws for electrospraying:

- Flow rate ($D_{particle} \propto Q^{1/2}$)
- Concentration ($D_{particle} \propto \varphi^{1/3}$)
- Conductivity ($D_{particle} \propto (1/K)^{1/6}$)

Figure 1.10: The influence of electrospraying parameters on particle size. a) Non-dimensional influence of processing parameters according to b) empirical scaling laws from literature.

1.2.4 Challenges with electrospun scaffolds

Over the past two decades, electrospinning was explored using more than fifty different (natural/synthetic) polymers and has gained wide spread interest as a potential technique to develop tissue regenerative scaffolds [192, 193]. Tissue specific applications included: skin, nerves, muscle, bone, cartilage, ligament and vasculature [194–196]. Apart from the many advantages that electrospinning could offer as a scaffold production technique (e.g. ease of manufacturing, ECM morphological resemblance, high surface area, cost, scalability etc. [93, 138, 139, 194–197]), there are limitations that are hindering the healing performance of such implants [139, 175, 179, 198, 199]. Functional tissue restoration using conventional electrospun scaffolds is often limited by poor ingrowth due to insufficient structural porosity and interconnectivity, blood clot formation, a lack of proper vascularisation and/or excessive inflammation. Several strategies have therefore been investigated to enhance both i) architectural and ii) biochemical cues that would promote scaffold healing [139, 179, 198, 199]. The sections to follow will reflect on the current scaffold porosity enhancement and drug incorporation techniques to address the underlying structural and chemical challenges.

1.2.5 Porosity enhancement techniques

Poor cellular infiltration is a critical concern for the *in vivo* usage of electrospun structures as TE scaffolds [139, 179, 199, 200]. Scaffold architecture (pore size, porosity, fibre diameter and fibre alignment) is known to have a direct influence on how cells behave (attach, migrate and proliferate) and therefore, the device's overall healing performance [198, 201]. Although conventional electrospun scaffolds are considered to be porous, they have inherently small pores, a tight packing density and are layered (2D) rather than interconnected, 3D structures [139, 179, 198, 199]. Consequently, tissue ingrowth and vascularisation of such scaffolds have been found to be only superficial (*in vivo*) - leaving the rest of the scaffold hypoxic and without waste removal or nutrient supply systems [139].

There is an ongoing dispute on the ideal pore size and porosity for TE scaffolds [139, 197, 202]. Despite some suggesting that a desirable pore size is 20-40 µm [201–204], the general consensus is that the pores should be adjustable for wider range of 5-500 µm [200, 205]. Moreover, the average pore size and its morphology should be optimised to accommodate tissue specific cell types, since cells differ in size (round cells usually range between 5-20 µm [198, 206, 207]) and behaviour (attach, migrate and proliferate) [205]. In terms of scaffold porosity, a higher porosity is desirable as it promotes tissue ingrowth and diffusion of nutrients/waste. However, the enhancement of both porosity and pore sizes are associated with mechanical losses. It is therefore suggested that scaffold pore size and porosity should be balanced with the required mechanical properties [200].

Addressing these challenges, several techniques have been considered to enhance electrospun scaffold porosity and pore sizes. The different approaches can be categorised as parametric optimisation, collector modification, post-processing and the inclusion and removal of sacrificial components. As an initial attempt, scaffold porosity/pore size can be improved by optimising fibre orientation, fibre fusion or fibre diameter by controlling the electrospinning parameters as summarised in Table 1.4. The average pore size and total porosity of scaffolds with aligned fibres are known to be smaller/lower than those formed by random orientated fibres [182]. Reducing the degree at which fibres are fusing with adjacent ones has shown to increase both the average pore size and porosity compared to scaffolds with more fibre fusion [208]. The average fibre diameter is probably the most common architectural property of electrospun scaffolds to control (considering Table 1.4). Moreover, it is known that fibre diameter has a positive relationship with fibre diameter and pore size [209, 210]. Tomadakis *et al.* developed a model to describe the characteristic pore size (D_{pore}) as a function of fibre diameter (D_{fibre}) and porosity (P). This relationship, $D_{pore} = -\frac{D_{fibre}}{\ln(P)}$, correlated well with experimental data when porosity was P = 80-88% [211], and was also

confirmed by others [151, 210, 212].

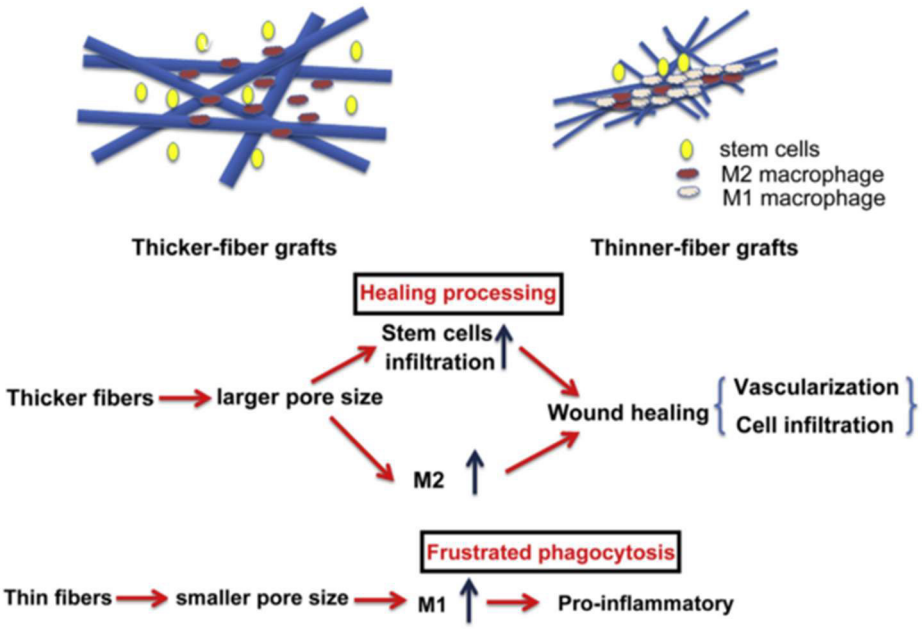

Figure 1.11: Host response towards thick compared to thin-fibrous scaffolds. Diagram acquired from [210].

By parametric control over fibre diameter, Wang *et al.* produced PCL scaffolds with enhanced porosity (84%) and pore sizes (40 µm) when microfibres (6 µm) were spun instead of nanofibres (66%, 6 µm and 700 nm) [213]. The authors showed an improved healing performance (cellular ingrowth, collagen secretion and vascularisation) of the microfibrous scaffolds relative to that of the nanofibrous scaffolds. Such findings were explained by a higher density of M2 polarised macrophages (tissue remodelling phenotype) found inside the microfibrous scaffolds (larger pores), while M1 macrophages (pro-inflammatory phenotypes) were in abundance within the nanofibrous scaffolds (small pores) - illustrated in Figure 1.11. Unfortunately, controlling scaffold pore size/porosity by parametric optimisation is not independent of fibre morphological changes. Increasing fibre diameter facilitates cellular infiltration, however, it could also reduce cellular attachment when fibres are too thick [142, 214]. It is therefore advisable to obtain a balance between scaffold fibre diameter and pore size that would allow for functional tissue restoration [139]. Scaffold porosity/pore sizes can be enhanced independently of fibre diameter by post electrospinning techniques such as ultrasonication [149, 215, 216], gas foaming [217–220] or laser ablation [212, 221, 222].

Specialised collectors have also been investigated to increase/control inter-fibre spaces during the electrospinning process. Over the last few years, such designs included patterned surfaces [223–225] (charged geometries), perforated cylinders [201, 203, 226] (tubes with pressurised airflow) or even the use of a liquid bath as the collector [227, 228]. All the above-mentioned techniques have the potential to produce highly porous scaffolds (P >90%) and exhibit some control over pore size (ranging from 2 to 500 µm). However, their applications are limited due to associated disadvantages such as restricted scaffold thickness, heterogenous distribution of enlarged pores, inability to retain the original scaffold shape/dimensions or complicated translation to a geometric specific application such as a small calibre (2-4 mm) vascular graft [139, 199].

Alternatively, removable materials can be included while electrospinning structural fibres, to act as temporary space holders (porogens) and selectively extract them afterwards to create additional voids in the resulting scaffold. Porogens for selective removal from electrospun scaffolds have already taken the form of water-soluble fibres [153, 178, 209, 229–232] and microparticles [148, 233] or salt [234, 235] and ice [205, 208, 236, 237] crystals. Some of the porosity enhancement strategies mentioned in this section are on display in Figure 1.12.

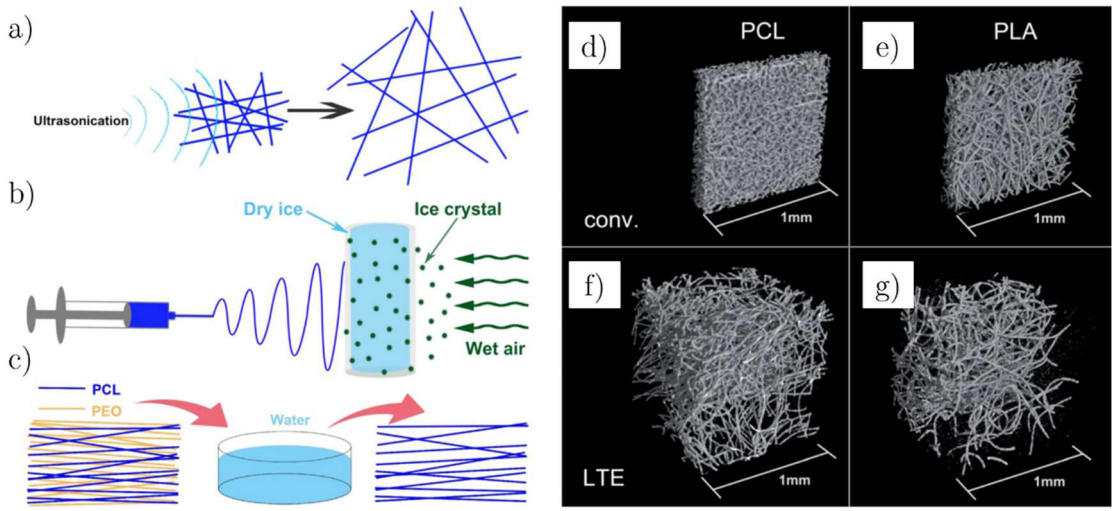

Figure 1.12: Techniques to enhance electrospun scaffold porosity. Porosity enhancement by a) ultrasonication b) low temperature collecting and c) sacrificial fibre removal as demonstrated by [199]. Nano-CT scans of PCL and PLA scaffolds (d-e) and their LTE porosity-enhanced versions (f-g) [205].

Wang *et al.* showed that tissue ingrowth of silk fibroin scaffolds could be enhanced (*in vitro* and *in vivo*) by the removal of water-soluble (polyethylene glycol - PEG) microparticles that were electrosprayed while simultaneously electrospinning of the structural fibres [148]. Simonet *et al.* developed the low temperature electrospinning (LTE) technique [205, 208]. Briefly, scaffold porosity and pore sizes are enhanced by evaporating/melting ice crystals that were simultaneously embedded between the deposited fibres due to condensed moisture from the air near a cold collector (filled with dry ice, -70°C). Leong *et al.* have shown that LTE produced scaffolds allowed for a higher degree cellular infiltration and vascularisation (*in vivo*) compared to those prepared by conventional electrospinning [237]. The LTE process is separated from the rest of the techniques by having the added ability to homogenously increase 3D void spaces [205]. At the time of writing, such homogeneity has not yet been achieved for the selective removal of electrosrpayed microparticles. However, fine control over the electrospraying process should allow for the production of smaller porogens at larger quantities (e.g. 30µm particles sprayed from multiple sources) and potentially, enhance the porosity with a more homogeneous distribution of pores compared to the current approach (50µm particle from a single source [148, 233]). Nevertheless, both the LTE and selective removal of electrosprayed particles approaches have been acknowledged as translatable techniques towards vascular graft and/or heart valve applications [205, 238].

1.2.6 Drug incorporation techniques

In addition to the architectural advantages of electrospun scaffolds, bioactive agents can be incorporated into fibres to be delivered in a localised, controlled manner over a strategic period of time that would assist in functional tissue restoration [198]. A localised delivery also has the advantage of eliminating the side effects associated with systemic delivery [239]. In the past, molecules such as antibiotics [240], DNA [241], growth factors [242], anti-thrombotic (e.g. heparin) [243] and anti-inflammatory (e.g.

dexamethasone) [244] drugs have been incorporated and delivered from electrospun scaffolds. Current electrospun scaffold drug incorporation techniques can be categorised as either a one-step or post processing methodology. Emulsion, co-axial and blend electrospinning are examples of one step drug encapsulation techniques while physical absorption and surface modification are post processing approaches (Figure 1.13 illustrates the differences between these techniques).

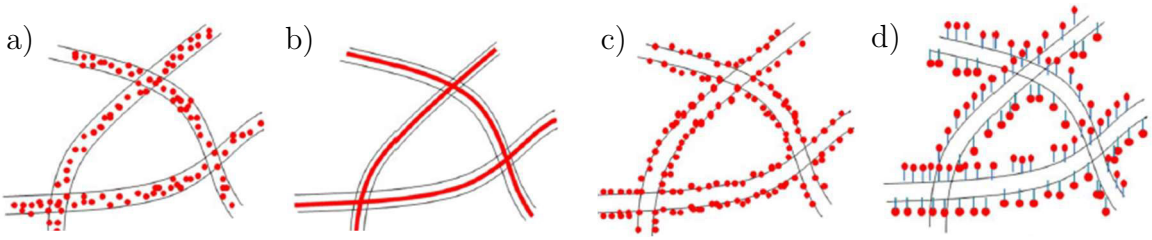

Figure 1.13: Drug incorporation techniques for electrospun fibres. a) blend/emulsion electrospinning, b) co-axial encapsulation, c) physical absorption and d) surface modification. Adopted from [54].

Drug incorporation by blend [98, 198] or emulsion [198, 245] electrospinning simply requires the polymer solution to be doped with the selected agent before processing (either solubilised or in an emulsion state). At optimal conditions, the drug can be encapsulated during the fibre formation phase either uniformly (blend) or in concentrated pockets (emulsion). Although, a uniform drug distribution by blend electrospinning is usually achievable only when the solution of polymer-drug is either hydrophobic-hydrophobic or hydrophilic- hydrophilic [54]. Co-axial electrospinning requires the use of a co-axial needle where two solutions are individually supplied to construct a core-shell configured fibre [246–249]. For such a fibre, multiple combinations of drug and its associated carrier material may be loaded in the core, shell or encapsulated into both. Furthermore, fibres can be coated with bioactive molecules by physically absorbing the agent from a solution or surface modification by chemical immobilisation post electrospinning [104]. The latter usually requires functionalisation of the polymer properties by plasma treatment, chemical treatment or surface graft polymerisation [250]. Nevertheless, both blend electrospinning and the surface modification drug incorporation techniques will be investigated during this project as an attempt to further enhance scaffold healing responses.

1.3 Synthetic biomaterials and bioactive agents

The section to follow introduces the synthetic biomaterials selected for this project, namely, Pellethane® (Pel) and DegraPol® (DP). Moreover, experimental conditions to produce fibrous scaffolds from both materials using the electrospinning process are summarised from literature. Next, the bioactive molecules selected for this project gets introduced: heparin and dexamethasone, followed by summaries of previous attempts of incorporating them into electrospun scaffolds. Finally, a short section on drug release kinetics and their associated models are provided.

1.3.1 Pellethane®

Pel is a segmented polyetherurethane composing of poly(tetramethylene oxide) (PTMO) as the soft-segment and a hard-segment made up of an aromatic junction unit 4,4'methylene-di-phenyldiisocyanate (MDI) and chain extender 1,4-butanediol (BDO) [251], as shown in Figure 1.14. This biomaterial holds a good balance between physicochemical and biological properties as well as ease of processing. Although Pel may undergo oxidative degradation, it is generally considered to be hydrolytically stable [251]. Over many years, the *in vivo* applications of Pel included, artificial ventricles, pacemaker leads, heart valves or cardiovascular tubing and catheters [252].

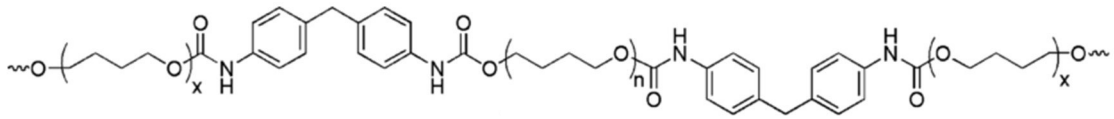

Figure 1.14: Chemical structure of Pellethane®. Poly(tetramethylene oxide) (PTMO) as the soft-segment and a hard-segment made up of an aromatic junction unit 4,4'methylene-di-phenyldiisocyanate (MDI) and chain extender 1,4-butanediol (BDO) [251] and shown by [253].

Moreover, Pel has been a material selection in previous studies towards the development of an electrospun small diameter vascular graft [140, 153, 254–256]. Table 1.5 is a summary of the electrospinning parameters used for processing Pel. A typical vascular graft scaffold is produced from a Pel solution of 5-20wt% in THF/DMF that is supplied at a flow rate of 0.6-5 ml/h using a charged (10-20kV) needle of 0.3-1.4 mm (inside diameter) situated at a distance 90-200 mm away from a rotating collector.

Such parameters produced scaffolds with average fibre diameters of 0.5-8 µm and porosities 63-76%. These conditions can be used as a starting point for producing the biostable (Pellethane®) implants for this project.

Table 1.5: Processing parameters for electrospinning of Pellethane®

C %	Solvent(s) ratio %[w/w]	Flow rate [ml/h]	Collector [mm] rotation [rpm]	Translation [mm/min]	Needle Di [mm]	Distance [mm]	Voltage [kV]	Temp. [°C] RH [%]	Fibre Pore [um]	Porosity [%]	Ref
7	DMF	2.4	n/a n/a	n/a	1.0	n/a	<20	n/a n/a	0.5 n/a	n/a	[254]
16-18	THF	0.7	1.6 n/a	n/a	1.4	110	15	n/a n/a	3.0-8.0 n/a	63-70	[255]
5	HFIP	0.6	2.1 200	480	0.4	90	20	28 28	0.9 n/a	71	[140]
10-20	DMAC:MEK (1:2)	5.0	2.5 400	n/a	0.3	150	10	n/a n/a	1.5-3.0 n/a	n/a	[256]
15	THF:DMF (1:1)	3.0	25 5000	2.6	1.2	200	20	20-24 20-28	1.8 4.0	76	[153]

1.3.2 DegraPol®

DegraPol® (DP) is a biodegradable polyester urethane block copolymer (chemical structure shown in Figure 1.15). The degradation products of both the hard and soft segments are considered non-toxic [94, 257]. The mechanical properties can be altered to meet specific TE applications by adjusting the hard to soft segment ratio [258–260]. Moreover, hydrolytic degradation of DP is controllable, independent of mechanical properties, by varying the glycolide content at the soft segment side of the co-polymer, normally 0, 15, 30 or 40%. Thus, DP with a higher glycolide content has a faster degradation rate (e.g DP30 degrades faster compared to DP0).

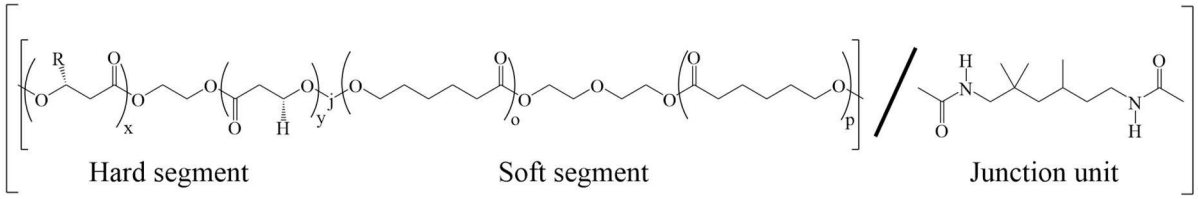

Figure 1.15: Chemical structure of DegraPol®. Poly((R)-3-hydroxybutyric acid)-diol (hard-segment) linked with 2,2,4-trimethylhexamethylene diisocyanate (junction unit) to an amorphous segment of poly(e-caprolactone-co-glycolide)-diol (soft-segment), [261, 262].

Although this polymer has gained some traction in the field of TE, there are a lot of unexplored opportunities with regards to its use in electrospun scaffold development. Therefore, studies using DP over the last two decades have been collected (an extended

summary of all studies as well as the chemical composition of the copolymer used in each investigation can be found in Appendix A2). Applications where DP was investigated specifically as an electrospun TE scaffold (summarised in Table 1.6) included: skeletal muscle, cartilage, tendon, smooth muscle and cardiovascular designs. In these studies, DP has shown positive results for a wide array of cell types (*in vitro*) and has been evaluated for up to 12 weeks *in vivo*. At the time of writing, no investigations were found that conducted a long-term evaluation (12 weeks) of the fast degrading DP30. Additionally, no *in vivo* evaluation of a bioactive DP electrospun scaffold, of any kind, was found.

Table 1.6: Summary of DegraPol® electrospun TE applications

TE Application	DP Type	Drug [ng/g]	Fibre Pore [um]	Porosity [%]	UTS E [MPa]	*in vitro*	*in vivo*	Ref
Skeletal muscle	DegraPol	n/a	10 n/a	n/a	n/a 10	Myogenic cells	n/a	[263]
General	DegraPol	n/a	3-7 10-100	n/a	0.4 20 [km]	Fibroblasts	n/a	[261]
General	DegraPol	n/a	12 60	64-91 (LTE)	n/a 0.4-1.0 [km]	n/a	n/a	[208]
Skeletal muscle	DegraPol	n/a	10 n/a	n/a	n/a n/a	Myoblasts	n/a	[264]
Cartilage regeneration	DegraPol	n/a	6-25 30-80	n/a	n/a n/a	Chondrocytes (static & dynamic)	Rabbits for 8 weeks	[265, 266]
General	DegraPol	n/a	10-20 n/a	n/a	n/a n/a	Fibroblasts & endothelial cells	n/a	[267]
Cardiovascular	DegraPol DP30	n/a	7 n/a	80	0.5 1.0	n/a	n/a	[21]
General	DegraPol	n/a	3-10 n/a	75-93(PEG)	n/a 0.5-2.2 (r) 10 (a)	Fibroblasts	n/a	[178]
Blood vessel	DegraPol	n/a	1-7 7-45* converted	n/a	n/a	Whole blood	n/a	[268]
Tendon regeneration	DegraPol	n/a	n/a n/a	75	n/a n/a	n/a	Rabbits for 12 weeks	[269]
Tendon regeneration	DegraPol new	n/a	n/a n/a	75	n/a n/a	n/a	Rabbits for 6 weeks	[270]
Smooth muscle	DegraPol DP15	n/a	3.6 n/a	71	n/a n/a	Smooth muscle cells	Rat for 8 weeks	[271]
Tendon regeneration	DegraPol classic/new	n/a	10±7 n/a	75	n/a 13 (class) 3 (new)	n/a	Rabbits for 12 weeks	[272]
Cardiovascular	DegraPol DP30	n/a	7±2 n/a	76	1.0±0.2 5.6±1.3	n/a	n/a	[273]
Tendon regeneration	DegraPol classic/new	PDGF-BB ~13	1-7 n/a	60-80	0.2-1.3 1.5-2.3	Tenocytes	n/a	[262]

A typical DP electrospun scaffold was produced using the following conditions: a polymer solution of 8-30wt% in chloroform (or combinations of chloroform and HFIP)

supplied at a flow rate of 0.1-12 ml/h using a charged (5-20 kV) needle of 1.0 mm (inside diameter) situated at a distance 100-300 mm away from a rotating collector. Parameters within this range produced scaffolds (excluding the porosity enhancement techniques) with average fibre diameters of 1.0-25 µm and porosities 60-83%. These conditions (summarised in Table 1.7) can be used as a starting point for developing the biodegradable scaffolds for this project.

Table 1.7: Processing parameters for electrospinning of DegraPol®

C %[w/w]	Solvent(s) ratio %[w/w]	Flow rate [ml/h]	Collector Do [mm] rotation [rpm]	Translation [mm/min]	Needle Di [mm]	Distance [mm]	Voltage [kV]	Temp. [°C] RH [%]	Fibre Pore [um]	Porosity [%]	Ref
30	$CHCl_3$	n/a	n/a n/a	n/a	n/a	n/a	18	n/a n/a	10 n/a	n/a	[263]
27	$CHCl_3$	4.0	n/a 300	n/a	n/a	200	18	-70 n/a	3-7 10-100	n/a	[261]
28	$CHCl_3$	4.0	80 n/a	n/a	1.0	200	20	200-220K, 300K 15-85	12 60	64-91 (LTE)	[208]
25	$CHCl_3$	n/a	n/a 0.4-7.6 m/s	n/a	n/a	n/a	18	n/a n/a	10 n/a	n/a	[264]
25-27	$CHCl_3$	1.2-3.6	5 300	n/a	n/a	200	n/a	-170, 20-25 40-60	6-25 30-80	n/a	[265, 266]
28	$CHCl_3$	n/a	n/a n/a	n/a	n/a	n/a	20	200-220K, 300K 30, 50, 85	10-20 n/a	n/a	[267]
20	$CHCl_3$	1.4	5 95	2.6	n/a	200	13	n/a n/a	7 n/a	80	[21]
24	$CHCl_3$	4.0-12.0	80 330-1670	n/a	n/a	100-250	n/a	n/a n/a	3-10 n/a	75-93(PEG)	[178]
15-20	$CHCl_3$+HFIP [75:25]	0.1-1.0	80 n/a	n/a	n/a	150-250	5-15	n/a n/a	1-7 7-45* converted	n/a	[268]
25	$CHCl_3$	n/a	4 n/a	n/a	1.0	200	15	n/a n/a	n/a n/a	75	[269]
25	$CHCl_3$	n/a	4 n/a	n/a	1.0	200	15	n/a n/a	n/a n/a	75	[270]
24	$CHCl_3$+HFIP [80:20]	1.0	80 700	n/a	n/a	300	15	n/a n/a	3.6 n/a	71	[271]
25	$CHCl_3$	n/a	4 n/a	n/a	1.0	200	15	n/a n/a	10±7 n/a	75	[272]
24	$CHCl_3$	8.0	25 7200	2.6	n/a	300	15	n/a n/a	7±2 n/a	76	[273]
8-16	$CHCl_3$+HFIP [80:20]	0.5-3.0	4 n/a	50 mm [speed n/a]	1.0	150-200	10-18	22-23/35	1-7 n/a	60-80	[262]

1.3.3 Heparin

Heparin is a natural therapeutic agent that was discovered at John Hopkins University over a century ago. Isolated from either porcine intestine or bovine lung, heparin is clinically used since 1935 as a potent anticoagulant for the treatment/prevention of

thrombosis (blood clotting) [274]. Found on cellular surfaces and in the natural ECM, this compound is a highly sulphated and heterogenous polysaccharide (molecular weight of about 15 kDa) that is part of the glycosaminoglycans (GaGs) family [275]. Its molecular structure, the most complex among the GaGs, may comprise of six different uronic acid and glucosamine linked disaccharides formed from the ten monosaccharides identified in Figure 1.16.a. The repeating sequence of heparin mainly consist (70 or 90% for porcine or bovine origins respectively) of IdoA(2S)-(1→4)-GlcNS(6S) while the remainder is made up of uronic acid and glucosamine linked disaccharides with various degrees of sulfation and N-acetylation (Figure 1.16.b, [276, 277]).

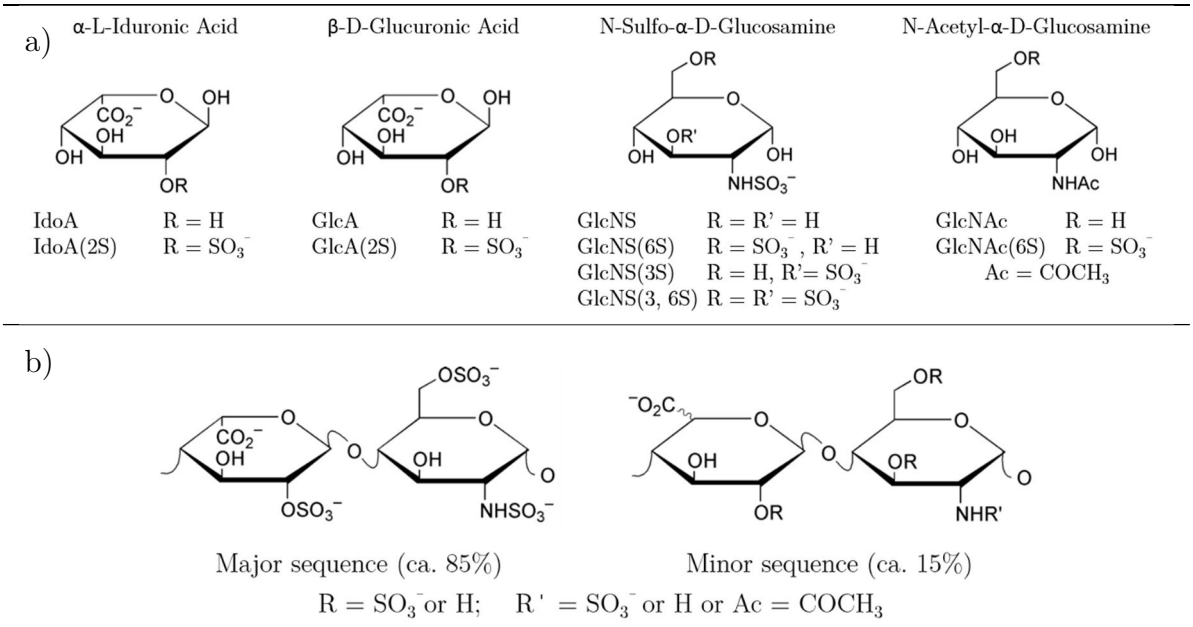

Figure 1.16: Chemical composition of heparin. a) monosaccharides; b) major and minor repeating disaccharides. Adopted from [276]

Heparin predominantly interacts with neighbouring proteins via electrostatic mechanisms, but hydrophobic effects, hydrogen bonding and the formation of secondary structures may also occur [278]. This diverse interactivity makes heparin a potential binding partner for numerous proteins, e.g.: antithrombin [279], lysozyme [280] and specific growth factors (GFs). Moreover, heparin is considered to guard its captured molecules from fluctuations in pH, heat as well as enzymatic degradation [281]. Basic fibroblast growth factor (bFGF) [282], fibroblast growth factor (FGF-2) [283], transforming growth factor-b (TGF-b) [284], platelet-derived growth factor-BB

(PDGF-BB) [285] and vascular endothelial growth factor (VEGF) [286, 287] are all GFs known to have affinity with heparin. Consequently, this agent does not only possess useful antithrombotic properties, it has also been shown to moderate inflammation, promote cell adhesion, inhibit smooth muscle cell proliferation [288, 289] and stimulate angiogenesis [290–293] (although it is also studied for its potential anti-angiogenicity [294]). It is therefore no surprise that heparin has been used to coat biomaterials since the 1960's and, more recently, gained significant interest in the field of tissue engineered scaffold development [295].

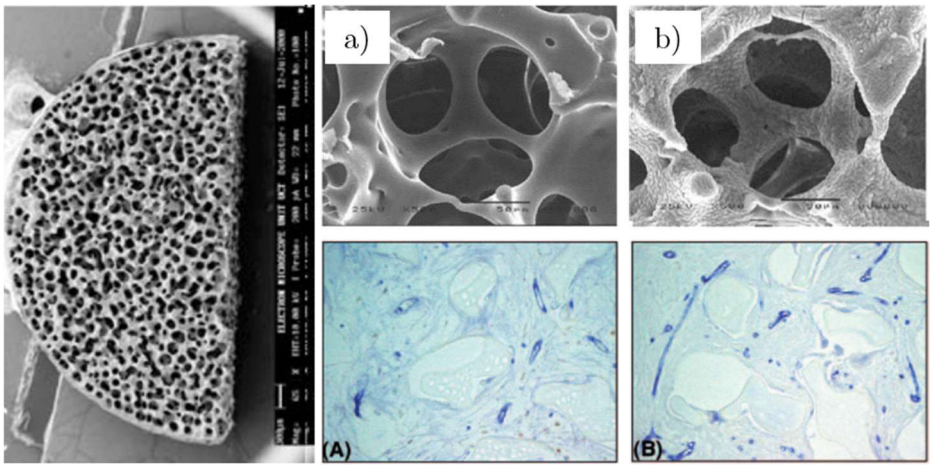

Figure 1.17: Improved vascularisation of heparinised polyurethane foam discs. a) macropores without; and b) with heparin surface coatings. Adopted from [292].

Vascularisation of tissue engineered scaffolds is essential for *in vivo* survival, but remains an elusive challenge [296]. In the absence of new blood vessel formation, tissue ingrowth is restricted to 100-200 µm (cells would die beyond this) due to the diffusion limit of oxygen from native capillaries [297]. Angiogenesis is the formation of new vasculature from pre-existing blood vessels through proliferation, migration and remodelling of endothelial cells (EC's) [298]. Strategies to encourage angiogenesis of TE structures include optimisation of scaffold architecture, biomechanics and/or the incorporation of bioactive molecules that would attract proangiogenic GFs [55, 299, 300]. Cabric *et al.* demonstrated heparin's ability to bind to proangiogenic growth factor, VEGF, with the aim of attracting endothelial cells (ECs) and thereby induce angiogenesis and revascularisation. After two days of *in vitro* culture, the authors

showed that human isolated pancreatic islets with surface immobilised heparin were surrounded with positively stained VEGF and attracted 150% more ECs (and favoured cellular adhesion) when compared to the un-heparinised controls [301]. Bezuidenhout *et al.* showed that polyurethane (PU) discs (which had well-defined, interconnected 150 µm pores) with surface immobilised heparin (38 mg/g) enhanced vascular density of newly ingrown tissue by 62% compared to the untreated controls in a rat subcutaneously after 28 days of implantation (Figure 1.17). Furthermore, Janse van Rensburg *et al.* filled similar microporous PU discs with degradable/nondegradable polyethylene glycol (PEG) hydrogels incorporated with/without heparin (0.6 mg/g). The slow release of heparin (zero order kinetics), when covalently bound to degradable PEG gels, enhanced vascularisation of the local tissue by 50% when compared to the controls (without heparin) after 28 days of implantation in a subcutaneous rat model [302]. These studies, and many other [303–306], recognized heparin's potential not only to create antithrombotic surfaces (for cardiovascular application such as vascular grafts and heart valves) but its effectiveness to promote angiogenesis when either surface immobilised or slowly eluted from TE scaffolds. Aiming to achieve similar results with electrospun scaffolds, several studies were identified where heparin was either surface modified or eluted from heparin blended electrospun fibres (see Figure 1.18 for an illustration of the two different types of heparin incorporation).

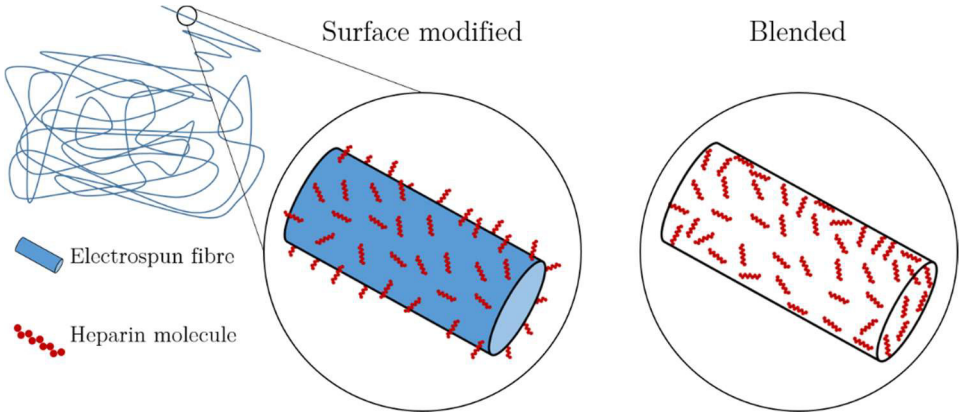

Figure 1.18: Illustrative diagram of heparin incorporated electrospun fibres.

A few groups have attempted to attach heparin to the surfaces of electrospun fibres. Voorneveld *et al.* studied tissue ingrowth of porosity-enhanced Pellethane scaffolds

(using a sacrificial fibre technique) with and without covalently attached heparin (8mg/g, as shown in Figure 1.19). Heparinised groups had little to no influence on tissue ingrowth, inflammation or vascularisation after 28 days in a rat subcutaneous model [153].

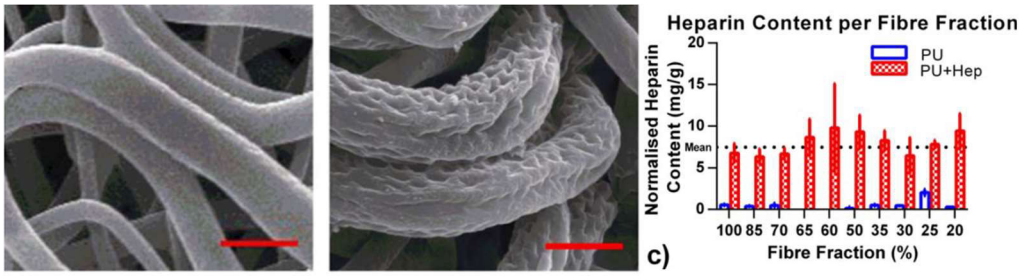

Figure 1.19: Heparin surface modified Pellethane fibres.As shown by [153].

In terms of blend electrospinning heparin, Luong-Van *et al.* incorporated unmodified heparin in PCL fibres using a cascaded co-solvent system of water, methanol and dichloromethane (heparin is soluble in water, and not DCM nor methanol). The authors only incorporated heparin at relatively low concentrations 0.05-0.5wt%. The system precipitated when concentrations reached 1wt%. Release rate of 20-25% in first 24 hours and 55-60% after 14 days for concentrations 0.05-0.5wt% (both had a followed a Fickian diffusion model). Vascular smooth muscle cells were treated with and without heparin (before and after electrospinning). Heparin, before and after electrospinning, successfully inhibit VSMC proliferation (40% reduction in net growth) when compared to the untreated groups. Confirming, to some extent, that the bioactivity of heparin was unaffected by the harsh conditions (hazardous solvents and high electrostatic fields) associated with the electrospinning process [243]. In a different blend electrospinning study, low molecular weight heparin (3 kDa) was by itself or covalently bonded to four-arm star PEG to form PEG-LMWH compound and blended with either PEO/H_2O or PLGA/DMF carrier polymers to form electrospun fibres at concentrations that ranged from 3.5-85 mg/g. Incorporation of LMWH or LMWH-PEG in PLGA at a concentration of 0.2wt% enhanced the scaffold's ability to bind to BFGF when compared to the untreated control fibres. Interestingly, LMWH-PEG was more effective than LMWH to bind to the growth factors due to LMWH being more imbedded in the

scaffold and LMWH (being a smaller molecule) was more susceptible to diffusion despite them having the same concentration at inception [307]. Centola *et al.* seeded heparin releasing PLLA/PCL electrospun scaffolds (incorporated at 0.8 mg/g) with human mesenchymal stem cells and analysed them in terms of morphology, mechanical tensile strength, cell viability and differentiation. Methanol was used as a co-solvent to add the unfractioned heparin to a PLLA/DCM spinning solution prior to processing. Kurpinski *et al.* investigated cellular infiltration of biodegradable PLLA electrospun scaffolds with and without surface modified heparin *in vitro* and *in vivo*. The infiltration of bovine aortic endothelial cells seeded on heparinised PLLA scaffolds was similar when compared to the control groups (*in vitro*). On the contrary, a higher density of positively stained endothelial cells ($CD31^{+}$) and macrophages ($CD68^{+}$) were observed *in vivo* (7 days in a dermal rat model) for the scaffolds with surface immobilised heparin compared to the unheparinised controls [308]. The different outcomes were attributed to the complex multi-cell signalling environment that exist in an *in vivo* model and are, not yet, fully replicated *in vitro*. Nevertheless, a higher density of both endothelial cells and macrophages (specifically M2 phenotypes which orchestrates the healing process in ways that promote angiogenesis and tissue remodelling [204] and [309]) are indications of an improved healing response.

Blend electrospinning of heparin (hydrophilic) with common biodegradable polymers (hydrophobic) is challenging. Kwon *et al.* modified heparin to a tri-n-butylammonium salt of heparin (HepTBA, amphiphilic) before dissolving it into the electrospinning solution of PLCL/HFIP [310]. Although the authors showed successful incorporation, the only *in vitro* studies that were performed were an elution study (1, 5 and 10wt%) to show the release profiles of HepTBA in a phosphate buffered saline (PBS) media. Results showed a burst release (7, 16 27%) followed by sustained release of (31, 36 and 53%) over 4 weeks (as seen in Figure 1.20). This is a promising heparin incorporation especially towards a vascular graft application. However, more *in vitro* research (e.g. bioactivity and/or cytotoxicity) is needed before moving towards *in vivo* studies.

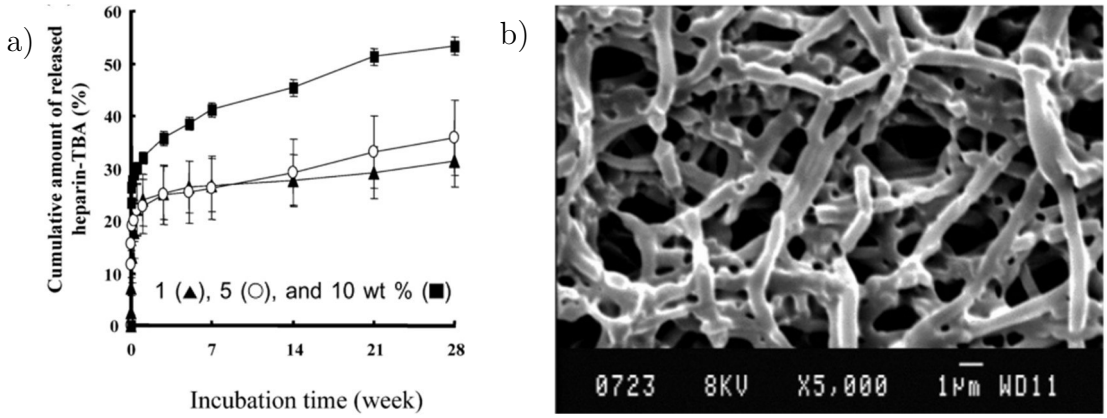

Figure 1.20: Heparin-TBA incorporated PLCL electrospun scaffolds.a) release profile for HepTBA at 1, 5 and 10wt%; b) SEM of 5wt% HepTBA fibres at 4 weeks of incubation. Adopted from [310].

Table 1.8 is a summary of electrospun scaffolds with either surface modified (SM) or heparin blended (BE) into the fibres. It should be noted that an electrospun scaffold eluting the HepTBA compound has not yet been evaluate *in vivo*. Such an investigation may provide useful information to the TE community, especially if HepTBA could promote scaffold vascularisation.

Table 1.8: Examples of electrospun scaffolds with heparin incorporation Drug incorporation techniques: surface modification (SM) or blend electrospinning (BE).

Molecule [load]	Drug solvent(s)	Method	Polymer [solvent(s)]	*In vitro* Model	*In vivo* Model	Ref.
Heparin [N/a]	N/a	SM	PLLA [HFIP]	Enhanced EC infiltration	Enhanced vascularisation	[308]
Heparin [8mg/g]	N/a	SM	Pellethane [THF/DMF]	N/a	No significant enhancement	[153]
Heparin [N/a]	N/a	SM	PLLA [HFIP]	Enhanced EC infiltration	N/a	[311]
Heparin [0.3-1.2mg/cm^2]	N/a	SM	CS & PCL [TFA/DCM & $CHCl_3$/MeOH]	Reduced platelet adhesion	N/a	[312]
Heparin [0.05-0.5wt%]	H_2O	BE	PCL [DCM:MeOH 7:3]	Prevented VSMC proliferation	N/a	[243]
LMWH and PEG-LMWH [8-10mg/g]	H_2O/DMF	BE	[PEO & PLGA] [H_2O & DMF]	Enhanced BFGF binding	N/a	[307]
Heparin [0.8mg/g]	MeOH	BE	PLLA & PCL [DCM]	Stem cell study	N/a	[313]
HepTBA [1-10wt%]	HFIP	BE	PLCL [HFIP]	N/a	N/a	[310]

1.3.4 Dexamethasone

A major concern for implantable scaffolds made from synthetic biomaterials is their potential to induce a non-specific host response [239, 314]. Therefore, scientists have suggested the incorporation of controllable delivery systems of anti-inflammatory agents to moderate foreign body response, and thereby, improve the long-term performance of medical devices [31, 314, 315]. Dexamethasone (Dex) is an anti-inflammatory steroid that has been shown to reduce scaffold inflammatory response when delivered locally [239, 316, 317]. Dex was found to effectively reduce inflammation in rats (250-350 g) when delivered twice at a daily dosage of 1 mg/kg days post-operatively [318–321]. Considering an electrospun scaffold with a typical mass of 10-15mg, an effective dose of Dex would translate to an incorporation load 3-7wt%. Dex has been incorporated into electrospun scaffolds before (see Table 1.9) at dosages varying 0.3-20wt%. Although, the only study that showed effective *in vivo* results used a load of 5.7wt%, which is also in agreement with the above translation dosage. Solvent(s) used for blend electrospinning of this drug included: HFIP, $CHCl_3$, DMF, DCM and ethanol. This information could be useful to consider when designing a Dex eluting electrospun scaffold.

Table 1.9: Examples of electrospun scaffolds with dexamethasone incorporation. Drug incorporation by blend electrospinning (BE).

Molecule [load]	Drug solvent(s)	Method	Polymer [solvent(s)]	*In vitro* Model	*In vivo* Model	Ref.
Dex [0.3wt%]	HFIP	BE	PLLA [HFIP]	Enhanced osteogenic proliferation	N/a	[322]
Dex [5.7wt%]	$CHCl_3$:DMF (75:25) DCM:DMF (62.5:37.5)	BE	PCL and PLLA [$CHCl_3$/DMF] and [DCM/DMF]	Allowed stem cell attachment and proliferation	Reduced inflammatory response	[239]
Dex [5-20wt%]	$CHCl_3$:DMF (7:3)	BE	PCL [$CHCl_3$/DMF]	Enhanced osteogenic activity	N/a	[244]
Dex [0.5-2wt%]	$CHCl_3$:EtOH (9:1)	BE	PEOT/PBT [$CHCl_3$/EtOH]	Enhanced osteogenic differentiation	N/a	[323]

1.3.5 Drug release kinetics

Diffusion is considered to be the main mechanism behind the release kinetics of bioactive molecules from electropsun scaffolds [241–244, 324–326]. Many factors may influence their diffusion profiles, such as fibre/scaffold architecture, polymer degradation, solubility of both drug and polymer or the physiological conditions. Besides the architecture and material selection of the delivery device (mean diffusion distance and polymer degradation rate [198]), the drug type and its polymorphic form, crystallinity, molecular size, the total load in the polymer matrix and the drug's solubility in the release medium are known factors that influences the release kinetics of a drug from the same polymer matrix [327, 328]. A sustained delivery, zero-order release kinetics, is considered an ideal release mechanism for many drug delivery applications [329, 330]. For such a mechanism, the release of the agent is constant over time regardless of its concentration.

Table 1.10: Models used to describe drug dissolution. The amount of drug dissolved (U), release constant (k), release exponent (ω) and time (T). Adopted from [327]

Model	Equation
Zero order	$U_T = U_0 + k_0 T$
First order	$ln\, U_T = ln\, U_0 + k_1 T$
Second order	$U_T/U_\infty (U_\infty - U_T) k_2 T$
Hixson-Crowell	${U_0}^{1/3} - {U_T}^{1/3} = k_s T$
Weibull	$log[-\ln(1 - U_T/U_\infty)] = b * log\,(T) - log(a)$
Higuchi	$U_T = k_H \sqrt{T}$
Baker-Lonsdale	$(3/2)[1 - (-U_T/U_\infty)^{2/3}] - (U_T/U_\infty) = kT$
Korsmeyer-Peppas	$U_T/U_\infty = kT^\omega$
Quadratic	$U_T = 100(k_1 T^2 + k_2 T)$
Logistic	$U_T = A/[1 + e^{-k(T-y)}]$
Gompertz	$U_T = Ae^{-e-k(T-y)}$
Hopfenberg	$U_T/U_\infty = 1 - [1 - k_0 T/C_0 a_0]^\omega$

Mathematical models are useful to engineers/scientists to describe the release of delivery devices. Such formulations can be used to predict dosages at certain timepoints and provide important parameters for further optimisation of delivery effectiveness [331]. Therefore, numerous models have been developed to describe drug dissolution

from a polymer matrix (as summarised in Table 1.10). Among these, zero-order, Higuchi and Korsmeyer-Peppas are generally consider to best describe the drug release phenomena from polymer matrices [327]. Interpretation values given in Table 1.11 are used to distinguish between diffusion transport mechanisms: Fickian diffusion, Non-Fickian transport, case II transport or super case II transport.

Table 1.11: Interpretation values for diffusion release kinetics. Adopted from [331]

Release exponent (ω)	Drug transport mechanism	Rate as a function of time
0.5	Fickian diffusion	$T^{-0.5}$
0.45< ω = 0.89	Non-Fickian transport	$T^{\omega-1}$
0.89	Case II transport	Zero order release
Higher than 0.89	Super case II transport	$T^{\omega-1}$

1.4 Research proposal

1.4.1 Problem statement

Small diameter vascular grafts made from expanded polytetrafluoroethylene (ePTFE) show full endothelialisation after relatively short periods of implantation in animals. Unfortunately, such grafts are almost completely without endothelium when used in humans, even after 10 years of implantation [22]. The small efforts of endothelialisation that does occur in human, is due to the outgrowth of endothelial cells at the anastomoses (graft ends sutured to the native vessel) and is limited to approximately 10-20mm (referred to as transanastomotic (TA) endothelialisation) [332]. This limited TA endothelialisation and overall poor healing responses are known reasons why half of the ePTFE grafts occlude within the first five years after implantation in medium sized applications [333, 334]. It is believed that the emphasis should be on transmural endothelialisation (through the graft's wall - TM) instead of TA endothelialisation. Studies performed by UCT's Cardiovascular Research Unit (CRU) indicated that a healthy endothelial lining is limited due to insufficient porosity, pore sizes and interconnectivity through the graft's wall [29, 335]. The scaffold of an ideal vascular graft should not only facilitate tissue ingrowth but also provide routing for cellular

waste, nutrient and oxygen supply [336]. At the time of writing, a synthetic vascular graft with the embedded biological signals that would allow function tissue regeneration (*in situ* tissue engineered - off-the-shelf) has not yet been clinically realised for small diameter applications (<6 mm) [64, 138, 337]. Such a device (with an annual need of 1.8million prostheses) would have a substantial impact in the fight against CVD.

1.4.2 Objectives

The microenvironment of an ideal scaffold should provide the i) architectural and/or ii) biochemical cues that are attractive to cells, and ultimately, facilitate functional tissue restoration. Considering these challenges for electrospun TE scaffolds and keeping a vascular graft application in mind, the following objectives were formulated for this project:

Development of biostable TE electrospun scaffolds (Pellethane®):

- Establishment of optimal conditions to electrospin and electrospray biostable fibres and water-soluble microparticles respectively.
- Enhancement of scaffold porosity and pore sizes by simultaneous inclusion and subsequent removal of 30 µm porogens electrosprayed from multiple sources.
- Immobilisation of heparin to the surfaces of porosity-enhanced scaffolds to create an anti-thrombotic and pro-angiogenic scaffold.
- Investigation of the influence of porosity enhancement and heparin surface modification on scaffold architecture and mechanical properties.
- Evaluation of the healing response towards biostable electrospun scaffolds in a rat subcutaneous implantation model for up to 3 months: show improvement of i) tissue ingrowth for high-porosity scaffolds and ii) vascularisation for heparinised scaffolds.

Development of biodegradable TE electrospun scaffolds (DegraPol®):

- Establishment of optimal conditions to electrospin biodegradable fibres.

- Simulation of the electric field as a function of base electrode surface area and investigation of its effect(s) on the electrospinning process.
- Enhancement of scaffold porosity and pore sizes by low temperature electrospinning.
- Incorporation of dexamethasone into electrospun fibres via blend electrospinning to moderate the inflammatory response by localised delivery.
- Modification of heparin to an amphiphilic salt that would allow drug incorporation into the scaffold via blend electrospinning to provide anti-thrombotic and pro-angiogenic properties by localised delivery.
- Assessment of the bioactivity and cytotoxicity of the modified heparin.
- Investigation of the different *in vitro* release mechanisms associated with dexamethasone and heparin.
- Investigation of the influence of scaffold drug incorporation on architectural and mechanical properties.
- Evaluation of the healing response towards degradable electrospun scaffolds in a rat subcutaneous implantation model for up to 3 months: show i) moderation of inflammation for dexamethasone incorporated scaffolds and ii) improvement of vascularisation for heparin incorporated scaffolds.

2 Materials and Methods

This chapter provides information on the selected materials and summaries of the standardised methods used during the development of non- and -degradable electrospun scaffolds. Optimal conditions for producing a selection of scaffolds for *in vivo* evaluations are provided. Finally, on overview of the animal study, implant/explant procedures, histological and associated quantifications are described.

2.1 Materials

The reagents used for this project were purchased from Sigma-Aldrich (Pty) Ltd. (RSA), Fluka (Buchs, Switzerland), Merck Millipore (RSA), Saarchem Holpro Analytic (RSA) and Oakwood Chemicals (USA), unless specified otherwise. Dexamethasone and heparin sodium were obtained from Pharmacia & Upjohn Company LLC (i.e. Pfizer Inc, USA) and Celsus Laboratories (USA) respectively. The two biomaterials chosen for scaffold development were, a thermoplastic elastomer called Pellethane® (2363-80AE, 1.12 g/cm^3, Lubrizol, USA) and a biodegradable polyester urethane block copolymer called DegraPol® (DP0 and DP30, 1.15 g/cm^3, ab medica, Lainate, Italy). Polyethylene glycol (PEG, 10 and 20 kDa) was used for developing water-soluble microparticles as scaffold porogens.

2.2 Preparation of polymer films

Polymer films of DP and Pel for bulk material characterisation (mechanical properties and *in vitro* degradation studies) were prepared using a heat-press. Methods on heat-pressing DP and Pel films have been described before [254, 260]. In similar fashion, dried polymer powder/pellets were placed, at a mass of 3g, between two temperature controlled plates covered with Mylar sheets (held at either 120°C for DP0/DP30 or 180°C for Pel). The material was compressed for 5 min at 20 MPa. The carefully

removed films (n = 2 per material) were transparent, free from defects and had a thickness of 200-300 µm.

2.3 Polymer degradation in aqueous solutions

The rate of hydrolytic degradation in aqueous solutions of polymer films/electrospun scaffolds was characterised by mass loss (%) over time. The initial mass (m_0) of each sample (10x10 mm square, n = 3 of each group) was recorded before being placed inside a glass tube along with 1 ml of aqueous solutions - physiological (PBS at pH = 7.4), acidic (1.0M HCl at pH = 0.8) or basic (1.0M NaOH at pH = 13.0). Each tube top was sealed with Parafilm® (to prevent evaporation) and placed inside an incubator at 37°C. The mass was again recorded at each selected time point (m_t) after the fluid was drained and the material was dried (1 hour in a vacuum oven at 50°C followed by another 24 hours at room temperature in a fume hood). Sample mass was determined with a five-decimal balance (XS105, Mettler-Toledo AG, Greifensee, Switzerland). The mass loss percentage at each time point was expressed as:

$$Mass\ loss\ \% = \left(1 - \frac{m_t}{m_0}\right) 100 \tag{2-1}$$

2.4 Measuring solvent evaporation rates

The rate at which 1,1,1,3,3,3-hexafluoro-2-propanol (HFIP) or chloroform ($CHCl_3$) evaporated, either in pure form or in a DP30 solution (φ = 18wt%), was characterised by mass loss over time (2, 3, 4, 5 and 24hours, n = 3 per group). Approximately 650mg of solvent or solution (the exact mass (m_0) was determined using a five-decimal balance) was transferred to an empty polypropylene cap of known mass (m_{cap}). The samples from all four groups (having a combined solvent volume <5 ml) were placed inside a sealed glass desiccator (5 L) filled with argon gas to prevent mass changes due to hygroscopic effects. The combined mass of each solution/solvent filled cap (m_t) was recorded at the selected time points followed by refilling the desiccator. Solvent evaporation was determined using equation (2-2) where $m_{solvent} = m_0(1 - \varphi)$ and φ

= 18wt% or φ = 0wt% for samples containing DP solutions or pure solvents respectively.

$$Solvent\ evaporation\ \% = \left(\frac{(m_{cap} + m_0) - m_t}{m_{solvent}}\right)100 \quad (2\text{-}2)$$

2.5 Solution viscosity determination

Solution viscosities were determined using a viscometer (Brookfield DVI Prime with a small sample adapter - spindle no.21). Both the DP (24wt%DP30 in 50:50% HFIP:$CHCl_3$) and Pel (16wt%Pel in 50:50% THF:DMF) solutions were rotated (21-22°C and 60-64% RH) at a speed of 6rpm until a stable measurement (converging at ±8 cPoise) was obtainable.

2.6 Scanning electron microscopy

Dry specimens were placed on metal stubs and sputter coated with gold (120 ms at 35 mA and 1.4kV, Polaron SC7640, Quorum Technologies, England) before imaging with a Zeiss (LEO) 1450 Scanning Electron Microscope (SEM) operating at 15-20 keV. Images of electrospun or electrosprayed fibres or particles were captured at suitable magnifications for their respective image analyses.

2.7 Nuclear magnetic resonance spectroscopy

All compounds were prepared by dissolution (4 mg/ml) and microfiltration (0.45 µm) in either deuterated chloroform ($CDCl_3$) or heavy water (D_2O). Nuclear Magnetic Resonance (NMR) spectra were recorded at room temperature (RT) using a Bruker DRX-400 spectrometer at standard operating conditions (10 s recycle delay, 128 scans). The resulting signals were processed (MestReNova, v11.0, Spain) for phase correction, baseline subtraction and numerical integration.

2.8 Heparin surface immobilisation

Heparin was attached to the surfaces of Pel electrospun scaffolds by a covalent bonding

technique [153, 286, 292, 338]. Briefly, the porosity-enhanced groups were removed from their porogen extraction solutions of deionised water (DI):ethanol (90:10) and rinsed thrice in DI water only. Next, the scaffolds were grafted with acrylic acid/acrylamide co-polymer by immersing them in a solution of acrylic acid (4.0 M), acrylamide (1.0 M) and coper nitrate (0.1 M). Cerium ammonium nitrate (0.006 M, $(NH_4)_2[Ce(NO_3)_6]$) was added after oxygen removal by argon gas bubbling. Scaffolds were sonicated in this solution for 40 min at RT (Integral Systems Ultrasonic UMC5, 100 Watts, RSA). Then, the scaffolds were aminated during a 2 hour reaction (sonicated at RT) with ethylene diamine (EDA, 0.5 M) in 2-(N-morpholino)-ethanesulfonic acid (MES, 0.5 M) buffer solution (pH = 5.0) also containing 1-ethyl-3(3-dimethyl-aminopopyl) carbodiimide (EDC, 0.05M). Finally, heparin was covalently attached to Pel fibre surfaces through reductive amination. Aminated scaffolds were treated with a solution of nitrous acid de-aminated heparin (2 mg/ml) in acetate buffer (0.2 M sodium acetate, 0.2 M acetic acid, pH = 4.6) with addition of sodium cyanoborohydride (NaCNBH3, 0.016 M). Afterwards, the heparinised samples were rinsed trice with DI water and washed overnight on a platform shaker (New Brunswick Scientific C1, USA). Following the final wash, scaffolds were freeze-dried for 48hours (VirTis manifold dryer, United Scientific, RSA).

2.9 Heparin confirmational staining

The presence of heparin on electrospun scaffold surfaces was confirmed by positive staining (purple) with a Toluidine Blue (TB) solution (0.025wt% toluidine blue in 0.025 M tris base, 0.025 M tris acid). This heparin staining technique has been used before [280, 286]. Briefly, each heparinised or control sample (10x10 mm) was placed in a 24 well plate (Sigma Aldrich, RSA) followed by 1 ml of TB solution and stirred for 5 min on a platform shaker. Afterwards, the TB solution was removed from each well using a plastic pipette and the samples were rinsed thrice with 1ml of DI water. During the heparin surface modification process, each step was visually confirmed with a positive

stain of TB (blue|white for positive|negative grafting), Ponceau S (red|white for positive|negative amination) and again with TB (purple|dark blue for positive|negative heparinisation).

2.10 Surface heparin quantification

The amount of heparin on the surface of heparinised Pel scaffolds was quantified by an adapted calorimetric method, known as the 3-methyl-2-benzothiazolinehydrazone-hydrochloride (MBTH) assay [339]. Dry scaffolds with and without surface heparin (n = 5 per group) were submerged in DI water (250 µl). Afterwards, 500 µl of nitrous acid solution (0.025 M HNO_2 in 0.9 M HCl) was added and sonicated at RT for 30 min. The degradation reaction was stopped by the addition of an ammonium sulfamate solution (1 M, 250 µl), mixed with a vortex mixer and then transferred into a clean test tube. Each scaffold was rinsed with a NaCl solution (1 M, 500 µl) which was added to the degradation solution. Next, 500 µl of MBTH solution (0.011 M) was added to the degraded heparin (15 min at 50°C). The MBTH molecule was complexed by the addition of a $FeCl_3$ solution (9.031 M, 500 µl, 20 min at 50°C).

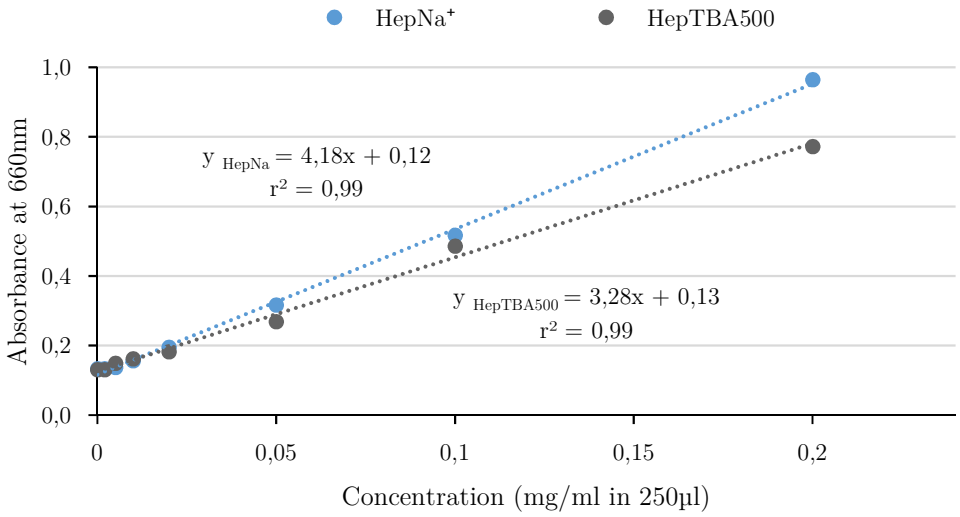

Figure 2.1: Typical absorbance curves for heparin concentration determination.

The resulting solution was transferred to a disposable cuvette and its absorbance was measured at a wave length of 660 nm (Shimadzu UV-1601PC spectrometer, Canada).

Finally, scaffold heparin content (mg/g) was determined using a standard curve (generated using the same MBTH-assay methodology) from known concentrations (0–0.2 mg/ml, 8 data points). Typical MBTH-assay absorbances curves can be seen in Figure 2.1.

2.11 Heparin modifications

Sodium salt of heparin ($HepNa^+$, porcine derived, 12 kDa, 196 U/mg) was modified to HepTBA by ion-exchange [310] in which the sodium ions of $HepNa^+$ were exchanged for H^+ and subsequently replaced by tributylamine (TBA), as shown in Figure 2.2. The current project not only produced fully substituted HepTBA (complete TBA complexation), but also investigated heparin products with controllable TBA content.

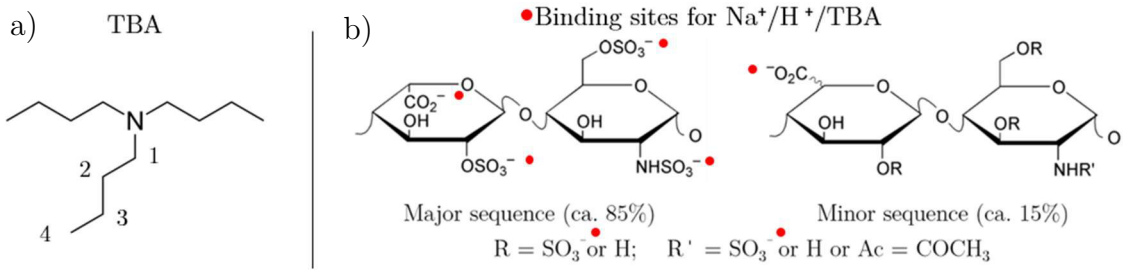

Figure 2.2: Ion-exchanges during the heparin-TBA modification process. a) numbering reference for the methyl groups of TBA; b) sites where ion-exchanges are expected to occur on the heparin molecule.

Briefly, 1 g of $HepNa^+$ was dissolved in 100ml of DI water (pH = 6.5). Assisted with compressed air, the solution was passed through a glass column (D_i = 10.8 mm) packed with resin (7.5 g, 50Wx8 [H^+], 200-400 mesh, Dowex®, Sigma Aldrich) at a flow rate of 5 ml/min (11 s/cm). Another 100 ml of DI water was passed through the same column to yield a 200 ml stock solution of heparin acid ($HepH^+$/DI water, 5 mg/ml, pH = 2.0). Next, heparin with various degrees of TBA substitutions were produced by reacting different concentrations (as indicated in Table 2.1) of tributylamine/methanol solutions (TBA/MeOH, 10 ml) with 40ml of the $HepH^+$ stock solution (stirring for 2 hours). The MeOH was subsequently evaporated (RII Rotavapor Buchi, at 122 mbar and 40°C for 1 hour) until a volume of approximately 40 ml remained. Thereafter, the unreacted TBA was removed by liquid-liquid extractions with hexane (3x100 ml). All

HepTBA/DI solutions were freeze-dried for 48 hours to obtain white powdery products.

Table 2.1: Reagent concentrations for Heparin-TBA ion-exchange processes

Compound	TBA/MeOH (mg/ml)	$HepH^+$/DI (mg/ml)
$HepH^+$	0	N/a
HepTBA25	4	5
HepTBA50	8	5
HepTBA75	12	5
HepTBA100	16	5
HepTBA500	80	5

The relative peak intensities (^{1}H NMR spectra in D_2O) between the average methyl/methylene protons of TBA and the acetyl protons of heparin were used to describe and compare the degree of TBA complexation for each of the HepTBA products. For quantification purposes, a ratio between the integrated proton signals (Λ) were calculated using the following equation (the functional groups of TBA were numbered according to the sequence shown in Figure 2.2.a):

$$\left(\frac{TBA}{Ac}\right)_{H\ NMR} = \frac{\frac{1}{4}\left[\frac{\int_H \Lambda_{TBA_1}}{2} + \frac{\int_H \Lambda_{TBA_2}}{2} + \frac{\int_H \Lambda_{TBA_3}}{2} + \frac{\int_H \Lambda_{TBA_4}}{3}\right]}{\frac{\int_H \Lambda_{Ac}}{3}} \tag{2-3}$$

2.12 Cell viability assay

The XTT viability assay has been used to characterise the biocompatibility of seeded TE scaffolds (natural and synthetic) by measuring the number of metabolically active cells over time [340, 341]. XTT is a tetrazolium derivative that is reduced to the highly coloured formazan dye by mitochondrial dehydrogenase enzymes. Thus, an increase or decrease of formazan dye indicate cellular proliferation or death respectively. The current study was designed to evaluate the *in vitro* effects on rat smooth muscle cell (rSMC) proliferation when treated with/without heparin at a dosage that would simulate an extreme case of instantaneous resorption of a 5wt% loaded electrospun DP scaffold (a typical sample of 10 mg and 100 mm^2). Briefly, sterile heparin/PBS stock

solutions were prepared to contain 2,5 mg/ml of $HepNa^+$, HepTBA25, HepTBA75, HepTBA500 or no heparin (to serve as the control treatment). All solutions were filtered, 0.2 µm GVS filter unit and DB20 syringe, and transferred to 5 ml self-standing screw cap tubes. Approximately 5000 rSMC were seeded (at -24 hours) for five groups (n = 4 per group) in a 96-well plate (Sigma-Aldrich). Treatments (a total volume of 100 µl at a pH of 7.4) were given at 0 hours to the pre-seeded cells in the form of 80 µl MCDB medium (M8537, Sigma-Aldrich) plus 20 µl of a blinded treatment solution. Therefore, the final concentration of a heparin treated well was 500 µg/ml (equivalent to the total dose delivered by a typical 10 mg scaffold loaded at 5wt%). At 72 hours of incubation, the media was removed and each well was washed twice with 100 µl of sterile PBS. Thereafter, fresh media (100 µl of MCDB) and the XTT detection fluid (50 µl, containing an electron coupling solution at a ratio of 1:50) was added to each well containing cells, and three empty ones to serve as background readings. The cells were returned to the incubator for 2 hours, after which absorbance readings (light scattering) of each well were taken at 450 nm and subtracted by that measured at 655 nm using a Bio-Rad microplate reader (170–6800; BioRad, RSA). The cells were photographed for morphological changes before (-24 and 0 hours) and after (24, 48 and 72 hours) treatments. All procedures were performed under sterile conditions.

2.13 Thromboelastography

The anti-thrombotic activity of modified/unmodified heparin was analysed using a non-invasive diagnostic instrument, TEG®5000 thromboelastograph hemostasis analyser (Haemonetics Corporation, USA). Firstly, all sample channels (n = 8, four analysers with two channels each) were tested and approved for their accuracy against the provided Level I biological control fluid (see Appendix A3 for the calibration results). Heparin treatments, $HepNa^+$ or any form of HepTBA were prepared at 0.01 mg/ml in PBS, were added (110 µl) to 1 ml of citrated whole human blood extracted from Vacuette collection tubes (coagulation sodium citrate 3.2%, 9NC, BD Medical, RSA).

A sample (1 ml) of this blood plus treatment mixture was transferred to a Kaolin-coated vial (BD Medical, RSA) and gently inverted five times. Next, 340 µl of the mixture was placed inside a disposable, pre-warmed (37°C) TEG® analyser cup (Haemonetics) that contained 20 µl of calcium chloride ($CaCl_2$ at 0.2 M, Haemonetics). Finally, the oscillating blood clotting process was recorded with the provided TEG®5000 software. The following parameters were recorded: reaction time (R, time from inception until the waveform breaches 2 mm above the baseline), clot formation time (K, time from 2 to 20 mm above the baseline), rate of clot strength build-up (α) and the maximum amplitude (MA, i.e. clot strength). Following the same operating procedure, the activity of HepTBA500 was also evaluated as an eluate from electrospun scaffolds after 48 hours of *in vitro* incubation (PBS at 37°C). The eluates (110 µl) were normalised (HepTBA500/PBS at 0.018 mg/ml) and compared to equimolar heparin concentrations of the un-modified version ($HepNa^+$/PBS at 0.01 mg.ml). Table 2.2 summarises the selected blood treatments and their sample sizes for TEG analysis.

Table 2.2: Heparin treatments for whole blood thromboelastographic analyses

Treatment (110µl PBS)	Concentration (mg/ml)	Sample size
$HepH^+$	0.01	1
$HepNa^+$	0.01	2 & 3
HepTBA25	0.01	2
HepTBA50	0.01	2
HepTBA75	0.01	2
HepTBA100	0.01	2
HepTBA500 (before electrospinning)	0.01 & 0.018	2 & 3
HepTBA500 (after electrospinnning)	0.01 & 0.018	2 & 3
Control (PBS only)	N/a	2 & 3

2.14 Scaffold drug release characterisation

Drug loaded electrospun scaffolds were prepared in sealed glass tubes (15x20 mm strips immersed in 1 ml PBS) and incubated under static conditions (37°C). The elution fluid of each sample was collected for drug content measurement, and replaced with new PBS (1 ml) at selected time points (see Table 2.3). The eluates (200 µl) of Dex

incorporated scaffolds (1, 2 or 5wt%) were analysed for content release by UV spectroscopy (rectangular quartz cuvettes at a wave length of 241 nm). The concentration of eluted Dex (mg/ml) was calculated from a standard absorbance curve generated using known Dex/PBS data points. Eluates (250 µl) of scaffolds that contained HepTBA500 (at 1, 2 or 5wt%) were analysed for heparin content using a modified MBTH-assay (in a similar fashion as mentioned in section 2.10). Briefly, each eluate was reacted (sonicated at RT) with 500 µl nitrous acid solution (0.025 M HNO_2, 1 M HCl) for 30 min followed by the addition of 250 µl ammonium sulfamate solution (1 M). This mixture was diluted with 300 µl NaCl solution (1 M), reacted with 500 µl MBTH solution (0.011 M) for 15 min (sonicated at 50°C) followed by 500 µl of $FeCl_3$ solution (0.031 M) reacted for 20 min (sonicated at 50°C). Finally, the resulting colorimetric solutions were transferred to disposable cuvettes and their absorbances were measured by UV spectroscopy (wave length of 660 nm). A standard absorbance curve for HepTBA500 was generated, at known concentrations, and was used to calculate the concentration (mg/ml) of released HepTBA500 from each sample (a new curve was re-created for each batch of measurements, e.g. in Figure 2.1). The theoretical drug content (Dex or HepTBA500 to scaffold, mg/g) was determined by normalising the released concentrations with the initial scaffold masses. Release curves were expressed as instantaneous and/or cumulative delivery rates.

Table 2.3: Selected time points for *in vitro* drug elution studies. *Scaffolds produced for *in vivo* evaluations.

Sample	Time points (days)	Sample size
DP30 (control)	1, 2, 3, 4, 5, 6, 14, 22, 30 & 44	3
DP30 + 1 or 2wt% Dex	1, 2, 3, 4, 5, 6, 14, 22, 30 & 44	3
DP30 + 1 or 2wt% HepTBA500	1, 2, 3, 4, 5, 6, 14, 22, 30 & 44	3
*DP30 (control)	1, 2, 3, 5, 7, 10, 15, 21, 30 & 90	3
*DP30 + 5wt% Dex	1, 2, 3, 5, 7, 10, 15, 21, 30 & 90	3
*DP30 + 5wt% HepTBA500	1, 2, 3, 5, 7, 10, 15, 21, 30 & 90	3

Furthermore, the elution curves of the scaffolds selected for *in vivo* evaluations, those loaded at 5wt%, were correlated with each of the drug release models listed in Table

2.4. Model variables (k and/or n), and their correlation with the experimental data, were determined using a nonlinear least squares optimisation approach (Levenberg-Marquardt algorithm, Matlab). Finally, the best fit model (i.e. the function that produced the highest r^2 value) were used to describe the release kinetics of each drug.

Table 2.4: Curve fitting models used to describe *in vitro* drug release kinetics. The amount of drug dissolved (U), release constant (k), release exponent (ω) and time (T).

Zero-order	First-order	Higuchi	Korsmeyer-Peppas
$U_T = U_0 + kT$	$lnU_T = lnU_0 + kT$	$\frac{U_T}{U_\infty} = k\sqrt{T}$	$\frac{U_t}{U_\infty} = kT^\omega$

2.15 Polymer solution preparations

All electrospinning/electrospraying solutions were prepared by 24 hour magnetic stirring at RT, depending on volume, using glass test tubes or bottles (Pyrex®). After mixing, solutions were left to rest for 1hour to equalise the minimal heat generated by stirring and to remove bubbles before transferring to a syringe for processing. Concentrations were expressed as weight-by-weight percentage (wt%) for polymer to solvent, unless stated otherwise (i.e. weight-by-volume, w/v).

2.16 Experimental setup for electrospinning/electrospraying

The experimental setup for TE scaffold production consisted of a custom-built rotating-translating mechanism with adjustable speed settings (only 0-5000 rpm and 1.4 mm/s were investigated during this project). Three high voltage power supplies were available (two ES30P-5W and one ES30N-5W power unit, Gamma High Voltage Research, USA). The negative power supply was used to charge the rotating collector (kept at -1 kV) while the two identical positive power supplies were for electrospinning (primary source, 0-30 kV) and electrospraying (secondary source, 0-30 kV) respectively. Two dual-syringe pumps (SE400B, Fresenius, Bad Homburg, Germany) were used to feed polymer solutions to needle-base electrode configurations on opposite sides of the

collector (blunt hypodermic needles connected to charged aluminium plates). The Taylor cone was visualised for real-time control on an LCD display via a CCD camera (Techgear Eaglescope, China) connected to a laboratory computer. The collecting rotational speed and ambient conditions (temperature and humidity) were recorded with a non-contact tachometer and a thermo-hygrometer (Lasec, South Africa). A typical experimental setup used during this project can be seen in Figure 2.3 (this configuration was snugly fitted inside a fume hood for the extraction of built-up solvent fumes through the top and side chamber holes).

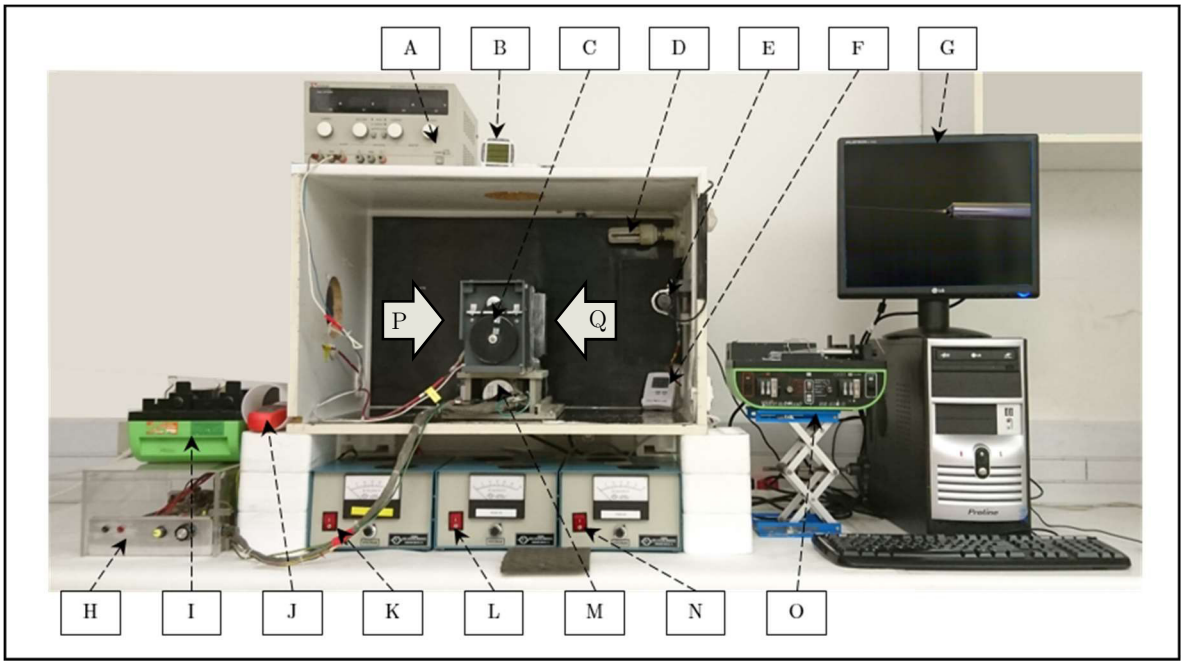

Figure 2.3: A typical experimental setup for electrospinning/spraying. [A] Rotary speed controller; [B] Digital timer; [C] Collector DC motor; [D] Background light source; [E] CCD camera; [F] Humidity and temperature sensor; [G] Taylor cone display; [H] Translational speed controller; [I] Secondary syringe pump; [J] Handheld tachometer; [K] Primary positive power supply; [L] Negative power supply; [M] Translation stepper motor; [N] Secondary positive power supply; [O] Primary syringe pump; [P] and [Q] indicate the sides for electrospraying and electrospinning respectively.

Hollow cylindrical collectors (outside diameters of 25 and 75 mm, Figure 2.4.a-b) with one-side removable lids were used for collecting at room and low temperatures (when filled with dry ice). Both collector types were mounted on 6mm diameter shafts. Small holes were drilled (1 mm) on one side of the collector to allow for internal gas expansion caused by the release of CO_2 from the dry ice.

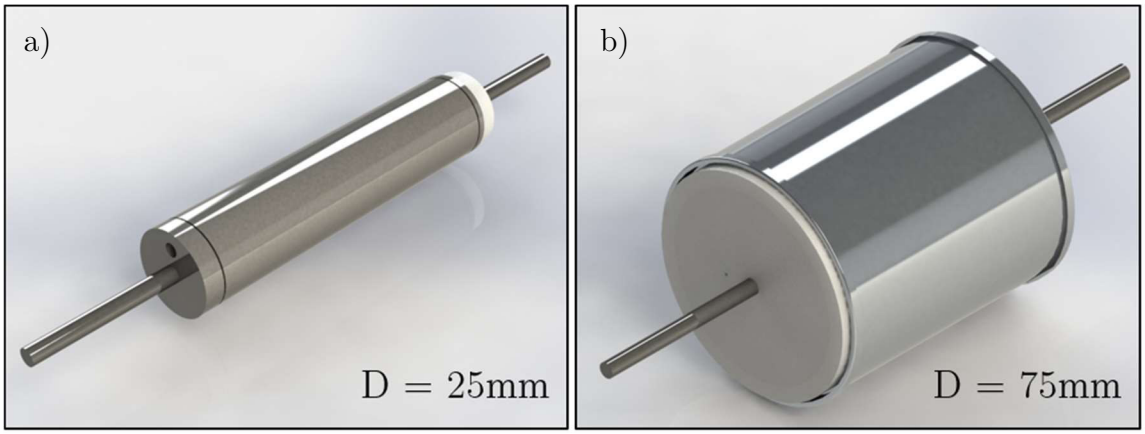

Figure 2.4: Hollow collectors used for rotational collecting. a) small and b) large collectors with respective outside diameters (D). Models were created in SolidWorks.

An auxiliary electrospraying station was purposely designed for upscaled microparticle production while simultaneous electrospinning was allowed on the opposite site of the collector. Briefly, a base electrode with the same dimensions to the one at the electrospinning side (60x60 mm aluminium plate) was attached to a mobile foot piece as indicated in Figure 2.5.a. Furthermore, blunt cut needles protruded 10 mm from the base electrode at a pitch of 12 mm (a maximum of three needles were used as indicated in Figure 2.5.b).

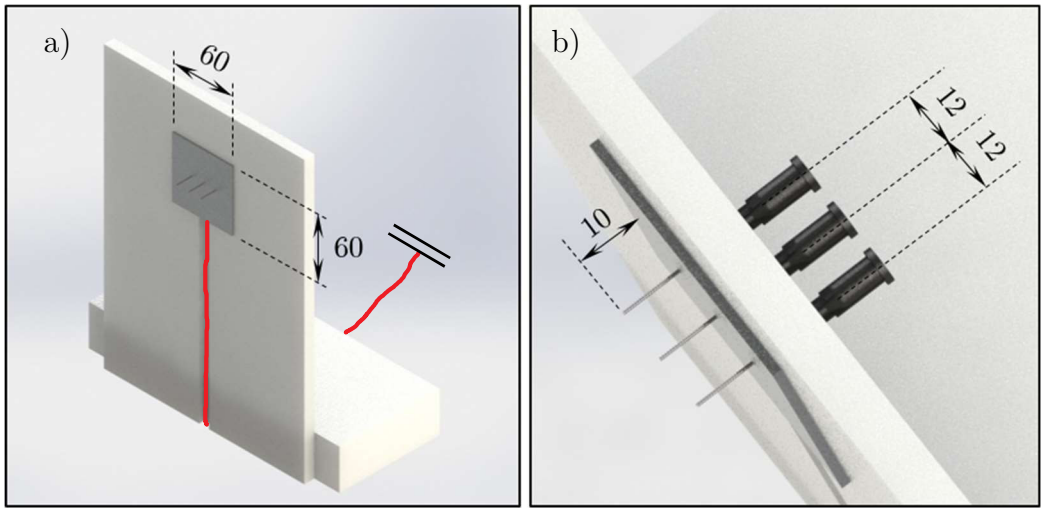

Figure 2.5: Needle and base electrode configuration for electrospraying. a) full view of the auxiliary electrospraying station with b) close-up on a multiple needle configuration (triple G22 needles). All dimensions are in mm. Models were created in SolidWorks.

2.17 Electric field simulations

The potential influence of base electrode size (variable surface areas) on the electrohydrodynamics during a typical electrospinning process was investigated. Firstly, the electric field intensity produced by a positively charged base electrode was mathematically modelled as a thin annular disc (previously derived by [342]) of inner radius (r_i) and outer radius (r_o) which carried a uniform charge density (ρ_s). The charge enclosed by a differential surface element (ds') was represented by $\rho_s \rho' d\rho' d\phi'$, as shown in Figure 2.6.

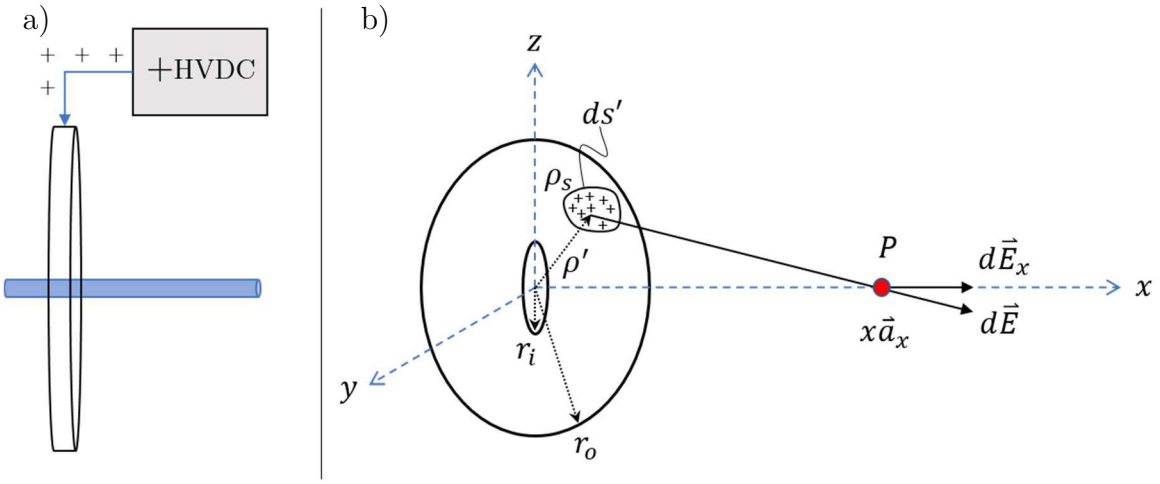

Figure 2.6: Model of an annual disc as a base electrode for electrospinning. a) a simple needle and base electrode configuration charged by a positive high voltage direct current (+HVDC) power supply, b) the electrical field intensity at P due to a uniform charge distribution (adapted from [342]).

Applying charge symmetry with respect to a point observation, the electric field intensity ($\vec{\mathbf{E}}$) at any point (P) along the x-axis ($x > 0$, i.e. away from the base electrode towards the collector) was expressed by equation (2-4):

$$\vec{\mathbf{E}} = \frac{\rho_s}{4\pi\epsilon_0} \int_{r_i}^{r_o} \int_0^{2\pi} \frac{\rho' d\rho' d\phi'}{[\rho'^2 + x^2]^{\frac{3}{2}}} x\overrightarrow{a_x} \tag{2-4}$$

, and simplified as:

$$\vec{\mathbf{E}} = \frac{\rho_s x}{2\epsilon_0} \left[\frac{1}{(r_i^2 + x^2)^{\frac{1}{2}}} - \frac{1}{(r_o^2 + x^2)^{\frac{1}{2}}} \right] \overrightarrow{a_x} \tag{2-5}$$

The changes that base electrode size may have on the electric field was simulated by

solving equation (2-5) for three different annual disc dimensions (r_i = 1.5 mm and r_o = 8, 16 and 32 mm) while all other variables were assigned with constant values (ϵ_0 = 8.854×10^{-12} F/m, $\rho_s = W/\pi(r_o{}^2 - r_i{}^2)$ and W as the charge generated by 20 kV over a typical electrospinning distance of x = 0-300 mm). The effect was visualised by converting the numerical data to line plots (Matlab). Expanding from this analysis, electric field investigations were also explored using an electrostatic simulation environment called Coulomb3D V9.30 (short-term licence ID: 50869, Integrated Engineering Software, Canada).

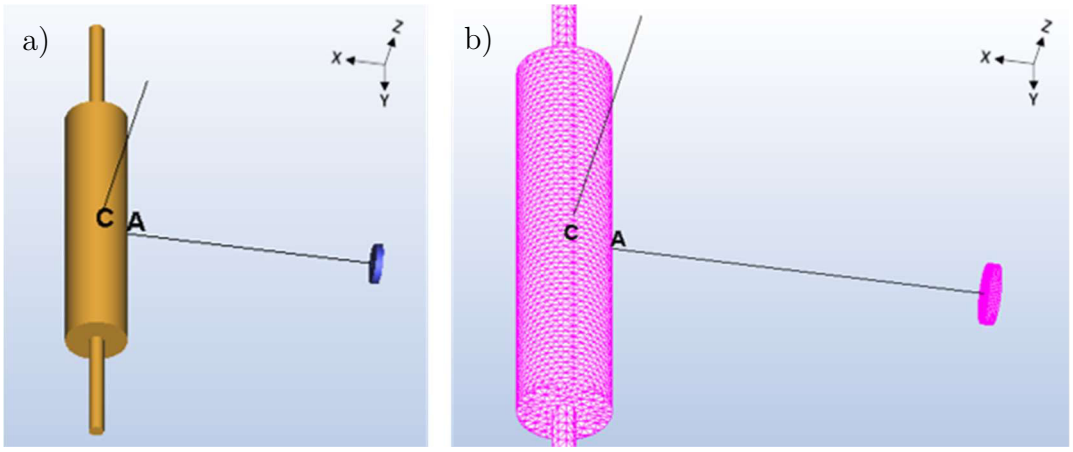

Figure 2.7: Base electrode and collector model used for 3D simulations. a) CAD models imported into Coulomb3D from SolidWorks, b) messed models using triangular elements. The notations C and A refer to the centre and the face of the collector respectively.

Three-dimensional models of the annular base electrodes (r_i = 1.5 mm and r_o = 8, 16 and 32 mm) and a typical collector (as shown in Figure 2.4.a) were created in SolidWorks (2015 student version). The models (Figure 2.7) were imported into the simulation environment and meshed with 2D triangular elements (5000 plus an extra 2000 manually applied at base electrode centre). The working fluid (electrospinning chamber) was assigned as air at 20°C, 101 kPa. The material properties listed in Table 2.5 were assigned to the collector and base electrodes as specified. Simulations were executed for variable voltages (12-20 kV) applied to each of the base electrodes (outside diameters of 16, 32 and 64 mm) at variable distances (10-30 cm) from the negatively charged collector (-1 kV). Finally, the numerical data from all simulations were exported as text files from which 3D plots were generated, using Matlab, of voltage

V(x) and electric field intensity, Em(x).

Table 2.5: Material properties of parts used for electric field simulations.

Property	Collector	Base electrode
Steel type	316L	3CR12
Electrical conductivity (S/m)	1 474 900	1 351 351
Thermal conductivity at 500°C (W/mK)	40	21
Elastic modulus (GPa)	200	193

2.18 Electrospraying parametric studies

The parameters investigated for the control and optimisation of electrospayed water-soluble, PEG microparticles included: solution properties (dielectric constant, molecular weight and concentration), collecting distance and needle diameter. Moreover, the possibility of particle production upscaling was also investigated. The electrospraying station described in Figure 2.5 were used for all the studies listed in Table 2.6.

Table 2.6: Parametric investigations for developing electrosprayed porogens.

Parameter	Range	Analysis
Solution properties	Dielectric constants: 4.8, 17.8 or 32.0. Molecular weight: 10 or 20 kDa. Concentrations: 20-50%.	Particle diameter (n = 2)
Collecting distance	10-24cm (increments of 2 cm)	Particle aspect ratio, circularity and area (n = 3)
Needle diameter	D_i = 0.26-1.37 mm (G25, 23, 22, 21, 20, 18 and 15)	Particle diameter (n = 3)
Multiple needles	Single, double and triple configurations	Collecting distribution (n = 1)

The flow rate was held constant at 1 ml/h (based on initial studies not shown). The collecting distance, needle and solvent selection were set at 200 mm, G22 (D_i = 0.72 mm) and $CHCl_3$, unless specified otherwise. The exposed surface area of the Taylor cone produced from needles with different diameters were calculated by $A_{Tcone} = \pi r\sqrt{r^2 + l^2}$, where r = $D_i/2$ and l is the length of the Taylor cone as measured using ImageJ software (NIH Image, USA) from photographs taken during these experiments using. Distribution of particles collected from multiple needles were visualised by the

contrast created from pre-sprayed solutions dyed with either Toluidine blue or Rhodamine. After electrospraying, the particle colours were revealed (blue/pink) by slowly rotating the collector through steam generated from a flask of boiling water. The resulting particle distribution was photographed after 1min of steaming.

2.19 Electrospinning parametric studies

Collecting speed and flow rate were the parameters investigated for optimising the electrospinning conditions of Pel at 16wt% in 50:50wt% THF:DMF. During both studies, a blunt hypodermic needle (G15), which protruded 20 mm from a charged base electrode (60x60 mm aluminium plate at 12-16 kV), was used to feed the Pel solution at a distance of 250 mm between the needle tip and the face of a negatively charged (-1 kV) collector (Figure 2.4.a). The flow rate was held constant at 2 ml/h in the case of the collecting speed study (1000-5000 rpm) while the speed was held at 1000 rpm during the flow rate study (1-4 ml/h). The influence on fibre diameter, fibre orientation and mechanical properties were analysed during these developmental studies (Table 2.7). The fibre orientation index obtained at different rotational speeds (rpm) was also express as a function of tangential velocity (v_c, m/s) for comparison and scalability purposes.

Table 2.7: Parametric investigations for developing biostable scaffolds

Parameter	Range	Analysis
Collecting speed	1000, 2000 or 5000 rpm	Fibre orientation (n = 4) and mechanical properties (n = 3)
Flow rate	1, 1.5, 2, 2.5 or 4 ml/h	Fibre diameter (n = 4)

The processing parameters explored for optimising DP electrospinning were collecting speed, solution properties (solvent system variations and concentrations), base electrode size, collecting temperature and the addition of a drug incorporated at different concentrations. While each of these parameters were varied, all others were kept constant. A flow rate of 2 ml/h and a G15 needle were used, unless stated

otherwise. The collecting distribution (surface area of collected fibres, mm^2) was calculated by multiplying the known collector circumference with the measured longitudinal length of collected material. The different base electrode surface areas were created by exposed holes (circles with diameters of 10 and 25 mm) cut from electrical insulation covers (5 mm thick) which shielded the rest of the charged 60x60 mm aluminium plate. The covers were fitted so that the needle would protrude from the centre of the hole at a same length that it would without the cover, 2 mm. LTE was performed by filling the hollow collectors with dry ice. Drugs were incorporated by simple add-mixture. The amount of drug was calculated to the weight of the polymer (1, 2 or 5wt%) and simply added to the spinning solvent system (50:50% $CHCl_3$:HFIP) before dissolving the polymer at RT. The ice chamber was re-filled every 30 min in the case of using the large collector. The effect(s) that processing adjustments had on electrospun scaffolds were analysed as indicated in Table 2.8.

Table 2.8: Parametric investigations for developing degradable scaffolds.

Parameter	Range	Analysis
Collecting speed	500, 1000 or 3000 rpm	Fibre orientation (n = 4)
Solution properties	Co-solvent ratios of 0-100% (for HFIP to $CHCl_3$) and polymer concentration of 20, 25 or 30wt%	Collecting distribution (n = 1), fibre diameter (n = 6) and pore size (n = 6)
Base electrode size	3600, 490 or 80 mm^2	Collecting distribution (n = 1), fibre diameter (n = 2) and pore size (n = 2)
Collecting temperature	RTE (~295 K) compared to LTE (~203 K) at low or high concentrations (20 or 24wt%) collected on small or large collector (25 or 75 mm)	Morphological observations and collecting time (n = 2)
Drug incorporation	1 or 2wt% for both Dex and HepTBA500	Release and kinetics (n = 3) and *in vitro* degradation (n = 3)

2.20 Porosity enhancement by electrospinning and spraying

Composite structures of electrospun fibres (~2 µm) and removable porogens (~30 µm)

produced by a single/triple electrospraying source were investigated as an approach to scaffold porosity enhancement. Briefly, an experimental setup for simultaneous electrospinning and electrospraying was used as depicted in Figure 2.3. A solution of 16wt% Pel (in 50:50% THF:DMF) was electrospun (2 ml/h, G15 needle) using the primary positive power supply (14 kV) at a distance of 250 mm from a negatively charged collector (25mm in diameter at -1 kV and roto-translating at 1000 rpm and 1.4 mm/s). On the opposite side (200 mm away), 48wt% PEG_{10kDa} (in $CHCl_3$) was electrosprayed from a single or triple needle (G22) configuration as shown in Figure 2.5. The spraying flow rate was 1 ml/h per needle throughout the process (90 min each time). Control samples were produced by electrospinning Pel (90 min) without simultaneous electrospraying. The collected sheet of material was removed and cut into 10x10mm samples using a steel ruler and a sharp blade (n = 3 or n = 40 per group for the pilot or the implants for *in vivo* assessments). After recording their individual masses ($m_{beaded\ scaffold}$), the samples were vigorously shaken in a 1 L glass bottle (24 hours on a platform shaker) containing 600 ml of DI water/ethanol (90:10, v/v) that was replaced after 12 hours. Next, the washed scaffolds were transferred to test tubes containing 3 ml of DI water and freeze-dried for 48 hours. Mass of the dried scaffolds ($m_{scaffold}$) were determined using the five-decimal balance while the dimensions (thickness: t; surface area: wl, Figure 2.8) were measured (n = 5 locations per image, ImageJ) from scaled photographs taken with a stereo microscope (Nikon, SM2800).

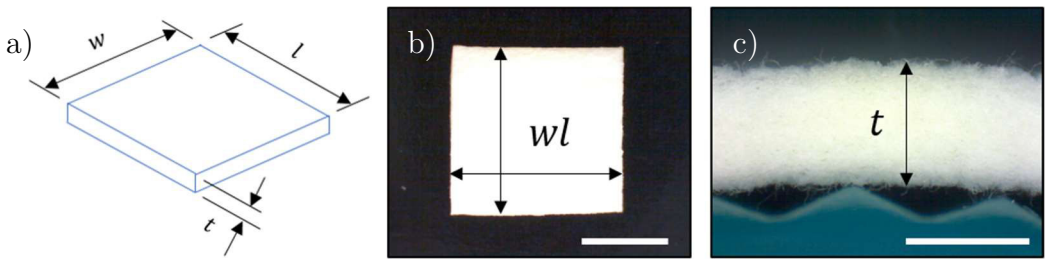

Figure 2.8: An illustration of scaffold volume determination. a) Diagram of scaffold volume, examples for measuring scaffold b) surface area (scale bar 5 mm) and c) thickness (scale bar 1 mm).

Finally, scaffold porosity was calculated by equation (2-6):

$$P = (1 - \frac{\vartheta_p}{\vartheta_b})100 \quad (2\text{-}6)$$

Where $\vartheta_p = \frac{m_{scaffold}}{\rho_{polymer}}$, $\rho_{polymer}$ is 1.12 g/cm^3 or 1.15 g/cm^3 for Pel or DP and $\vartheta_b = lwt$.

Gravimetrical determination of electrospun scaffold porosity, equation (2-6), has been described and used by many others [153, 178, 198, 208, 269, 343, 344]. The mass percentage of beads of the composite material before the washing process was defined by equation (2-7):

$$Bead\ fraction\ \% = \left(\frac{m_{beaded\ scaffold} - m_{scaffold}}{m_{beaded\ scaffold}}\right)100 \quad (2\text{-}7)$$

2.21 Mechanical characterisation

All polymer samples selected for mechanical characterisation were prepared as rectangular strips (30x5 mm, gauge length of 10 mm) and tested using universal tensile tester (Instron 5544 equipped with a 500N load cell, Norwood, USA) and custom made stainless steel claws with rubber inserts to minimise slippage. The experimental setup is shown in Figure 2.9.a-b.

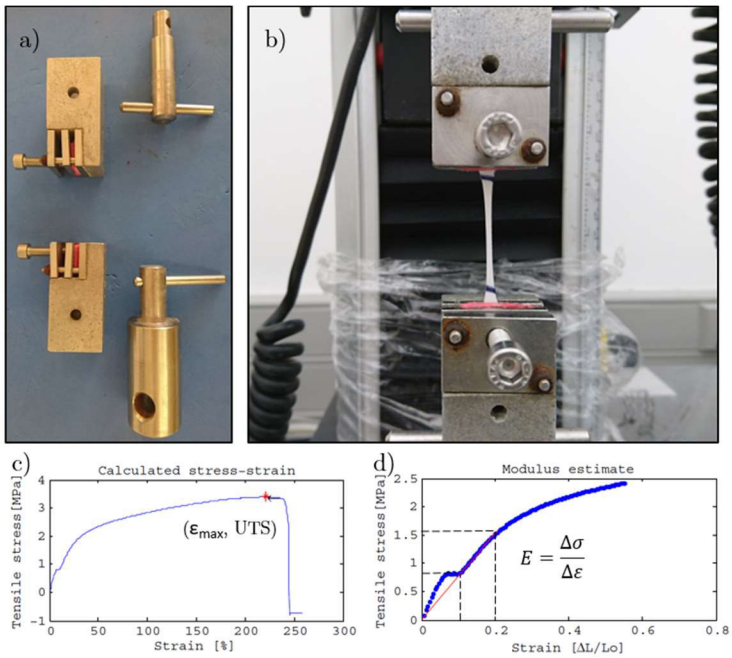

Figure 2.9: Tensile testing of polymer specimens. a) Custom-made grips used for testing all samples. Typical examples of b) a specimen being pulled and the output of a results report indicating c) maximum elongation, ultimate tensile strength and d) the elastic modulus.

Dry specimens of known thicknesses (measured as shown in Figure 2.8.c) underwent

tensile testing until failure at 66 mm/min (a strain rate of 11%/s, based on the compliance of a healthy blood vessel and a heart rate of 72 bpm [345, 346]). Next, the raw data captured by the Intron system was imported into Matlab and processed as stress-strain plots (an example of the output of a mechanical report can be found in Appendix A4). The maximum recorded stress and its corresponding strain value were defined as the ultimate tensile strength (UTS) and maximum elongation (ε_{max}) respectively. Young's modulus (E) was determined by the slope of the line fitted between the 10-20% strain region (see Figure 2.9.c-d). A summary of all mechanical experiments is shown Table 2.9.

Table 2.9: Summary of specimens tested for mechanical properties. Testing directions for electrospun scaffolds, with respect to the collector, were either circumferential (C) or longitudinal (L).

Study description	Material (number of groups)	Testing direction	Sample size in each direction per group
Heat pressed films	Pel, DP0 and DP30	N/a	n = 6
Different fibre orientations	Pel (3)	C and L	n = 3
Scaffolds for implantation	Pel (3) and DP30 (3)	C and L	n = 6

2.22 Scaffold architectural characterisation

Semi-automated macros were compiled with ImageJ (NIH Image, USA) to process images of electrosprayed or electrospun structures for architectural characterisation.

2.22.1 Electrosprayed microparticles

Bright field microscopy (20X objective at 2.00X digital zoom, Nikon Eclipse 90i, Japan) was used to photograph PEG particles collected on microscope slides. Photos were taken to create adequate contrast with respect to the background (converting Figure 2.10.a to b by adjusting the fine focus) at three different locations per slide (middle, left and right). The acquired images were processed with a self-constructed processing sequence to obtain information on individual particles. Briefly, photos were scaled (µm/pixel), converted to an 8-bit image and underwent an automated median threshold filter to obtain a binary frame of white background and black particles (as shown in

Figure 2.10.c). Next, the built-in particle analyser was used to measure the area ($A_{particle}$), aspect ratio (AR) and circularity (C) of individual particles. Finally, the averages and standard deviations were calculated for the total particles measured per group. The conversion of particle area to a circular diameter was $D_{particle} = \sqrt{4A_{particle}/\pi}$.

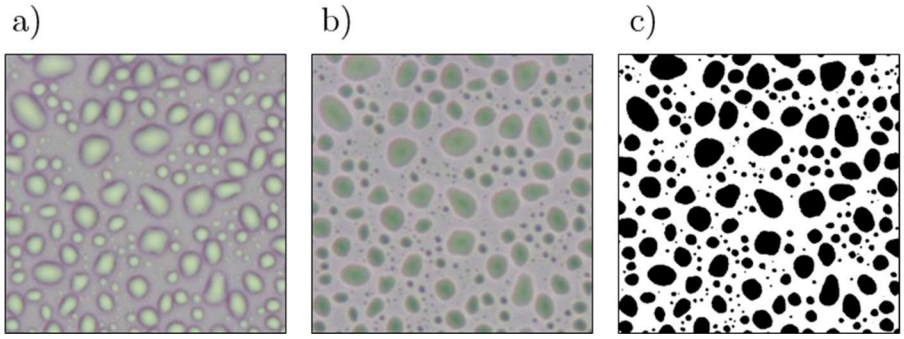

Figure 2.10: Image processing of electrosprayed microparticles. Examples of the a) original bright field, b) adjusted for higher contrast and b) binary images used for processing.

2.22.2 Electrospun fibres

Images were captured (using SEM as described in section 2.6) of the lumenal, ablumenal and cross-sectional surfaces from three snippets per electrospun sheet. Cross sectional images were kept for illustrative purposes while photos of the lumenal (n = 2) and ablumenal (n = 2) surfaces were used for 2D image processing (selected magnifications were X500 or X200 for Pel (~2 µm) or DP (~5 µm) electrospun fibres). From these images (n = 12 per group, 4 per sample times 3 for the number of electrospun sheets), the average fibre diameter, orientation index and equivalent pore size were determined.

2.22.2.1 Fibre diameter measurement

The average fibre diameter was calculated by manual measurements as described in literature [178, 262, 268]. First, a diagonal line was overlayed from the lower left to the upper right corner of the scaled image (µm/pixel, as defined by its scale bar) as demonstrated in Figure 2.11.

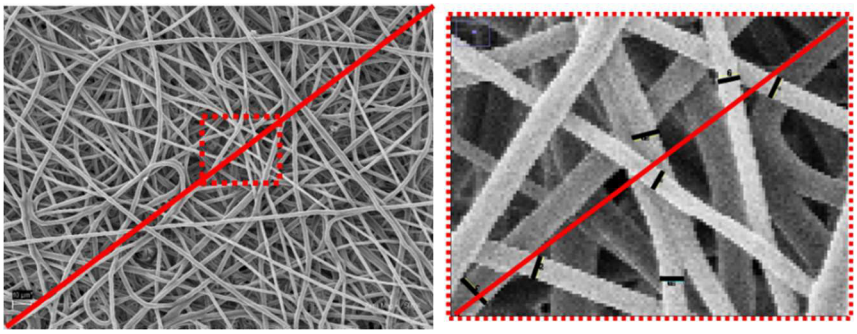

Figure 2.11: Manual measurements of fibre diameters from SEM images.

The width of each fibre that was intersected by the diagonal line was measured perpendicular to its length. The average fibre diameter and standard deviation were determined from all thickness measurements collected per scaffold group (approximately 40 fibres/image).

2.22.2.2 Fibre orientation quantification and visualisation

The entire SEM image (excluding the bottom scale bar) was used as the region of interest for quantifying and visualising fibre orientation of electrospun scaffolds. The degree of fibre alignment of each scaffold was quantified by its orientation index (OI, $0 \leq OI \leq 1$). The OI was measured as the image's overall pixel coherency using the OrientationJ plug-in (developed by [347–349] and previously used to evaluate alignment of electrospun fibres [153]).

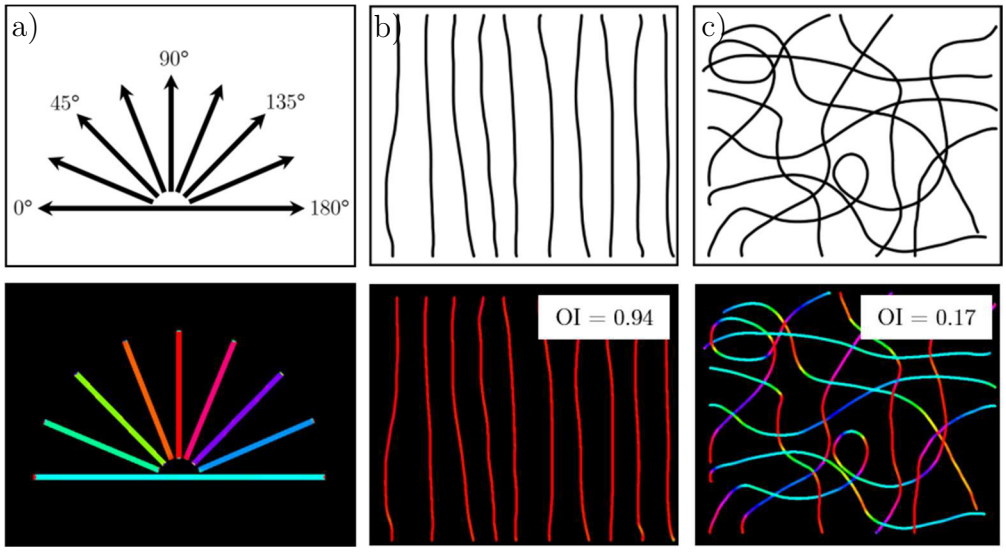

Figure 2.12: A demonstration of fibre orientation characterisation. a) semi-circle of defined angles and ten animated fibres representing either b) aligned or c) random orientated scaffolds with their respective orientation indices (OI).

An *OI* of unity represented perfect alignment while a value approaching zero indicated more randomly orientated fibres. This numerical representation of orientation was further complimented by colour mapping the direction of individual fibres. The colour survey was also generated by the OrientationJ plug-in (custom inputs: hue = orientation, saturation = x-gradient and brightness = y-gradient). Finally, *OI* averages and standard deviations were determined for all images representing each group, and the output images from the colour surveys were saved for illustrative purposes. The above described methodology is demonstrated in Figure 2.12 where ten theoretical fibres were processed that following either a uniform direction (b) or random paths (c).

2.22.2.3 Pore size determination

The methodology of an automated image processing sequence for measuring the two-dimensional pore sizes of electrospun scaffolds is summarised (frame-by-frame) in Figure 2.13.

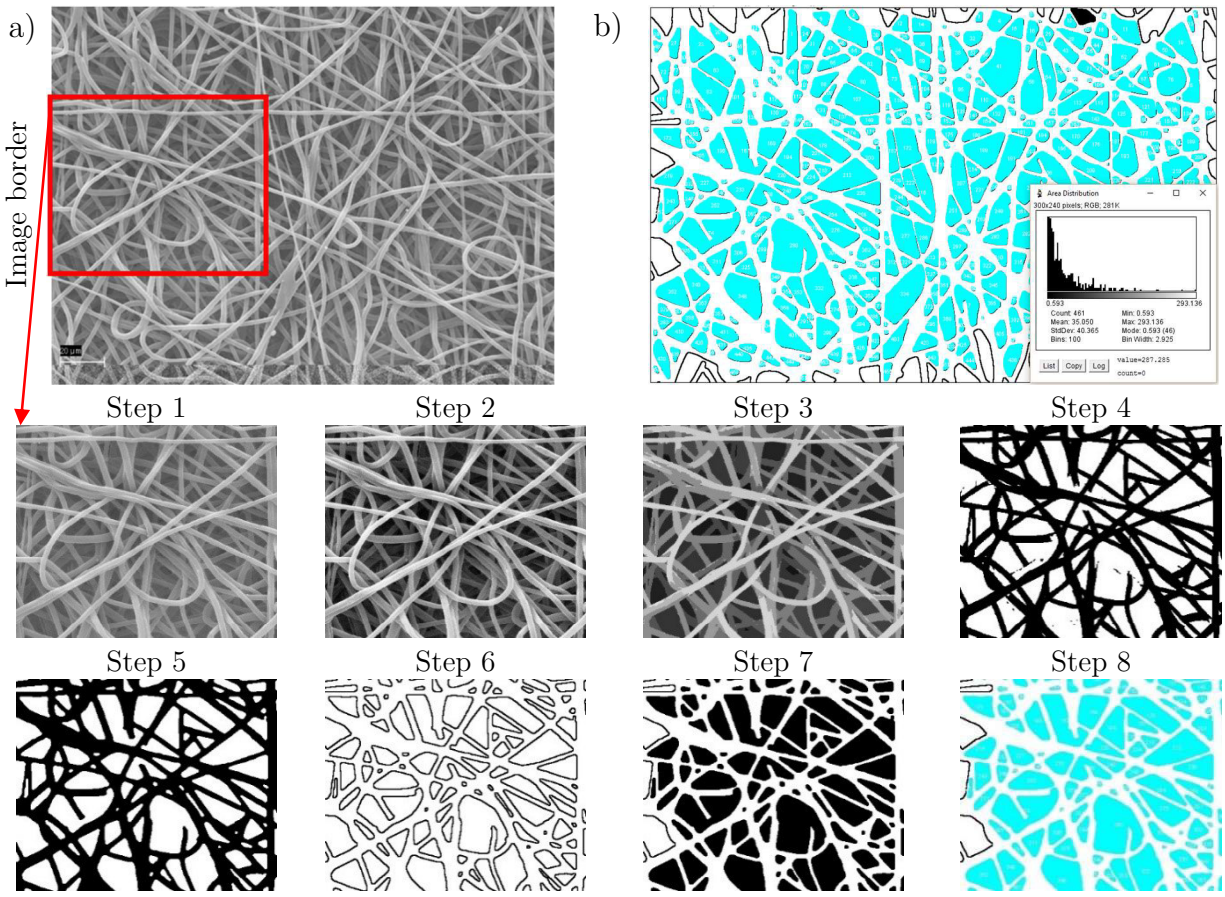

Figure 2.13: Image processing of electrospun scaffolds for pore size determination. a) the original and b) final processed image. Steps 1 to 8 demonstrate the intermediate frames during processing.

Briefly, the original SEM image was imported, scaled (µm/pixel), cropped to remove the scale bar and underwent contrast enhancement (0.3% pixel saturation, steps 1 to 2). A statistical region merging algorithm (developed by [350]) was applied (Q = 25) to merge the colour intensities of the same layered fibres (steps 2 to 3). Next, the images were made binary by applying an auto threshold filter (step 4) followed by a median filter (a radius of 3.5 pixles, step 5) to smooth out excess noise. The pore boundaries were defined by applying the built-in function 'find edges' (step 6) and filled with black pixels by using the 'fill holes' function (step 7). Finally, the pore areas (excluding the ones touching the image borders) were measured by the built-in particle analyser (step 9). The average pore area and standard deviation were determined from all pores measured per scaffold group (approximately 400 pores/image). Pore size was expressed as an equivalent circular diameter by converting area to diameter: $D_{pore} = \sqrt{4A_{pore}/\pi}$.

2.23 Healing evaluation of electrospun scaffolds

The healing performance of TE scaffolds developed during this project was investigated using a rat subcutaneous implantation model (as previously used by the UCT-Cardiovascular Research Unit [55, 153, 292, 302, 338, 351], and others specific for electrospun scaffold evaluations [130, 148, 153, 233, 237, 340, 352–359]). All procedures were in accordance with the Animal Protection Act (Act 71 of 1962), the Veterinary and Paraveterinary Professions Act (Act 19 of 1982) and the South African National Standard for the Care and Use of Animals for Scientific Purpose (SANS 10386:2008). This study (protocol 015-047) was also approved by the Departmental Research Committee and the Animal Ethics Committee of UCT. Moreover, individuals involved in the handling of animals were all trained and registered as veterinarians or para-veterinarians with the South African Veterinary Council (SAVC). Registration number for the author of this thesis: AL16/15395.

The sections to follow provide i) an overview of the study, ii) the processing parameters used for implant manufacturing, iii) the procedures used for implant and explantation

of samples, iv) the selective immunohistochemistry and v) histological image processing techniques for data collection.

2.23.1 Implant manufacturing and study overview

The selection of TE scaffolds for healing evaluations in a six-implantation-site model were divided into two main material groups (Pel and DP), each having three products (as listed in Table 2.10).

Table 2.10: Scaffold groups selected for subcutaneous implantation

Polymer group	Product	Scaffold description
Pellethane® (2363 80AE)	LP	Low-porosity scaffold produced by conventional electrospinning
	HP	High-porosity scaffold produced by combined electrospinning and elecrospraying
	HP+Hep	High-porosity scaffold with surface modified heparin
DegraPol® (DP30)	LTE	Low temperature electrospun scaffolds
	LTE+Dex	Low temperature electrospun scaffolds containing 5wt% dexamethasone
	LTE+Hep	Low temperature electrospun scaffolds containing 5wt% HepTBA500

The biostable (non-degradable Pel) implant groups included a porosity-enhanced scaffold (HP) produced by the combined electrospinning/spraying technique (section 2.20) and one produced by conventional electrospinning (LP) for comparison. Furthermore, the high-porosity groups were coated with heparin (HP+Hep, as described in section 2.8) to analyse its potential to influence the overall scaffold healing response. All bio-degradable scaffolds (DP) were produced by low temperature collecting (section 2.19). Two of these groups were incorporated with either 5wt% Dex (LTE+Dex) or 5wt% HepTBA500 (LTE+Hep) to analyse each drug's effect(s) against the healing performance of scaffolds without localised drug delivery (LTE). The parameters used to produce these products are summarised in Table 2.11. Enough scaffolds were produced for porosity measurements (n = 40 of 10x10 mm samples per group, equation (2-6)) from which subcutaneous implants were randomly selected (n =

24 per group) and sterilised using ethylene oxide gas. The remaining samples were used for representative characterisation in terms of architecture (pore size, fibre diameter and alignment, section 2.22), mechanical properties (strips of 5x30 mm were prepared, section 2.21) and drug surface concentration (section 2.10) or release kinetics (section 2.14).

Table 2.11: Electrospinning parameters used for implant production. DP, Pel and PEG are the polymers used for producing degradable, biostable electrospun scaffolds and water-soluble electrosprayed porogens respectively. *The collecting time for producing LP (without electrospraying).

Parameter	DP (LTE)	Pel (LP and HP)	PEG (porogens)
Solution concentration (wt%)	24	16	48
Solvent(s)	$CHCl_3$:HFIP	DMF:THF	$CHCl_3$
Co-solvent ratio	50:50%	50:50%	N/a
Flow rate (ml/h)	2.0	2.0	1.0 x 3
Needle size	G15	G15	G22 x 3
Collector size (mm)	75	25	25
Base electrode size (mm^2)	3600	3600	3600
Distance from collector (mm)	210	250	200
Collecting speed (rpm)	400	1000	1000
Translating speed (mm/s)	1.4	1.4	1.4
Applied voltage (+kV)	9	14	20
Collecting voltage (-kV)	1	1	1
Collecting time (hours)	3.5	3.0* and 1.5	1.5

The sample size for the *in vivo* evaluation, n = 6, for each group was calculated using GPower (V3.0.1, Universität Kiel, Germany) for the detection of an expected 20% difference of the mean healing performance (comparing the quantified results of tissue ingrowth, collagen, cellular, macrophage or vascular densities between scaffold groups) based on a standard deviation of 10%, a statistical power of 90% and a two-tailed student-t test with a 5% probability of making a type I error (as suggested by [360, 361]).

The time-line for the study was designed to evaluate the scaffolds over an implantation period of three months with sample retrieval dates at 7, 14, 28 and 84 days (as shown in Figure 2.14.a). Therefore, 24 animals (Wistar male rats, six per cage) were acquired one week in advance (-7 days) to allow for acclimatisation, and to establish a pre-

surgery base-line with respect to their behaviour and body mass (310.5±16.8 g on day 0). Rats were hydrated and fed *ad libitum*. Subcutaneous implantation surgeries were performed on day 0. Each of the products listed in Table 2.10 were randomly assigned (using the random generator in MS Excel) to a corresponding implantation site numbered 1-6 (Figure 2.14.b) of a randomly picked rat from each cage. Next, the implantation sites were rotated clockwise while keeping the same sample allocation sequence for the other five rats. Thus, each product (n = 6) was implanted in a different anatomical position (n = 6) in each of the six rats per group, thereby, eliminating location specific healing responses.

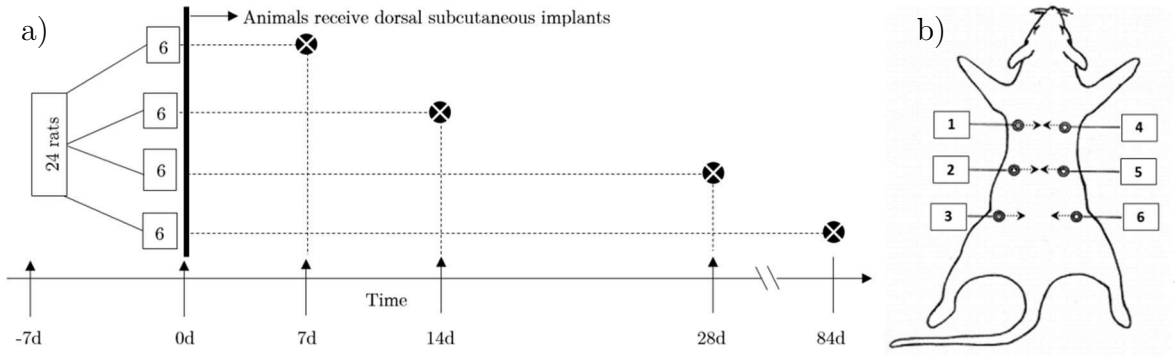

Figure 2.14: An overview of the *in vivo* assessment of electrospun scaffolds. Experimental time-line and the rat subcutaneous implantation model.

2.23.2 Subcutaneous implant and explant procedures

Following the seven days of acclimatisation, animals were medicated with buprenorphine (0.05 mg/kg) by subcutaneous injection (G25 needle) at 45-60 min preoperatively. All procedures took place in a room that was separate to the animal housing room. Rats were anaesthetised in an inhalation chamber at 5% isoflurane with an oxygen flow rate of 2 l/min (1bar and 21°C) for approximately 3 min (or until the animal has lost consciousness and normal breathing patterns were observed). Anaesthesia was maintained by delivering 1.5% isoflurane with an oxygen flow rate of 1.5 l/min through a custom-made nose cone. The surgical area (dorsal skin) was clipped to remove the hair and prepared using betadine iodine and F10 Skin Prep solutions. Ocular lubrication was applied to the eyes for the prevention of corneal desiccation. A heated plate (37°C) was used to maintain the animal's body temperature throughout

the surgical procedures (which lasted 35 min/rat on average). To limit contamination, all surgical procedures were performed under sterile conditions using sterile drapes, instruments (autoclaved) by a scrubbed surgeon following aseptic and Halstead's surgical principles. Six evenly spaced incisions of 10 mm in length were made using a scalpel blade parallel and on either side (3 per side) of the dorsal midline. Subcutaneous pockets of 20x20 mm in length and width were made at each longitudinal incision by lateral blunt dissection using surgical scissors (without interconnecting adjacent pockets). Next, sterile implants were pre-wetted by submersion in sterile PBS for 1 min, and were carefully placed within their pre-assigned pockets (one per pocket). The incisions were closed with 5/0 nylon sutures and a 16mm curved reverse cutting needle (Ethicon, Johnson & Johnson, RSA) using an intradermal cross matrass suture with a buried knot. Postoperatively, rats were moved to a separate recovery room where they were monitored under a heat lamp until fully conscious and ambulatory before they were reunited with their original group (6 per cage) in the housing room. All animal received another buprenorphine injection 8hours post operatively. The rats were continuously monitored for 8hours following their surgeries, and weighed every day for the next three days. Thereafter, rats were monitored daily and weighed weekly. As anticipated, all animals survived the surgical procedures and none were euthanised before their pre-determined dates. On explantation dates, animals were euthanised by an overdose inhalation of halothane (5%) in an enclosure for 15 min followed by a lethal intracardiac injection (1ml saturated KCl). Death confirmed animals were dissected in prone position. The dorsal skin was laterally reflected to reveal the subcutaneous samples in a mirrored order. Each sample with its accompanied tissue were carefully removed using surgical scissors and forceps. Next, scaffolds were cross sectioned in halves using a sharp microtome blade. The explanted halves were stored in 5 ml test tubes containing either 2 ml of zinc (IHC Zinc fixative, BD Pharmingen, USA) or 10% formalin fixation solutions. The zinc solutions were replaced after 48 hours. Finally, all fixation fluids were drained after 4 days and the samples were transferred to labelled

cassettes for histological processing. Figure 2.15 summarises the implant/explant procedures and lists the histological stains associated to each of the fixation fluids.

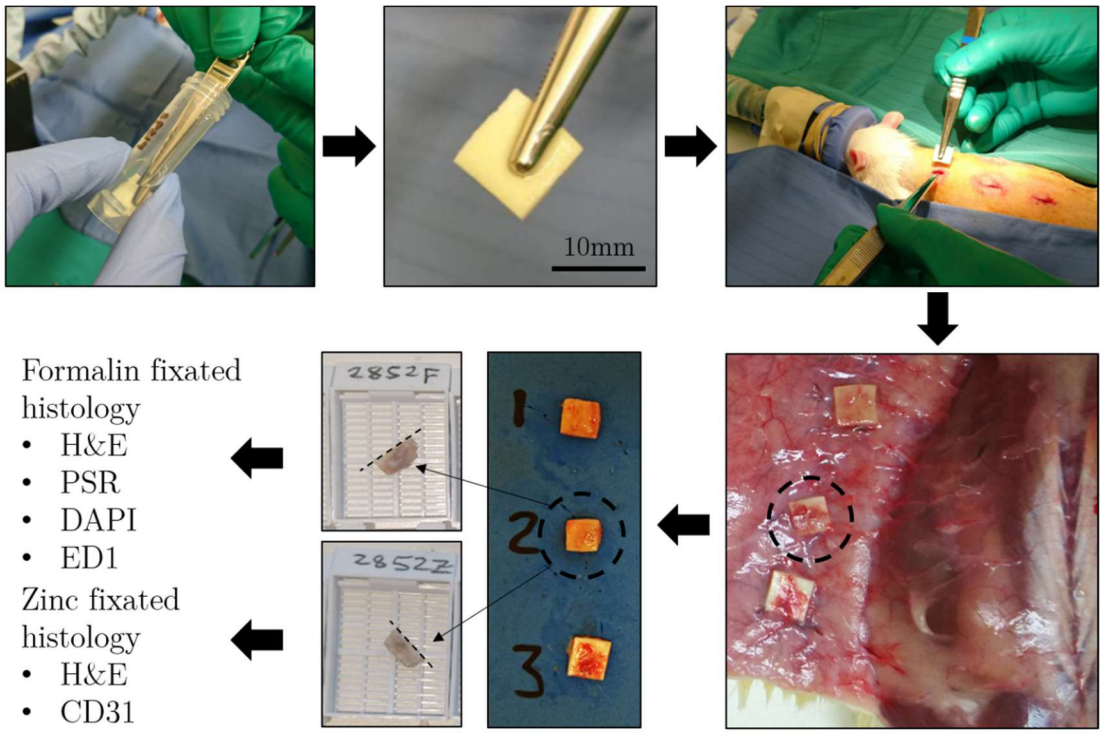

Figure 2.15: Summary of subcutaneous implant and explantation procedures. The first row represents the implantation procedure while the bottom row displays the explant process (e.g. 28 days).

2.23.3 Histology of explants

Histological preparations were performed at the Histology group of the Cardiovascular Research Unit. Briefly, fixed samples were dehydrated by immersion in ascending grades of alcohol, embedded in wax, cut into 5 µm sections, mounted onto slides and de-waxed using 2,2,4-trimethylpentane (3 times for 20 min each). After hydration in descending grades of alcohol, sections of formalin fixated implants were stained with Hematoxylin and Eosin (H&E, Merck, Germany and BDH, England), Picroserius Red (PSR) and anti-ED1 (Serotec Ltd, Oxford, UK) (Cy3 secondary antibody) counter stained with 4',6-diamidino-2-phenylindole (DAPI). Zinc fixated samples were stained with anti-CD31 (Fitzgerald International, North Acton, MA) and H&E. Photographs were captured using a stereo microscope (Eclipse 90i with a fluorescence unit, Nikon, Japan) equipped with a digital camera (DS-Ri1, Nikon, Japan). H&E stains were photographed using the 2X objective (digital zoom 1.0X, calibration 3.22 µm/pixel and

analog gain 1.0X) while PSR images were recorded at 4X objective (digital zoom 1.0X, calibration 1.61 µm/pixel and analog gain 1.0X). Both CD31 and DAPI/ED1 (fluorescence) prepared slides were taken at a higher magnification (10X objective, digital zoom 0.8X, calibration 1.61 µm/pixel and analog gain 4.0X). The photographs were stitched together at an overlap of 10% using NIS-Elements software (Nikon, Japan).

2.23.4 Image processing for scaffold healing evaluation

2.23.4.1 Tissue ingrowth

Tissue ingrowth of scaffolds explanted on 7, 14, 28 and 84 days was quantified by batch image processing (ImageJ) of both formalin and zinc fixated H&E stained micrographs (288 images, n = 6 per group per time point times two fixation media). The processing sequence included the following steps, the scaled cross-sectional image of an explant was manually cropped alongside its scaffold boundary ($A_{scaffold\ cross-section}$) and pasted on a blank image (white background), as shown in the Figure 2.16.

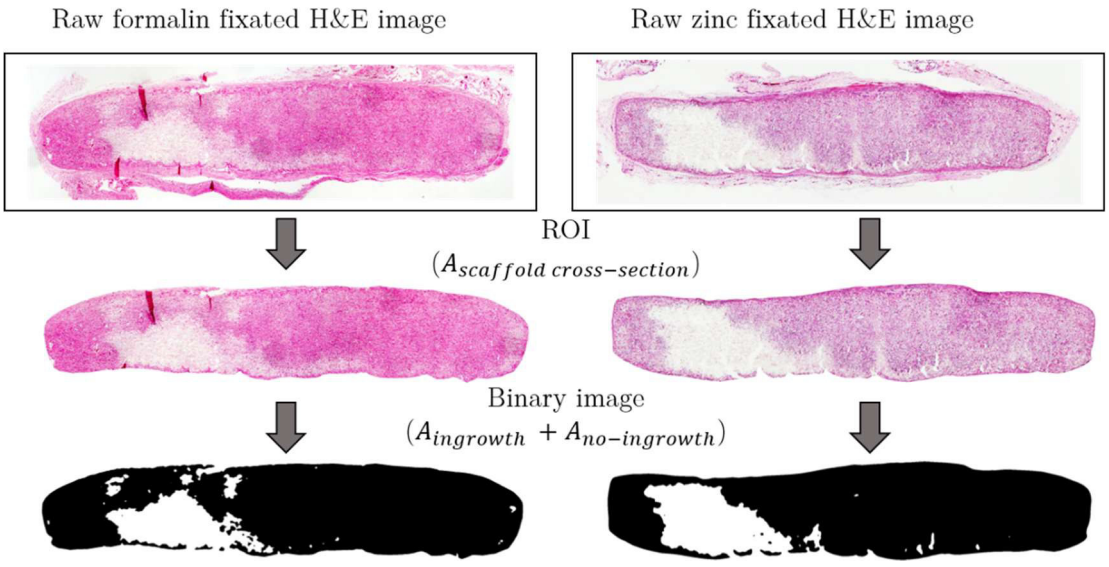

Figure 2.16: Image processing for quantification of scaffold tissue ingrowth.

Next, the image was run through an RGB filter (Red, Green, Blue) that was trained to isolate H&E positive pixel intensities (100:255, 0:200, 20:225) from the rest of the image. A Gaussian blur algorithm with a decay radius of 5 pixels was used to merge neighbouring cells together. The resulting image was made binary, black to represent

the area that was infiltrated by cells ($A_{ingrowth}$) and white for acellular areas ($A_{no-ingrowth}$). Finally, tissue ingrowth was expressed as the percentage of the scaffold that was colonised by cells, equation (2-8):

$$Tissue\ ingrowth\ \% = \left(\frac{A_{cellular\ infiltrated}}{A_{scaffold\ cross-section}}\right)100 \tag{2-8}$$

2.23.4.2 Collagen density

The deposition of collagen inside scaffolds that were explanted on 7, 14, 28 and 84 days was quantified by image processing of PSR micrographs (144 images, n = 6 per group per time point). Briefly, the scaled cross-sectional image of an investigated specimen was manually cropped alongside its scaffold boundary ($A_{scaffold\ cross-section}$) and pasted on a blank image. A custom RGB filter (202:255, 13:180, 68:210) was subsequently applied to isolate the positively stained collagen (pixels representing PSR) from the rest of the image. The filtered micrograph was converted to a binary image (black = $A_{collagen}$ and white = $A_{no-collagen}$), as depicted in Figure 2.17.

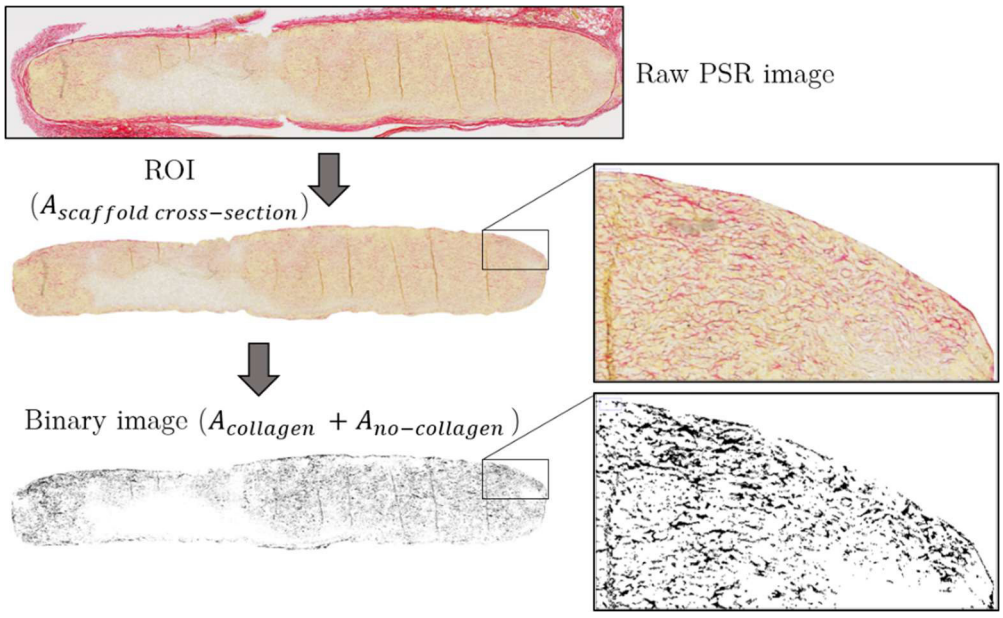

Figure 2.17: Image processing for quantification of scaffold collagen deposition.

The effective tissue area inside of an ingrown scaffold (infiltration area minus the scaffold material) was calculated as a function of each scaffold's cross-sectional area (ROI), tissue ingrowth percentage (from the processed H&E results) and porosity (as

measured before implantation), equation (2-9):

$$A_{tissue} = A_{scaffold\ cross-section} \cdot tissue\ ingrowth\% \cdot scaffold\ porosity\% \quad (2\text{-}9)$$

Finally, collagen density was expressed by equation (2-10):

$$Collagen\ density\ (\mu m^2/\mu m^2) = \frac{A_{collagen}}{A_{tissue}} \quad (2\text{-}10)$$

2.23.4.3 Cellularisation and macrophage density

Cellular and macrophage densities were both quantified from the DAPI/ED1$^+$ images taken of explants from 28 and 84 days (72 images, n = 6 per group per time point). Images were processed by cropping the scaffold area ($A_{scaffold\ cross-sectio}$) from the rest of the scaled image and pasting it on a blank image. Next, trained RGB filters were used to split the current ROI into separate images containing only the pixels intensities that represented DAPI (0:90, 20:200, 60:255) and ED1$^+$ (25:230, 5:85, 0:70) areas respectively (as demonstrated in Figure 2.18).

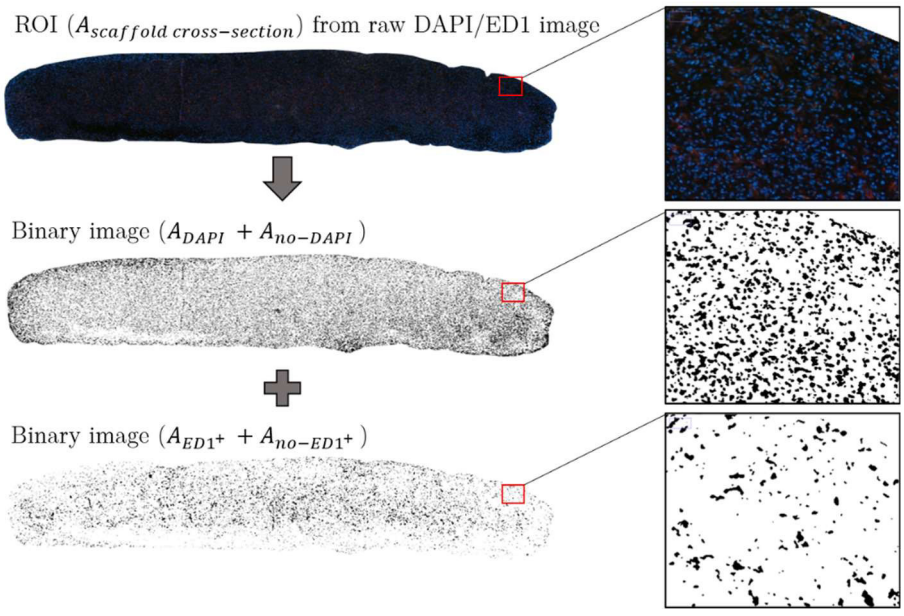

Figure 2.18: Image processing for quantification of cellular densities

Each of the filtered micrographs were converted to binary images, one that represented nuclei (black = A_{DAPI} and white = $A_{no-DAPI}$) and the other contained the macrophages (black = A_{ED1^+} and white = A_{no-ED1^+}). The area density of nuclei and macrophages per ingrown tissue area were determined from equations (2-11) and (2-12) respectively,

where A_{tissue} was determined according to equation (2-9).

$$Cellular\ density\ (\mu m^2/\mu m^2) = \frac{A_{DAPI}}{A_{tissue}} \quad (2\text{-}11)$$

$$Macrophage\ density\ (\mu m^2/\mu m^2) = \frac{A_{ED1^+}}{A_{tissue}} \quad (2\text{-}12)$$

Furthermore, the densities were also expressed in their numbers per mm^2 of ingrown tissue, as described by equations (2-13) and (2-14). The number of nuclei (n_{nuclei}) and macrophages (n_{nuclei}) from the binary images were counted by the built-in particle analyser after noise reduction, 'despeckle', and 'fill holes' functions were applied.

$$Cellular\ density\ (nuclei/mm^2) = \frac{n_{nuclei}}{A_{tissue}} \quad (2\text{-}13)$$

$$Macrophage\ density\ (macrophages/mm^2) = \frac{n_{macrophages}}{A_{tissue}} \quad (2\text{-}14)$$

2.23.4.4 Vascularisation

Scaffolds explanted on 28 and 84 days were also analysed for vascularisation by image processing of CD31 micrographs (72 images, n = 6 per group per data point). The processing sequence included the following steps, the scaled cross-sectional image of an explant was manually cropped alongside its scaffold boundary ($A_{scaffold\ cross-sectio}$) and pasted on a blank image as shown in Figure 2.19.

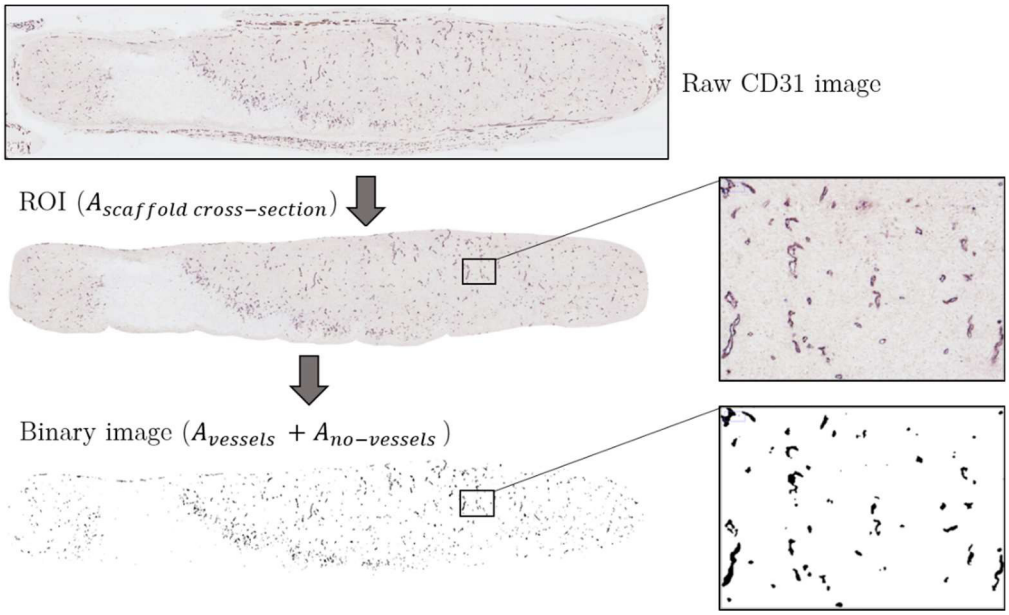

Figure 2.19: Image processing for quantification of scaffold vascularisation.

An RGB filter, specifically trained for each batch, was applied to isolate the endothelial cells (CD31 positive pixels) from the rest of the image. The resulting micrograph was converted to a binary image followed by applying 'dilate', 'erode', 'outline' and 'fill holes' built-in functions (black = $A_{vessels}$ and white = $A_{no-vessels}$). In similar fashion to scaffold cellularisation, vascular densities (as area or number as counted by the particle analyser) were calculated by equations (2-15) and (2-16), where A_{tissue} is determined from tissue ingrowth from zinc fixated H&E and equation (2-9).

$$Vascular\ density\ (\mu m^2/\mu m^2) = \frac{A_{vessels}}{A_{tissue}} \tag{2-15}$$

$$Vascular\ density\ (vessels/mm^2) = \frac{n_{vessels}}{A_{tissue}} \tag{2-16}$$

All image processing data were imported into Matlab from which graphs, averages and standard deviations were produced.

2.24 Statistical analysis

Graph error bars and in-line references of results were expressed as mean±standard deviation (unless stated otherwise). The statistical models used for the analysis of variance and significance (P value) between data sets depended on the nature of its distribution (parametric or non-parametric). Firstly, the distribution of data sets were investigated by the Shapiro-Wilk normality test (a Matlab script was compiled based on theory from the original author [362]) followed by a Q-Q plot. Analysis of variance were based on one-way ANOVA and the student-t test models if data sets were found to be normally distributed. Otherwise, non-parametric models Kruskal–Wallis one-way analysis of variance and the Wilcoxon sign-rank test were used to determine the P-values between data sets. A value of $P<0.05$ was assumed to be significant. A typical statistical report for a sample size of $n = 6$ can be seen in Appendix A5. In the case of linear regression, the correlation between the model and data set was optimised for least mean squares (unless stated otherwise). Computations and the plotting of graphs were performed using either Matlab (R2013a) or Microsoft Office Excel (2016).

3 Results and Discussion

This chapter summarises the results and discussion for the development of biostable, Pellethane® (Pel), and degradable, DegraPol® (DP), TE scaffolds. The subsections include studies on bulk material properties, parametric control of the electrospinning and electrospraying processes, combined electrospinning and spraying for porosity enhancement, drug incorporation and elution, implant manufacturing and finally subcutaneous *in vivo* assessments.

3.1 Material studies of polymer films

This section explores Pel and DP (DP0 and DP30) films in terms of their mechanical properties and accelerated degradation. The follow-up sections, 3.2 and 3.3, describe the development of fibrous structures from the selected biomaterials.

3.1.1 Mechanical properties

The tensile test results for heat pressed films made from Pel, DP0 or DP30 are illustrated in Figure 3.1. Mechanical properties were characterised in terms of ultimate tensile strength (UTS), maximum elongation (ε_{max}) and modulus of elasticity (E).

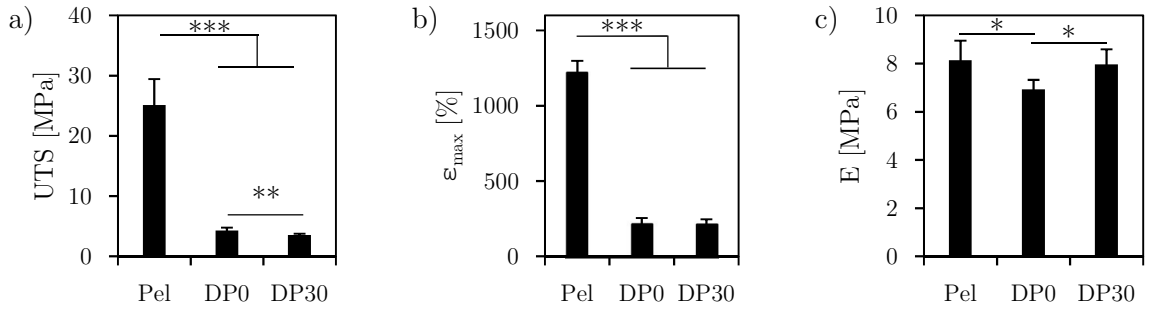

Figure 3.1: Mechanical properties of polymer films. a) Ultimate tensile strength (UTS), b) maximum elongation (ε_{max}) and c) elastic modulus (E). ***P<0.001/**P<0.01/*P<0.05. [n = 6].

Pel films had a UTS (25.11±4.32 MPa) and ε_{max} (1213±84%) approximately five times higher than that of either of the DP groups (P<0.001). The modulus of Pel

(8.13±0.82 MPa) was similar to that of DP30 (7.96±0.64 MPa, P>0.5) but significantly higher than that of DP0 (6.92±0.39 MPa, P<0.05). Within the DP groups, DP30 was slightly weaker (3.50±0.25 compared to 4.27±0.48 MPa, P<0.01), had similar ε_{max} (216±29 to 216±38%, P>0.9) but a higher stiffness (P<0.05) when compared to the properties of DP0.

The tensile testing results for Pel films are similar to those of previous studies (UTS 35-40 MPa with maximum elongations well over 700%) [254]. Likewise, mechanical results for DP correlate with previous work [272]. Mechanical properties for DP can be altered by varying the hard to soft segment ratio (a hard segment dominating DP is stronger) [258, 363]. In this case, that ratio is constant between DP0 and DP30 (40:60% hard to soft segment). Although the inventors of DP intended to control degradation (glycolate fraction on the soft segment side) independently of mechanical properties, in this case, the slight mechanical differences between the tested DP groups can be attributed to the glycolate content (0 compared to 30 mol-% for DP0 and DP30 respectively) [259, 260]. In comparison, hydrolytically resorbable polyesterurethanes (such as DP) have a different mechanical behaviour (different molecular chain mobility) when compared to biostable polyurethanes (such as Pel) due to the weaker ester bonds that exist in the poly(α-hydroxy ester) co-polymers found in the hard/soft segment chemistry (PCL and PHB-diols in this case) of DP [252].

3.1.2 Degradation in aqueous solutions

The percentage mass loss for the selected polymers incubated under physiological (pH = 7.4, a), acidic (pH = 0.8, b) or basic (pH = 13.0, c) conditions can be seen in Figure 3.2. Pel films had no significant mass loss after 20 days (P>0.1) while DP30 showed a faster degradation rate when compared to DP0 regardless of the media (P<0.05). Both DP groups degraded at a faster rate in a base medium (8% and complete disintegration for DP0 and DP30 respectively by day 5) when compared to mass loss measured at pH levels of 7.4 or 0.8 (0 and 1% for DP0 and DP30).

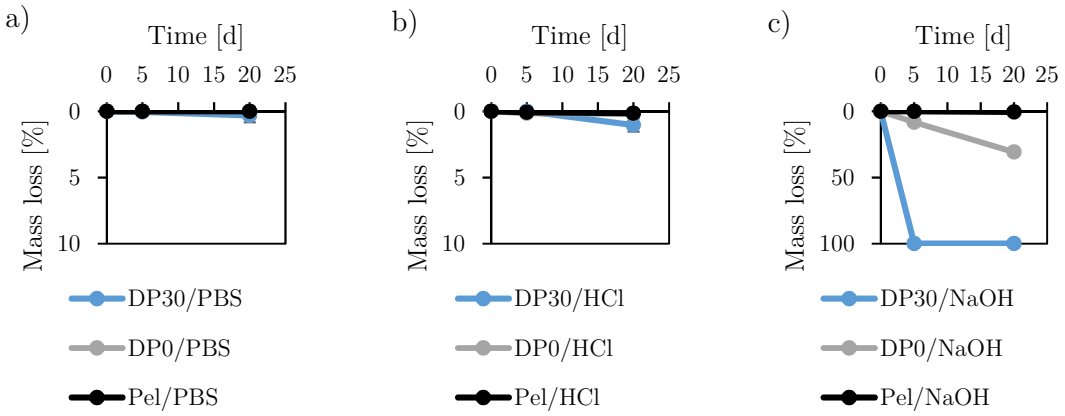

Figure 3.2: Accelerated degradation of polymer films in different media. a) PBS (physiological), b) 1.0 M HCl (acidic) and c) 1.0 M NaOH (basic). [n = 3]

Although previous studies have reported that Pel products would crack and degrade under harsh environmental conditions (e.g. *in vitro* oxidation with hydrogen peroxide [364], silver nitrate [365] or long-term *in vivo* implantation [366]), Pel did not show significant mass loss due to the short selected time frame and milder conditions. The observation of a faster DP degradation rate in a basic compared to an acidic medium agrees with a previous study on the rate of hydrolysis of aliphatic polyesters (PCL and PLA) in similar conditions. Hydrolytic cleavage of the polyester backbone is enhanced in the strong basic (pH ≥ 13) compared to strong acid (pH ≤ 1) conditions due to the stronger nucleophile (OH^-) that is available in the base environment when compared to that found in the acidic solution (H^+) [367]. DP30 showed significant degradation while DP0 did not show any mass loss because of the higher glycolate fraction on the soft segment side (0 compared to 30 mol-%). Similar observations were also reported in a previous study of DP films with various glycolate content fractions (DP33 showed earlier signs of degradation compared to DP0 after 100 days *in vitro* 37°C, pH = 7 buffered aqueous solutions) [260]. With the aim of developing biostable, non-degradable and degradable TE scaffolds, Pel and DP30 were the chosen biomaterials for the remainder of the project.

3.2 Biostable scaffold development

3.2.1 Electrospinning of biostable fibres

This section summarises the influence of controllable electrospinning parameters on the morphological outcome when processing Pel. Parametric studies were essential, due to the complexity of the spinning process, to understand and select optimal/acceptable conditions for implant ready scaffold production. The explored parameters included collecting speed and volumetric feed rate of Pel solutions.

3.2.1.1 Colleting speed

The influence of collecting speed on fibre orientation was quantified and visualised (pixel coherency) for Pel electrospun scaffolds (Figure 3.3). Furthermore, the mechanical changes due to fibre orientation were also investigated and are shown in Figure 3.4.

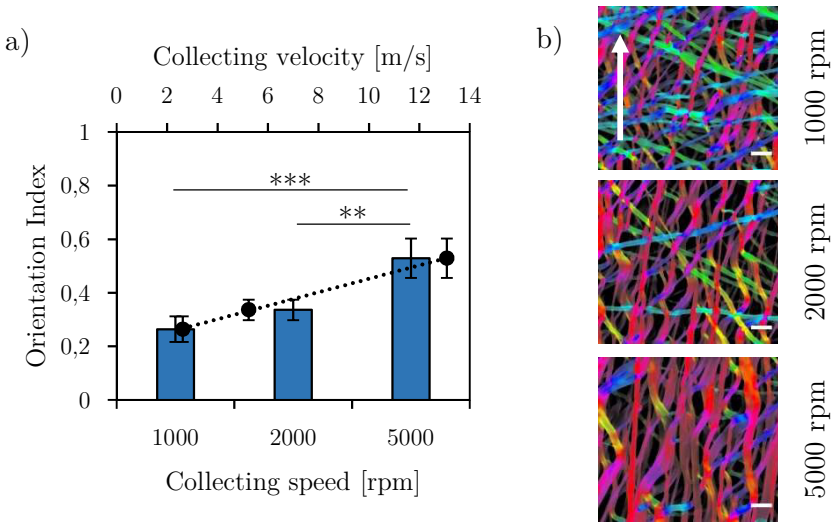

Figure 3.3: Fibre orientation for Pel scaffolds at different collecting speeds. a) orientation index as a function of collecting speed (velocity conversions are based on a 25 mm diameter collector); b) representative SEM images, white arrow indication circumferential direction. Scale bars are 10 µm. ***P<0.001/**P<0.01/*P<0.05. [n = 4]

The orientation indices increased from 0.26±0.05, 0.34±0.04 to 0.53±0.07 when Pel fibres were collected at 1000, 2000 and 5000 rpm respectively. The relationship between orientation index and collecting velocity was best described as $OI = 0.025v_c + 0.2$ (r^2 = 0.99), velocity in m/s (Figure 3.3.a). Colour encoded SEM images in Figure 3.3.b

illustrates the higher degree of orientation obtained at higher collecting speeds (observably fewer blue/green/yellow diagonal fibres and more red/pink/purple fibres in line with the collecting direction).

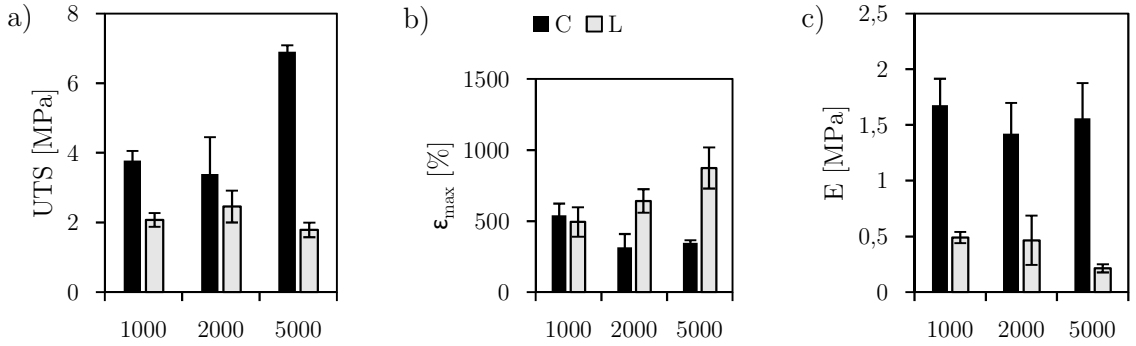

Figure 3.4: The influence of fibre orientation on mechanical properties. a) Ultimate tensile strength (UTS), b) maximum elongation (ε_{max}) and c) elastic modulus (E). [n = 3].

Mechanically, Pel scaffolds collected at 5000 rpm had a circumferential UTS nearly twice as strong as the UTS obtained at 2000 or 1000 rpm (6.90±0.19 and 3.39±1.10 or 3.78±0.28 MPa, $P<0.005$). Although the UTS for the 5000 rpm was on average lower in the longitudinal direction, there were no significant mechanical strength differences between the speed groups ($P>0.08$). Maximum elongation increased in the longitudinal (493.6±103 to 873.8±145%, $P<0.05$) and decreased in the circumferential direction (539.0±84 to 347.0±18%, $P<0.05$) for collecting speeds 1000 to 5000 rpm. An elastic modulus of approximately 1.5 MPa was obtained in the circumferential direction regardless of the collecting speed ($P>0.3$) and was 3-7 times greater when compared to E (0.21±0.04 to 0.49±0.05 MPa) in the longitudinal direction ($P<0.01$).

In accordance with expectation, circumferential uptake velocity directly influences fibre orientation (upregulating collecting speed encourages fibre alignment). This parametric relationship (using rotating collectors) was also shown in previous investigations [178, 180–183]. Scaffold strength was expected to be enhanced and maximum elongation reduced in the circumferential direction when collected at higher speeds [178, 181, 182]. This is due to more fibres being bundled in the same direction (reducing inter-fibre spaces) and in turn, increases the scaffold's bulk tensile resistance. Control over fibre

orientation, and therefore mechanical properties, are of importance to design scaffolds to maintain a certain compliance or burst pressure (e.g. vascular grafts application) that matches that of the native tissue [368]. Although this project has not yet produced vascular grafts, the data gathered from the current experiments may be useful to optimise the mechanical properties of Pel scaffolds when translated to a small diameter collector.

3.2.1.2 Flow rate

The fibre diameter of Pel collected scaffolds at different flow rates can be seen in Figure 3.5. Overall, a faster feed rate (Q) produced larger fibres at the expense of a broader distribution (1.0, 1.5, 2.0, 2.5 and 4.0 ml/h produced fibres of 1.41±0.3, 1.65±0.4, 2.14±0.5, 2.11±0.9 and 3.08±0.9 µm). The relationship between flow rate and fibre diameter was estimated to be $D_{fibre} = 0.55Q + 0.87$ µm ($r^2 = 0.97$). The Taylor cone at 4.0 ml/h was constantly interrupted by excess solution dripping form the needle tip. Conversely, the cone at 1.0 ml/h became periodically unstable due to insufficient solution at the tip. Flow rates between 1.5-2.5 ml/h had stable Taylor cones and allowed uninterrupted spinning.

Although small changes in flow rate may not have a significant influence on fibre diameter (as previously stated for electrospinning PCL at 0.6-1.5 ml/h [176]), several authors have confirm the existence of a positive relationship (thicker fibres are produced at higher flow rates) [132, 177, 178]. This is mainly due to a larger initial jet diameter caused by an increase of solution volume at the tip of the needle which leads to thicker fibre formation [169]. Secondly, the formation of fibres with larger diameters at higher feed rates may also be due to a lower degree of jet whipping (and consequently less fibre stretching) caused by a decrease in charge density as a result of a greater fluid volume [84].

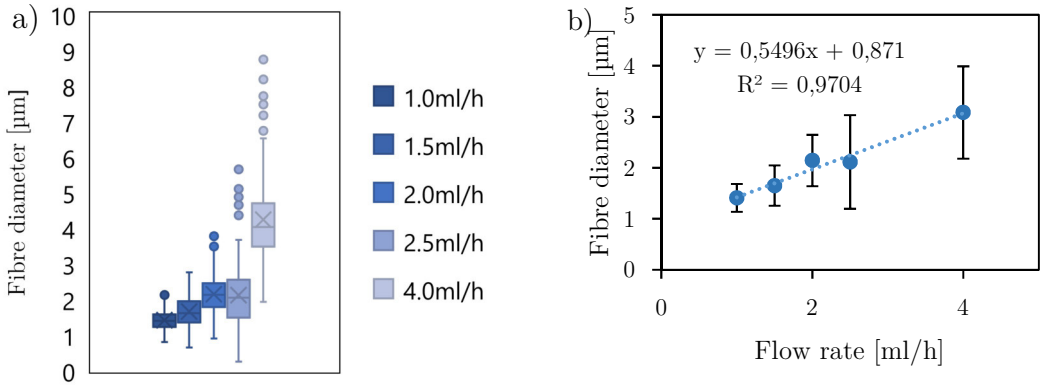

Figure 3.5: The influence of flow rate on electrospun Pel fibre diameter. a) Box and whiskers representation, b) linear trend between fibre diameter and flow rate. [n = 4, >20 fibres per image]

It is known that a unique flow rate exists, specific to each spinning solution, where fibre uniformity is optimised [177]. In the current case study, a flow rate of 2 ml/h was not only able to maintain a stable Taylor cone for >3 hours but also produced fibres with a narrower diameter distribution (uniformity) at a greater average (larger fibres have the inherent advantage of creating larger pores - [210]). Taking the results and observations into consideration, the optimal flow rate for Pel was selected at 2 ml/h.

3.2.2 Electrospraying of soluble microparticles

Parametric studies were essential to understand and control microparticle production. The explored parameters and their influence on electrosprayed polyethylene glycol (PEG) particle morphology included solution properties, collecting distance, needle diameter and production scalability. The flow rate for all studies were held constant at 1 ml/h (based on initial trails, data not shown).

3.2.2.1 Solution properties

The influence of solvent properties on electrosprayed particle diameter was investigated for three different solvents, MeOH, HFIP and $CHCl_3$, at a concentration of 20% (w/v) PEG_{20kDa}. A gauge 15 needle (G15) and a collecting distance of 20 cm were used. The particles produced from the selected solvents were distinguishable in terms of their sizes as observed at the same magnification SEM images presented in Figure 3.6.

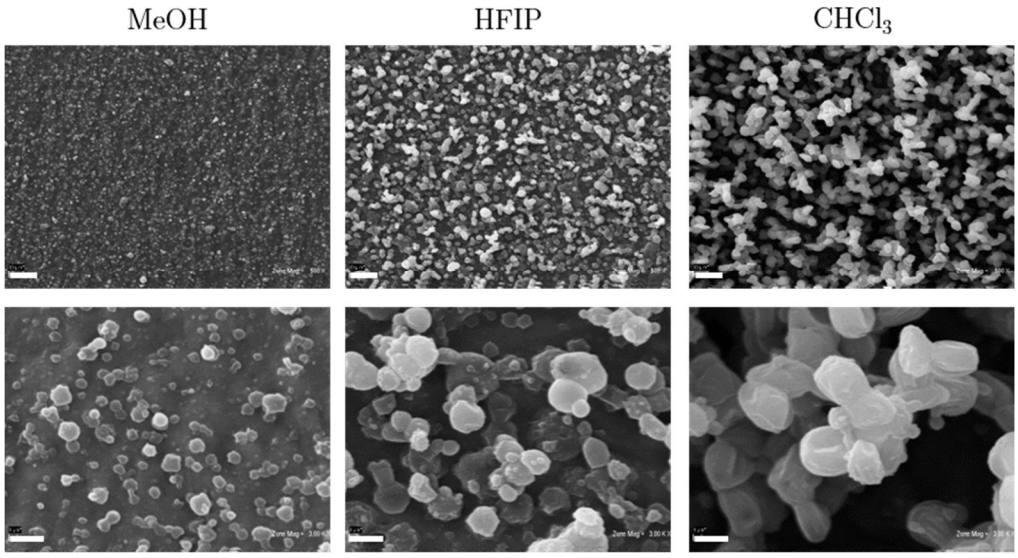

Figure 3.6: Electrosprayed PEG particles from different solvents. Scale bars are 20 and 5 µm for top and bottom SEM images respectively.

Particles sprayed from a low dielectric solvent ($CHCl_3$, $\varepsilon = 4.8$, $D_{particle} = 5.00 \pm 0.7$ µm) were larger when compared to the particles processed from solvents with higher dielectric constants ($\varepsilon = 17.8$ and 32.0, $D_{particle} = 1.46 \pm 0.4$ and 2.94 ± 0.9 µm for MeOH and HFIP). A convincing inverse correlation was found, Figure 3.7.a, for particle diameter as a function of dielectric constant ($D_{particle} = -0.13\,\varepsilon + 5.5$ µm, $r^2 = 0.98$) while other solvent properties did not follow a clear trend (as seen in the table from Figure 3.7.b).

a)

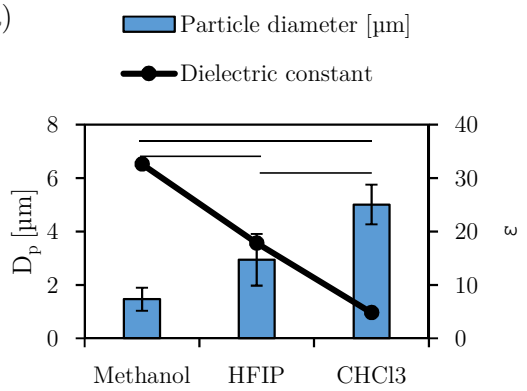

b)

	MeOH	HFIP	$CHCl_3$	
T_{BP}	64	58	61	[°C]
ε	32.0	17.8	4.8	-
γ	22	16	27	[dyn/cm]
ρ	0.79	1.60	1.49	[g/ml]
D	1.46 ±0.4	2.94 ±0.9	5.00 ±0.7	[µm]

Figure 3.7: The influence of dielectric constant on electrosprayed particles. a) relationship of particle diameter and dielectric constant; b) table of results for average particle diameter (D) for each solvent with different boiling points (T_{BP}), dielectric constant (ε), surface tension (γ) and density (ρ). [n = 2, >30 particles/image]

An organic solvent with a lower dielectric constant gives rise to a less conductive solution (may be expressed as $K \propto e^{-\frac{1}{\varepsilon}}$). This dependence can be explained by the

increased electrostatic attraction between ion pairs as the dielectric constant decreases (qualitatively known as the Nernst-Thomson rule). Moreover, the observation of larger particles can be expected when the solution conductivity is decreased. Droplet charge density is what drives this occurrence. A higher charge density will result in a greater degree of Coulombic fission (CF) before complete solvent evaporation occurs (CF, an event when electrostatic forces overcome droplet surface tension, and explode into smaller satellite particles, due to a decline in solution volume while electrostatic charge remain constant) [72, 369]. This parametric relationship is in accordance with the scaling laws of atomisation where particle diameter has the following relationship with solution conductivity $D_p \propto K^{-\frac{1}{6}}$. Therefore, the larger particles produced from a lower dielectric solvent system (chloroform in this case) were in agreement with electrohydrodynamic theory, as well as previous observations [370, 371]. In the face of universal atomisation applications, i.e. drug delivery devices where particles are made at nanoscale [184, 372–375], $CHCl_3$ was a useful solvent selection for optimising microparticle size (towards the aim of producing >30 µm spheres to act as temporary space holders within a fibrous network).

3.2.2.2 Collecting distance

Theoretically, larger particles can be obtained by increasing the molecular weight (M_w) and/or the volume fraction (φ) of the polymer solution (scaling laws section 1.2.3). This is true only until a point is reached where fibre (instead of particle) formation will take place. At such a point (the Rayleigh limit), macromolecular entanglement (chain overlap) is sufficient to resist the forces that governs jet breakup and result in continuous fibre formation post to the Taylor cone region (the forces to resist are solution surface tension and the successive CF's). For simplistic control, the molecular weight for all subsequent studies on electrospraying of PEG/$CHCl_3$ was therefore fixed (10 kDa instead of 20 kDa) and the concentration was varied to continue particle optimisation (preferably >30 µm). Furthermore, the influence of collecting distance (a

parameter that is often overlooked) on particle area ($A_{particle}$), aspect ratio (AR) and circularity ($C_{particle}$) were investigated for 40wt% PEG_{10kDa} /$CHCl_3$ sprayed from a G15 needle. The results are presented by bright field microscope images (Figure 3.8) and the data are summarised in Figure 3.9.

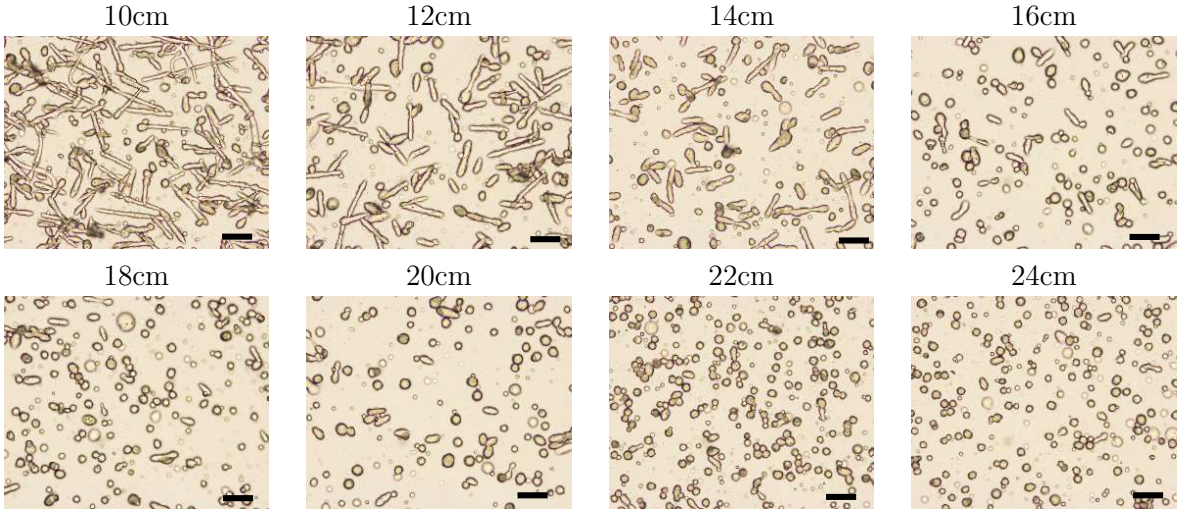

Figure 3.8: Particle morphology of electrosprayed PEG particles over a distance. Scale bars are 50 µm.

An abundance of short strand fibres (40.8±29 µm and 8.1±2 µm of length and diameter) or microspheres (13.0±2 µm) were observed at collecting distances ≤12 cm or ≥18 cm respectively. The variation of particle geometry, as a function of the distance between the needle and collector, was supported with the image analysis results where particles at 10-12 cm had a high AR (4.1±2.9), low $C_{particle}$ (0.5±0.2) and high $A_{particle}$, (363±248 µm^2) when compared to particles measured at 18-24 cm which had a low AR (1.2±0.4), high $C_{particle}$ (0.9±0.1) and a low $A_{particle}$ (133±74 µm^2). In summary, a particle underwent the following geometrical changes as it was collected at distances away from the nozzle (illustrated by Figure 3.9.d): short strand fibre (10-12 cm), elongated ellipse (12-14 cm), mid-pinched ellipse (14-18) and finally spherical microparticles with associated satellite particles (18-24 cm). Furthermore, 20 cm was found to be a suitable collecting distance to allow simultaneous electro-spinning and -spraying due to minimal electric field interference with the opposite base electrode (not too close to repel the incoming electrospun fibres away from the collector) and at a position that would permit maximising particle (spherical) diameter while having

acceptable polydispersity.

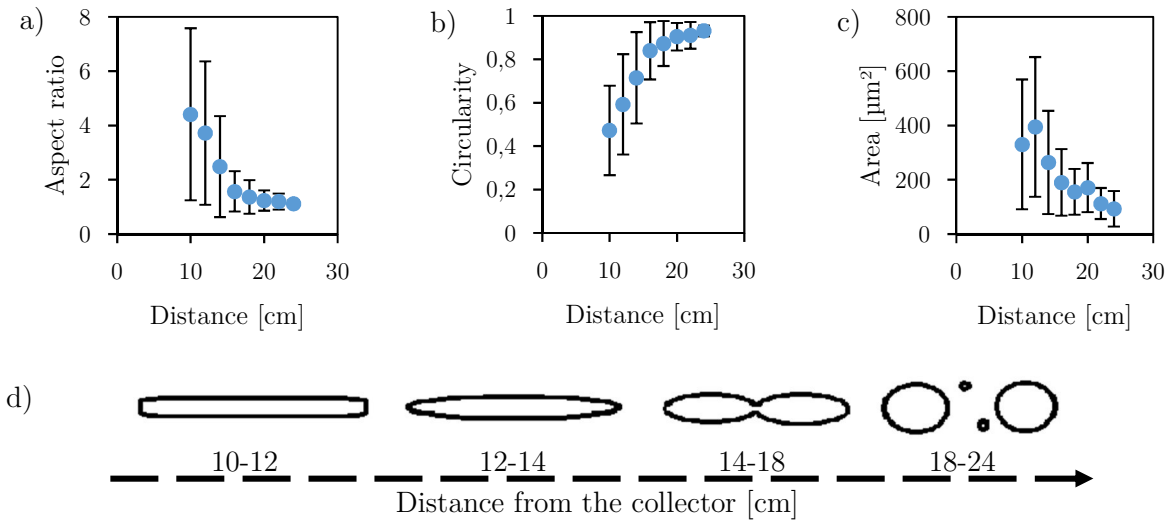

Figure 3.9: The influence of collecting distance on electrosprayed particles, d) visualisation of particle formation towards the collector

Collecting distance is a parameter that can be optimised to a point where particles have the least polydispersity and the best spherical geometry for a set of experimental conditions [375]. Another study reported that particle reproducibility (morphologically) was limited at a distance that is too close to the collector (15 cm in their experiments) while particles collected at a distance further away (20-25 cm) had a narrower size distribution [376]. It is also known that the electric field between the needle and collector is stronger at shorter distances [377]. Therefore, electrosprayed particles are expected to be smaller at distances closer to the collector compared to particles collected at distances further away. The latter assumption was experimentally confirmed by others [190]. In contrast to this, particle area from the current experiments decreased as collecting distance increased (Figure 3.9.c). This observation can be explained because the initial particles, collected at closer distances, were short strand fibres and not yet particles - an elaboration on this statement will follow. Elongated particles and short strand fibres have been identified before [189]. The authors described this phenomenon as an interplay between chain entanglement and CF. Elongated or irregular shaped particles can be formed before complete solvent evaporation, and

remain frozen, since the energy required to break molecular entanglement is far greater than that present during CF [378]. Complementing this tentative explanation, the current study is an elegant step-by-step display of how particles are formed during flight towards the collector. At closer distances to the Taylor cone (referring to Figure 3.9.d), short strand fibres/elongated particles are extruded from the straight jet due to sufficient chain overlapping which initially resist sphere formation (surface tension). Further away from the base electrode, a decline in electric field strength causes elongated particles to relax and allow for surface tension to compete against the prior dominating electric stresses. Eventually, spherical particles are formed even further down the path due to dominating surface tension and successive CF. Each step was frozen in its current geometrical state because the charges were neutralised as soon as the particle landed on the grounded collector and/or the solvent evaporation process was fast enough to preserve the particle's shape.

3.2.2.3 The influence of needle diameter at optimal concentration

An increase in polymer concentration of 40 to 48wt% resulted in particles that measured more than twice the diameter (13.0±2 to 30.3±14 µm, $P<0.001$). Moreover, it was found that the needle size had little to no influence ($P>0.5$) on particle diameter when electrospraying with 48wt% PEG_{10kDa}/$CHCl_3$ (G25 to G15, with inside diameters of 0.26-1.37 mm, produced particles within the range of 31.5±15 µm). The diameter of particles produced from seven different needles are shown in Figure 3.10.

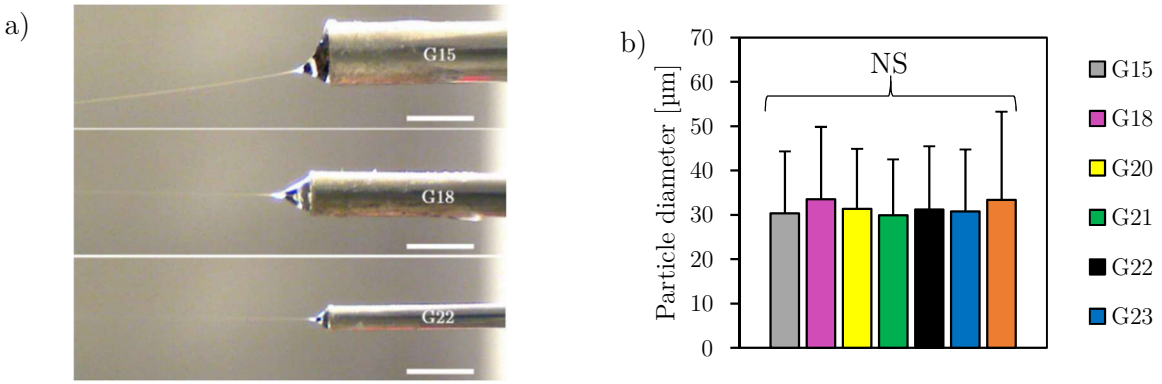

Figure 3.10: The influence of needle diameter on electrosprayed particle size. a) Taylor cones of needle gauges G15, G18 and G22 [scale bar at 2 mm], b) average particle diameter NS = no significance.

A concentration of 48wt% was found to be the upper bound to electrospray $PEG_{10kDa}/CHCl_3$ from a clear solution at RT. Solutions ≥50wt%, although initially transparent, precipitated during the cooling process and lead to solution build-up or 'needle clogging' which ultimately prevented continuous electrospraying at RT. Although 48wt% was a uniform solution prior to processing, solution build-up was also observed when a large diameter needle was used (such as G15, which was also used in the previous experiments). The time of uninterrupted electrospaying at the optimal concentration of 48wt% was observed to have a dependency on the surface area of the exposed Taylor cone which in turn was controllable by needle gauge selection. A needle size of G15 (id = 1.77 mm), G18 (id = 1.23 mm) and G22 (id = 0.72 mm) produced Taylor cones surface areas of 3.95, 2.45 and 0.90 mm^2 while all other parameters were kept constant. Uninterrupted spraying time was increased from <5 min to >2 hours when the inside diameter of the needle decreased by 1 mm (simply swopping the G15 with a G22 needle). In summary, continuous production of water-soluble microparticles with diameters >30 µm (as presented by Figure 3.11) was achievable with a solution of 48wt% $PEG_{10kDa}/CHCl_3$ (at RT) that was electrosprayed at a flow rate of 1 ml/h from a G22 needle (connected to a positively charged base electrode of 60x60 mm) and collected at 20 cm.

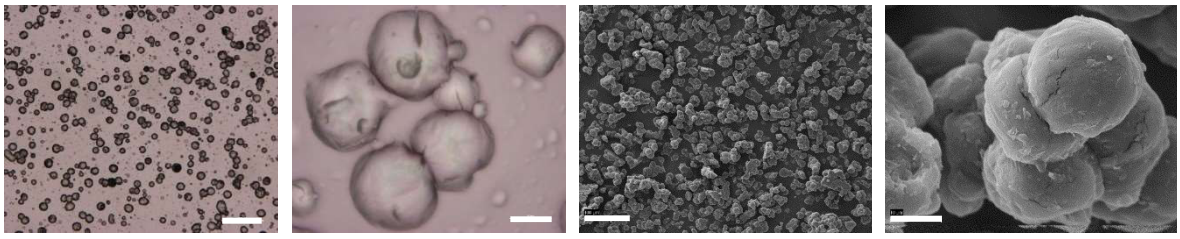

Figure 3.11: Electrosprayed polyethylene glycol microparticles. Scale bars are 200 and 20 µm for low and high magnifications for both optical and SEM photographs.

It is generally assumed that larger particles will be produced when electrospraying with larger sized needles (those with lower gauge numbers). This statement roughly relies on the obvious dependency that the diameter of the needle determines the base of the Taylor cone and consequently the size of the particle. Although this parametric relationship has previously been observed while electrospraying with two different

needle gauges (G26 or G24, id = 0.26 or 0.31 mm [31]), conflicting results have also been reported [32]. In a previous study, 10%(w/v) PCL_{50kDa} was dissolved in pure chloroform and electrosprayed from either a G26 or a G21 needle (id = 0.26 or 0.51 mm) [33]. The authors found that needle diameter had no significant influence on the measurable size of the collected particles. Another study also reported that particle size had no dependency on capillary diameter (the tested range was id = 0.12-0.58 mm) [34]

3.2.2.4 Multiple needles

Multiple needles were investigated as an attempt to upscale particle production rates. Initially, a double needle configuration was tested (side by side needles at 12 mm apart). It was found that the two jets repelled each other in such a fashion that caused an uneven distribution of material on the surface of the collector (more accumulated on the sides than in the middle). A linear array of 3 needles, at a pitch of 12 mm, provided a smooth distribution of particles which uniformly covered the entire length of the collector (as observed in Figure 3.12).

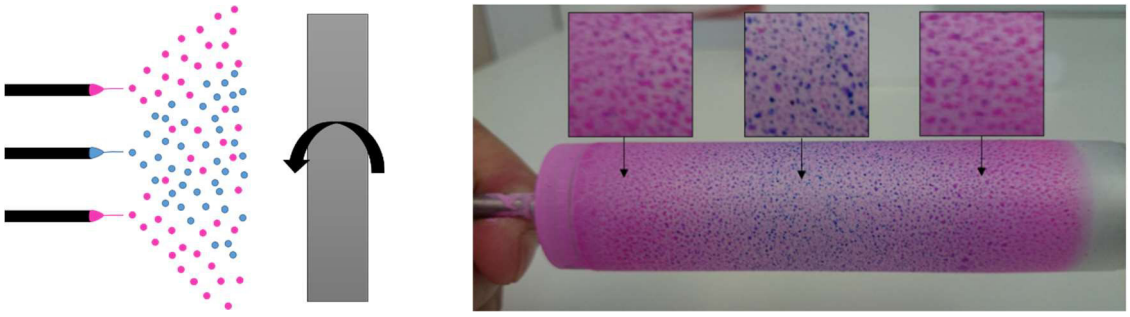

Figure 3.12: Particle distribution of a triple needle electrospray configuration

Previous research also showed successful upscaling of the electrospraying process. In their particular configuration, PLGA was electrosprayed from parallel needles (id = 0.06 mm) at a pitch of 0.7 mm [189]. The configuration under current investigation (triple G22 needles at a pitch of 12 mm) was adopted for a higher particle production rate.

3.2.3 Combined electrospinning and spraying

The composite materials produced by simultaneous electrospinning and electrospaying (using a single or triple needle configuration) of Pel fibres and water-soluble PEG microparticles are compared to the scaffolds produced by conventional electrospinning in Figure 3.13. The SEM images represent scaffold cross sections followed by low and higher magnification photographs of the top view (abluminal side). Embedded microparticles can be observed in the images where electrospraying were introduced.

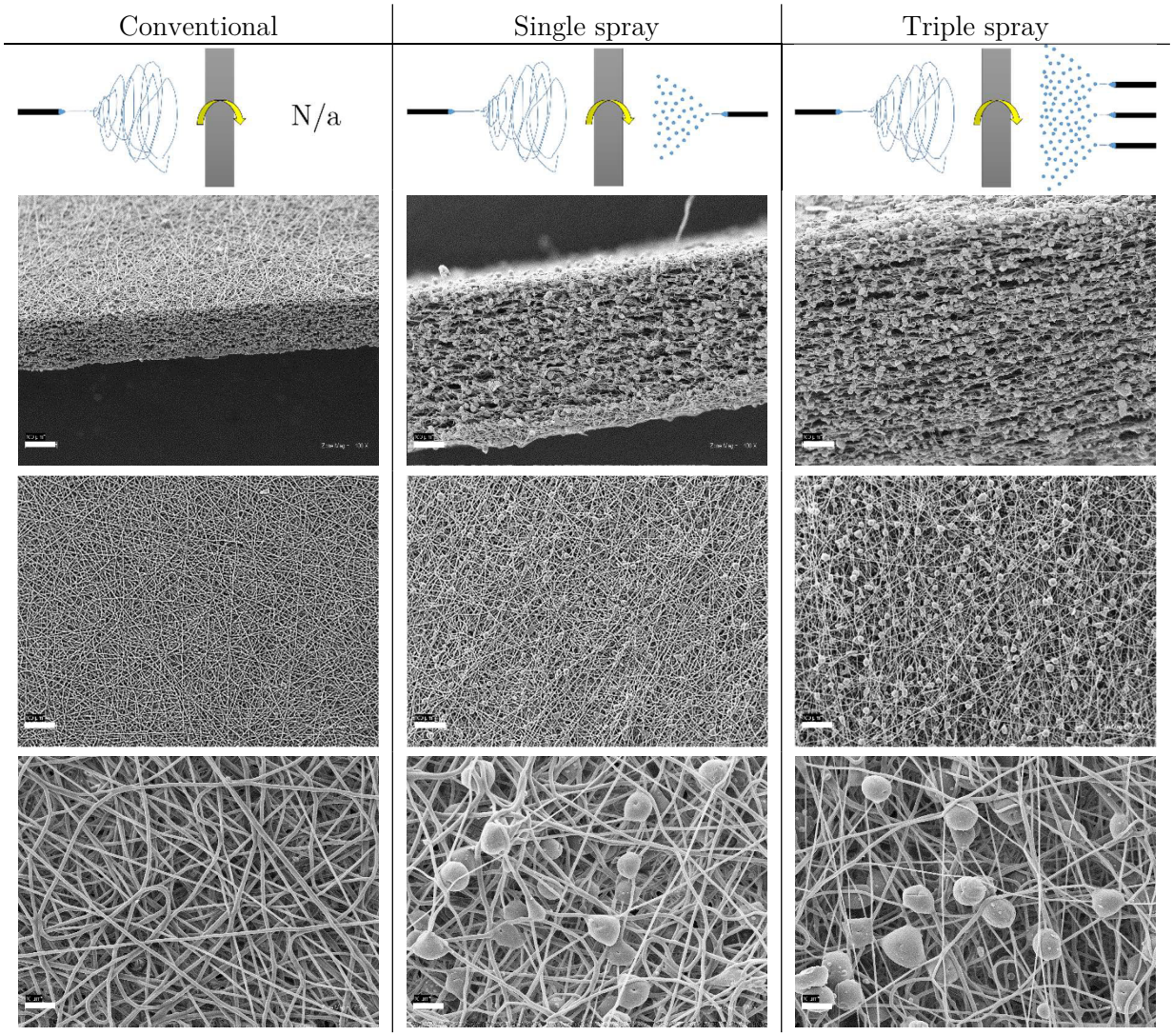

Figure 3.13: Composite materials created by combined electrospinning and spraying. Scale bars are 100 µm (cross sectional and low magnification top view images) and 20 µm (higher magnification images).

The porosity of conventional electrospun scaffolds increased from 78.6±0.5 to 88.9±0.5% ($P<0.001$) or 92.9±0.4% ($P<0.001$) after bead removal from the composite materials created by either a single (bead fraction of 64%) or a triple (bead fraction of

73%) needle spraying configuration system respectively. The enhancement of 3D interconnectivity and slightly larger pores are visually observed in the cross sectional and top view images of Figure 3.14.

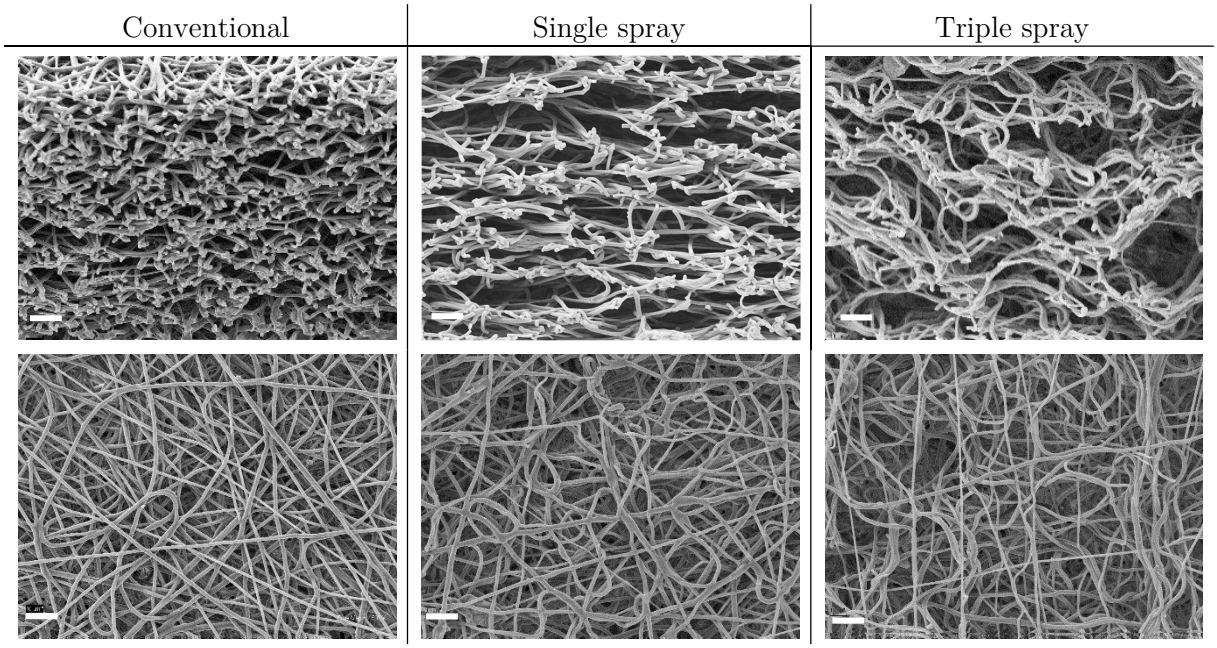

Figure 3.14: Porosity-enhanced scaffolds after sacrificial bead removal. All scale bars are 20 µm.

Simultaneous electrospraying PEG microparticles opposite to electrospinning Pel fibres (a close-up view of the composite material can be seen in Figure 3.15.a) had no significant influence on the resulting fibre diameters (1.9±0.5 µm) regardless of the number of needles used ($P>0.5$). The scaffold thickness of conventional electrospinning (228±9 µm) was increased to 495±33 µm or 976±60 µm (after bead removal) when a single or triple array of needles were used to include the microparticles. The particles, which acted as temporary space holders, slightly increased the two-dimensional pore size of conventional scaffolds from 9.7±3 µm to 10.3±4 µm ($P>0.1$) or 10.7±5 µm ($P<0.05$) for a single or triple needle configuration respectively. The results are summarised in Figure 3.15.b.

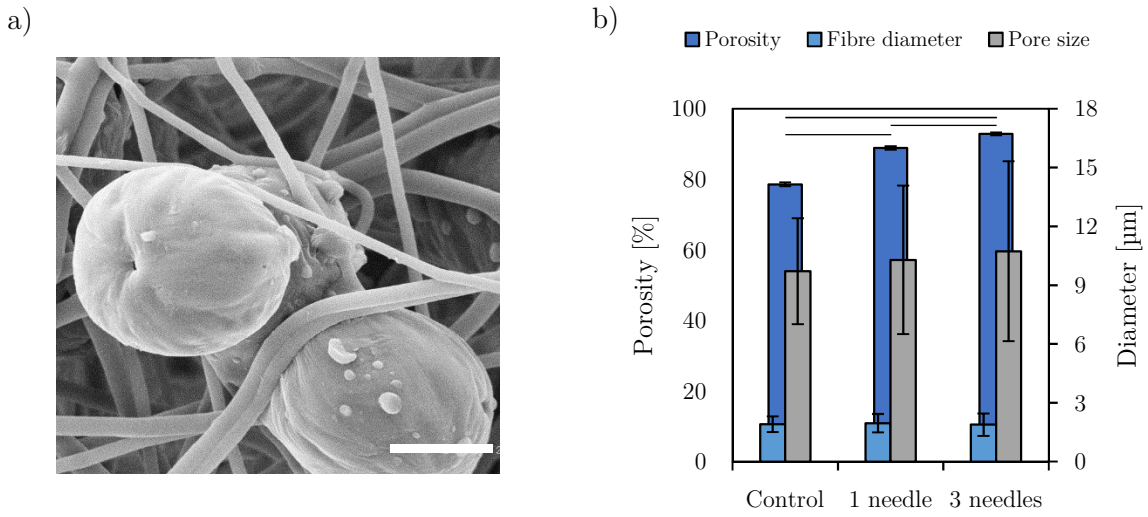

Figure 3.15: Combined electrospinning and spraying results. a) Pel fibres and PEG porogens close-up SEM image [20 µm scale bar]; b) scaffold porosity, fibre diameter and pore size results.

The porosity after porogen incorporation and removal was greater than that of the conventional scaffolds because of the volume expansion caused by the inclusion of temporary microbeads while the structural mass (fibres) remained constant (porosity equation 2-6). A triple needle configuration had a greater influence on porosity due to a higher particle production rate which resulted in a higher bead to fibre fraction when compared to a single production source. The apparent inadequacy to enlarge scaffold pore size can be explained by a closer inspection to the SEM images presented in Figure 3.16. Even though a two-dimensional quantification of pore size (via image processing) might produce the same results in both Figure 3.16.a and Figure 3.16.b, there are notably more 3D space created in Figure 3.16.b (where the 30 µm microbead use to be, indicated by the red circle) compared to the densely packed fibres from Figure 3.16.a.

Previous studies have also investigated combined electrospinning and spraying and obtained results similar to that of the current study - porosity enhancement of natural (84-95%, [148]) and synthetic (87-94%, [233]) electrospun scaffolds. Although these authors also showed enhanced cellular infiltration *in vitro* and *in vivo* (in a subcutaneous model), there were no mention and/or quantification of scaffold inflammation nor vascularisation (angiogenesis being one of most important challenges in tissue engineered scaffolds [296, 379] and therefore a useful measurement for long-

term *in vivo* performance). Moreover, larger porogens (~50 µm) were sprayed from a single source compared to the current developed technique which included smaller particles (~30 µm) produced from multiple electrospraying sources. A large sum of smaller particles has the potential to uniformly influence the architecture of the scaffold by shaping individual fibres. On the other hand, a lower quantity of widespread large particles only has a local effect on the fibres that were in contact with the removed particle and effectively creating scattered concentrations of high and low fibrous densities. Nevertheless, the current study showed that shaping individual fibres has the additive advantage of creating wavy fibres which could be useful to mimic the curled collagen/elastin fibres found in the ECM of an aortic wall or valve shown in Figure 1.3 (introduction chapter). The following section was therefore proposed to investigate the *in vivo* performance of scaffolds produced with this newly revised approach to electrospun porosity enhancement.

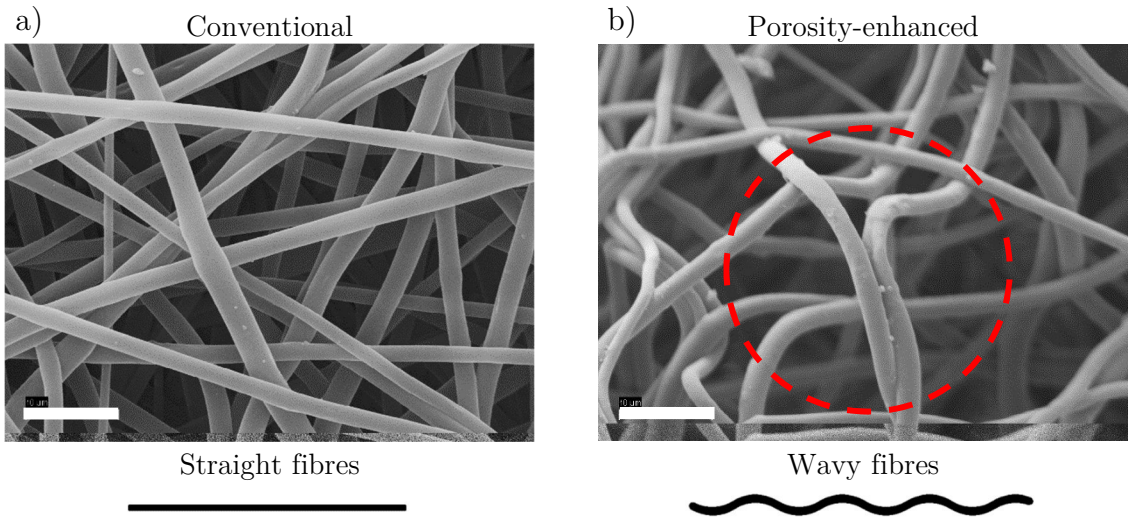

Figure 3.16: Architectural comparison of conventional and high-porosity scaffolds. SEM images of a) conventionally produced and b) porosity-enhanced electrospun structures. The red circle represents a washed out 30 µm PEG particle. Scale bars are 10 µm.

3.2.4 Biostable implant production

The Pel scaffolds produced specifically for subcutaneous implantation included a conventional low-porosity (LP) and porosity-enhanced structure (HP) without and with surface immobilised heparin (HP+Hep). Figure 3.17 presents each implant group with a cross section, a top view and a close-up of the fibre's surfaces.

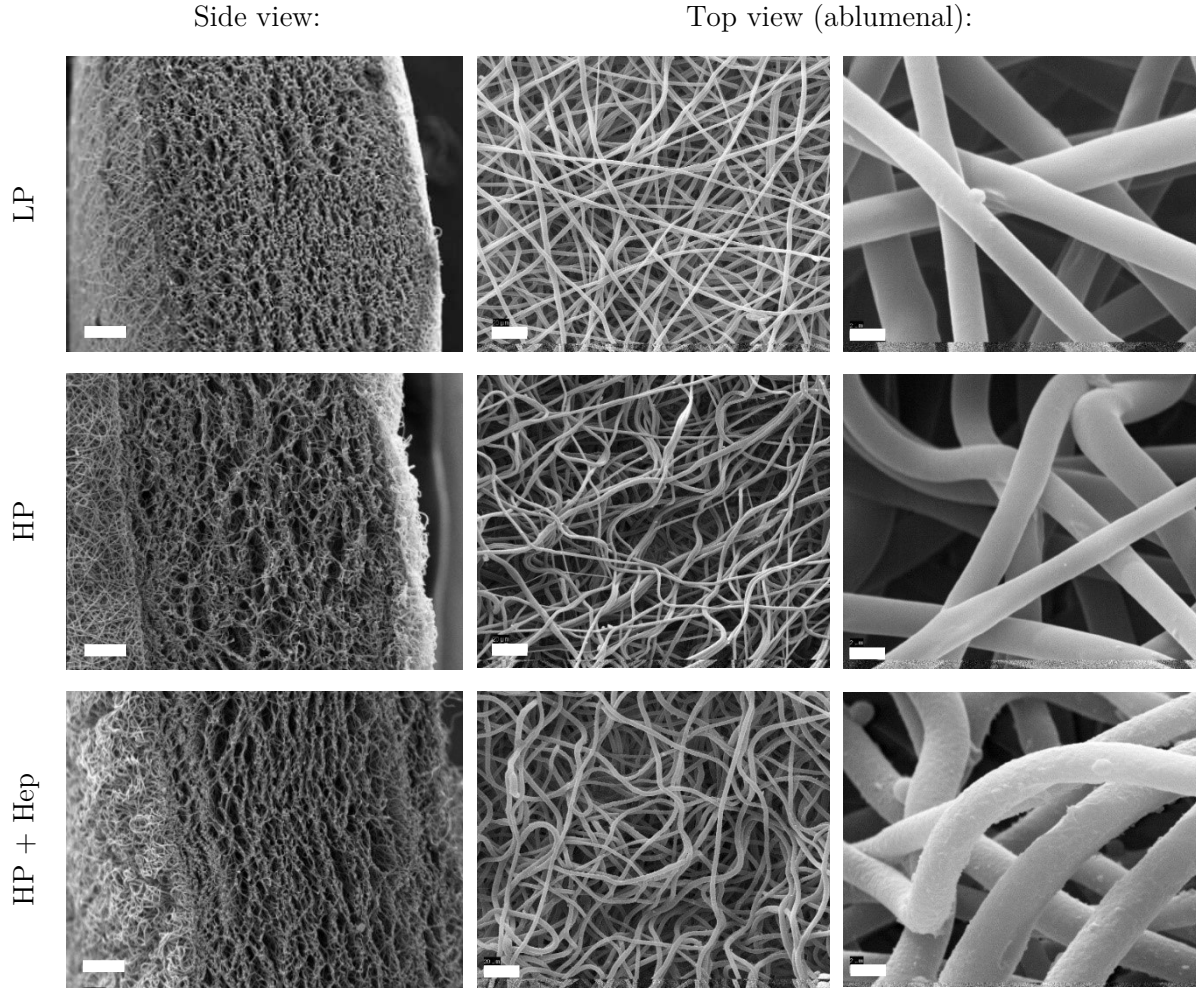

Figure 3.17: Biostable scaffold selection for subcutaneous implantation. Scale bars for the cross-sectional SEM images are 100 µm, ablumenal images are 20 and 2 µm for the low and high magnifications respectively.

Conventional electrospinning of Pel (solution viscosity of 3150±8 cPoise) produced fibres with an average diameter of 2.14±1.4 µm (LP) and a scaffold thickness of 1021±141 µm. The combined electrospinning and spraying technique did not influence the resulting (HP) fibre diameter when compared to LP ($P>0.3$, Figure 3.19.a). This result, also consistent with the previous section (Figure 3.15.b), suggests that sufficient

solvent evaporation occurred before collector impact for both Pel fibres and PEG microparticles. The heparinisation of HP fibres increased the average diameter from 2.02±0.6 to 2.59±0.5 µm ($P<0.001$), a previous study also confirmed an increase in fibre thickness (1.8 to 3.6 µm) as a result of covalent heparin attachment to electrospun Pel surfaces [153]. The surfaces of the un-heparinised fibres (LP and HP from images in Figure 3.17) appeared smooth compared to a more rippled surface roughness on the heparinised groups (also seen by [153]). A close-up of the heparin layer (dehydrated) of HP+Hep surfaces can be seen in Figure 3.18. Furthermore, heparinised fibres appeared to be 'welded' at their contact interfaces (as indicated by the red arrow in Figure 3.18). It is likely that the respective heparin gel layers of the fibres in contact with each other merged during the dehydration process (freeze drying) and/or grafted together by gel/amines during the heparinisation process.

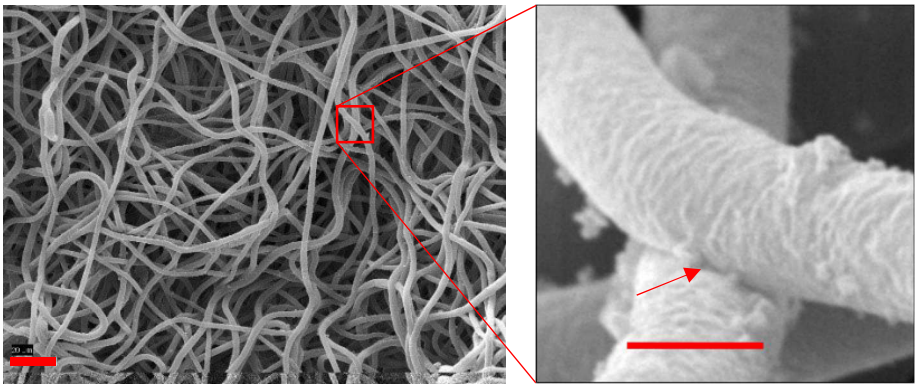

Figure 3.18: Fibre morphology of heparinised Pellethane® fibres. Scale bars are 20 and 2 µm for the low and high magnification SEM images respectively.

Combined electrospinning and spraying of Pel fibres and PEG microparticles (average diameter of 30±14 µm and bead-fibre composite fraction of 68.6±3%) produced scaffolds with a porosity 11% higher than that of the conventional spun scaffolds (LP to HP was 79.7±2 to 91.1±1%, $P<0.001$). These porosity measurements were in line with the results obtained from the scaffolds produced in the previous developmental section (Figure 3.15.b). Heparinisation only slightly decreased the average porosity by 0.4% ($P<0.05$, Figure 3.19.b). The porosity of heparinised scaffolds were expected to slightly decline due to the added mass of heparin (a result also seen by other coated

electrospun fibres [380]). All biostable implant groups (LP, HP and HP+Hep) had similar fibre orientation indices (0.177±0.1, 0.194±0.1 and 0.187±0.1, P>0.5, Figure 3.19.c) and 2D pore sizes (6.07±4, 6.51±5 and 6.49±5 µm, P>0.2, Figure 3.19.d). A total frequency of 18% of the pores measured for any of the high-porosity groups (HP or HP+Hep) were measured to be between 15 and 25µm while 14% of the pores were in that range for the lower porosity groups (Figure 3.19.e).

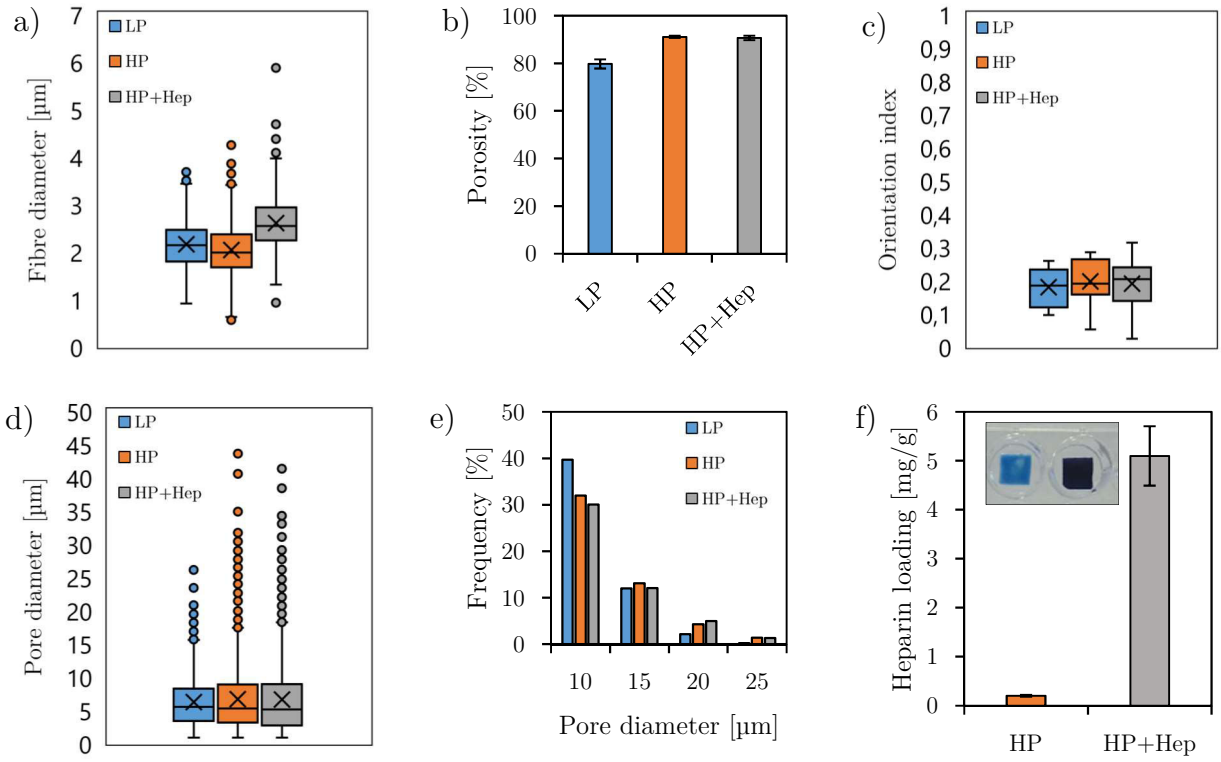

Figure 3.19: Characteristics of biostable implant groups. a) scaffold porosity [n = 40]; b) fibre orientation index [n = 12]; c) fibre diameter [n = 12, >40/image]; d) scaffold pore size [n = 12, >250/image]; e) frequency of total pores between 10-25 µm [>3000 pores/group]; f) surface immobilised heparin load [n = 5] and confirmation stains [n = 1].

A higher number of enlarged pores were found for the high-porosity groups due to the voids created by the sacrificial extracted PEG particles. Although, the inadequacy of 2D image quantification to display the impact of removable microparticles on creating additional 3D spaces is again highlighted here (as explained in the previous section, Figure 3.16). The presence of surface immobilised heparin on the high-porosity groups was confirmed with a positive (dark) Toluidine blue stain and was quantified at 5.1±0.6 mg/g (compared to HP controls of 0.2±0.0 mg/g, Figure 3.19.f). The surface load of

heparin is in a similar range to previous studies (7.5±1.6 mg/g for Pel electrospun scaffolds with 76-90% porosities and 1.8±0.1 µm fibres [153] and 6.6±2.0 mg/g for PU disks with 82% porosity [286]).

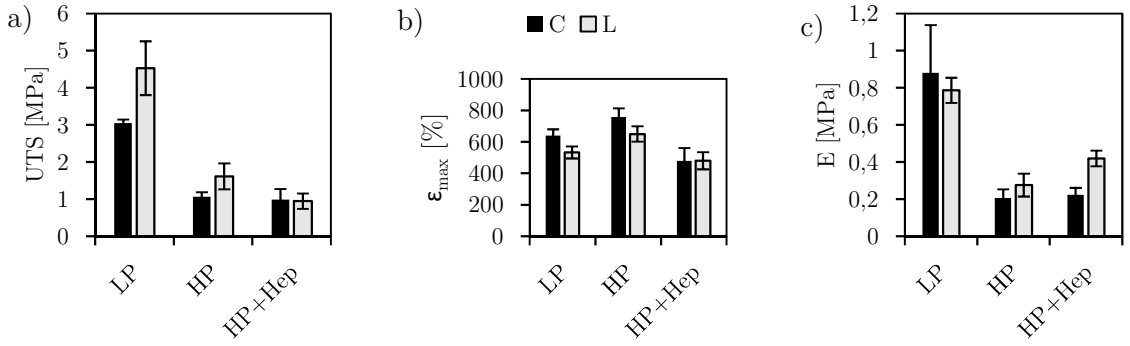

Figure 3.20: Mechanical properties of biostable implant groups. a) Ultimate tensile strength (UTS), b) maximum elongation (ε_{max}) and c) elastic modulus (E). [n = 6]

Mechanically, conventional electrospun scaffolds had a UTS 50% greater (P<0.001) in the longitudinal (4.53±0.7 MPa) compared to the circumferential direction (3.05±0.1 MPa) and was approximately 3 times stronger than any of the high-porosity groups regardless of measuring direction (P<0.001, Figure 3.20.a). The heparin surface modification did not significantly influence mechanical strength in the C direction (1.06±0.1 and 0.97±0.2 MPa for HP and HP+Hep, P>0.5) but did produce a scaffold that was slightly weaker in the L direction when compared to its non-heparinised counterpart (1.61±0.7 and 0.95±0.2 MPa for HP and HP+Hep, P<0.05). The maximum elongation of LP (638±42%) was lower than that of HP (758±56%, P<0.05) but higher than HP+Hep (478±83%, P<0.01) in the circumferential direction (Figure 3.20.b). Both LP (533±38%) and HP (650±49%) had a lower ε_{max} in the L direction compared to C (P<0.01) while HP+Hep experienced a similar strain in both directions (P>0.9). The Young's modulus of LP (0.88±0.3 and 0.79±0.1 MPa, for C and L) was 4 times higher (P<0.001) than that of HP (0.21±0.1 and 0.28±0.1 MPa) or HP+Hep (0.22±0.0 and 0.42±0.1 MPa) in the C direction and nearly twice as stiff in the L testing direction (P<0.001, Figure 3.20.c). Effectively, heparinisation slightly increased the Young's modulus of the dehydrated porosity-enhanced scaffolds. Furthermore, the

elastic modulus for LP was similar in both testing directions ($P>0.4$) while HP ($P<0.05$) and HP+Hep ($P<0.001$) was less stiff in the C compared to the L direction.

Porosity-enhanced electrospun scaffolds are known to have a weaker mechanical strength and rigidity (modulus) due to the loss in bulk material, but has the potential to be more compliant towards native tissue, when compared to their normally produced counter parts [153, 178, 230, 232]. Mechanical properties were shown in previous studies to be controllable by controlling the sacrificial fibre fraction (by flow rate) of removable fibres during dual electrospinning [153, 178]. A similar approach could be adopted here to control the bead fraction (using a set number of needles instead of flow rate) to control the mechanical compliance to match that of the targeted tissue. Furthermore, the heparinisation of Pel fibres have also been shown to have an effect on the bulk mechanical properties [153]. Similar to the results obtained in the current study, the authors observed an increase in Young's modulus and a lower maximum elongation when compared to un-heparinised scaffolds. These effects could be related to the added material (the mass of a heparin layer made the scaffolds stiffer) and the chemical processing (weakened the scaffold's structural integrity). An additional effect that could also have resulted in a more rigid matrix, could have been due to fibres 'welded' at their contact interfaces (HP+Hep) compared to lose fibres (HP), as it was observed in Figure 3.17 and Figure 3.18.

3.2.5 Healing assessment of biostable implants

This section is a summary of the 12week, *in vivo* assessment (rat subcutaneous model) for the biostable scaffolds. The *in vivo* performance of each implant was analysed and quantified in terms of tissue ingrowth followed by collagen, cellular, macrophage and vascular density.

3.2.5.1 Scaffold tissue ingrowth

Representative H&E (the dark pink areas shown positively stained tissue) micrographs for the biostable implant groups are shown in Figure 3.21 for 7, 14, 28 and 84 days

respectively.

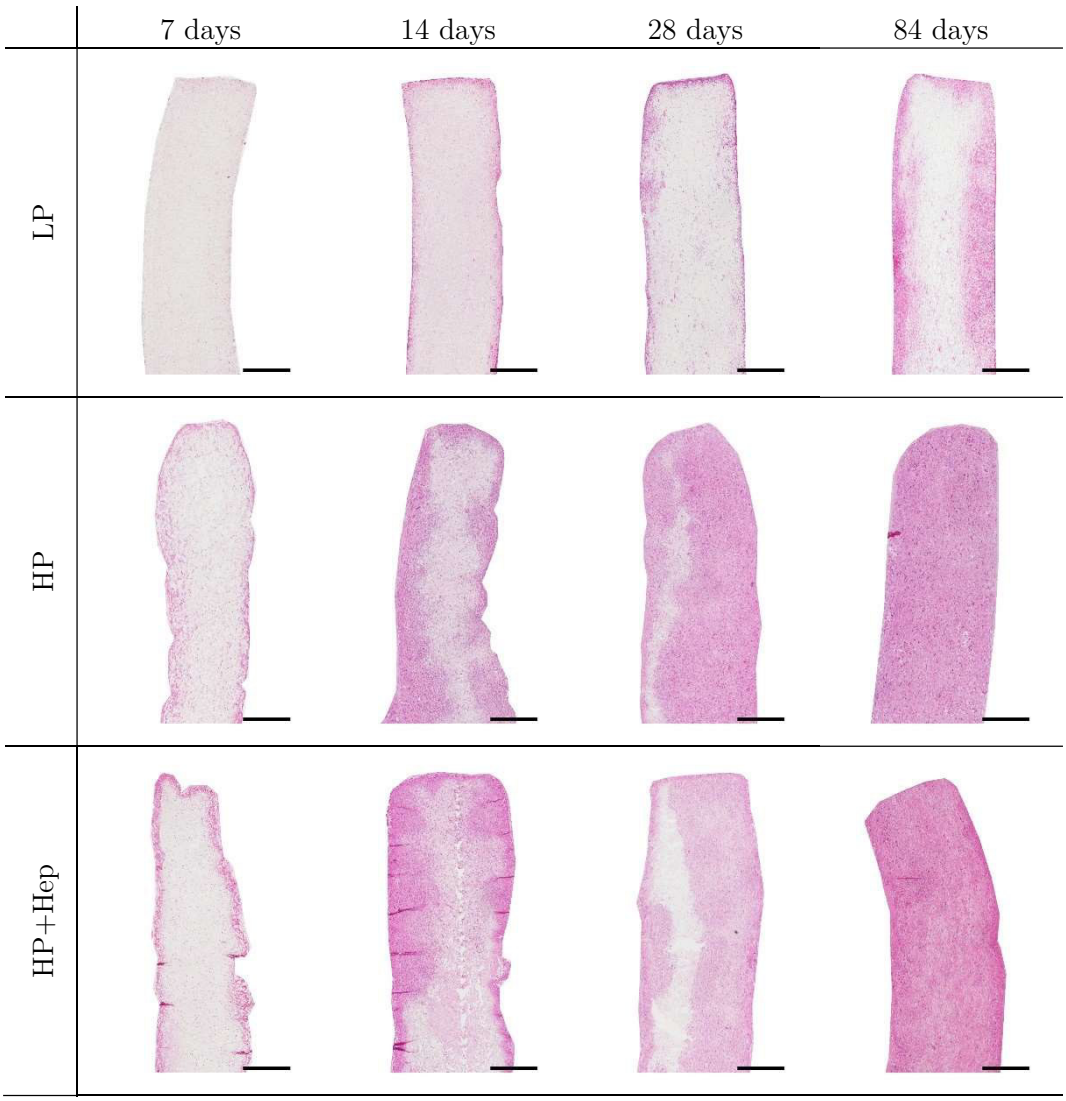

Figure 3.21: Representative H&E micrographs of biostable implant groups. Scale bars are 500 µm.

Cellular infiltration occurred from all surfaces (there appeared to be no preferred side) and observably increased over time for all biostable scaffolds, as illustrated by the representative H&E micrographs. Tissue ingrowth of conventional electrospun scaffolds (LP) followed a linear trend of $0.48T_{days} + 2\%$ ($r^2 = 0.99$), and was limited to 42% at 84 days (Figure 3.22). Conversely, the enhanced porosity groups showed a much higher ingrowth rate and were almost fully ingrown after 28 days. The ingrowth profiles of HP and HP+Hep were indistinguishable up to the first two time-points. On day 28, HP was 30% more ingrown than HP+Hep (89.8±12% and 58.5±17, $P<0.05$), after which both obtained full ingrowth at the final time point (99.5±0 and 99.1±0%,

P>0.2). Similar ingrowth profiles for all Pel groups were observed with the quantified result from the zinc fixated H&E micrographs (Appendix A6).

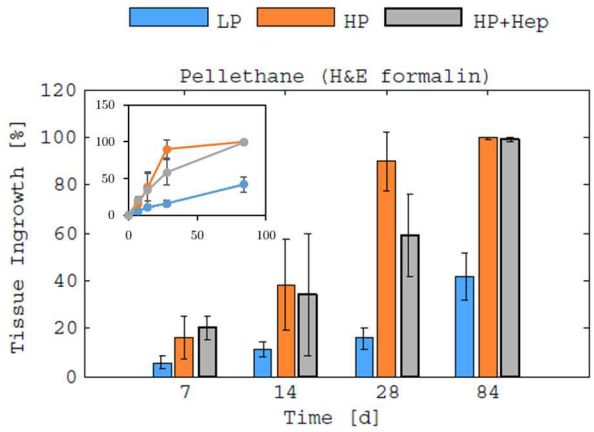

Figure 3.22: Tissue ingrowth of biostable implant groups.Graph insert: scaled x-y plot of tissue ingrowth for each group.

A relatively slow cellular migration rate and limited infiltration depth (only the peripheral areas) of scaffolds produced by standard electrospinning, as seen in this study, have also been reported by many others [153, 233, 237, 352, 354, 381]. The pore sizes, and their level of interconnectivity, of LP scaffolds were insufficient to accommodate cells and their associated oxygen/nutrient supply to penetrate and survive beyond a depth of 200-300 µm, even after 3 months of implantation. The cells that have indeed survived within the LP scaffolds, were probably kept alive by supplies from the surrounding tissue (due to the oxygen diffusion limit being in the range of 100-200 µm [297]). The faster migration rate and full tissue ingrowth of a ~1 mm thick porosity-enhanced scaffold (by adding and removing sacrificial components to yield 90-95% porosities) has also been observed by others [148, 153, 352]. This result can be explained, not only by the known correlation between tissue ingrowth rate and scaffold porosity, but also, by the presence of sufficient interconnected three-dimensional pores (created by the 30 µm porogens) that accommodated cellular migration along with the required support networks (nutrients, oxygen and waste) which allowed long-term survival. Retrospectively, heparinisation of high-porosity groups had a minimal influence on tissue ingrowth, when compared to the controls, after 3 months of implantation. The initial retardation (7-28 days) may have been due to the slightly

lowered porosity, thicker and slightly fused fibres as a result of the heparinisation process that hindered early stage cellular infiltration.

3.2.5.2 Collagen density

Representative PSR (the red areas are positively stained collagen) micrographs for the biostable implant groups are shown in Figure 3.23 for 7, 14, 28 and 84 days respectively.

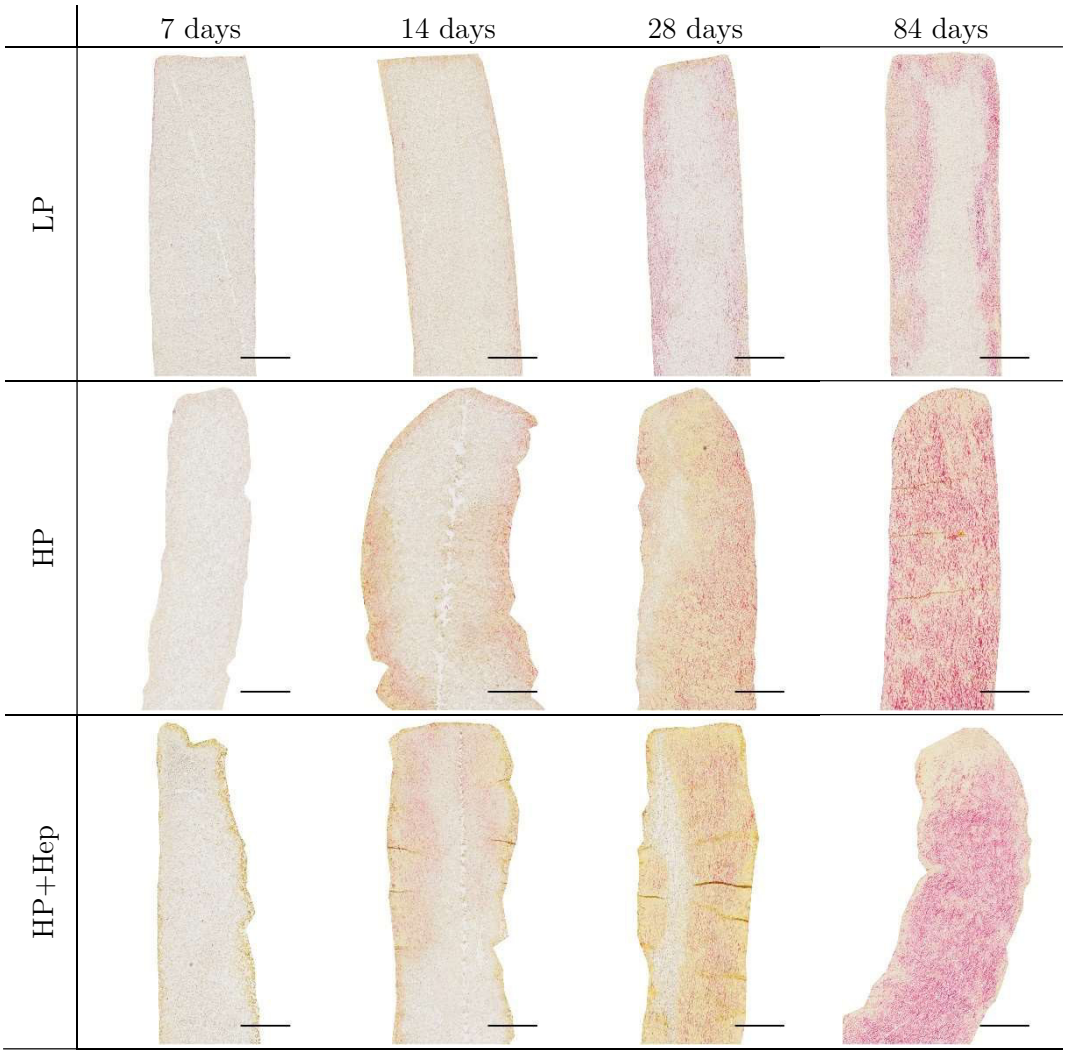

Figure 3.23: Representative PSR micrographs of biostable implant groups. Scale bars at 500 µm.

There were no significant differences of collagen density between the groups at any of the measured time points between 7-28 days ($P>0.1$, Figure 3.24). Nevertheless, the measured collagen deposition between 28 and 84 days doubled inside both high-porosity scaffolds (0.15 ± 0.1 to 0.29 ± 0.1 µm²/µm², $P<0.05$) while collagen in the lower porosity scaffolds was at a constant ($P>0.3$) yet in a lower ($P<0.05$) range of 0.23 ± 0.1 µm²/µm². Collectively, the percentage of collagen area per tissue area for all groups increased at

a rate of approximately 6%/week between 7 and 28 days (1-19%) and nearly plateaued to 0.6%/week between 28 and 84 days (19-25%) - as shown by the inserted plot in Figure 3.24.

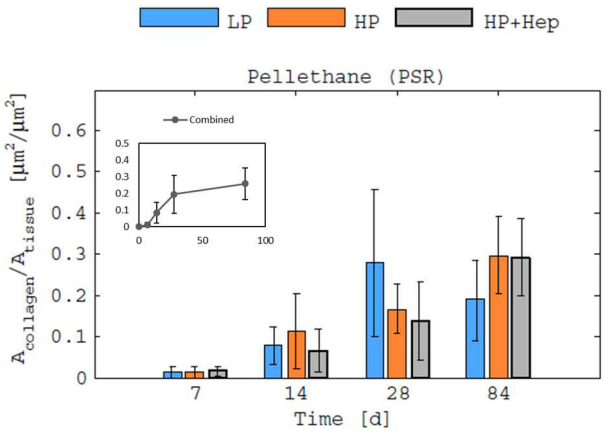

Figure 3.24: Collagen deposition of biostable implant groups.Graph insert: x-y plot representing the combined collagen density of all groups.

Collagen deposition is associated with the tissue remodelling process (cells secreting new ECM [343]) and also plays a crucial role in strengthening tissues that are under high biomechanical stresses, e.g. blood vessels/heart valves. Following injury, collagen fibres found in blood vessel walls (or vascular grafts) are known to increase circumferentially and longitudinally in order to re-establish homeostatis in response to mechanical cues [382, 383]. In another study, the collagen and elastin content inside electrospun heart valves increased over time and eventually matched that of the native tissue after 12 months of implantation (*in vivo* sheep model) [63]. The authors also made a positive remark towards the formation of an increasingly organised and more matured collagen/elastin fibrous matrix found in the leaflets of the heart valves as a function of time. Furthermore, other studies have also confirmed positive relationships between collagen density and scaffold architecture (porosity[352] and pore sizes[384]). The measured collagen density was higher inside porosity-enhanced electrospun scaffolds (1mm thick PCL implants that had a 60% PEO sacrificial fibre fraction before removal) compared to conventional (lower porosity) groups after 12 weeks (obtained full tissue ingrowth at this point) of implantation in a subcutaneous model [352]. Cells seeded in gelatin scaffolds with larger pores had a higher collagen (type I, II and X)

deposition rate when compared to smaller pores (pores sizes were tested from 50-500 µm) [384]. High collagen densities could, however, also be associated with scar tissue formation. Previous researchers classified scar tissue, histologically, as highly packed clusters of collagen. In contrast, scar-less/regenerative healing was classified as organised and evenly distributed collagen fibres, similarly to the native tissue [385]. Therefore, the increasing collagen densities over time followed by elevated contents for the porosity-enhanced groups (which was due to larger 3D pores and higher porosities) after 12 weeks of implantation agree with current literature. Moreover, the 'organised and matured' nature of the collagen fibres observed in the high-porosity groups had more regenerative characteristics compared to the concentrated ridges (scar tissue formation characteristics) found along the tissue inner boundaries of the low-porosity groups.

3.2.5.3 Cellular density

Representative micrographs for the degradable implant groups are shown in Figure 3.25 for 28 and 84 days respectively. The blue areas, DAPI, are positively stained nuclei and the red areas, ED1, are positively stained macrophages.

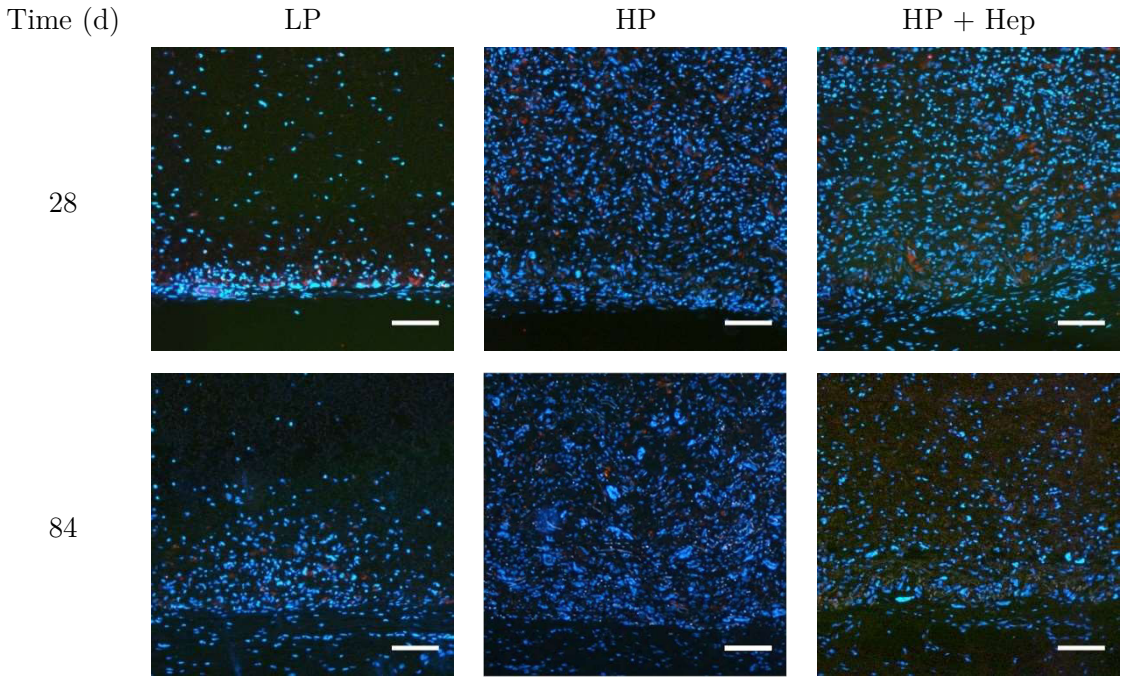

Figure 3.25: Representative ED1 micrographs of biostable implant groups. Scale bars are 100µm

The ratio of DAPI area per tissue area (A_{DAPI}/A_{tissue}) inside the conventional electrospun scaffolds (0.47±0.1 µm²/µm²) was twice as high as that of the high-porosity (0.20±0.1 µm²/µm²) or heparinised high-porosity groups (0.23±0.1 µm²/µm², $P<0.05$) at 28 days (Figure 3.26). At 84 days, LP (0.12±0.1 µm²/µm²) had a similar cellular density when compared to either of the porosity-enhanced groups ($P>0.4$) while the density found in HP was double than that of the HP+Hep groups (0.20±0.1 µm²/µm² or 0.10±0.1 µm²/µm², $P<0.05$). Over time (28 compared to 84 days), A_{DAPI}/A_{tissue} inside LP and HP+Hep scaffolds decreased ($P<0.01$ and $P<0.05$) while HP remained similar ($P>0.8$).

The number of nuclei counted per tissue area for LP (4355±1486/mm²) was nearly 1500/mm² nuclei more than the number counted for HP (2460±641/mm²) or HP+Hep (2825±362/mm², $P<0.05$) after 28 days. There was no significant difference ($P>0.3$) between the number of nuclei counter per tissue area for HP and HP+Hep at day 28. In agreement with the measured A_{DAPI}/A_{tissue} over time, the number of nuclei inside LP (2254±446/mm²) and HP+Hep (1968±492/mm²) scaffolds decreased from 28 to 84 days ($P<0.05$ and $P<0.05$) while HP (2603±296/mm²) remained similar ($P>0.6$).

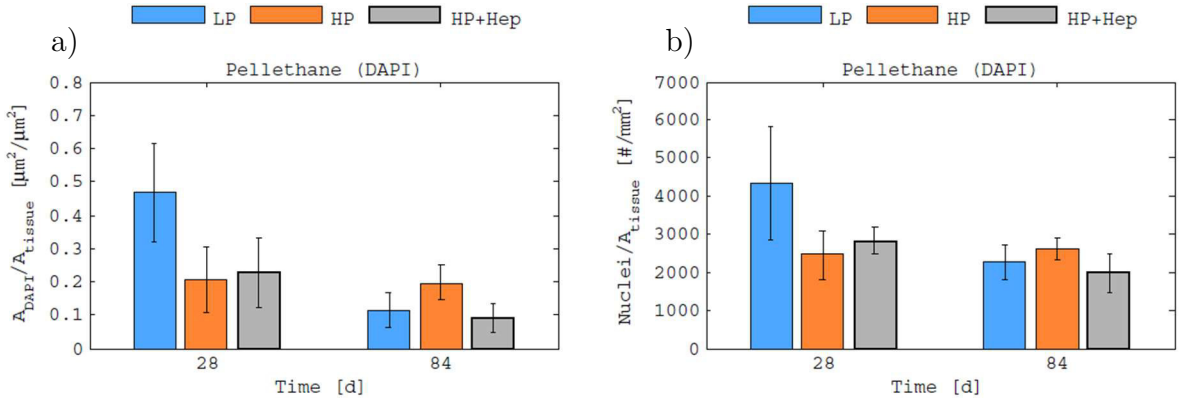

Figure 3.26: Cellular density of biostable implant groups. Cellular density in a) area and in b) number.

Many suggested that complete regeneration of implantable TE scaffolds would be encouraged by rapid cellularisation and maintaining a healthy density [210, 338, 352, 386]. Scaffolds with ideal cellularities have been associated with superior ECM secretion and vascularisation (mainly due to an abundance of M2-macrophages, i.e. the proangiogenic and remodelling phenotype) when compared to those with lower cellular

counts [210]. Furthermore, maintaining a healthy cellular density over a prolonged period could also result in a faster enzymatic degradation rate of the scaffold material [238]. Several researchers have quantified *in vivo* cellularity for TE scaffolds. Porous polyurethane disks (82% porosity, 160µm pores) had a cellularity of 1500/mm^2 after 10 days of implantation in a rat subcutaneous model [338]. Porosity-enhanced electrospun scaffolds (a PCL construct which contained 60% PEO prior to removal) obtained a cellular density of 1200/mm^2 after 12 weeks (subcutaneously) while the low-porosity groups (0% PEO) had a 600/mm^2 at the same time point [352]. Additionally, electrospun PCL scaffolds (83% porosity, 30 µm pores) maintained a cellular density of 2000-3000/mm^2 between 28-100 days as vascular grafts in a rat circulatory model [210]. More of the same results were found for porosity-enhanced PCL scaffolds (93% porosity, 26 µm pores), which had a density of 2500-4500/mm^2 while conventional electrospun scaffolds (87% porosity, 4 µm pores) obtained a cellularity of 1000-3000/mm^2 between 1 to 3 months as a vascular grafts in a rabbit carotid circulatory model [238]. It is evident, from these studies, that cellular density positively correlated with porosity (and to some extend pore size). Also, a density of 3000/mm^2 (give or take a thousand cells) can be expected from scaffolds with high porosities (>90%). The cellularities measured for the current high-porosity groups were, as suggested by literature, in a healthy range. Despite a superior cellularity expected for the porosity-enhanced groups, the abnormally high density measured after 28 days for the low-porosity groups could be explained by the clustering of frustrated cells at the peripheral areas of the LP scaffolds (i.e. a high cellular count normalised to a small tissue ingrowth area will naturally result in a high density). The main reason for these frustrated cells would be due to the pores being too compact and small for the cells to penetrate the scaffold.

3.2.5.4 Macrophage density

The macrophage densities presented in Figure 3.27 are the quantified results of the positively stained macrophages (ED1 - red areas), as can be seen from the samples in Figure 3.25.

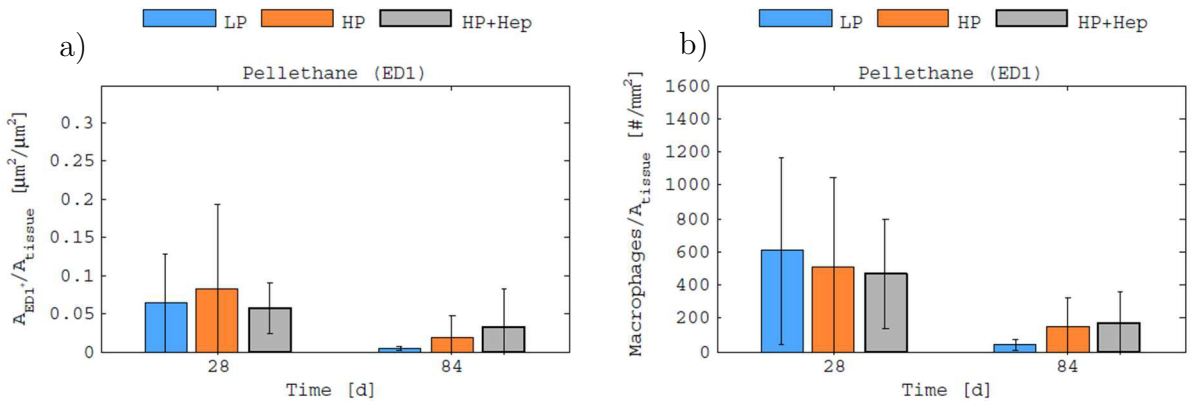

Figure 3.27: Macrophages per tissue area of biostable implant groups. Macrophage density in a) area and in b) number.

There were no significant differences in macrophage area density (A_{ED1^+}/A_{tissue}) or macrophages counted per tissue area between the Pel groups at any of the measured time points ($P>0.1$). Collectively, the ED1$^+$ area and macrophage count was approximately 0.05 µm²/µm² and 500 macrophages/mm². Despite the apparent decrease in macrophage densities over time (28 compared to 84 days), only LP had a lower A_{ED1^+}/A_{tissue} ($P<0.05$) and macrophage count ($P<0.05$) while HP and HP+Hep remained unchanged ($P>0.08$).

Macrophages are known to play an intricate role in effective healing of implantable medical devices [387, 388]. Following injury, macrophages are activated in response to the signals received at the implantation site (damaged tissue). Polarised macrophages can conveniently be subdivided in to two opposing phenotypes (M1/M2) [204]. M1 cells are the "classically activated" pro-inflammatory macrophages while the M2 type (anti-inflammatory) promotes tissue remodelling and vascularisation (known to be a supplier of proangiogenic molecules such as VEGF [389]). Among other signals, scaffold micro-architecture is also known to stimulate macrophage polarisation. Authors have shown, *in vitro* [201] and *in vivo* [210], that electrospun scaffolds with thicker fibres and their inherently larger pores tended to activate more M2 macrophages rather than M1 which were found to be in larger numbers when in contact with thinner fibres and smaller pores. The macrophages labelled in the current study (ED1$^+$) included both M1 and M2 phenotypes. Despite not being able to distinguish between the phenotypes found in

the different groups, the apparent decrease of macrophage densities over time may be attributed to a less aggressive foreign body reaction towards the implants at the end of the study.

3.2.5.5 Vascular density

Representative CD31 micrographs (the dark areas are positively stained endothelial cells) for the degradable implant groups are shown in Figure 3.28 for 28 and 84 days respectively. The dashed lines in the LP groups represent the tissue area (the red line is at the base of the scaffold while the black line indicates the tissue ingrowth boundary in the direction towards the middle of the scaffold).

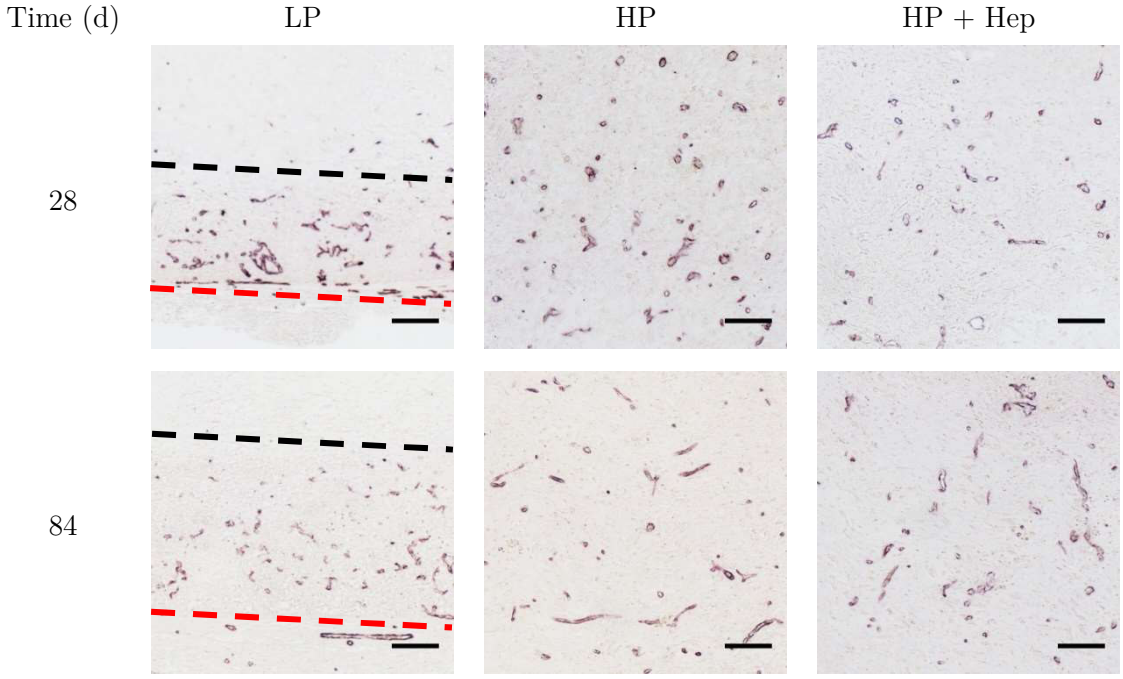

Figure 3.28: Representative CD31 micrographs for no-degradable implant groups. Scale bar: 100 µm.

Blood vessel area per tissue area ($A_{vessels}/A_{tissue}$) inside the LP scaffolds (0.036±0.030 $\mu m^2/\mu m^2$) was not significantly different ($P>0.1$) when compared to that of HP (0.026±0.003 $\mu m^2/\mu m^2$) or HP+Hep (0.008±0.007 $\mu m^2/\mu m^2$) at 28 days of implantation (Figure 3.29). Although, $A_{vessels}/A_{tissue}$ for HP scaffolds was 3 times larger than that of HP+Hep at 28 days ($P<0.01$). At the last time point, $A_{vessels}/A_{tissue}$ for HP+Hep (0.010±0.003 $\mu m^2/\mu m^2$) was lower than both HP (0.021±0.004 $\mu m^2/\mu m^2$, $P<0.01$) and LP (0.030±0.020$\mu m^2/\mu m^2$, $P<0.05$) scaffolds.

There were no differences in the number of vessels counted per tissue area between any of the groups at 28 days. At 84 days, the number of vessels per A_{tissue} for LP (278±191/mm²) and HP (148±21/mm²) were similar (P>0.1) while HP+Hep had fewer vessels (111±19/mm², P<0.05). Vascular density did not significantly change (neither vessel area nor vessel count per tissue area) for any of the groups over time (P>0.5), i.e. between 28 and 84 days.

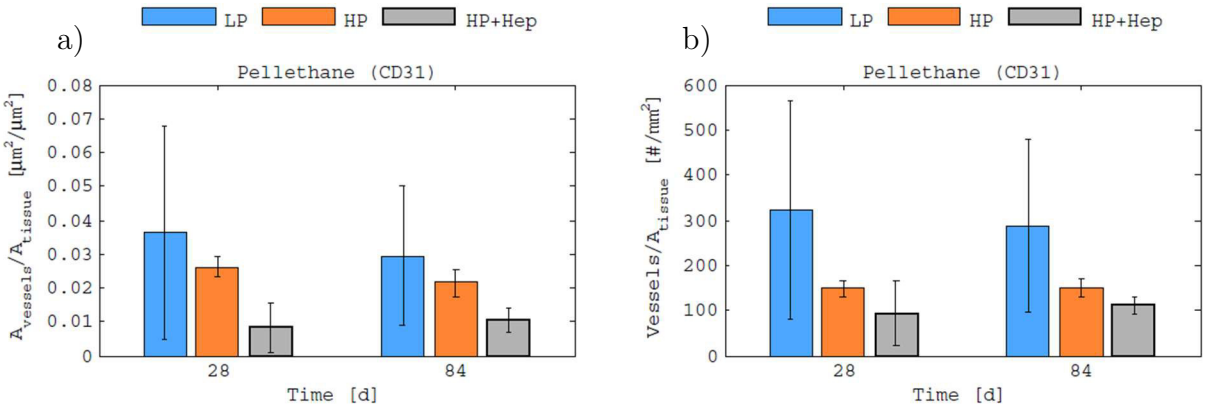

Figure 3.29: Blood vessels per tissue area of biostable implant groups. Vascular density in a) area and in b) number.

Although the low-porosity groups appeared to have had a greater vascular density, compared to the high-porosity groups, it is important to remember that these regions (only found in peripheral areas) contained frustrated cells due to the limited ingrowth spaces (with reference to sections 3.2.5.1 and 3.2.5.3). Moreover, the centre of the LP scaffolds was consistently acellular even after 3 months of implantation. These are not desirable healing indications and therefore not recommended for long-term implantation [379]. On the contrary, the ingrowth spaces created by the dissolved PEG porogens (porosity-enhanced groups) accommodated endothelial cells to migrate deep into the scaffolds and encouraged the remodelling of a healthy vasculature throughout the entire scaffold. Enhanced *in vivo* vascularisation have been associated with greater porosity and larger pore sizes of TE scaffolds in previous studies [55, 153, 202, 210]. The vascular densities measured for the high-porosity groups in the current study were comparable to that of other high-porosity electrospun scaffolds reported in literature (100-300/mm² [238]). Despite previous success on improved *in vivo* vascularisation of

porous polyurethane disks with surface modified heparin (6.6±2.0 mg/g [286]), heparinised electrospun scaffolds have also been reported (with a similar surface load of 7.5±1.6 mg/g [153]) to have no influence on vascular densities after 28 days of implantation. While the dependency on heparin surface concentration might be ruled out by such opposing results, a possible explanation could be hidden in the scaffold architecture (i.e. foams with well defended pores compared to fibrous structures). Adding a heparin layer to well defined, rigid structures did not influence the effective pore sizes of the scaffolds [290, 292]. In contrast, the heparinised fibres in the current study were 'welded' together at their touching interfaces and resulted in a more rigid structure (supported by Figure 3.18 and mechanical results from Figure 3.20). These architectural changes reduced the effective pore size by inhibiting cells from moving individual fibres (HP+Hep) compared to the loose, freely movable fibres of the control (HP) samples. Effectively, the vascularisation process of HP+Hep was delayed as a result of a slower ingrowth rate (as shown in section 3.2.5.1).

3.3 Biodegradable scaffold development

3.3.1 Solvent evaporation rates

Among the solvents capable of dissolving DP at room temperature, $CHCl_3$ and HFIP were selected (only chlorinated and fluorinated solvents dissolved DP out of 21 tested compounds, see Appendix A7 for the complete list). $CHCl_3$ and HFIP, as pure solvents, achieved complete evaporation by the 2 hour time point (651.5±11 mg to 1.2±2 mg, 99.8±0.3%) as shown in Figure 3.30. Dissolving DP at a concentration of 18wt% in either of the solvents reduced the 2hour evaporation rate by approximately 12% and 40% for DP/$CHCl_3$ (87.9±1.2%) and DP/HFIP (61.6±0.9%) respectively. Furthermore, the evaporation rate of HFIP from HFIP/DP was delayed, 20% on average, when compared to $CHCl_3$/DP between 2 to 4 hours and only managed to evaporate more than 90% after 24 hours.

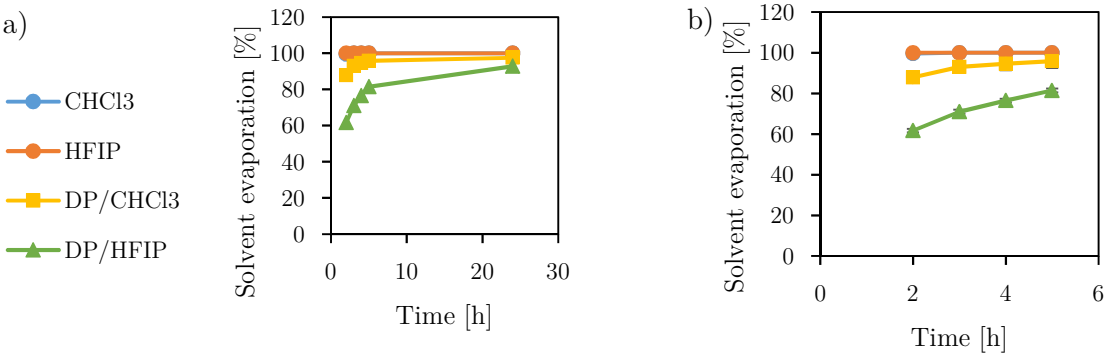

Figure 3.30: DP solvent evaporation rate comparison. a) Solvent evaporation profiles for $CHCl_3$ and HFIP over 24 hours; b) evaporation profiles between 2-5 hours. [n = 3].

A hydrogen bonding may form between a carbonyl (C=O) and an alcohol (OH) functional group. This affinity could be enhanced by the presence of fluorine atoms found in fluorinated alcohols (six in the case of HFIP) [390]. The results from the current study showed that pure $CHCl_3$ and HFIP had approximately the same evaporation rates due to similar properties at RT (boiling point, vapor pressure and density, as shown in Appendix A1). The delayed evaporation rate that was found for HFIP from DP/HFIP compared to $CHCl_3$ from DP/$CHCl_3$ may therefore be explained by the presence of hydrogen bonds between HFIP (and the absence thereof in the case

of $CHCl_3$) and the pairs of carbonyls found in each of the hard, soft and junction repeating units of DP (see chemical structures in Figure 3.31).

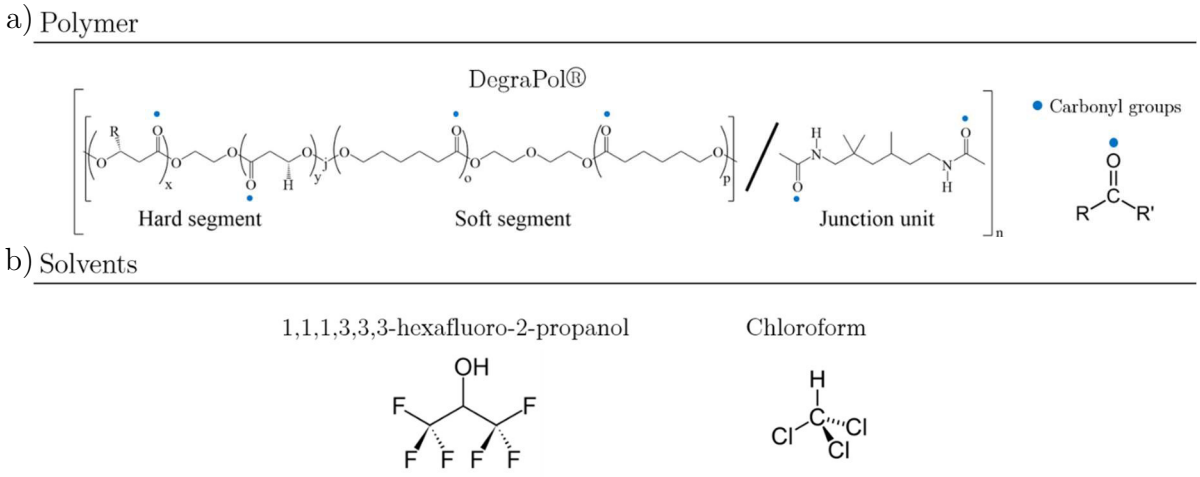

Figure 3.31: Chemical structures used for degradable scaffolds development. a) structure of DegraPol® where the blue dots indicate carbonyl groups identified in the repeating unit; b) solvents used for electrospinning.

3.3.2 Scaffold drug incorporation

3.3.2.1 Heparin modification

The chemical modification (ion exchange) of heparin sodium ($HepNa^+$) to HepTBA was confirmed with NMR. Representative ^1H NMR spectra before and after the resulting ion exchange process are illustrated in Figure 3.32. The solvent reference peaks (D_2O) are indicated with an arrow between 4.7-4.8 ppm while the internal reference peaks, heparin's acetyl group (Ac), can be found at 4.2-4.3 ppm. TBA proton peaks, indicated by numbers (1-4), are shown between (3.4-3.6), (1.9-2.1), (1.6-1.8) and (1.2-1.4 ppm) respectively.

Increasing the reacted TBA/MeOH concentration of 4.2, 8.0, 12.2, 16.4 or 80.0 mg/ml to form heparin variations that are labelled HepTBA25, 50, 75, 100 and HepTBA500 (Figure 3.33.a) resulted in a linear increase (24.1±0.2, 47.1±0.7, 68.4±1.1 and 79.6±0.6 for HepTBA25-100) of the ratio of the average integrated TBA proton peaks to that of the Ac peaks (Figure 3.33.b). This ratio plateaued when heparin acid ($HepH^+$) was reacted with excess TBA (HepTBA500 had a maximum integral ratio of 83.9±1.2). An ^1H NMR spectrum of TBA alone plus the protonated version of heparin ($HepH^+$), prior

to its reaction with TBA/MeOH, can be found in Appendix A8.

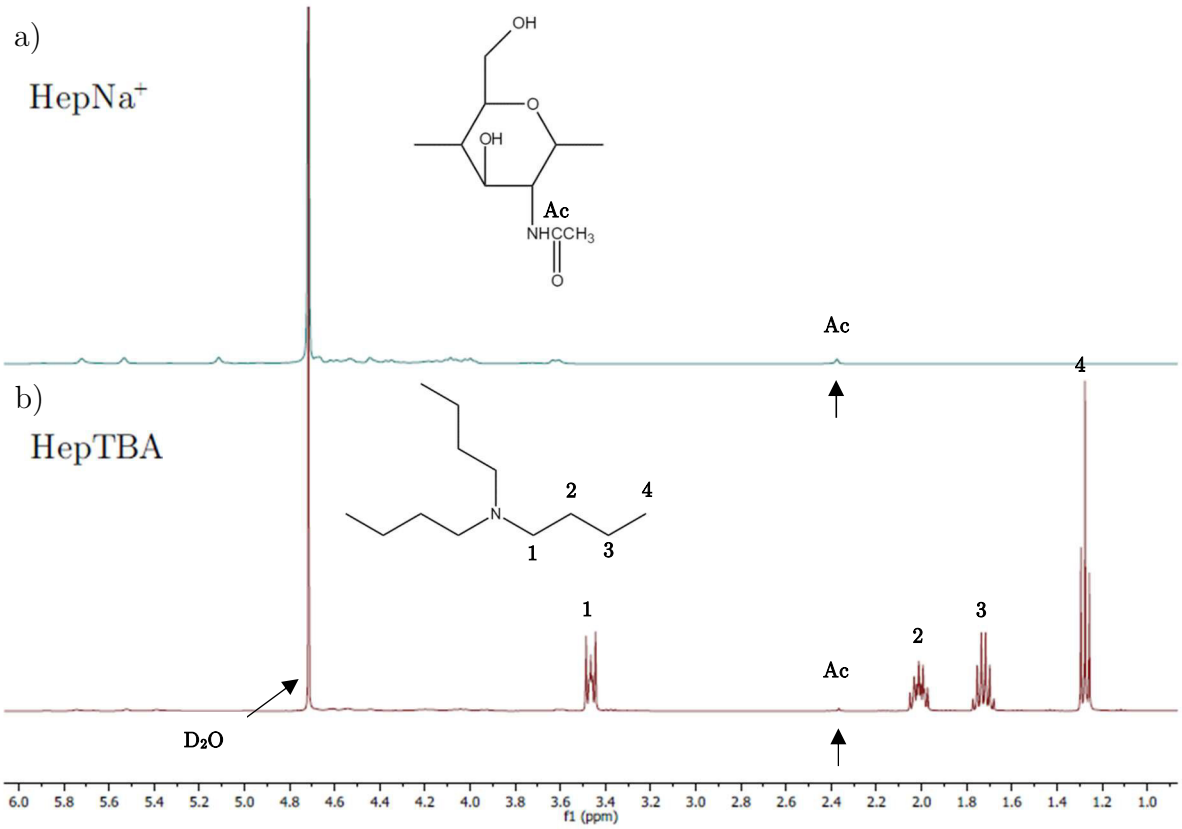

Figure 3.32: The ion-exchange of heparin sodium to heparin-tributylammonium. a) ^{1}H NMR spectra of heparin sodium and b) heparin-tributylammonium.

Sodium salt of heparin is known for being insoluble in typical, less polar than water, organic electrospinning solvents [243, 310, 391]. A chemical modification, replacing the sodium ions with tributylamine, was previously proposed to expand heparin's solvent solubility array and therefore its biomaterial incorporated applications [310]. These authors successfully produced an amphiphilic salt of heparin that was not just soluble in water but also in HFIP. Here, reported for the first time, are data captured for a finer control over this modification (i.e. controlling the amount of H^+ replaced with TBA^+ after all Na^+ were removed). Adjusting the TBA content of this heparin conjugate has potential influences on its solubility and bioactivity which will be showcased in the sections to follow. Nevertheless, the positive relationship found in the current study between TBA-to-Ac proton signals and the concentration of TBA ions in the methanol reaction solution was as expected. A higher number of protons on the

backbone of heparin were replaced with TBA molecules due to its higher availability at higher concentrations in the reaction solution. This trend, of course, was also expected to reach a maximum (which can be seen in Figure 3.33.b) when all available H^+ ions where replaced with TBA^+ ions despite them being in excess.

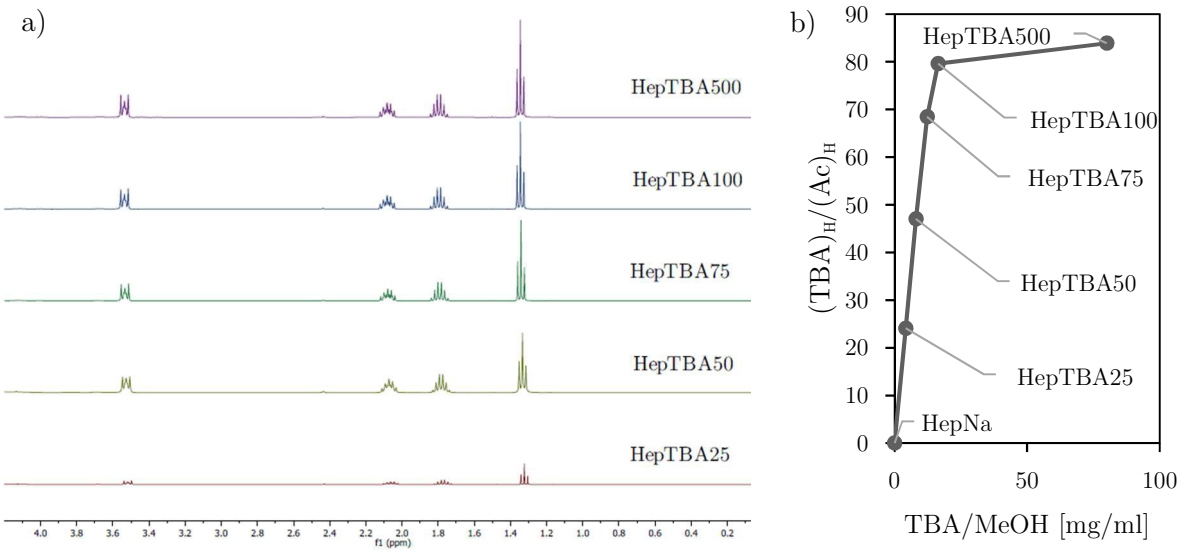

Figure 3.33: ^{1}H NMR spectra of heparin-tributylammonium variations.

3.3.2.2 Drug solubility in organic solvent systems

The solubility of heparin, in the form of HepTBA500, was positively altered for a wide range of organic solvents when compared to the solubility of $HepNa^+$. HepTBA500 was found to be soluble, tested at 5% (w/v), in the selected DP solvents (HFIP and $CHCl_3$, previous authors also confirmed solubility in HFIP [310]) and a selection of other common electrospinning solvents (ethanol, isopropanol, THF and DMF) while $HepNa^+$ was soluble in only water (the lower bound testing concentration was 0.1%). Successful solubility of HepTBA variations (transparent solutions at RT) was found to favour higher TBA content products. This could be attributed to TBA's inherent hydrophobic side chains which, at increasing concentrations, increased HepTBA's hydrophobicity and therefore solubility in less polar solvents. Solubility tests with DP solvents showed that HepTBA25 and HepTBA50 was soluble in HFIP but not $CHCl_3$ while higher TBA content products (HepTBA75, 100 and 500) dissolved in both solvents. Both dexamethasone (only soluble in chloroform at <0.2 (w/v)%) and HepTBA (regardless

of the TBA content) favoured dissolution in HFIP compared to $CHCl_3$. Moreover, both drugs precipitated out of solution when DP was added to drug/$CHCl_3$ solutions. In contrast, drug/HFIP or high HFIP content of drug/HFIP:$CHCl_3$ solutions remained homogeneous when DP was dissolved (concentrations 18-24wt% were tested). A solvent system of HFIP/$CHCl_3$ at 50:50% was therefore selected to allow incorporation of both drugs into identical (transparent) DP electrospinning solutions. A summary of drug/solvent solubility at a concentration of 5(w/v)% is shown in Table 3.1.

Table 3.1: Solubility of drug selection in DegraPol® electrospinning solvents. Soluble (S)/in-soluble (I).

Drug/solvent	$CHCl_3$ 5 (w/v)%	HFIP 5 (w/v)%	$CHCl_3$:HFIP(50:50%) 5 (w/v)%
$HepNa^+$	I	I	I
$HepH^+$	I	I	I
HepTBA25	I	S	S
HepTBA50	I	S	S
HepTBA75	S	S	S
HepTBA100	S	S	S
HepTBA500	S	S	S
Dexamethasone	I	S	S

3.3.2.3 In vitro elution of heparin or dexamethasone

Drug release profiles for DP scaffolds electrospun at RT containing 0, 1 or 2wt% of either heparin (HepTBA500) or Dex over a period of 45 days are shown in Figure 3.34.a and Figure 3.34.b respectively (SEM micrographs were taken of the 2wt% loaded samples). Furthermore, the mass loss for each group was also determined after 90 days (Figure 3.35). HepTBA500 incorporated at 1wt% released 25, 56 and 109% of the total dosage on 1, 6 and 44 days. The release for 2wt% were 27, 38, 57% of the total dosage on 1, 6, and 44 days. Dex incorporated at 1wt% released 21, 75 and 87% of the total dosage on 1, 6 and 44 days. The release for 2wt% were 20, 86, 97% of the total dosage on 1, 6, and 44 days.

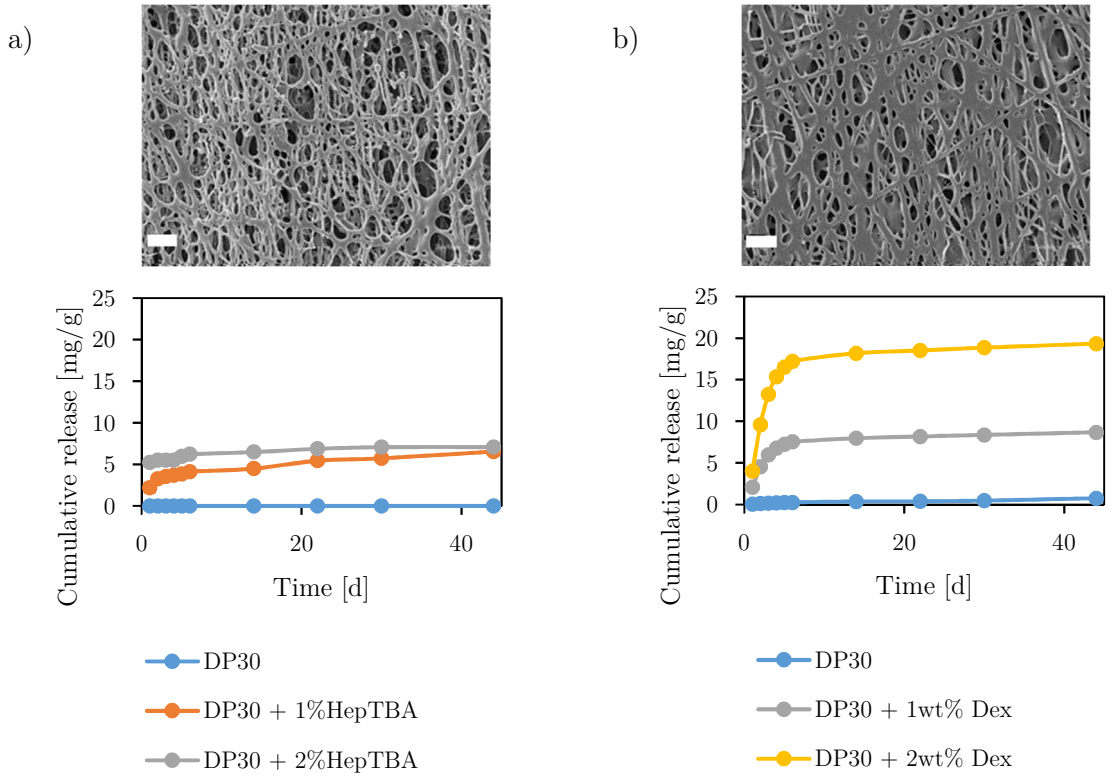

Figure 3.34: Drug elution study from RT electrospun scaffolds. a) Heparin-TBA500 and b) Dexamethasone at 2wt% concentrations with their respective release profiles (1 and 2wt%). SEM image scale bars are 20 µm.

Besides the architecture and material selection of the delivery device (mean diffusion distance and polymer degradation rate [198]), the drug type and its polymorphic form, crystallinity, molecular size, the total load in the polymer matrix and the drug's solubility in the release medium are known factors that influences the release kinetics of a drug from the same polymer matrix [327, 328]. Thus, Dex could have had a faster delivery rate compared to HepTBA500, at the same concentrations, due to the large difference in molecular size (300Da vs 12kDa). Smaller particles (Dex in this case) were expected to have a faster diffusion rate compared to larger particles when both were imbedded in the same polymer matrices and eluted from the same incubation fluid (both drugs were highly soluble in PBS). Faster delivery rates were expected for drugs at higher dosages due to a greater concentration gradient inside the polymer matrix [198]. This dependency was also seen by previous drug elution studies with variable concentrations similar to that of the current study for both a modified heparin-TBA [310] and dexamethasone [244].

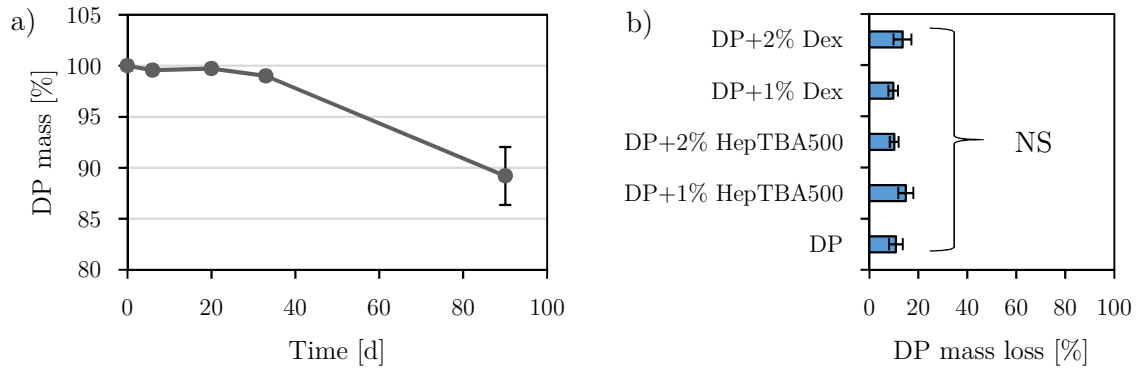

Figure 3.35: Mass loss of DP electrospun scaffolds *in vitro*. a) DP scaffold mass loss profile over time; b) mass loss for drug containing samples at 90 days. [n = 3].

DP scaffolds followed an *in vitro* mass loss of approximately 0.12%/day over the first 90 days of incubation (Figure 3.35.a). Neither the drug type nor its concentration, HepTBA500/Dex at 1/2wt%, had a significant influence on the mass loss percentages when compared to the drug-free DP scaffolds (with the lowest single comparison being $P>0.1$, Figure 3.35.b). Collectively, all DP scaffold groups (initial mass of 14.9±4 mg) lost between 8-18% (or 11.8±3% on average) of its original mass after a period of 3 months.

The *in vitro* degradation of DP electrospun scaffolds, high glycolide content DP30 in particular - also used in the current study, have been investigated before. The molecular weight (Mw) of DP decreased from 78 kDa (day 0), 41 kDa (14 days) to 26 kDa (day 28) while sustaining a mere 0.2-2% mass loss over the period of a month [21, 273]. Although the current study was extended to 3 months, a mass loss of 1% at day 33 is in line with the previous studies. Therefore, a similar molecular weight decrease (54% after 28 days) was also expected [273]. These characteristics, high molecular weight decrease with minimal mass loss, classifies DP's degradation mechanism as bulk degradation (and not surface erosion). Briefly, ester chains of typical poly(α-hydroxy esters) were cleaved by water molecules that diffused deep into the polymer matrices inside the electrospun fibres which resulted in an overall reduction in molecular weight of the bulk material. Significant mass loss only occurred at a later stage. If DP degraded by means of surface erosion (the primary mechanism identified for PCL, PGA, PLLA

and PGS [392]), the scaffolds would have experienced a linear mass loss throughout the study while retaining the internal structure's molecular weight (explained based on theories proposed in [393]).

3.3.2.4 Anti-thrombogenic properties of heparin variations

The time to initiate a clot within a sample of human blood (reaction time, R_{TEG}) treated with heparin sodium ($HepNa^+$, 0.01 mg/ml) was delayed by more than 6 times when compared to samples where heparin was not present (R_{TEG} values of 49.0±4.0 and 7.6±0.8 min respectively, $P<0.01$). Conversely, heparin sodium stripped from all Na^+ ions (heparin in acid form, $HepH^+$) had a reaction time similar to the control samples (7.2 min).

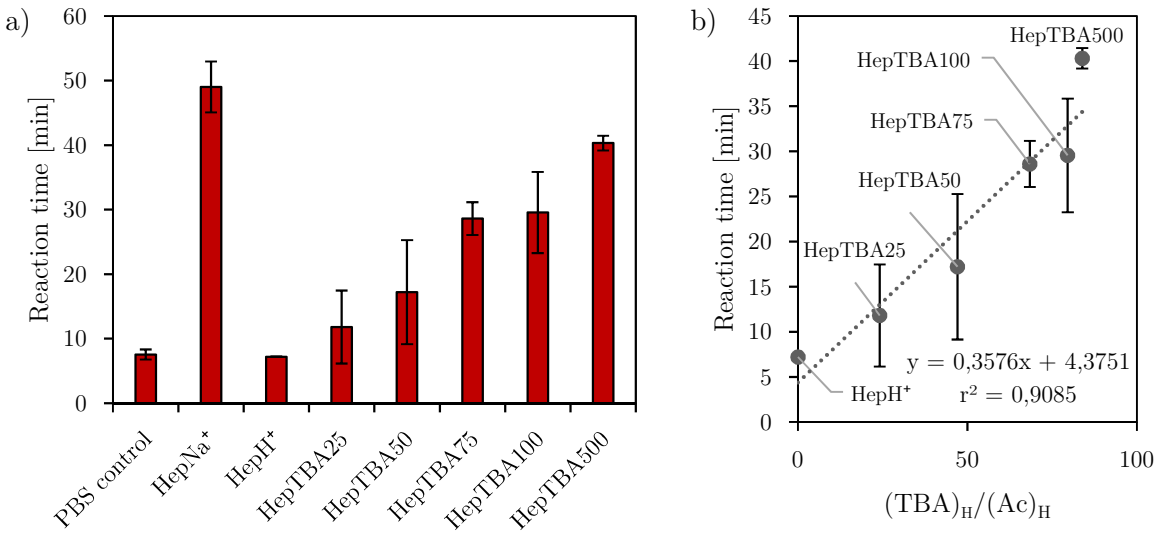

Figure 3.36: Reaction times of human blood treated with heparin variations. a) R_{TEG} values for heparin variations [n = 1 for $HepH^+$, n = 2 for all other]; b) linear correlation between TEG reaction time and TBA content (as determined by NMR).

All variations of heparin-TBA (at 0.01 mg/ml) were found to be anti-thrombotic to some extent, $R_{TEG\_HepTBA} > R_{TEG\_control} > 8$ min (11.8±5.7, 17.2±8.1, 28.6±2.5, 29.6±6.3 and 40.3±1.1 min for HepTBA25, 50, 75, 100 and HepTBA500, Figure 3.36.a). The time to initiate a blood clot was slower when blood was treated with higher TBA content compounds (i.e. when more H^+ were replaced with TBA) compared to the lower TBA content heparins; a linear correlation ($R_{TEG} = 0.36\left(\frac{TBA}{Ac}\right)_{H\ NMR} + 4.4$ min, $r^2 =$

0.91) was fitted for the reaction time as a function of the integral ratio (as defined by equation (2-3)) of TBA to Ac from ^{1}H NMR results (Figure 3.36.b). Not only did HepTBA500 have the longest reaction time among the heparin-TBA variations, it was 9 minutes faster than the time of HepNa$^+$ at the same (w/v) concentration ($P<0.05$).

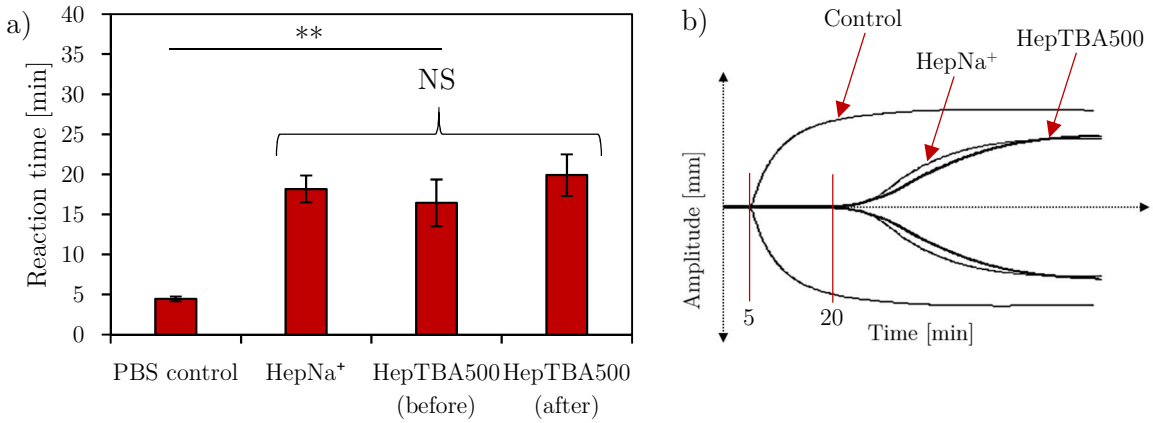

Figure 3.37: Anti-thrombotic properties of heparin before and after electrospinning. a) reaction time values; b) representative TEG graph. ** $P<0.01$. [n = 3].

The R_{TEG} for HepTBA500 (16.4±2.9 min) was within the same range than that of HepNa$^+$ (18.21±1.7 min, $P>0.4$) when they were tested at concentrations of 0.018 and 0.01 mg/ml respectively (molar equalised concentrations according to models proposed by [302]). Additionally, HepTBA500 retained its anti-thrombotic properties prior to processing and as a scaffold eluted product (the reaction times before and after electrospinning were 16.4±2.9 and 19.9±2.6 min respectively, $P>0.2$, Figure 3.37.a). Typical TEG profiles were overlayed for a blood control sample (which started to clot 4 times earlier than any version of heparin, $P<0.05$) and two barely distinguishable blood+heparin curves in Figure 3.37.b. HepTBA500 started to clot at the same time point (20 min), had a slightly sharper clotting angle (25 compared to 30°) and a similar maximum amplitude (50 mm) when compared to HepNa$^+$. Additional TEG results (clotting angle, maximum amplitude and K value) can be found in Appendix A3.

The blood clotting cascade can be prevented/interrupted by effective inhibition of activated factors Xa and IIa (thrombin). Antithrombin (AT-III), when activated by heparin, produces a 9000 and 17000-fold inhibitory activity against factor IIa and Xa

respectively [394]. Interactions between heparin and neighbouring proteins are usually ionic in nature (heparin behave, like DNA, as a polyelectrolyte). When the ionic compounds $HepNa^+$ or $HepTBA^+$ binds to AT-III, the positively charged amino acids of AT-III (a serpin - serine protease inhibitor) form ion pairs with the negatively charged sulfo (SO_3^- with high affinity) and carboxyl groups (COO^- with less affinity) – on the pentasaccharide sequence GlcNS6S3S of heparin [395, 396] (individual saccharides can be seen in Figure 1.16 of the introduction chapter) – by releasing the cations, Na^+ and TBA^+ respectively. Thus, it can be concluded that the lack of antithrombotic properties of $HepH^+$ is due to AT-III being unable to bind to the non-ionic COOH or SO_3H groups of $HepH^+$. Furthermore, HepTBA compounds with higher TBA contents had an increasing anti-thrombotic performance (i.e. longer reaction times) due to more activation sites for AT-III as more H^+ were replaced with TBA^+.

One of the major challenges associated with scaffold drug incorporation via blend electrospinning, is preventing sensitive agents/proteins from losing their bioactivity during or after processing [198]. The previous work on HepTBA showed that this heparin derivative had antithrombotic properties comparable to its commercial form ($HepNa^+$) [310]. Nevertheless, that study did not elaborate on whether the samples were tested before or after the electrospinning process. Here, the *in vitro* anti-thrombotic performance of HepTBA and its newly expanded derivatives are shown for the first time. Moreover, HepTBA500 was tested before and after electrospun fibre incorporation. These new results show that HepTBA is indeed able to retain its bioactivity despite the harsh conditions associated with electrospinning (i.e. strong solvents and high electric fields).

3.3.2.5 Cytotoxicity of heparin variations

The smooth muscle cells used for the viability assay (XTT) before (0 hr) and after (72 hr) heparin treatments, at the ultimate scaffold concentration of 0.5 mg/ml, are represented in Figure 3.38. After 3 days, the seeded cells were confluent (successful

proliferation occurred) and their morphology appeared to be unchanged (no signs of infection) when compared to the cells at inception.

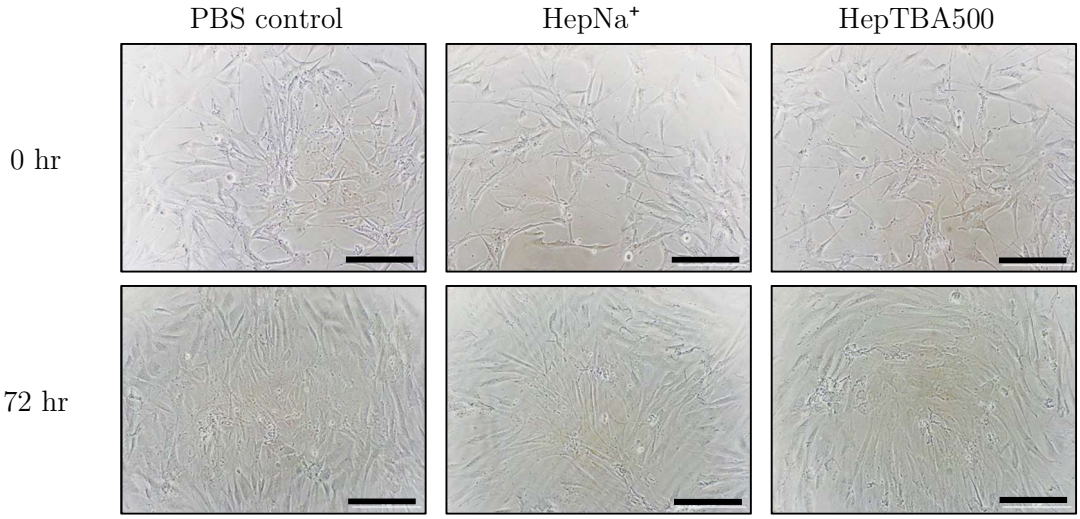

Figure 3.38: Rat SMC prior to and after heparin treatments. Scale bars are 50 µm

The absorbance measurements for all tested variations of heparin were similar (a collective absorbance of 1.12±0.05, P>0.07,) and slightly lower than that of the control samples (1.25±0.05, P<0.05, Figure 3.39a) but well above the background readings (0.26±0.02, P<0.001). After background removal (Figure 3.39b), the relative cell viability for $HepNa^+$ and HepTBA500 were 85.9±9 and 91.5±3% (no significant difference, P>0.1) while the control samples were 100.0±5% (higher than any version of heparin, P<0.05).

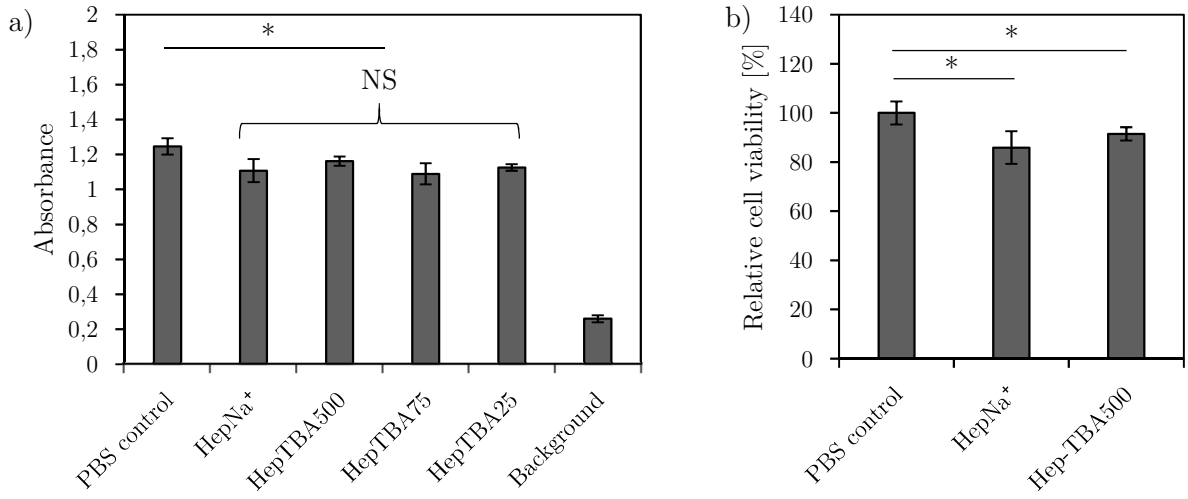

Figure 3.39: Rat SMC viability assay of heparin variations. a) Absorbance measurements taken as the difference between wave length 450 and 655 nm; b) viability for $HepNa^+$ and HepTBA500 after

background subtraction. *P<0.05; [n = 4]

Heparin is known to inhibit proliferation of smooth muscle cells (SMC) [288, 289]. Lee at al. showed that heparin, independently of dosage (tested at 0.05-0.1 mg/ml, which is lower than the current study), reduced human SMC growth by 30% when compared to untreated cells after 3 days of incubation (an MTS assay was used to quantify bioactivity of the hSMCs) [285]. Although the origin of the cells, concentration and type of assay were slightly different, these results agree with the findings from the current study, i.e. a 14% reduction of SMC growth also after 3 days of incubation. Importantly, replacing Na^+ ions with TBA^+ had no influence on heparin's cytotoxicity (or its ability to inhibit SMC proliferation), at a tested concentration of 0.5 mg/ml, regardless of the TBA ratio.

3.3.3 Electrospinning of degradable fibres

This section summarises the influence of controllable electrospinning parameters on the morphological outcome when processing DP. Parametric studies were essential, due to the complexity of the spinning process, to understand and select optimal/acceptable conditions for implant ready scaffold production. The parameters explored in this section were collecting speed, solution properties, base electrode configuration and collecting temperature.

3.3.3.1 Collecting speed

The influence of collecting speed on fibre orientation was quantified and visualised (pixel coherency) for DP electrospun scaffolds (Figure 3.40).

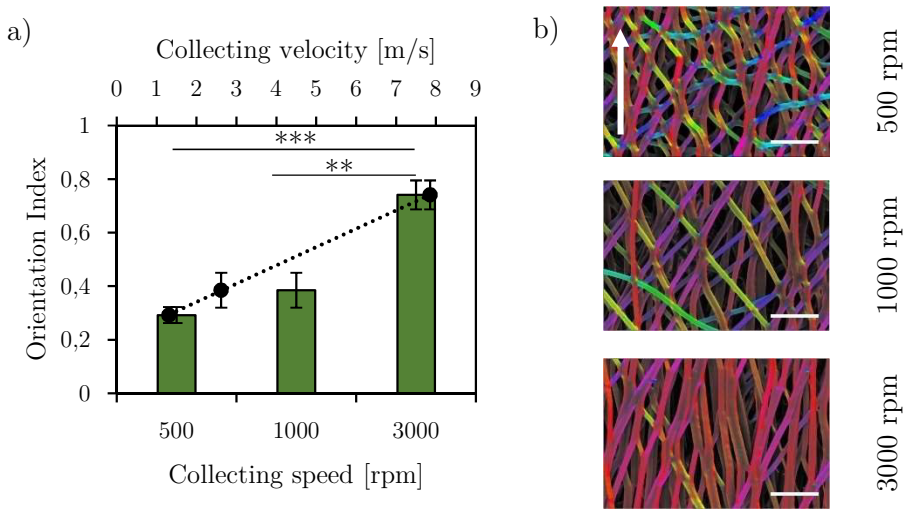

Figure 3.40: Fibre orientation for DP scaffolds at different collecting speeds. a) orientation index as a function of collecting speed (velocity conversions are based on a 25 mm diameter collector); b) representative SEM images, white arrow indication circumferential direction. Scale bars are 50 µm. ***P<0.001/**P<0.01/*P<0.05. [n =4]

The orientation indices increased from 0.30±0.02, 0.36±0.06 to 0.75±0.06 when DP fibres were collected at 500, 1000 and 3000 rpm respectively. The relationship between orientation index and collecting velocity (v_c, m/s) was best described as $OI = 0.068v_c + 0.2$ ($r^2 = 0.99$). Colour encoded SEM images in Figure 3.40.b illustrates the higher degree of orientation obtained at higher collecting speeds (less blue/green/yellow diagonal fibres and more red/pink/purple fibres in line with the collecting direction can be observed).

A higher degree of electrospun fibre alignment as a result of a faster tangential velocity of a rotating collector is a well-known parametric relationship [178, 180–183]. As mentioned before, section 3.2.1.1, alignment of electrospun fibres could be a useful tool for tailoring the mechanical properties of TE scaffolds to match that of the targeted tissue. Additionally, fibre alignment is also known to guide cellular growth in predetermined directions [397, 398]. Here, data are presented for specific control over fibre alignment of DP scaffolds spun from a solvent system with a low dielectric constant (i.e. pure $CHCl_3$, $\varepsilon = 4.8$). Interestingly, fibres from DP scaffolds were easier to align (obtained higher coherencies at lower speeds, e.g. 0.26 and 0.36 for Pel and DP at 1000 rpm) than Pel. This could be explained by the different solvent systems used for processing these two polymers. Greater electrostatic repulsions governed more whipping of Pel fibres, radial momentum, due to a more conductive spinning solution (solvents THF and DMF with $\varepsilon = 7.6$ and 36.7 respectively) when compared to a lower conducting solution, DP/chloroform, which resulted in less side to side movements during the instability phase. Collecting incoming fibres that are predominantly in a straight line, of course, are easier to align (at lower speeds) than fibres that are flying in multiple directions. One of the advantages of controlling fibre alignment by adjusting solution conductivity would be to avoid mechanical limitations (such as heat, vibrations or fatigue) associated with extreme rotational speeds required to obtain a certain degree of orientation on smaller diameter collectors. A probable application for this research project, depending on its success, would be to produce small diameter (4 mm) vascular grafts. Then, the translation of an OI of ~0.3 from a 25 mm to a 4 mm diameter collector, as an example, would require increasing the collecting speed of 2000 to 12500 rpm and 500 to 3125 rpm for Pel and DP respectively (based on predictive equations from Figure 3.3 and Figure 3.40). Such predictions are realistic when compared to previous attempts for producing 4 mm diameter grafts, speeds were on average 4000 rpm with outliers being 250 or 35000 rpm [138].

3.3.3.2 Solution properties

Morphological changes of electrospun DP scaffolds from different $CHCl_3$/HFIP solvent systems are represented by SEM images in Figure 3.41. Fibres spun from a pure $CHCl_3$ solvent system appeared to be smooth and cylindrical. The inclusion of HFIP to the spinning solution caused 'wet landing' (insufficient solvent evaporation) and consequent fibre 'fusion' (fibres merging with neighbouring fibres). Increasing the HFIP content lead to finer and more fused fibres (25-50% HFIP). Fibres obtained by further addition of HFIP (50-100%) was observed to have a flat (2D) 'ribbon' like appearance and made sample removal from the collector's surface more challenging (difficult to separate it from the collector's surface without tearing it in the circumferential direction).

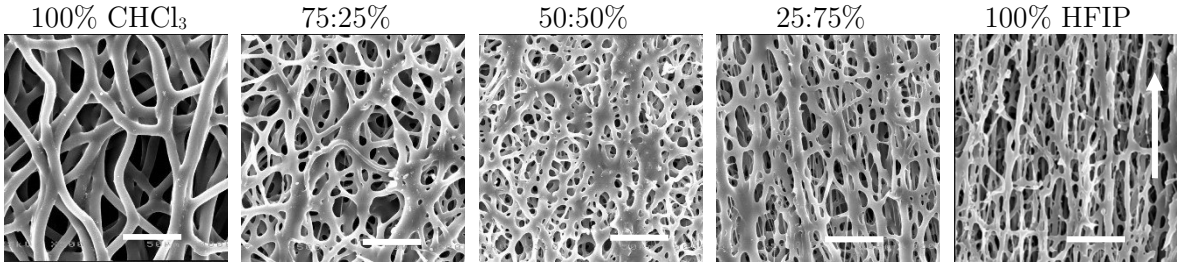

Figure 3.41: Fibre fusion at different solvent systems of DP scaffolds. Solutions were all at DP 20wt%. SEM images were taken of the ablumenal surfaces; scale bars are 50 µm.

Morphological changes of scaffolds produced at different DP concentrations spun from pure HFIP are represented by SEM images in Figure 3.42. An increase in concentration (20-30wt%) improved scaffold morphology to some extent, transforming flat ribbons (also seen at 100%HFIP in Figure 3.41) to more cylindrical fibres. However, the 'wet landing' and the resulting 'fusion' of fibres were not resolved by simply increasing the polymer concentration. A higher solution concentration (20 to 30wt%) also resulted in a smaller fibre distribution area/whipping radius (Figure 3.42), a longer straight jet segment (35 to 110 mm, Figure 3.43a), larger fibres (3.2±1.1 to 7.2±2.4 µm, $P>0.001$) and associated pores (5.0±5.6 to 19.6±18.8 µm, $P>0.001$). The average pore size appeared to have a linear dependency on the average fibre diameter of $D_{pore} = 3.6D_{fibre} - 7.4$ ($r^2 = 0.94$, Figure 3.43b).

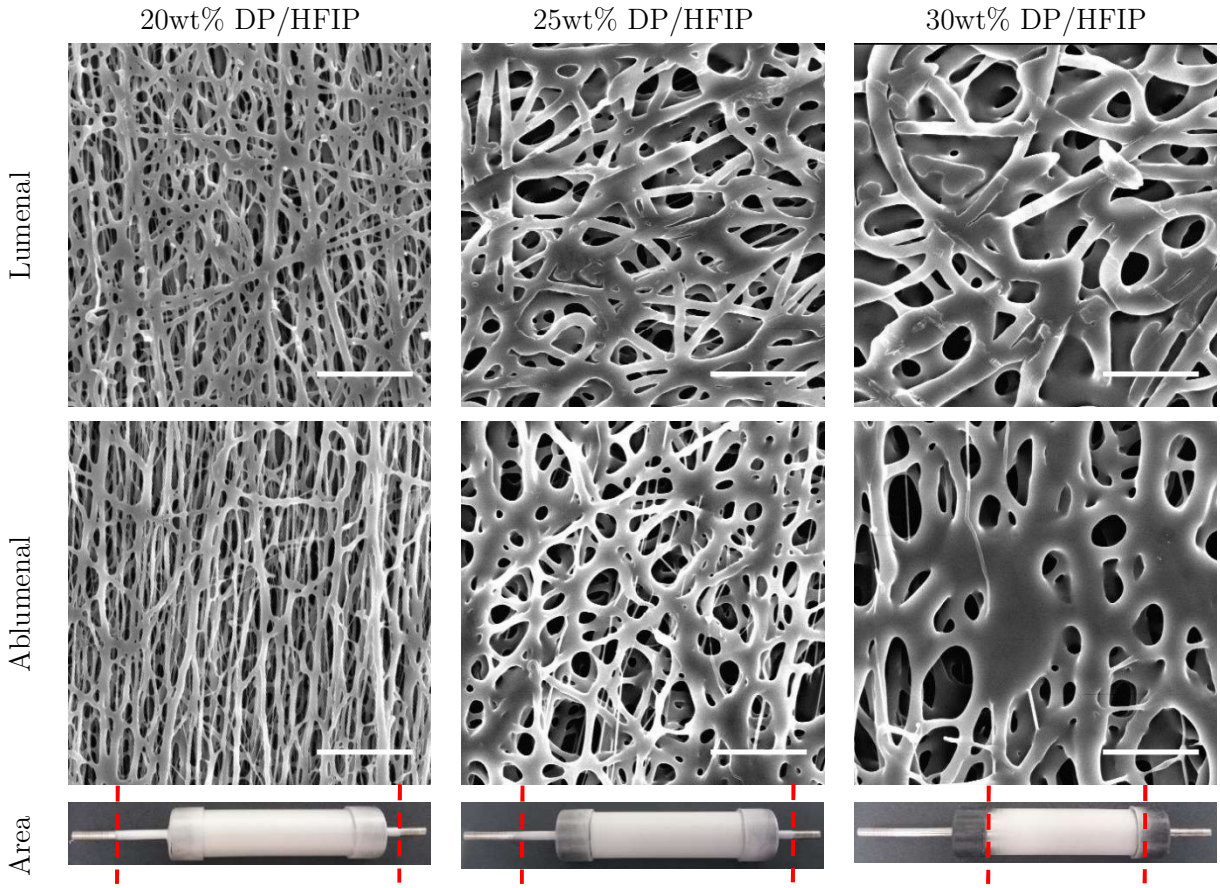

Figure 3.42: Scaffold morphology and distribution observed DP concentrations. SEM images were taken of lumenal and ablumenal surfaces. Scale bar are 50 µm. Red lines indicate start/end of collected area.

Although fused, an increase in concentration was expected to produce thicker fibres [107] and larger pores [210]. Reduced fibre diameters were also expected to be formed from solvents with higher dielectric constants [84]. You *et al.* also compared electrospinning chloroform with HFIP (polymers used were PLA, PLGA or PGA) [143]. This investigation showed that thinner fibres are obtainable when spinning with HFIP compared to chloroform, which is in line with the current study. Successful electrospinning (smooth, bead-free and cylindrical fibres) strongly relies on solvent properties and therefore the solvent selection [94]. Known for being the most often used electrospinning solvent [93, 94, 138, 139], HFIP has been the solvent of choice for processing many synthetic/natural polymers (see section 1.2.2.1 and Figure 1.8 for the advantages of electrospinning with HFIP). It is therefore curious that the majority of DP researchers chose chloroform as their gold standard solvent for electrospinning [21, 178, 208, 261, 263–265, 267, 269, 270, 272, 273] while only a few introduced a mixture

of $CHCl_3$ and HFIP [262, 268, 271] (with a 25% HFIP being the maximum fraction [268]). The fact that HFIP showed good solubility of DP at RT adds to the mystery (see DP solvents in Appendix A7). Perhaps the fusion phenomenon of fibres, as observed in the current study, is the main reason for HFIP not being selected to electrospin DP. Although the authors provided no explanations, only a single study mentioned fusion of DP fibres when HFIP was included in a co-solvent system (80:20% $CHCl_3$:HFIP) [262]. It seemed that the simplest approach to avoid fusion of DP fibres was to stay clear from using HFIP as a solvent. However, the current project aimed at incorporating both Dex and Hep into the same DP spinning solution - both drugs have poor solubility in $CHCl_3$ and considering DP's limited RT solvents, using HFIP as a solvent/co-solvent was appealing. Therefore, the sections to follow will include an attempt to explain this 'unspoken' phenomenon of DP fibre fusion, followed by proposed solutions to overcome this issue.

Firstly, the fusion of electrospun fibres have been seen before [134, 135, 142]. In these cases, fibres fused because of insufficient evaporation due to the inclusion of a co-solvent with a higher boiling point (DMF as co-solvent with THF for a segmented polyurethane) or an elevated flow rate or collecting speed. Despite them being valid explanations for their studies, they are not applicable to the current study due to HFIP having a lower boiling point than $CHCl_3$ and because both DP/$CHCl_3$ (smooth and separate) and DP/HFIP (fused) were electrospun at the same parameters (constant flow rate, concentration, distance from collector and collecting speed). An alternative explanation could be, and would also be consistent with the bulk experimental results from section 3.3.1, a delayed evaporation rate of HFIP from DP/HFIP compared to $CHCl_3$ from DP/$CHCl_3$ solutions due to the high affinity (hydrogen bonding) that exist between HFIP and DP. Briefly, a thin skin of DP would form around the unevaporated solution while fibres are traveling through the air and get dissolved again by its own core upon contact with the collector. Fibres above and adjacent to neighbouring fibres would merge and fused together to form structures seen in Figure 3.42.

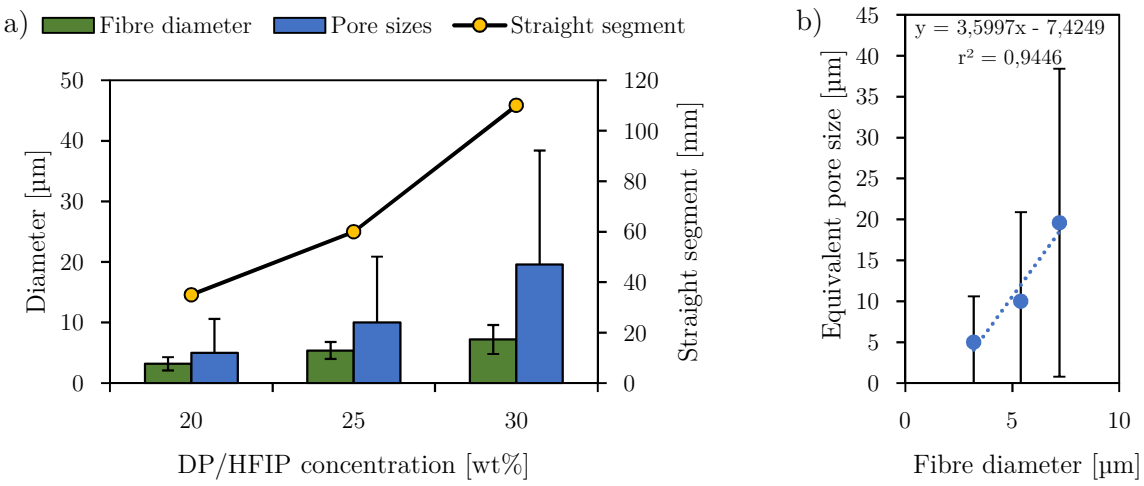

Figure 3.43: Scaffold architectural changes due to shifts in DP concentration. a) Electrospinning straight segment, resulting fibre diameters and pore sizes; b) linear trend between fibre diameter and pore size. [n = 2x3, >20 fibres per image & >100 pores per image].

3.3.3.3 Base electrode configuration

Focusing, steering or aligning fibre deposition with auxiliary electrodes have been shown to be an effective external parameter to control electrospun scaffold morphology [101, 399–404]. Here, the potential of adjustable base electrode surface area is investigated as a novel electrospinning parameter. Furthermore, base electrode size is also considered as a tool to decrease the degree of fibre fusion of DP spinning solutions.

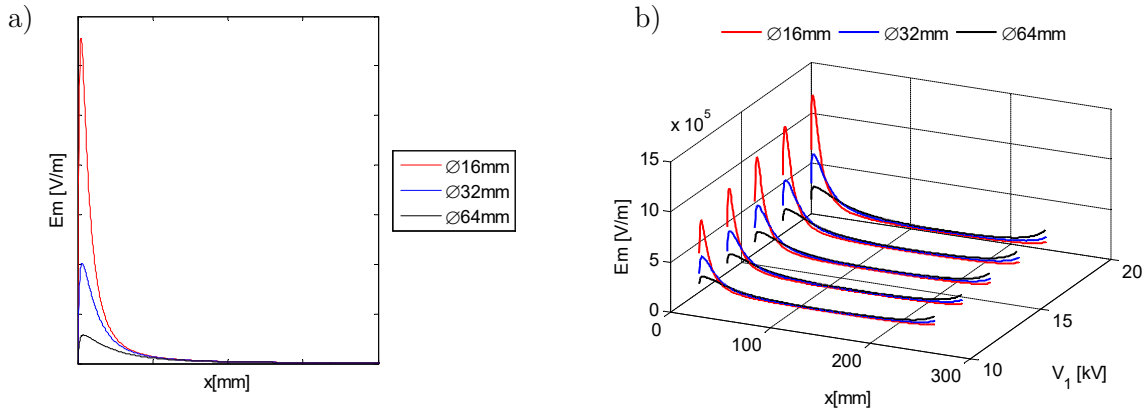

Figure 3.44: Electric field curves of annular disc shaped base electrodes. a) 2D plot for solving equation (2-5) for 16, 32 and 64 mm diameter discs; b) Coulomb3D results for applied voltages V_1 = 12-20 kV.

Numerical simulations of the electric field (Em, V/m), as a function of one dimensional distance (x, mm) from the base electrode (with diameter of 16, 32 or 64 mm) in the direction towards the collector, were calculated using equation (2-5) and Coulomb3D simulation software (Figure 3.44.a and Figure 3.44.b respectively). Curves from the

data captured by solving for equation (2-5) and the results obtained from Coulomb3D simulations were both consistent with observing the maximum electric field peaks (Em_{max}) at x<5 mm and that the peak values were strongly dependant on the disc's size (a smaller surface area produced a larger Em_{max}). A small disc (16 mm) produced a 440% higher Em_{max} than the large disc (7.32, 2.90 and 1.67x10^5 V/m for 16, 32 and 64 mm, Coulomb3D eg. at V_1 = 12 kV). Observations from 3D vector field visualisations (Figure 3.45) confirmed the high field intensity that was found near the surface of the base electrode and rapidly declines into a more uniform field towards the collector.

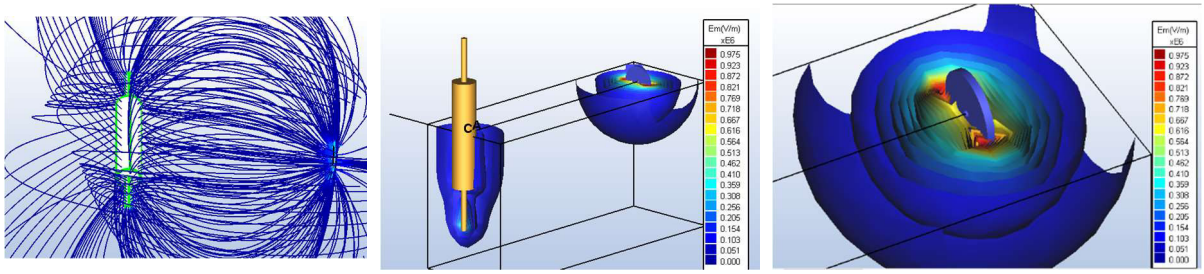

Figure 3.45: Electric field visualisations of a simple base electrode configuration. Produced using Coulomb3D from Integrated Engineering Software.

Per equation (2-5), electric fields were expected to peak at distances close to the base electrode regardless of the electrode size (as described by the roots of equation (2-5), see Appendix A9 for supporting graphs). Moreover, the highest field created by the smallest diameter annular base electrode was also expected due to a constant potential energy being distributed over a smaller surface area (i.e. a higher charge density is created by smaller base electrode).

The concept of using base electrode surface area as a controllable electrospinning parameter to alter scaffold morphology was tested for a low dielectric solvent system (20wt% DP/$CHCl_3$) using a large (3600 mm^2, LBe), medium (490 mm^2, MBe) and small (80 mm^2, SBe) base electrode. Reducing the size of the base electrode from LBe to SBe increased the fibre deposition area (36 to 90 cm^2), decreased the average fibre diameter (7.1±1.5 to 6.1±1.0 µm, P<0.01), increased scaffold pore size (15.1±6.0 to 17,7±7.7 µm, P<0.001) and showed observably less fibre fusion (Figure 3.46 and Figure 3.47).

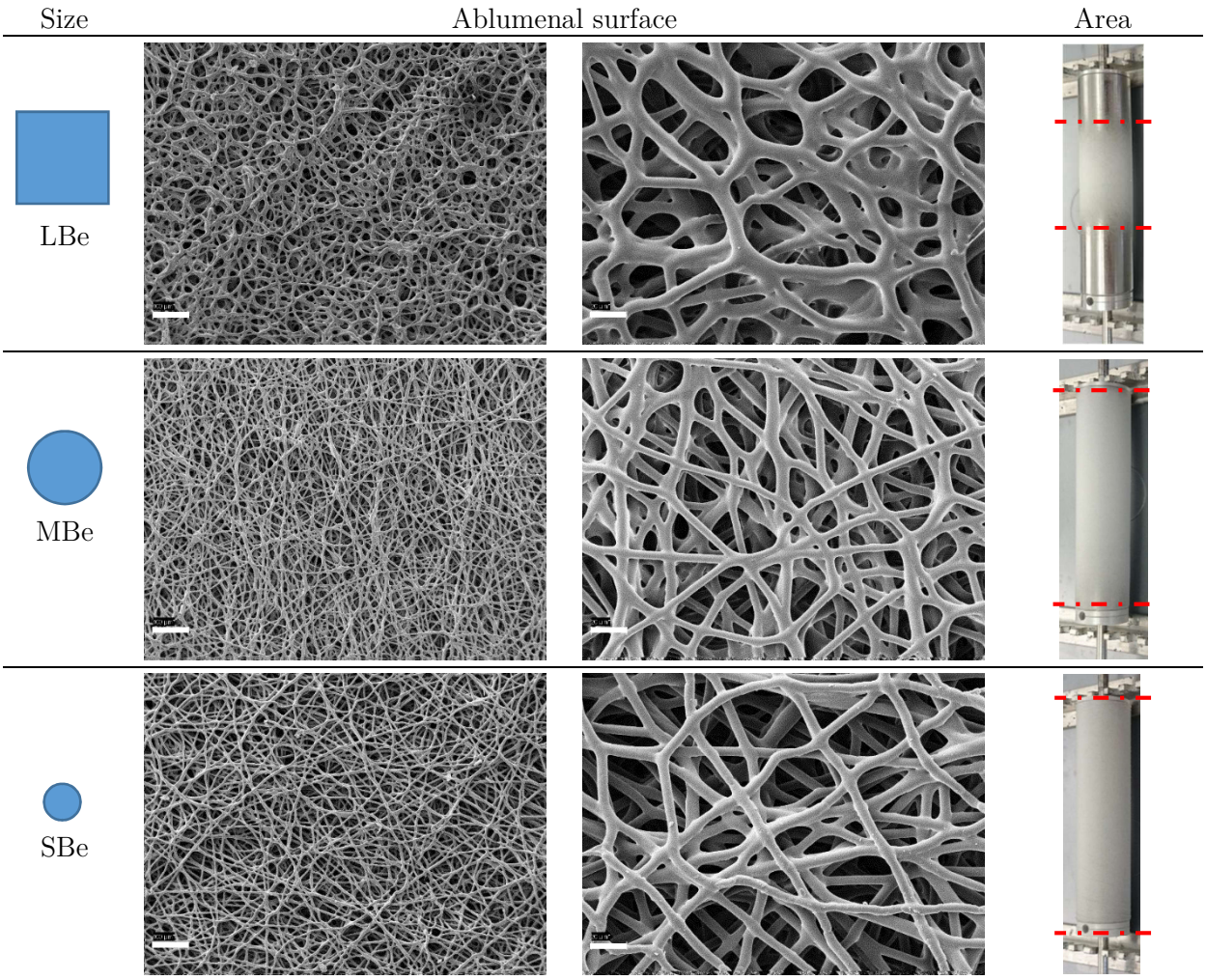

Figure 3.46: The influence of base electrode size on DP scaffold morphology.Scale bars are 100 and 20 µm. Red line indicates start/end of collecting area.

The concentrated charge from the SBe, as expected from the simulations, transferred more energy to the spinning solution compared to a larger electrode and induced a greater whipping radius with a subsequent wider distribution area. This outcome is consistent with a previous study for using a cylindrical focusing base electrode of multiple needles [401]. More whipping also caused further stretching of the solution filament (resulting in thinner fibres) and allowed for more solvent to evaporate which decreased the degree of fibre fusion before collection.

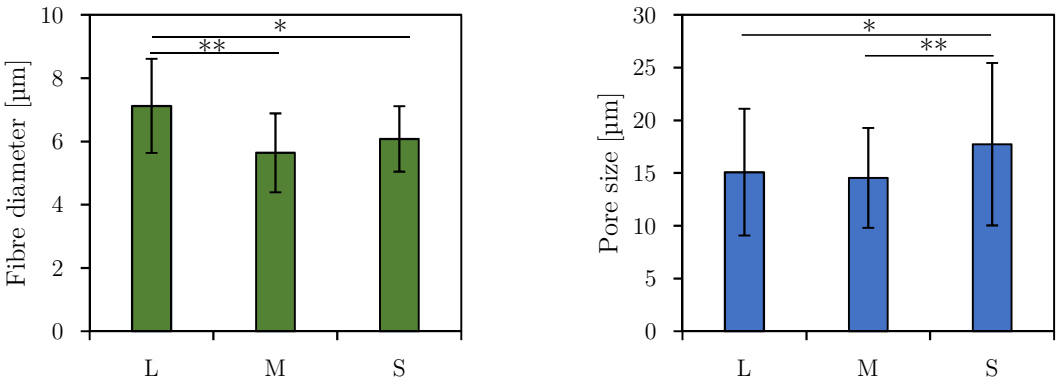

Figure 3.47: Influence of base electrode size on fibre diameter and pore size. **P<0.001/**P<0.01/*P<0.05. [n>30 fibres, n>150 pores].

Although the SBe reduced the degree of fusion of DP/$CHCl_3$ spun scaffolds (due to an enhanced electric field that caused a greater whipping radius), it failed to have the same effect when electrospinning with DP/HFIP (Figure 3.48). A charge concentrated base electrode that promotes additional solvent evaporation was still insufficient to break the affinity between HFIP and DP (the hydrogen bonding mentioned in the previous sections). Nevertheless, a base electrode with adjustable surface area could be a useful tool for additional control over the electrospinning process.

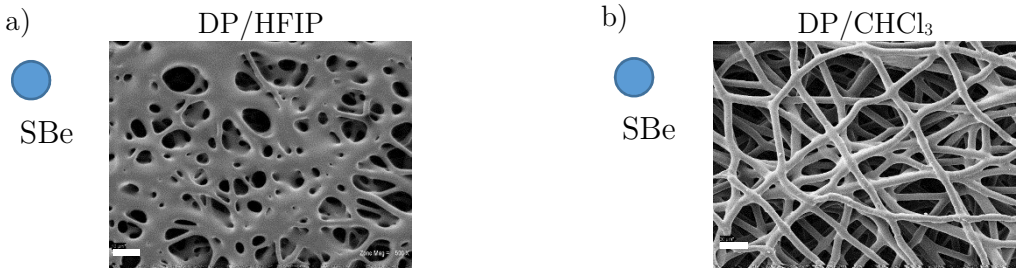

Figure 3.48: Morphology of DP spun scaffolds using a small base electrode. a) 20wt% DP spun from 100% HFIP; b) 20wt% DP spun from 100% $CHCl_3$. Scale bars are 20 µm.

3.3.3.4 Combined electrospinning and spraying

Attempts to enhance DP scaffold porosity using the combined electrospinning and electrospraying technique (section 2.20) failed. Microscope images taken approximately 5min post collecting showed how DP fibres would collapse down the sides of the beads and thereby, breaking fibre continuity (indicated by the black arrow, Figure 3.49.a-b). Not only did the unevaporated solvent dissolve the fibres but also the nearby beads as shown by the SEM images that were taken approximately 1hour post collecting (Figure

3.49.c-d). The result was a weak scaffold that collapsed on itself after time.

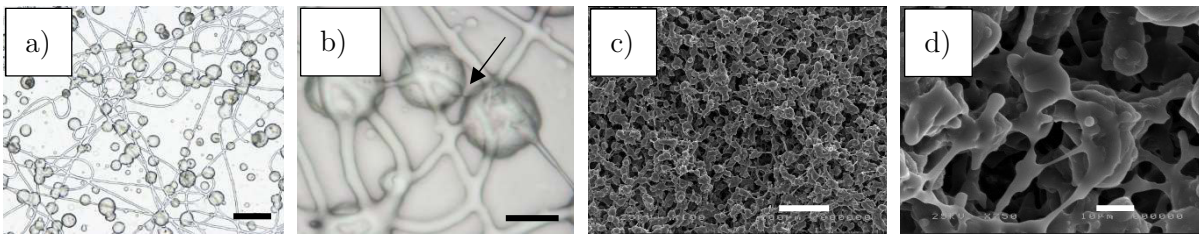

Figure 3.49: Combined electrospinning and spraying with DP and PEG. (a-b) microscope images scale bars are 100 and 25 µm; (c-d) SEM images scale bars are 200 and 20 µm.

Combined electrospinning and spraying was successful in producing high-porosity scaffolds with enhanced healing for Pel (shown in section 3.2.5) as well as previous studies [148, 233, 238]. Failure to apply this technique to DP mainly was due to the delayed evaporation rate of HFIP from the fibres after collection (explained in section 3.3.3.2). The microparticles were heavily affected by the presence of unevaporated HFIP from the DP fibres due the fluorinated alcohol also being a PEG solvent.

3.3.3.5 Collecting temperature

An alternative approach to successfully prevent the DP/HFIP fibre fusion phenomenon was required after manipulation of the previously mentioned parameters were insufficient (flow rate, polymer concentration, solvent ratios and base electrode area).

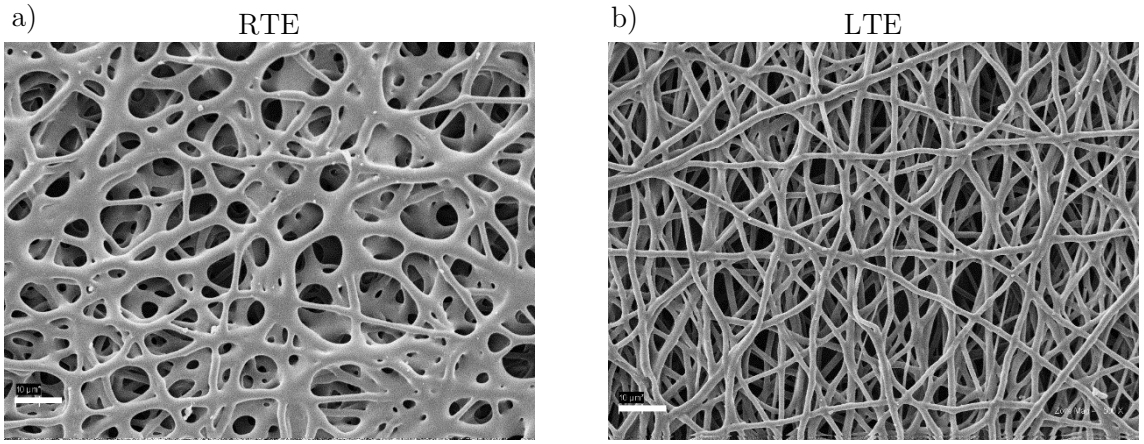

Figure 3.50: The influence of collecting temperature on DP electrospun fibres. A concentration of 20wt% (50:50% $CHCl_3$/HFIP) and the small (25 mm) collector were used. a) RT (22°C); b) low temperatures (approx. -70°C). Scale bars are 20 µm.

The new approach involved the use of dry ice (-78.5°C) to cool the collector to temperatures below the solvent freezing points (-60.3 and -3.3°C for $CHCl_3$ and HFIP)

so that fibres would 'snap freeze' into their volumetric positions upon contact with the collector's surface. This way, additional time would be provided for solvent to evaporation and/or sublimation before returning to a liquid phase. The influence of LTE on scaffold morphology was explored and optimised for a low or high DP concentration (20 or 24wt%) collected on a small or large collector (25 or 75 mm).

The 25 mm collector, filled with dry ice, successfully lowered the degree of fusion for 20wt% DP spun fibres. The transformation of fibres merging with neighbouring fibres in the case of room temperature electrospinning (RTE) to cylindrical and observably less fused fibres when collected on a cold collector (LTE) can be seen in Figure 3.50. The maximum collection time was <10 min before the collector started to heat up (noted when a clear metallic surface was exposed instead of white icicles) and had to be refilled with dry ice.

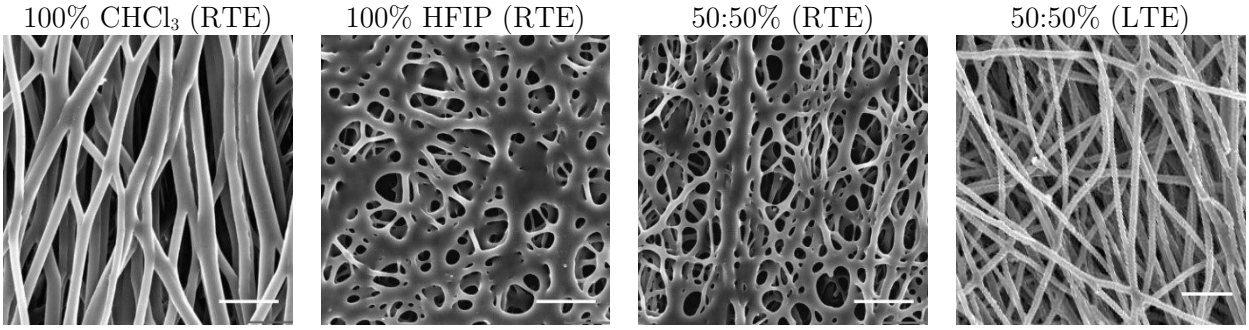

Figure 3.51: Electrospun fibre fusion correction by low temperature collecting. A concentration of 24wt% and the large collector (75 mm) was used. The percentages refer to the solvent content by weight. Scale bars are 50 µm.

The LTE process was optimised to further reduce fibre fusion (by increasing polymer concentration to minimise fibre solvent content) and to extend the collection time (by using a larger 75 mm collector). Spinning at a concentration of 24wt% resulted in (Figure 3.51): smooth individual fibres (approximately 10µm) when RTE from pure chloroform, heavily fused fibres when RTE from pure HFIP, less fused fibres when RTE from a 50:50% mixture and finally smooth individual fibres (approximately 5 µm) when LTE of the mixed solvent system. The 75 mm collector loaded with dry ice provided at least 1hour of continuous LTE.

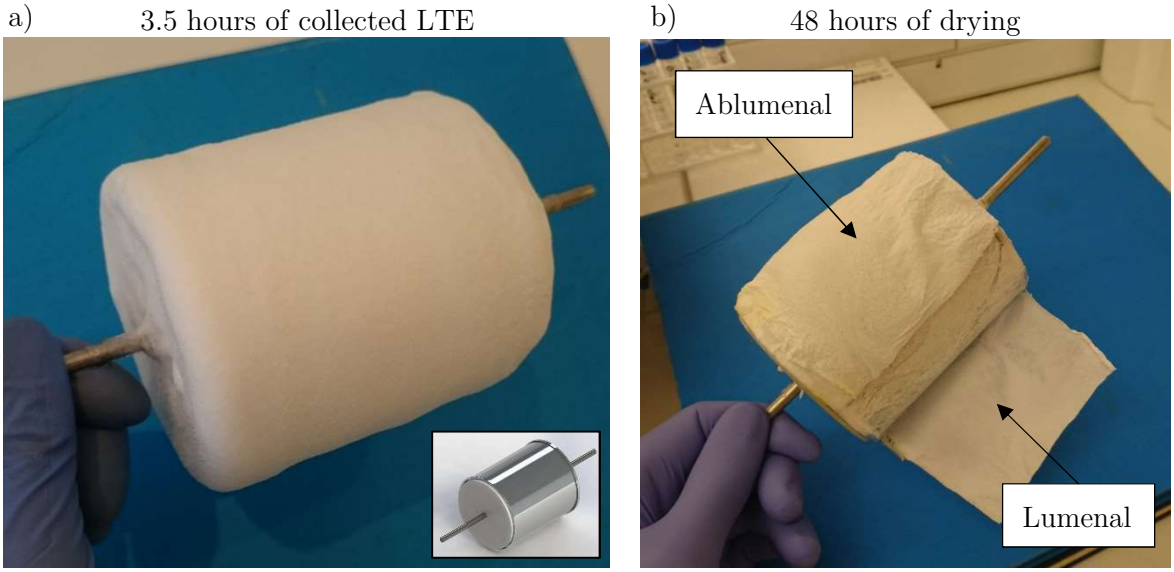

Figure 3.52: LTE with a dry ice and the large collector. a) 3.5 hours of 24wt% DP LTE; b) 48 hours post drying process.

Collecting LTE for 3.5 hours (and refilling the ice chamber every 30 min) resulted in an icy-fibrous composite layer (of ~10 mm thick) around the circumferential surface of the large collector (Figure 3.52). After 48 hours of drying, LTE scaffolds had an average porosity that was 40% higher than those obtained by RTE (83±3 to 43±11%, $P<0.001$). Interestingly, micro indentations (4.7±2.2µm) appeared on abluminal fibre surfaces at >3.5 hours of LTE (fibres collected at 10mm away from the collector's surface, Figure 3.53). This limitation, 3.5 hours of collecting time, was a trade-off between accompanied micro indentations and maximising scaffold thickness (as an attempt to reach 1 mm) for implant ready production.

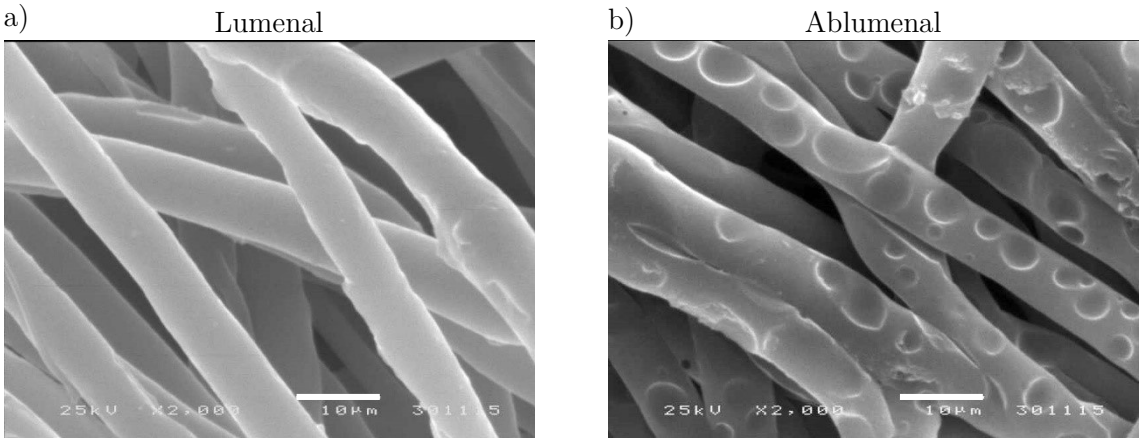

Figure 3.53: SEM images of LTE fibre morphology. a) luminal smooth fibres and b) micro indentations on ablumenal fibre surfaces. Scale bars are 10 µm.

The fusion of DP fibres electrospun from solvents that contained HFIP was resolved by LTE. A possible explanation could be that the HFIP inside the fibres reached a solid phase once captured by the cooled collector and evaporated during the drying process without dissolving the skin of the DP fibres. Furthermore, the structural porosity of DP scaffolds was increased by LTE when compared to RTE due to two possible reasons. Firstly, LTE has been known [205, 208, 236, 237] to be an effective porosity enhancement technique by including inter-fibre ice crystals that are formed from local air moisture to act as temporary space holders (much like the PEG microparticles from section 3.2.3). Secondly, LTE also increased scaffold porosity by preventing fibre fusion. This allowed fibres to form three dimensional stacks instead of merging into the same plane as in the case of RTE. The indentations observed on the ablumenal fibre surfaces (Figure 3.53) were made by the ice crystals due to the core fluid (DP/HFIP) not being completely frozen at roughly 10mm away from the collector's surface. It is proposed/assumed that the prolonged collection of material had an isolation effect that was significant enough to prevent the entrapped fluid inside the last layer of collected fibres to reach its solid phase. Thus, the unevaporated HFIP was still able to dissolve or swell the fibre's skin to such an extent that allowed the inter-fibre ice crystals to leave imprints. Dimpled fibres could be useful for applications where additional fibre surface area is required.

3.3.4 Biodegradable implant production

The degradable implants produced for the subcutaneous assesment included a low temperature collected DP control scaffold (LTE), a 5wt% dexamethasone incorporated DP scaffold (LTE+Dex) and one containing 5wt% of the modified heparin, HepTBA500, (LTE+Hep). Figure 3.54 presents each implant group with a top view and close-ups of both lumenal and ablumebal topographies.

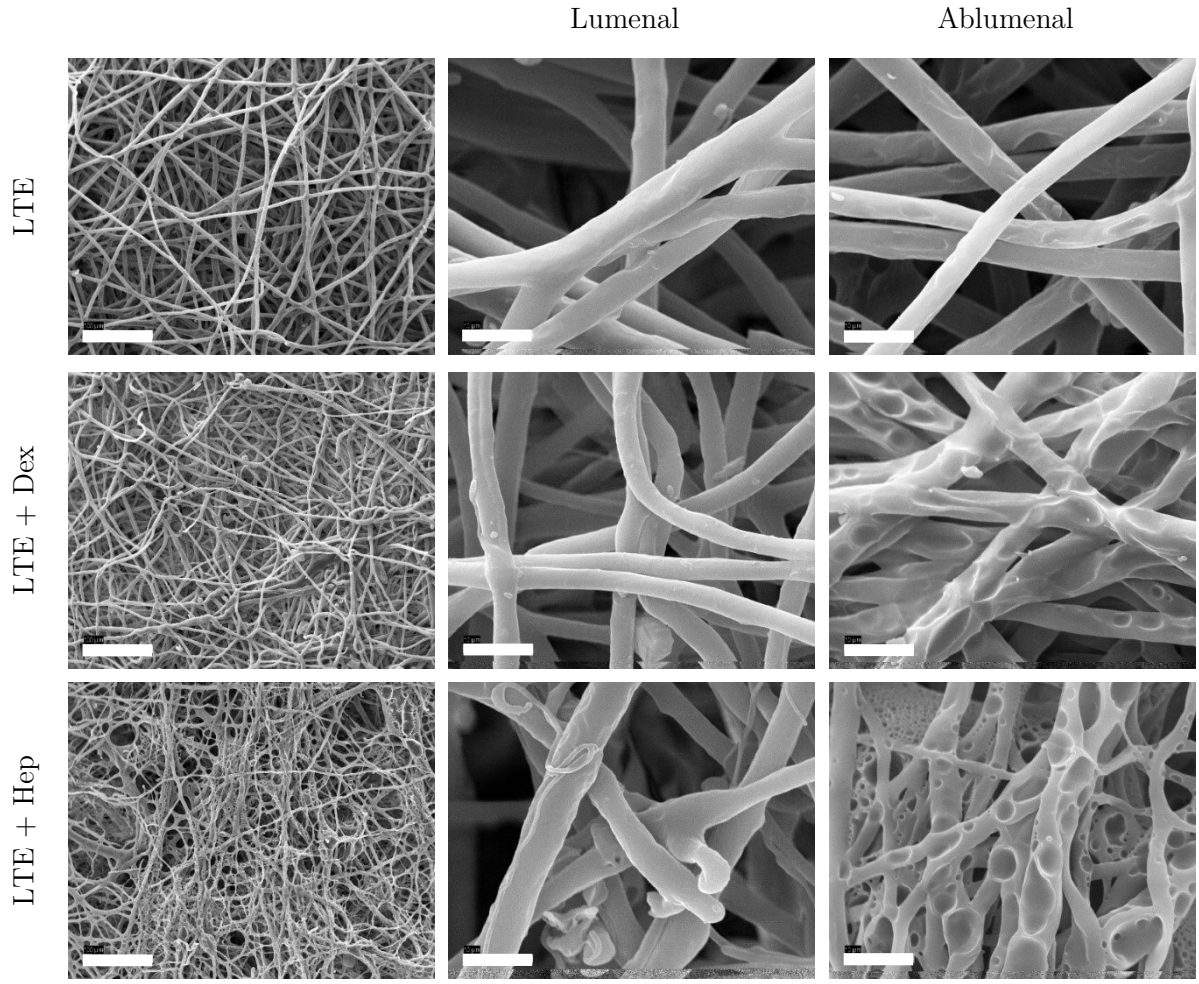

Figure 3.54: Degradable scaffold selection for subcutaneous implantation. Scale bars for the low (lumenal) and high (lumenal and ablumenal) magnification SEM images are 100 and 10 µm respectively.

LTE of DP (solution viscosity at RT was 6850±8 cPoise) produced fibres with an average diameter of 5.19±1.2 µm and a scaffold thickness of 636±96 µm (Figure 3.55.a). Drug incorporated fibres had comparable diameters ($P>0.09$) which were collectively smaller than that of the drug free scaffolds ($P<0.001$), 4.24±1.1 µm and 3.74±1.5 µm

for dexamethasone and heparin blended fibres respectively. Adding salts to an electrospinning solution is known to increase its conductivity (proportional to concentration [405]), which result in further fibre stretching and therefore, reduced fibre diameters [406]. Thus, adding drugs to DP solutions (especially ionic products) were also expected to produce thinner fibres. Supporting this assumption and the results from the current study, reduced fibre diameters have been reported as a result of heparin [243] and dexamethasone [244, 323] blend electrospinning. The porosity of LTE scaffolds was reduced (as shown in Figure 3.55.b) from 83.0±3% to 78.3±8% or 73.3±4% for scaffolds containing dexamethasone or heparin respectively ($P<0.01$), LTE+Dex scaffolds were more porous than LTE+Hep ($P<0.05$).

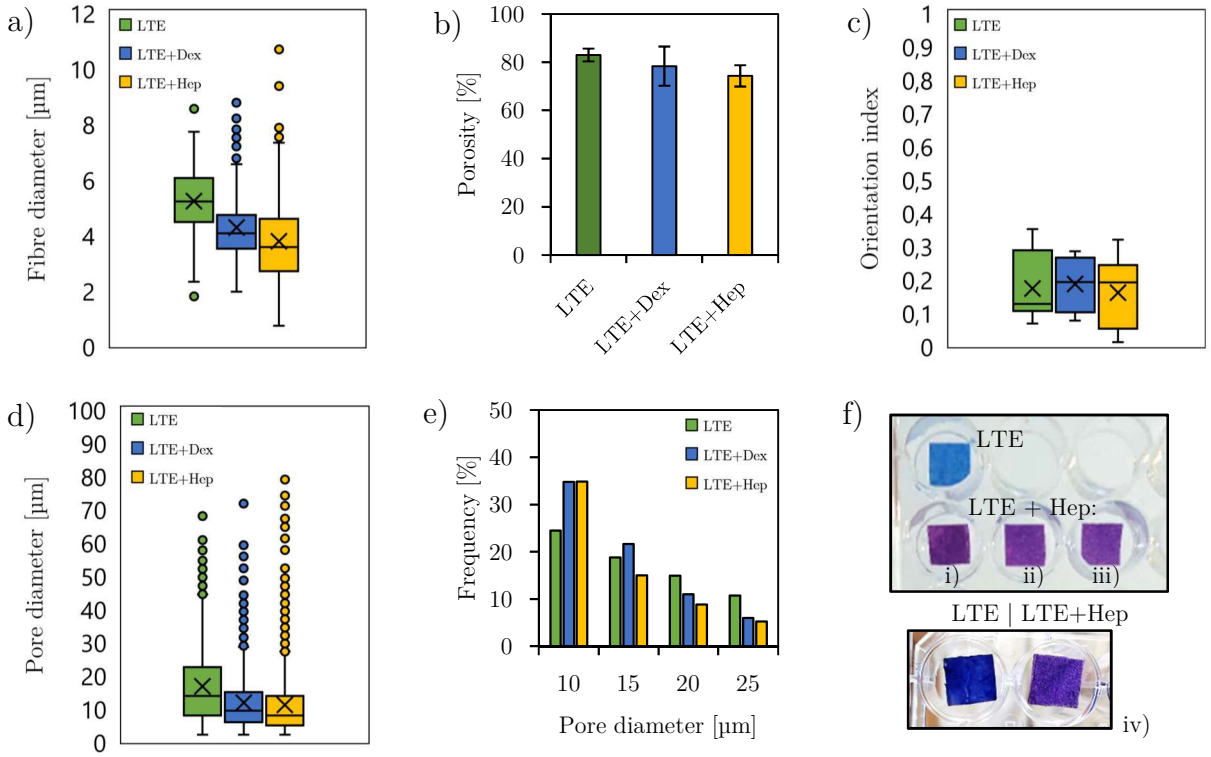

Figure 3.55: Characteristics of degradable implant groups. a) fibre diameter [>40 fibres/image]; b) scaffold porosity [n = 40]; c) fibre orientation index [n = 8]; d) scaffold pore size [>300 pores/image]; e) frequency of total pores between 10-25 µm [>2400 pores/group]; f) heparin confirmation stains (Toluidine blue).

All degradable implant groups had similar orientation indices ($P>0.6$), LTE (0.17±0.1), LTE+Dex (0.18±0.1) and LTE+Hep (0.16±0.1, Figure 3.55.c). Drug incorporation reduced the equivalent pore size (Figure 3.55.d and Figure 3.55.e) of LTE scaffolds

from 16.39±11 µm (44% of the total pores were within the range of $15<D_{pore}<25$ µm) to 11.56±9 µm (40% were $15< D_{pore} <25$ µm) and 10.85±10 µm (30% were $15<D_{pore}<25$ µm) for dexamethasone and heparin respectively ($P<0.001$). The average scaffold pore sizes between the drug incorporated groups were not significantly different ($P>0.3$). The smaller pore sizes of LTE+Hep/Dex scaffolds may be attributed to the decrease of fibre diameters and lower porosities associated with the inclusion of drugs (lower porosities and smaller fibres are theoretically expected to produce smaller pore sizes, $D_{pore} = -\frac{D_{fibre}}{\ln(P)}$, [211, 407]). The presence of heparin in LTE+Hep groups was confirmed with positive (purple) Toluidine blue stains i) immediately post processing and after ii) 1 min, iii) 48 hours and iv) 45 days of *in vitro* incubation (Figure 3.55.i-iv).

Drug-free DP scaffolds were slightly stronger in the longitudinal direction (0.56±0.1 MPa) than in the circumferential direction (0.32±0.2 MPa, $P<0.01$), as shown in Figure 3.56.a. Conversely, heparin incorporated scaffolds were stronger in the circumferential direction (0.41±0.1 MPa) than that of UTS in the longitudinal direction (0.21±0.1 MPa) while LTE+Dex was approximately 0.46 MPa in both directions ($P>0.4$). Although all three groups had similar orientation indices, fibres were more circumferentially aligned when a drug was added to the spinning solution (higher conductivity) when compared to the control fibres. Effectively, drug incorporation decreased mechanical strength in the L direction (more extreme in the case of Hep) and increased C strength (more extreme in the case of Dex). The maximum elongation, presented in Figure 3.56.b, was similar for each group in both circumferential and longitudinal directions ($P>0.1$). Collectively, drug incorporated scaffolds reduced the maximum elongation of LTE (123±14%) by 57% (66±15%, $P<0.001$) and 81% (42±13%, $P<0.001$) for LTE+Dex and LTE+Hep respectively. The elastic modulus (Figure 3.56.c) of LTE was more than double in the longitudinal direction (1.91±0.4 MPa) when compared to the modulus in the C direction (0.79±0.2 MPa, $P<0.001$).

Inversely, heparin incorporated scaffolds were half as stiff in the longitudinal direction (0.90±0.2 MPa) compared to the stiffness in the direction circumferential (1.91±0.4 MPa, $P<0.001$) while dexamethasone incorporated scaffolds had an E of approximately 1.7 MPa for both testing directions ($P>0.7$). On average, DP scaffolds had a Young's modulus in the region of 1.50±0.5 MPa regardless of drug incorporation or testing direction. The addition of biological agents influenced the electrohydrodynamics of the fibre formation process and resulted in significant morphological alterations (fibre diameter, porosity and pore sizes were affected). It is therefore no surprise that the drug incorporated scaffolds had slightly different mechanical properties compared to the drug-free samples. Electrospinning of Dex blended fibres was formely reported to produce scaffolds that were mechanically weaker (lower E, UTS and maximum elongation) than their drug-free controls [323]. Likewise, heparin incorporated scaffolds were also previously mentioned to have poor mechanical properties [313].

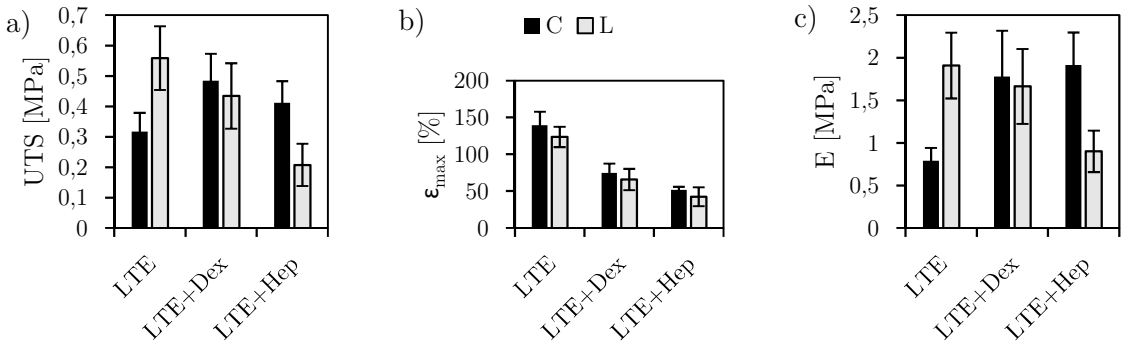

Figure 3.56: Mechanical properties of degradable implant groups. a) Ultimate tensile strength (UTS), b) maximum elongation (ε_{max}) and c) elastic modulus (E). [n = 6]

The *in vitro* release of HepTBA from LTE+Hep scaffolds over a period of three months is presented in Figure 3.57. A cumulative dosage of 40, 47 and 48% of the total load (indicated by the red line) was delivered on 1, 7 and 90 days respectively. Effectively, the first half of the incorporated HepTBA was released within the first week and the other half (at 25 mg/g) remained embedded within the fibres for the rest of the 3 month study (i.e. no measurable elution took place past 7 days). The assumption that the other 50% of the load was embedded within the scaffold is supported by the

confirmation of the presence of heparin at 45 days (a positive purple stain as previously demonstrated in Figure 3.55.f.iv).

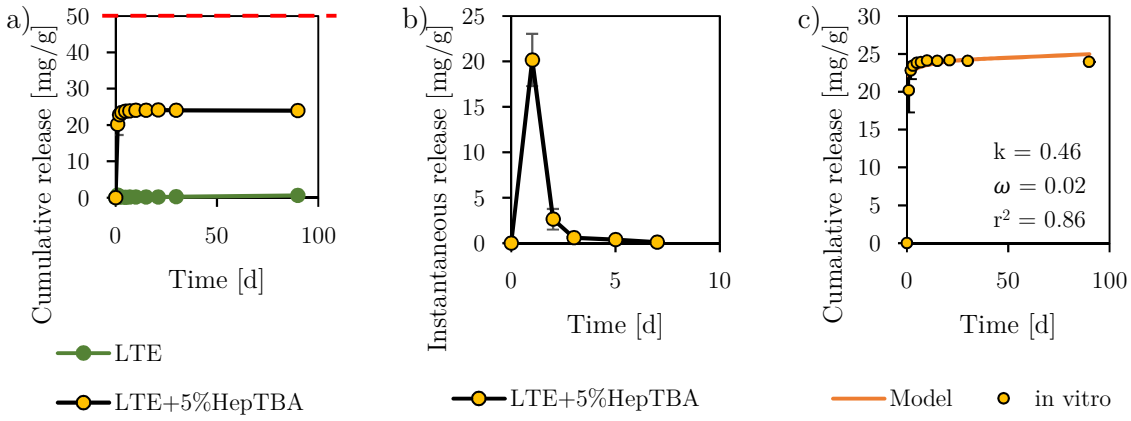

Figure 3.57: HepTBA *in vitro* release profiles from degradable implants. a) cumulative and b) instantaneous release profiles; c) fitted Korsmeyer-Peppas model for 90 days *in vitro* [n = 3].

The release of dexamethasone from LTE+Dex scaffolds over a period of three months is presented in Figure 3.58. The cumulative release of dexamethasone was 9, 36 and 78% of the total the dosage on 1, 7 and 90 days respectively. In contrast to the HepTBA elution profile, dexamethasone followed a near constant instantaneous release rate (3-5 mg/g per day) for the first week and depleted approximately 80% of its initial dosage (50 mg/g) by the end of the study. Table 3.2 are the results for fitting theoretical release models to the actual *in vitro* data obtained from measuring the release concentrations of both HepTBA and Dex loaded scaffolds.

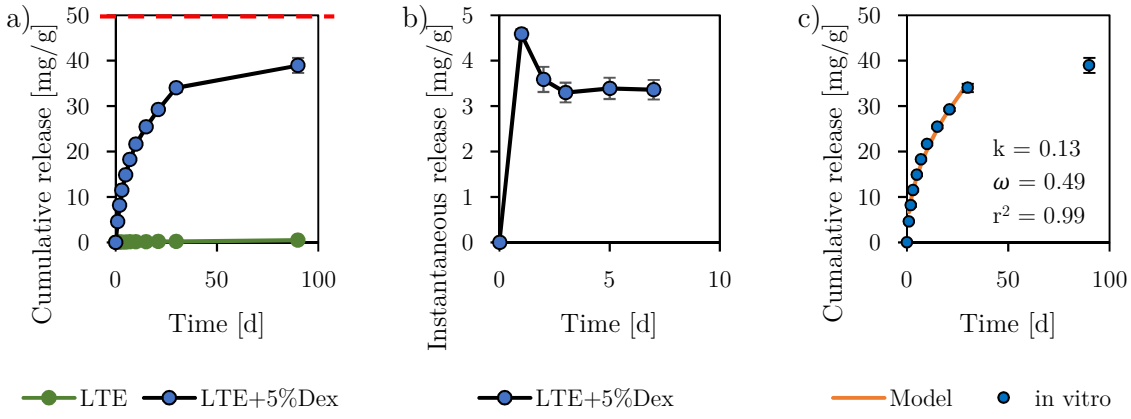

Figure 3.58: Dexamethasone *in vitro* release profiles from degradable implants. a) cumulative and b) instantaneous release profiles; c) fitted Korsmeyer-Peppas model for 90 days *in vitro* [n = 3].

The Korsmeyer-Peppas model was found to be a suitable model to describe the release

kinetics of both 5wt% incorporated HepTBA and Dex from LTE scaffolds. This model was fitted ($r^2 = 0.86$) for the entire length of the HepTBA release study (due to the validation of less than 60% release, i.e. $U_{90days}/U_{\infty}<0.6$ [329]) which resulted in a rate constant (k) of 0.46 and a release exponent (ω) of 0.02.

A comparison between the model and actual measurements are shown Figure 3.57.c. The release of dexamethasone followed a near perfect Korsmeyer-Peppas fit ($r^2 = 0.99$) with a k value of 0.13 and a release exponent of 0.49 (Fickian diffusion, $\omega = 0.5$). The model was applied to only the first month of data, due to $U_{90days}/U_{\infty}>0.6$ and $U_{30days}/U_{\infty}<0.6$, and can be seen in Figure 3.58.c.

Table 3.2: Theoretical models for LTE release kinetics of HepTBA and Dex

Model/	Zero-order		First-order		Higuchi		Korsmeyer-Peppas		
Drug	k	r^2	k	r^2	k	r^2	k	ω	r^2
HepTBA	2.96E-04	0.11	3.09E-04	0.09	1.66E-03	0.70	4.60E-01	0.02	0.86
Dex	6.78E-03	0.65	1.95E-03	0.44	1.06E-01	0.77	1.32E-01	0.49	0.99

Diffusion is considered to be the main mechanism behind the release kinetics of bioactive molecules from electropsun scaffolds [241–244, 324–326]. Many factors may influence their diffusion profiles, such as fibre/scaffold architecture, polymer degradation, solubility of both drug and polymer or the physiological conditions. Although there were slight architectural differences (fibre diameter, pore size and porosity), it is likely that the primary reason for the distinguishable release profiles for HepTBA and Dex was because of their vast difference in molecular size. Dex, being the smaller molecule, had a faster delivery rate when compared to that of HepTBA due to it being able to diffuse faster through the polymeric matrices [329], as demonstrated in section 3.3.2.3. Dex has been incorporated into electrospun scaffolds [239, 244, 322, 323]. In one study, PEOT/PBT electrospun scaffolds containing Dex at 0.5-2wt% [323] showed delivery characteristics comparable to that of the current study with 20 and 60% released on day 2 and 28 respectively ($\omega = 0.33$). This was similar to that of the release for LTE+Dex (16 and 67% for day 2 and 30, $\omega = 0.49$). These corresponding

results are confirmation that dexamethasone, blended into electrospun scaffolds, released via Fickian diffusion. On the other hand, the initial burst release and subsequent plateaued profile for HepTBA from LTE+Hep scaffolds was consistent with a previous incorporation and release of 1,5 and 10wt% HepTBA from PLCL electrospun scaffolds [310]. The authors showed that the cumulative release of HepTBA did not exceed 36/53% for the incorporated loads of 5/10wt% even after 4 weeks *in vitro,* which agrees with the current study (5wt% HepTBA from LTE+Hep did not exceed the 50% load even after 12 weeks). Although the original authors of HepTBA [310] did not analyse its release kinetics, others have shown that heparin sodium eluted from PCL electrospun scaffolds, at a concentration of 0.5wt%, followed a diffusion model with an exponent of $\omega = 0.1$ [243] (HepTBA from the current study was $\omega = 0.02$). Furthermore, profiles resembling the release of HepTBA, Figure 3.57, was also observed for the release of DNA (both heparin and DNA are considered to behave as polyelectrolytes, as mentioned in section 3.3.2.4) from PLGA/PLA-PEG electrospun scaffolds [241], as well as heparin sodium from PU films [408]. The evidence provided in literature, the *in vitro* release results from the current study together with the positive stains for heparin after 45 days of incubation (Figure 3.55.f.iv), supports a consensual description. That is, the release of HepTBA from DP electrospun scaffolds provided an initial burst release of heparin molecules followed by a second stage that may be regarded as surface modification rather than a sustained diffusive elution. Fortunately, such a heparin profile might be beneficial for medical devices such as vascular grafts. In this application, the initial, post implantation stages are crucial to prevent SMC proliferation and avoid intimal hyperplasia which usually causes graft failure [243]. Therefore, a LTE+HepTBA scaffold would not only inhibit initial SMC proliferation but will also provide an antithrombotic surface and promote tissue regeneration, these are known properties of scaffolds with heparinised surfaces [60, 292, 338, 409].

3.3.5 Healing assessment of biodegradable implants

This section includes results and discussion for the *in vivo* assessment (rat subcutaneous model) of the specifically selected degradable scaffolds in terms of quantified tissue ingrowth followed by collagen, cellular, macrophage and vascular density.

3.3.5.1 Scaffold tissue ingrowth

Representative H&E (the dark pink areas are positively stained tissue) micrographs for the degradable implant groups are shown in Figure 3.62 for 7, 14, 28 and 84 days respectively.

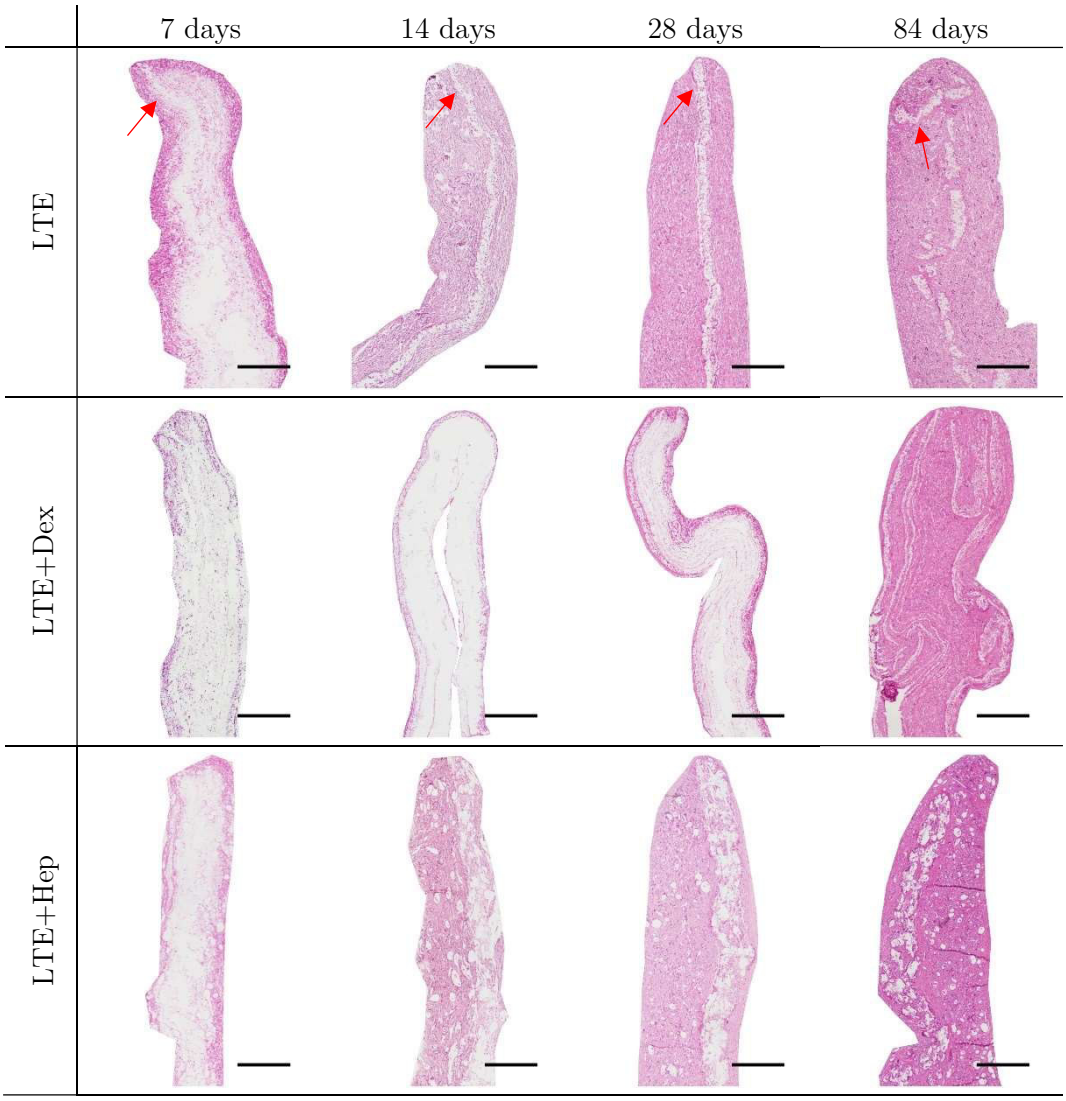

Figure 3.59: Representative H&E micrographs of degradable implant groups. Scale bars are 500 µm.

Degradable scaffolds had similar ingrowth percentages after the first week, between 13-25% (P>0.1). LTE+Dex followed a linear ingrowth rate over the period of 84 days

(1.05T+4.4%, r^2 = 0.99) while LTE and LTE+Hep both had rapid initial trends followed by plateaued curves towards the last time point (all groups ended between 88-98%, Figure 3.61). The ingrowth for heparin incorporated scaffolds were slightly lower than that of the control groups (43.0±14 and 72.0±5% compared to 68.3±12 and 84.4±8%, P<0.05) but higher than the dexamethasone incorporated scaffolds (17.1±9 and 40.1±24%, P<0.05) at time points 2 and 4 weeks. Scaffold degradation was observable at 84 days as indicated by the red arrows in Figure 3.59 with respect to the internal ridges described in Figure 3.60.

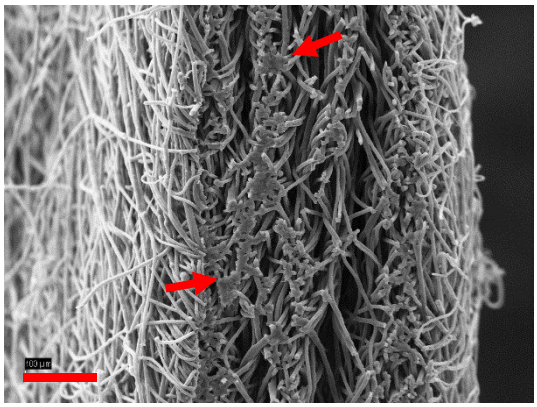

Figure 3.60: Internal ridges found in the cross section of LTE scaffolds. The red arrows indicate the layers of fibre laminations. Scale bar is 100 µm.

The ingrowth profiles for heparin and the drug-free LTE scaffolds suggested that the presence of HepTBA had little to no influence on the ingrowth rate of cells regardless of each scaffold's architectural differences (LTE+Hep had a lower porosity and smaller pore sizes when compared to LTE, Figure 3.55.b). On the other hand, the delayed tissue ingrowth for the LTE+Dex scaffolds, could be attributed to the architectural differences caused by the drug incorporation process and/or the localised delivery of dexamethasone. The changes in scaffold porosity/pore sizes seems to be an unlikely explanation when considering that the architecture of Dex loaded scaffolds were a closer match to that of the drug-free ones compared to the LTE+Hep scaffolds (which had nearly un-affected ingrowth rates). A more plausible explanation could be that the suppressed tissue ingrowth during the first month of the LTE+Dex scaffolds was caused by the sustained delivery of most of the dexamethasone load over that same period (*in*

vitro prediction was ~70% of the total dose within 30 days, Figure 3.58), and that full tissue ingrowth was only achievable at the end of the study when the drug was nearly depleted. Such an explanation is also be in line with others who showed that Dex incorporated scaffolds limited *in vivo* cellular infiltration while the drug maintained a sustained delivery [239, 314, 316]. The bulk degradation of the scaffold material, observed with reference to the internal ridges (Figure 3.59), appeared at a time point (>28 days) that was comparable with timelines from literature [21, 273] and *in vitro* results from the current project (Figure 3.35 from section 3.3.2.3). Several studies have concluded that the hydrolytic degradation rates for PCL scaffolds were indistinguishable between *in vitro* and *in vivo* [410, 411] while others suggested that degradation occurred faster *in vivo* due to its unique dynamics and enzymatic environment [108]. Nevertheless, a mass and molecular weight loss of ~20% (own data, section 3.3.2.3) and >56% (literature [21, 273]) was anticipated for three months of *in vivo* DP scaffold degradation.

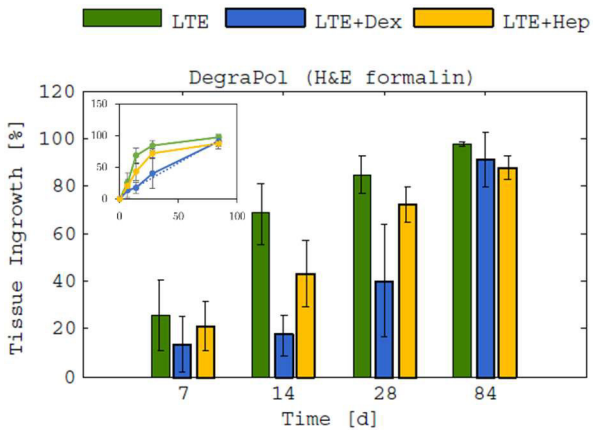

Figure 3.61: Tissue ingrowth of degradable implant groups. Graph insert: scaled x-y plot of tissue ingrowth.

3.3.5.2 Collagen density

Representative Picrosirius Red (PSR) micrographs for the degradable implant groups are shown in Figure 3.62 for 7, 14, 28 and 84 days (collagen is represented by the red areas). There were no significant differences of collagen density between the degradable implant groups at any of the measured time points (P>0.1). Collectively, the percentage of collagen area per tissue area increased at rate of approximately 6%/week

between 7 and 28 days (3-23%) and slowed down to 1.3%/week between 28 and 84 days respectively (23-33%, Figure 3.63).

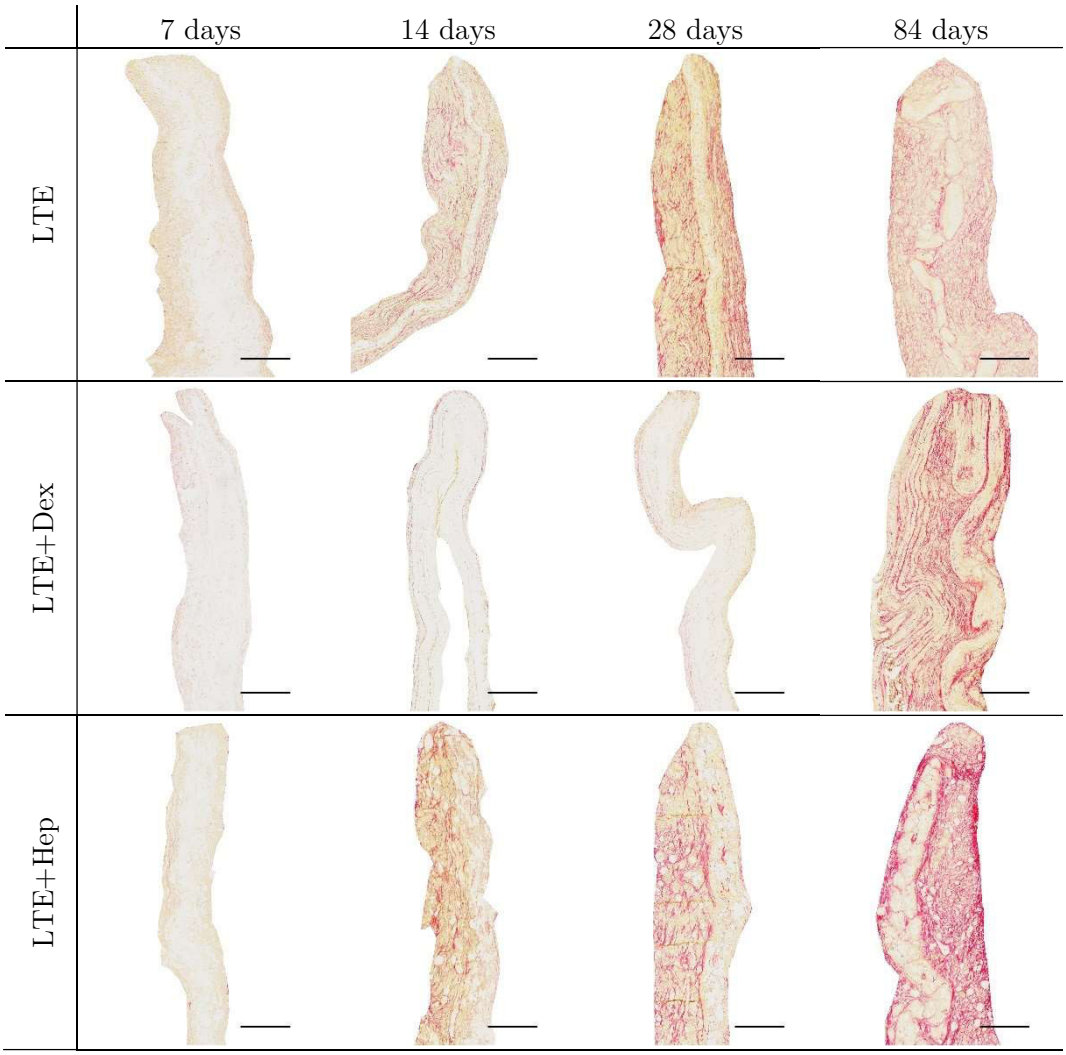

Figure 3.62: Representative PSR micrographs of degradable implant groups. Scale bars at 500 µm.

A lower collagen density would have been expected for scaffolds releasing dexamethasone due to the anti-inflammatory agent's ability to supress the infiltration of host immune cells and thereby, moderate collagen deposition [314]. This would have hold true given that inflammatory cells, i.e. activated macrophages, secrete cytokines such as monocyte chemoattractant protein-1 (MCP-1) that are known for the recruitment of host monocytes and thereby promoting EC, SMC, elastin and collagen formation [30, 238, 412, 413]. Although similar outcome was expected for the current case study, the collagen densities for the LTE+Dex scaffolds were not significantly lower and can therefore not draw the same conclusions. Nevertheless, the overall

deposited collagen was observed to be well organised and showed minimal signs of scar tissue formation - only near the fused ridges that were formed during the LTE process (as shown in Figure 3.62).

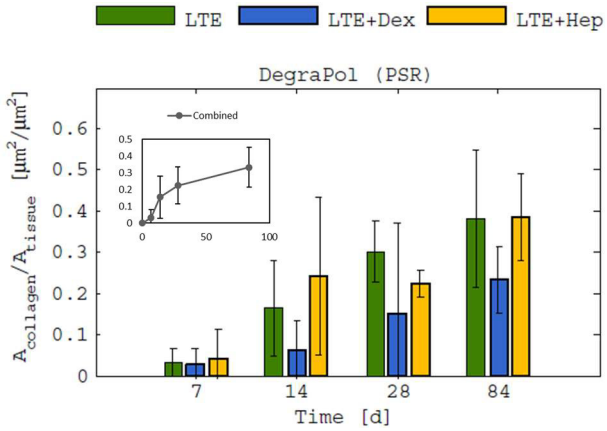

Figure 3.63: Collagen deposition of degradable implant groups.Graph insert: x-y plot representing the combined collagen density of all groups.

3.3.5.3 Cellular density

Representative ED1$^+$ micrographs for the degradable implant groups are shown in Figure 3.64 for 28 and 84 days respectively (blue = nuclei, red = macrophages).

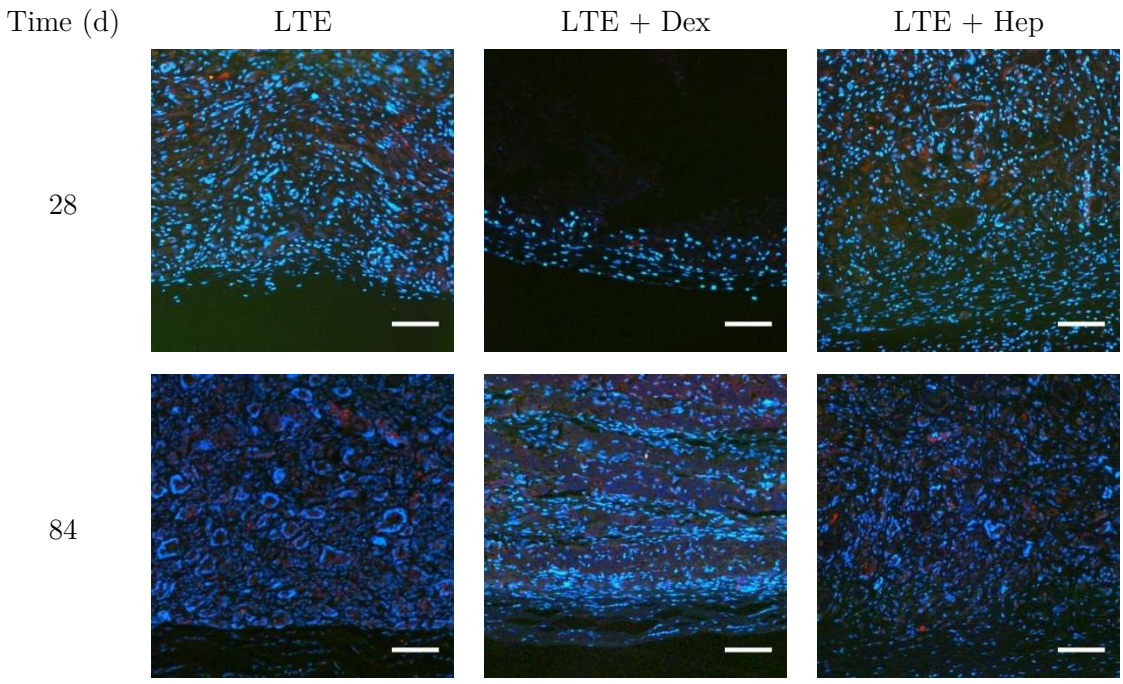

Figure 3.64: Representative ED1 micrographs of degradable implant groups. Scale bars are 100 µm

The DAPI area per measured tissue area (A_{DAPI}/A_{tissue}) within the degradable scaffold groups were similar at each of the measured time points (P>0.1, Figure 3.65). The

cellularity of heparin incorporated scaffolds was twice as high on 28 days (0.35±0.1 $\mu m^2/\mu m^2$) compared to that at 84 days (0.17±0.1 $\mu m^2/\mu m^2$, $P<0.05$), while the density for the other groups were relatively constant over time ($P>0.3$). The nuclei count per A_{tissue} was constant (on average 3025±380 nuclei/mm^2) for each degradable group over both time points (28 and 84 days, $P>0.4$) and was also comparable within the groups ($P>0.1$).

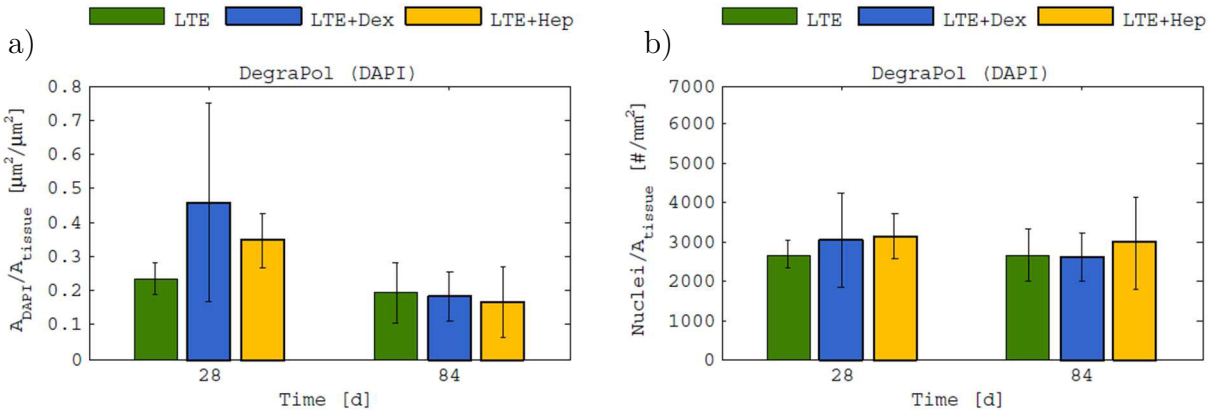

Figure 3.65: Cellular density of degradable implant groups. Cellular density in a) area and in b) number.

An overal cellularity of 3000 nuceli/mm^2 obtained by LTE scaffolds, with or without drugs, is comparable to that of the high-porosity Pel groups developed in this project as well as other porosity-enhanced scaffolds from literature (as explained in section 3.2.5.3). Moreover, maintaining a healthy cellular density over a prolonged period of three months is not only essential for implant survival but also beneficial towards scaffold degradation [238].

3.3.5.4 Macrophage density

The quantified macrophage densities are presented in Figure 3.66 from the positively stained ED1 areas (examples are shown in Figure 3.64). There were no differences in $ED1^+$ area (A_{ED1^+}) nor the number of macrophage per tissue area (A_{tissue}) between any of the degradable groups at any of the measured time points ($P>0.2$). Although all groups appeared to have a decline in macrophage density over time (28 compared to 84 days), only dexamethasone incorporated scaffolds had slightly lower densities (0.105±0.108 $\mu m^2/\mu m^2$ | 765±678/mm^2 compared to 0.006±0.011 $\mu m^2/\mu m^2$ |

48±64/mm², P<0.05) while LTE and LTE+Hep had no differences between the time points (P>0.1). Collectively, macrophage density for all three groups was 0.1 µm²/µm² | 590 macrophages/mm² at 28 days and 0.01 µm²/µm² | 113 macrophages/mm² at 84 days respectively.

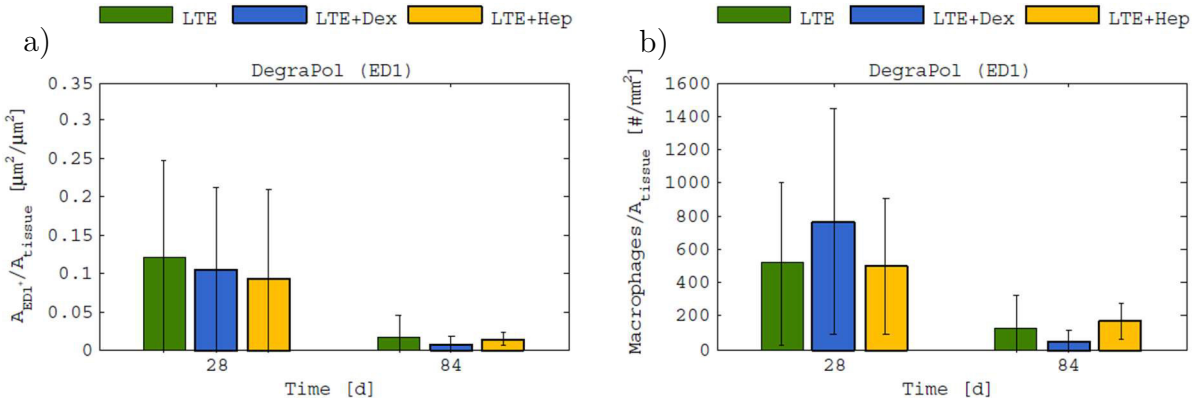

Figure 3.66: Macrophages per tissue area of degradable implant groups. Macrophage density in a) area and in b) number.

The density of infiltrated inflammatory cells, macrophages in particular, is an acceptable indication of foreign body response towards TE scaffolds [55, 239, 292, 414]. A higher density of activated macrophages, in general terms, has been associated with a greater immune response. Vacanti *et al.* have shown that the localised delivery of Dex (at a total load of 5.7wt%) from PCL or PLLA electrospun scaffolds were able to reduce the foreign body response (a lower macrophage density followed by a thinner fibrous capsule) in a rat subcutaneous model [239]. The quantification of macrophages for the current Dex releasing scaffolds (LTE+Dex) was unable to produce a similar outcome. Sample variation and/or the time frame selected for quantification (inability to measure earlier time points, <28 days, due to minimal tissue ingrowth - Figure 3.59) were possible limitations for not being able to show a significant *in vivo* effect of localised dexamethasone delivery. Despite its mentioned influence of moderating inflammation [288, 289], heparin releasing scaffolds did not affect the foreign body response, in terms of macrophage density, in the current case study nor in did it in a previous study of heparinised PU foams [292].

3.3.5.5 Vascular density

Representative CD31$^+$ (the dark areas are endothelial cells) micrographs for the degradable implant groups are shown in Figure 3.67 for 28 and 84 days respectively. The red line indicates the base of the scaffold for LTE+Dex at 28 days when tissue ingrowth was limited to the scaffold boundaries.

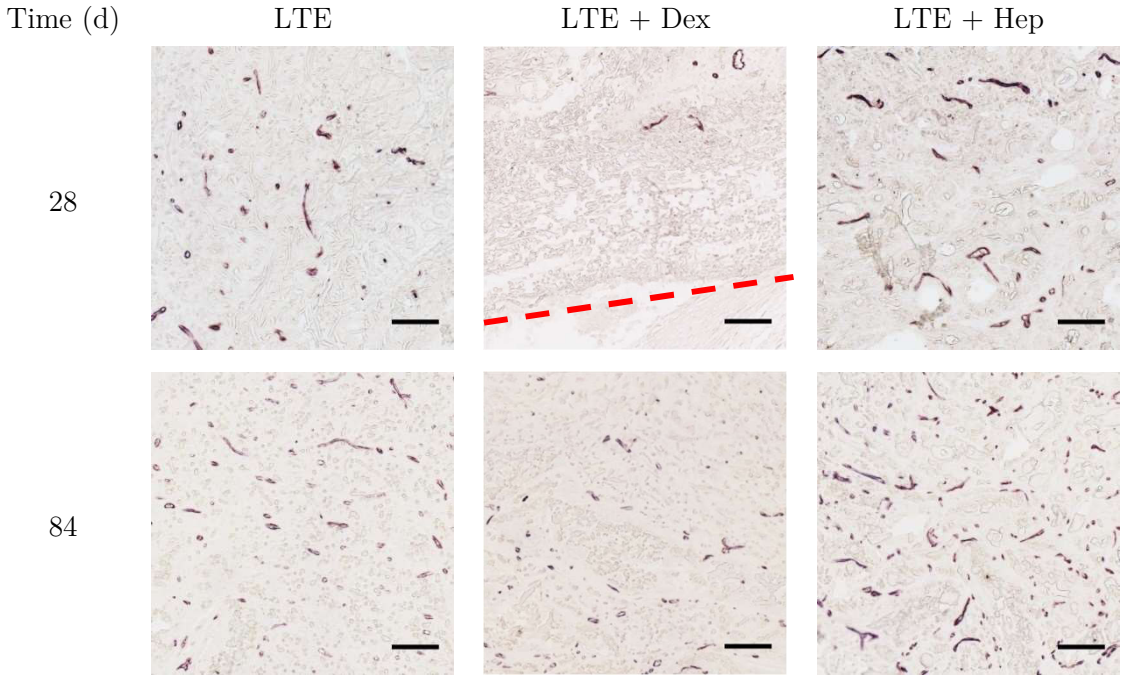

Figure 3.67: Representative CD31 micrographs of degradable implant groups. Scale bars are 100 µm. The red line indicates the scaffold boundary.

The vessel area ($A_{vessels}/A_{tissue}$) of LTE, LTE+Dex and LTE+Hep scaffolds were not significantly different at 28 days of implantation ($P>0.1$, Figure 3.68). At the end-point (84 days), the vessel area for the heparin incorporated scaffolds (0.053±0.01 µm²/µm²) was nearly twice as high as that of the control groups (0.028±0.01 µm²/µm², $P<0.01$) and 4 times higher than the dexamethasone incorporated scaffolds (0.013±0.01 µm²/µm², $P<0.01$). LTE+Dex was significantly lower than LTE ($P<0.01$). LTE+Hep was the only group that obtained a significantly higher vessel area over time (from 28 to 84 days, $P<0.01$).

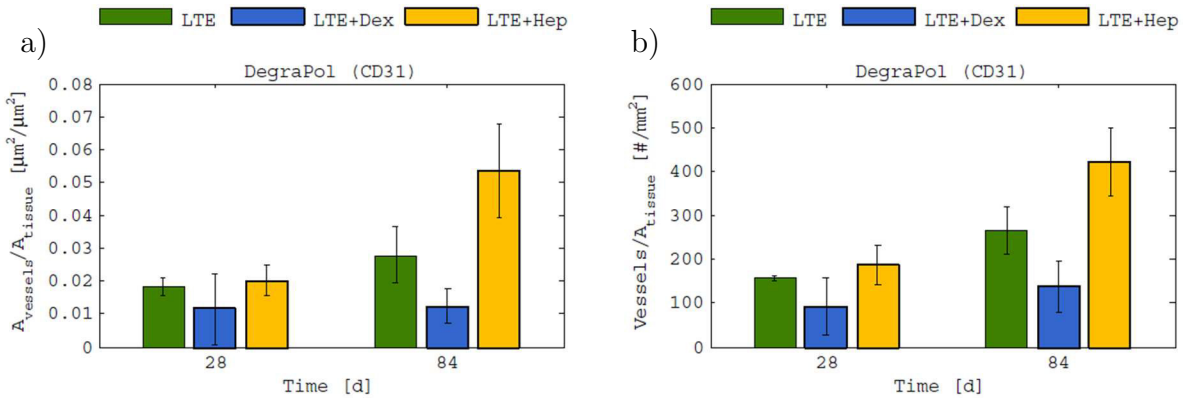

Figure 3.68: Blood vessels per tissue area of degradable implant groups. Vascular density in a) area and in b) number.

Heparin is known for enhancing the vascularisation process [290–293]. The presence of heparin inside LTE+Hep scaffolds did eventually highlight this effect, although not significant at 28 days, by producing enhanced vascular densities at the final time point. This was most likely due to heparin's ability to bind to proangiogenic growth factors (such as bFGF and VEGF) which in turn, were able to form more endothelial cells inside the scaffolds. Besides being a potent anti-inflammatory agent, dexamethasone releasing scaffolds have been recognised to also exhibit anti-angiogenic effects [415, 416]. Although the results from the previous section (3.3.5.4) did not show the anti-inflammatory effects of Dex, a secondary *in vivo* effect was confirmed by the reduced vascularisation of LTE+Dex scaffolds at the final time point. Nevertheless, this outcome was anticipated due to a theoretical decline in available proangiogenic growth factors as a result of less infiltrating inflammatory cells (i.e. macrophages).

4 Conclusion

In this chapter, conclusions are formulated for the investigations that led to the development of biostable and biodegradable TE scaffolds respectively:

Development of biostable electrospun scaffolds:

- Optimal conditions to successfully electrospin fibres (biostable, Pel) and electrospray particles (water-soluble, PEG) were established. As expected, electrospinning at a higher flow rate produced thicker fibres while speeding up the collector improved fibre alignment (and the mechanical strength in the circumferential direction). Selecting a solvent with a low dielectric constant and increasing the solution concentration resulted in the desired increase in diameter of electrosprayed particles. Increasing molecular weight on the other hand, had a limited effect on particle size as short strand fibres would be produced beyond a certain level. Interestingly, electrospraying at close distances (using conditions presented in this project) also altered the morphology of particles from microspheres to short strand fibres. Such geometries may be useful for future drug delivery and further TE developments.
- A combined electrospinning and electrospraying technique was used to increase the porosity of conventional electrospun scaffolds (<80%, LP). Selective removal of 30 µm porogens (electrosprayed from a triple array of spinnerets) from its original composite material of 2 µm fibres (produced by simultaneous electrospinning from a single source) was found to be an effective strategy to produce highly porous scaffolds (>90%, HP).
- Furthermore, heparin (Hep) was successfully immobilised by hydrogel grafting and covalent attachment to fibre surfaces of the high-porosity scaffolds (HP+Hep).
- Porosity-enhanced scaffolds were found to be mechanically weaker and less stiff

in both testing directions than the LP groups, but preserved sufficient structural integrity. The heparinisation process slightly reduced scaffold porosity, increased the average fibre diameter and result in a more rigid scaffold (fibres also appeared to be bonded at fibre-fibre interfaces) compared to an un-heparinised counterpart. Although both LP and HP groups had similar orientation indices and 2D pore sizes, fibres of HP scaffolds were observed to be individually 3D shaped 'wave like' (a similarity to actual ECM) due to the inclusion and removal of 30 µm spheres, rather than straight (as were the case for LP groups).

- The healing response towards biostable scaffolds presented in this project (LP, HP and HP+Hep) were evaluated in a rat subcutaneous implantation model for 7, 14, 28 and 84 days. Cellular infiltration into the HP groups was significantly improved with respect to the limited tissue ingrowth observed for LP scaffolds even after three months of implantation. This outcome is believed to be due to the additional pores created by the removal of 30µm porogens that was not only responsible for i) the architecture that facilitated cells to penetrate the entirety of the scaffold, but also ii) providing enough inter-fibre spaces for effective diffusion of nutrients and cellular waste that ensured long-term cellular survival. With regards to HP+Hep, the observed retardation of early tissue ingrowth, and the consequent delayed vascularisation, may have been the result of fibre-fibre bonds that impaired initial cellular infiltration. Heparinising high-porosity scaffolds did not further improve healing (especially in terms of vascularisation), but such TE scaffolds may be useful for applications such as vascular grafts or heart valves where anti-thrombotic surfaces are desirable. Nevertheless, the combined electrospinning and electrospraying technique presented in this project has much potential to produce TE scaffolds with improved healing capabilities.

<u>Development of biodegradable electrospun scaffolds:</u>

- In establishing electrospinning conditions for biodegradable fibres (DP), collecting at a higher velocity increased fibre orientation (as with Pel). Moreover, fibre

diameter correlated directly with solution concentration and indirectly with solvent conductivity.

- Decreasing the size of the base electrode (e.g. 80 mm^2 instead of 3600 mm^2) was observed to reduce fibre diameter, increase pore sizes and fibre collection area due to a greater induced electric field (as predicted by mathematical modelling and visualised in 3D field simulations). A size adjustable base electrode may provide tissue engineers with additional control over the electrospinning process for future TE scaffold developments.
- The addition of HFIP (required as a co-solvent to solubilise heparin in the spinning solution), caused fibres to fuse to adjacent ones. This phenomenon is believed to be a result of delayed HFIP evaporation due to carbonyl-alcohol (polymer-solvent) hydrogen bonding. Low temperature electrospinning (LTE) was used to successfully reduce fibre fusion and increase scaffold porosity and pore sizes.
- Dexamethasone (Dex) was successfully incorporated into biodegradable scaffolds by dissolving the drug in the processing solution prior to low temperature electrospinning (LTE+Dex).
- Hep was modified to its amphiphilic salt of heparin-tributylammonium (HepTBA) to render it soluble in the organic solvent system. This modified Hep retained its *(in vitro)* bioactivity before and after successful inclusion and elution into/from biodegradable scaffolds (LTE+Hep).
- Compared to heparin sodium, HepTBA has shown to have i) no adverse cytotoxic effects during a three-day viability study using rat smooth muscle cells and have ii) similar anti-thrombotic properties at equimolar concentrations using whole human blood.
- The *in vitro* release of incorporated Dex from LTE+Dex followed a near perfect Fickian diffusion model that delivered almost its entire dosage after three months. Release of HepTBA, from LTE+Hep scaffolds, had an initial burst release followed

by a second stage that could be regarded more of a surface modification rather than an elution due to half of its dose still embedded into the scaffolds even after three months of incubation. The distinguishable elution profiles for these drugs may have been due to their vast difference in molecular weight which resulted in different release kinetics (HepTBA, being a much larger molecule than Dex, defused at a slower rate).

- Incorporation of bioactive molecules affects the electrohydrodynamics of the electrospinning process which impacts both scaffold architectural and mechanical properties. A mechanically weaker, less porous scaffold with thinner fibres and consequently, smaller pores can be expected when incorporating either Dex or Hep into DP scaffolds.
- The healing response towards biostable scaffolds (LTE, LTE+Dex and LTE+Hep) were also evaluated in a rat subcutaneous implantation model for 7, 14, 28 and 84 days. Although Dex is an anti-inflammatory agent, the localised delivery of this drug from incorporated scaffolds (LTE+Dex) showed some reduction in cellular infiltration but, had no effect on scaffold inflammation. On the other hand, the localised delivery of Hep from LTE+Hep scaffolds showed a similar tissue ingrowth rate and, an enhanced scaffold vascularisation. Such an effect was as expected due to Hep's known ability to bind to pro-angiogenic growth factors, and thereby, promoting blood vessel formation. This, together with its anti-thrombotic properties, could make LTE+Hep scaffolds especially useful for applications such as vascular grafts and TE heart valves.

5 Recommendations

Although techniques were developed to produce tissue regenerative scaffolds with some success, many unexplored opportunities emerged. Therefore, this chapter provides suggestions for the continuation of the current research with regards to specific sub-topics. The recommendations below are either to improve or expand knowledge towards developing TE scaffolds that would promote ideal device-host integration:

An outlook on electrospraying

- Empirical formulas with parametric inputs (e.g. concentration, molecular weight and solvent properties) could be useful to predict and control PEG porogen sizes. Therefore, the creation of models based on the current scaling laws and validation with a large set of experimental data is recommended.
- Establishing optimal parameters (concentration, molecular weight and solvent system) for various polymers to controllably produce elongated particles (i.e. particles on the verge of electrospinning).
- Investigation of elongated particles as potential drug delivery devices for injectable medicines. Elliptical shaped particles may have the advantage of undergoing fewer collisions in a stream-line circulatory system compared to spherical geometries.
- Using knowledge obtained from this thesis to launch an investigation into short strand fibres as structural reinforcements for implantable TE devices (e.g. the leaflets of heart valves or inside hydrogels).

An outlook on electrospinning

- Studying the effect(s) on scaffold morphology (diameter and pore size) by adjusting the length of the charged needle that is extended beyond the base electrode (expected outcome: a longer needle length should be associated with greater whipping radius). If this is a useful parameter, design a mechanism that

could adjust the length in real-time.

- Building on the simulations (using Coulomb3D) and observations of base electrodes with different surface areas from the current study, investigate the effect(s) of electrode geometry (e.g. squares compared to triangles) and its material selection (e.g. aluminium compared to copper).
- Developing a climate controlled environment (with feedback on temperature and relative humidity) that could improve the reproducibility of the electrospun scaffolds.

Combined electrospinning and electrospraying as a porosity enhancement technique

- Finding the optimal porogen size by the same approach described in this project (suggested range to explore 5-50 µm) that would produce scaffolds with the best healing performances. Healing could be quantified in terms of macrophage (M1/M2) and vascular densities. For example, the optimal porogen size will be one used to created scaffolds with the lowest M1 and highest M2 and vascular densities.

Suggestions for novel DegraPol® TE scaffold developments

- Investigation of a bioactive, composite scaffold of electrospun DP fibres and electrosprayed DP microparticles. In this case, the bioactive agent (e.g. Dex or HepTBA) is incorporated into the particles instead of the fibres. That way, the need for LTE would be eliminated and the scaffold's structural integrity will not be compromised due to fibre-drug incorporation.
- Exploration of DP scaffolds produced by melt electrospinning or melt electrospinning writing (MEW). Among other things, such technologies are attractive due to their no-solvent approach which may accommodate electrospinning of DP fibres.
- Drug incorporation of bioactive agents into the core of DP fibres by co-axial encapsulation. Pilot studies of co-axial electrospinning were explored during this project. A complete needle design with initial results can be used as a starting

point (see hollow fibres as an example in Appendix A10).

On scaffold drug incorporation

- Recommendation of using core-shell DP fibres where HepTBA is incorporated into the shell and Dex inside the core. This way, HepTBA could provide an anti-thrombotic surface and improve healing (as shown in this study) while allowing the release of Dex via diffusion through the wall of the material.
- Investigation of DP or Pel electrospun scaffolds releasing bioactive nitric oxide (NO) for promoting angiogenesis. A comparison study of vascular densities produced by the *in vivo* release of NO compared to HepTBA would be useful information for future developments of producing vascular grafts.
- Investigation of localised Dex delivery at different concentrations to show reduced scaffold inflammation. The current study was unable to show a lower inflammatory response at a load of 5wt%. It is suggested to investigate the release of Dex at a broader range of 3-7wt% (as highlighted in section 1.3.4).

An outlook on the use of HepTBA for TE scaffolds

- Evaluation of the healing responses (including long-term patency rates) of DP electrospun vascular grafts with incorporated HepTBA in a circulatory *in vivo* model using the current load of 5wt%.
- Expanding on the current *in vitro* and *in vivo* success of HepTBA incorporated into electrospun DP scaffolds, this compound could also be explored using different materials (e.g. PCL, PLA or PGS) and other scaffold architectures (e.g. foams/sponges or even hydrogels).

Notes on translating production techniques to develop vascular grafts

- Using the current relationships developed between collecting speed and fibre orientation to downscale the electrospinning process to a smaller diameter collector (2-4 mm). Moreover, the mechanical properties could be optimised to match that of native blood vessels. Alternatively, fibre alignment may also be controlled by adjusting solvent ratios. For example, a higher degree of

anisotropy could be obtained by increasing the co-solvent content of THF or $CHCl_3$ in the case of Pel (THF:DMF) or DP(HFIP:$CHCl_3$).

- Producing vascular grafts by means of LTE. It is proposed to downscale the process by circulating a cold fluid (e.g. ethanol at -70°C) through a narrow tube (<4 mm) instead of using a large, dry ice filled enclosure as the collector. Unlike the current LTE collector, such a design would also ensure un-interrupted LTE for longer periods.
- Investigation of an alternative approach to avoid fusion of neighbouring DP fibres that were electrospun from HFIP:$CHCl_3$ solvent systems. Scaffolds could be collected with a charged fluid bath containing a solvent that is both miscible with HFIP and a DP non-solvent (e.g. water, isopropanol or methanol, Appendix A7). In this case, the HFIP entrapped in the fibres could have a faster diffusion rate towards the collecting fluid than the ambient air (as in conventional collecting) and might not have enough time to re-dissolve the polymer.

6 References

[1] Mann DL, Zipes DP, Libby P, Bonow RO, Braunwald E (2015) *Braunwald's Heart Disease: A Textbook of Cardiovascular Medicine* doi:10.1001/jama.294.3.376-a.

[2] Bovet P, Paccaud F (2012) Cardiovascular Disease and the Changing Face of Global Public Health : A Focus on Low and Middle Income Countries. *Public Health Rev* 33(2):397–415.

[3] Leeder S, et al. (2004) A race against time: the challenge of cardiovascular disease in developing economies. *New York Columbia Univ*.

[4] Go AS, et al. (2013) Heart disease and stroke statistics--2013 update: a report from the American Heart Association. *Circulation* 127(1):e6–e245.

[5] Pinto F, et al. (2016) Barriers to cardiovascular device innovation in Europe. *Eur Heart J* 37(2):140–144.

[6] David AK, Fields SA, Phillips DM, Scherger JE, Taylor RB (2005) *Taylor's Cardiovascular Diseases: A Handbook* (Springer Science & Business Media).

[7] Harlan BJ, Starr A, Harwin F (2012) *Illustrated handbook of cardiac surgery* (Springer Science & Business Media).

[8] Liu SQ (2007) *Bioregenerative engineering: principles and applications* (John Wiley & Sons).

[9] Zilla P, Brink J, Human P, Bezuidenhout D (2008) Prosthetic heart valves: Catering for the few. *Biomaterials* 29(4):385–406.

[10] Goldstein DJ, Oz MC, Rose EA (1998) Implantable left ventricular assist devices. *NEnglJ Med* 339(0028–4793 (Print) LA–eng PT–Historical Article PT–Journal Article PT–Review SB–AIM SB–IM SB–Q):1522–1533.

[11] Zhong L, Gao Y, Xia H, Li X, Wei S (2013) Percutaneous coronary intervention delays pacemaker implantation in coronary artery disease patients with established bradyarrhythmias. *Exp Clin Cardiol* 18(1):17–21.

[12] O'Brien B, Carroll W (2009) The evolution of cardiovascular stent materials and surfaces in response to clinical drivers: A review. *Acta Biomater* 5(4):945–958.

[13] Schwab SJ, Oliver MJ, Suhocki P, McCann R (2001) Hemodialysis arteriovenous access: Detection of stenosis and response to treatment by vascular access blood flow. *Kidney Int* 59(1):358–362.

[14] Kannan RY, Salacinski HJ, Butler PE, Hamilton G, Seifalian AM (2005) Current status of prosthetic bypass grafts: A review. *J Biomed Mater Res - Part B Appl Biomater* 74(1):570–581.

[15] Lysaght MJ, O'Loughlin JA, States U, Product GD, Journal A (2000) Demographic scope and economic magnitude of contemporary organ replacement therapies. *Am Soc Artif Intern Organs J* 46(5):515–521.

[16] Miller LW, Guglin M, Rogers J (2013) Cost of ventricular assist devices can we afford the progress? *Circulation* 127(6):743–748.

[17] Ratner BD (2016) A pore way to heal and regenerate: 21st century thinking on biocompatibility. *Regen Biomater* 3(2):107–110.

[18] Khardori N, Yassien M (1995) Biofilms in device-related infections. *J Ind Microbiol Biotechnol* 15(3):141–147.

[19] Beloin C, Hidalgo NF, Lebeaux D (2017) Understanding biofilm formation in intravascular device - related infections. *Intensive Care Med* 43(3):443–446.

[20] Vorp DA, Maul T, Nieponice A (2005) Molecular aspects of vascular tissue engineering. *Front Biosci* 10:768–789.

[21] Krynauw H, Bruchmüller L, Bezuidenhout D, Zilla P, Franz T (2011) Degradation-induced changes of mechanical properties of an electro-spun polyester-urethane scaffold for soft tissue regeneration. *J Biomed Mater Res B Appl Biomater* 99(2):359–68.

[22] Zilla P, Brink J, Human P, Bezuidenhout D (2008) Prosthetic heart valves: Catering for the few. *Biomaterials* 29(4):385–406.

[23] Gaspardone A, Versaci F (2005) Coronary stenting and inflammation. *Am J Cardiol* 96(12A):65L–70L.

[24] Kornowski R, et al. (1998) In-stent restenosis: Contributions of inflammatory responses and arterial injury to neointimal hyperplasia. *J Am Coll Cardiol* 31(1):224–230.

[25] Daebritz SH (2003) Introduction of a Flexible Polymeric Heart Valve Prosthesis With Special Design for Mitral Position. *Circulation* 108(90101):134II--139.

[26] Bezuidenhout D, Williams DF, Zilla P (2015) Polymeric heart valves for surgical implantation, catheter-based technologies and heart assist devices. *Biomaterials* 36:6–25.

[27] Remes A, Williams DF (1992) Immune response in biocompatibility. *Biomaterials* 13(11):731–743.

[28] Bryers JD, Giachelli CM, Ratner BD (2012) Engineering biomaterials to integrate and heal: The biocompatibility paradigm shifts. *Biotechnol Bioeng* 109(8):1898–1911.

[29] Zilla P, Bezuidenhout D, Human P (2007) Prosthetic vascular grafts: wrong models, wrong questions and no healing. *Biomaterials* 28(34):5009–27.

[30] Anderson JM, Rodriguez A, Chang DT (2008) Foreign body reaction to biomaterials. *Semin Immunol* 20(2):86–100.

[31] Morais JM, Papadimitrakopoulos F, Burgess DJ (2010) Biomaterials/Tissue Interactions: Possible Solutions to Overcome Foreign Body Response. *AAPS J* 12(2):188–196.

[32] Williams DF (2008) On the mechanisms of biocompatibility. *Biomaterials* 29(20):2941–2953.

[33] Anderson JM, Langone JJ (1999) Issues and perspectives on the biocompatibility and immunotoxicity evaluation of implanted controlled release systems. *J Control Release* 57(2):107–113.

[34] Williams DF (2009) On the nature of biomaterials. *Biomaterials* 30(30):5897–5909.

[35] Lanza R, Langer R, Vacanti JP (2011) *Principles of tissue engineering* (Academic press).

[36] Bezuidenhout D, Davies N, Zilla P (2002) Effect of well defined dodecahedral porosity on inflammation and angiogenesis. *ASAIO J* 48(5):465–71.

[37] Ratner BD, Bryant SJ (2004) Biomaterials: Where We Have Been and Where We Are Going. *Annu Rev Biomed Eng* 6(1):41–75.

[38] Murdock MH, Badylak SF (2017) Biomaterials-based In Situ Tissue Engineering. *Curr Opin Biomed Eng* 1:4–7.

[39] Sengupta D, Waldman SD, Li S (2014) From in vitro to in situ tissue engineering. *Ann Biomed Eng* 42(7):1537–1545.

[40] Sartori S, Chiono V, Tonda-Turo C, Mattu C, Gianluca C (2014) Biomimetic polyurethanes in nano and regenerative medicine. *J Mater Chem B* 2(32):5128.

[41] Li J, Connell S, Shi R (2010) Biomimetic Architectures for Tissue Engineering. *Biomimetics Learning from Nature*, pp 487–507.

[42] Dohmen PM, et al. (2007) Mid-Term Clinical Results Using a Tissue-Engineered Pulmonary Valve to Reconstruct the Right Ventricular Outflow Tract During the Ross Procedure. *Ann Thorac Surg* 84(3):729–736.

[43] Dohmen PM, Lembcke A, Hotz H, Kivelitz D, Konertz WF (2002) Ross operation with a tissue-engineered heart valve. *Ann Thorac Surg* 74(5):1438–1442.

[44] Dohmen PM, Lembcke A, Holinski S, Pruss A, Konertz W (2011) Ten Years of Clinical Results With a Tissue-Engineered Pulmonary Valve. *Ann Thorac Surg* 92(4):1308–1314.

[45] Cebotari S, et al. (2006) Clinical application of tissue engineered human heart valves using autologous progenitor cells. *Circulation* 114(SUPPL. 1):132–138.

[46] Shinoka T, Breuer C (2008) Tissue-engineered blood vessels in pediatric cardiac surgery. *Yale J Biol Med* 81(4):161–6.

[47] Naito Y, et al. (2003) Successful clinical application of tissue-engineered graft for extracardiac Fontan operation. *J Thorac Cardiovasc Surg* 125(2):419–420.

[48] Sands RW, Mooney DJ (2007) Polymers to direct cell fate by controlling the microenvironment. *Curr Opin Biotechnol* 18(5):448–453.

[49] Ingber DE (2008) Tensegrity-based mechanosensing from macro to micro. *Prog Biophys Mol Biol* 97(2–3):163–179.

[50] Langer R, Tirrell DA (2004) Designing materials for biology and medicine. *Nature* 428(6982):487–492.

[51] Daley WP, Peters SB, Larsen M (2008) Extracellular matrix dynamics in development and regenerative medicine. *J Cell Sci* 121(3):255–264.

[52] Haas KS, Phillips SJ, Comerota AJ, White J V (1991) The architecture of adventitial elastin in the canine infrarenal aorta. *Anat Rec* 230(1):86–96.

[53] Ye X, Zhao Q, Sun X, Li H (2009) Enhancement of mesenchymal stem cell attachment to decellularized porcine aortic valve scaffold by in vitro coating with antibody against CD90: a preliminary study on antibody-modified tissue-engineered heart valve. *Tissue Eng Part A* 15(1):1–11.

[54] Song W, Mitchell GR, Burugapalli K (2015) Electrospinning for Medical Applications. *Electrospinning: Principles, Practice and Possibilities*, pp 214–252.

[55] Bezuidenhout D, Davies N, Zilla P (2002) Effect of well defined dodecahedral porosity on inflammation and angiogenesis. *ASAIO J* 48(5):465–71.

[56] Zhang F, et al. (2011) Fabrication of gelatin-hyaluronic acid hybrid scaffolds with tunable porous structures for soft tissue engineering. *Int J Biol Macromol* 48(3):474–81.

[57] Zhang S (2003) Fabrication of novel biomaterials through molecular self-assembly. *Nat Biotechnol* 21(10). doi:10.1038/nbt874.

[58] Yoon JJ, Park TG (2001) Degradation behaviors of biodegradable macroporous scaffolds prepared by gas foaming of effervescent salts. *J Biomed Mater Res* 55(3):401–408.

[59] Hou Q, Grijpma DW, Feijen J (2003) Porous polymeric structures for tissue engineering prepared by a coagulation, compression moulding and salt leaching technique. *Biomaterials* 24(11):1937–1947.

[60] Zhu M, et al. (2014) Fabrication of highly interconnected porous silk fibroin scaffolds for potential use as vascular grafts. *Acta Biomater* 10:2014–2023.

[61] Park A, Griffith LG (1998) Integration of surface modification and 3D fabrication techniques to prepare patterned poly(L-lactide) substrates allowing regionally selective cell adhesion. *J Biomater Sci Polym Ed* 9(2):89–110.

[62] Lee SJ, et al. (2008) Development of a composite vascular scaffolding system that withstands physiological vascular conditions. *Biomaterials* 29(19):2891–2898.

[63] Kluin J, et al. (2016) In situ heart valve tissue engineering using a bioresorbable elastomeric implant – from material design to 12 months follow-up in sheep. *Biomaterials* submitted:101–117.

[64] Emmert MY, Fioretta ES, Hoerstrup SP (2017) Translational Challenges in Cardiovascular Tissue Engineering. *J Cardiovasc Transl Res* (10):139–149.

[65] Gilbert W (1900) *On the Magnet, Magnetick Bodies also, and on the great magnet the earth; a new Physiology, demonstrated by many arguments & experiments* (Chiswick Press, London).

[66] Koch A, Assis T (2010) *The Experimental and Historical Foundations of Electricity* (C.Roy Keys Inc., Montreal). 1st Ed.

[67] Rayleigh, Lord (1882) On the equilibrium of liquid conducting masses charged with electricity. *London, Edinburgh, Dublin Philos Mag J Sci* 14(87):184–186.

[68] Zeleny J (1914) The electrical discharge from liquid points, and a hydrostatic method of measuring the electric intensity at their surfaces. *Phys Rev* 3(2):69.

[69] Taylor G (1964) Disintegration of water drops in an electric field. *Proceedings of the Royal Society of London A: Mathematical, Physical and Engineering Sciences*, pp 383–397.

[70] Taylor G (1969) Electrically driven jets. *Proc R Soc London* 313(1515):453–475.

[71] Peng S, et al. (2015) Fabrication of Spinel One-Dimensional Architectures by Single-Spinneret Electrospinning for Energy Storage. *ACS Nano* 9(2):1945–1954.

[72] Castellanos A (1998) *Electrohydrodynamics* ed CISM International Center for Mechanical Sciences (Springer, Udine). 380th Ed.

[73] Larrondo L, St John Manley R (1981) Electrostatic fiber spinning from polymer melts. I. Experimental observations on fiber formation and properties. *J Polym Sci Polym Phys Ed* 19(6):909–920.

[74] Larrondo L, St John Manley R (1981) Electrostatic fiber spinning from polymer melts. II. Examination of the flow field in an electrically driven jet. *J Polym Sci Polym Phys Ed* 19(6):921–932.

[75] Larrondo L, St John Manley R (1981) Electrostatic fiber spinning from polymer melts. III. Electrostatic deformation of a pendant drop of polymer melt. *J Polym Sci Polym Phys Ed* 19(6):933–940.

[76] Doshi J, Reneker D (1993) Electrospinning process and applications of electrospun fibers. *… , 1993, Conf Rec 1993 …*:1698–1703.

[77] Reneker DH, Chun I (1999) Nanometre diameter fibres of polymer, produced by electrospinning. *Nanotechnology* 7:216–223.

[78] Reneker DH, Yarin AL, Fong H, Koombhongse S (2000) Bending instability of electrically charged liquid jets of polymer solutions in electrospinning. *J Appl Phys* 87(9):4531.

[79] Yarin a. L, Koombhongse S, Reneker DH (2001) Taylor cone and jetting from liquid droplets in electrospinning of nanofibers. *J Appl Phys* 90(9):4836.

[80] Reneker DH (2004) Darrell H. Reneker Haoqing Hou. doi:10.1081/E-EBBE.

[81] Reneker DH, Yarin AL, Zussman E, Xu H (2007) Electrospinning of Nanofibers from Polymer Solutions and Melts. *Adv Appl Mech* 41. doi:10.1016/S0065-2156(07)41002-X.

[82] Reneker DH, Yarin AL (2008) Electrospinning jets and polymer nanofibers. *Polymer (Guildf)* 49(10):2387–2425.

[83] Theron A, Zussman E, Yarin A (2001) Electrostatic field-assisted alignment of electrospun nanofibres. *Nanotechnology* 384. Available at: http://iopscience.iop.org/0957-4484/12/3/329 [Accessed December 11, 2014].

[84] Theron S a., Zussman E, Yarin a. L (2004) Experimental investigation of the governing parameters in the electrospinning of polymer solutions. *Polymer (Guildf)* 45(6):2017–2030.

[85] Qin XH, Wang SY (2006) Filtration properties of electrospinning nanofibers. *J Appl Polym Sci* 102(2):1285–1290.

[86] Ramakrishna S, et al. (2010) Science and engineering of electrospun nanofibers for advances in clean energy, water filtration, and regenerative medicine. *J Mater Sci* 45(23):6283–6312.

[87] Zucchelli A, Focarete ML, Gualandi C, Ramakrishna S (2011) Electrospun nanofibers for enhancing structural performance of composite materials. *Polym Adv Technol* 22(3):339–349.

[88] Mohrova J, Kalinova K (2012) Different structures of PVA nanofibrous membrane for sound absorption application. *J Nanomater* 2012(643043):1–4.

[89] Pierini F, et al. (2017) Single-Material Organic Solar Cells Based on Electrospun Fullerene-Grafted Polythiophene Nanofibers. *Macromolecules* 50:4972–4981.

[90] Persano L, Camposeo A, Pisignano D (2015) Active polymer nanofibers for photonics, electronics, energy generation and micromechanics. *Prog Polym Sci* 43:48–95.

[91] Sinha-Ray S, Zhang Y, Yarin a. L (2011) Thorny devil nanotextured fibers: The way to cooling rates on the order of 1 kW/cm2. *Langmuir* 27(7):215–226.

[92] Liu Y, Teng H, Hou H, You T (2009) Nonenzymatic glucose sensor based on renewable electrospun Ni nanoparticle-loaded carbon nanofiber paste electrode. *Biosens Bioelectron* 24(11):3329–3334.

[93] Bhardwaj N, Kundu SC (2010) Electrospinning: a fascinating fiber fabrication technique. *Biotechnol Adv* 28(3):325–47.

[94] Gubanska I, et al. (2015) Fabrication of polyurethane and polyurethane based composite fibres by the electrospinning technique for soft tissue engineering of cardiovascular system. *Mater Sci Eng C* 46:166–176.

[95] Ashammakhi N, et al. (2006) Biodegradable nanomats produced by electrospinning: expanding multifunctionality and potential for tissue engineering. *J Nanosci Nanotechnol* 6(9–1):2693–2711.

[96] Hohman MM, Shin M, Rutledge G, Brenner MP (2001) Electrospinning and electrically forced jets. II. Applications. *Phys Fluids* 13(8):2221–2236.

[97] Hohman MM, Shin M, Rutledge G, Brenner MP (2001) Electrospinning and electrically forced jets. I Stability Theory. *Phys Fluids* 13(8):2201–2220.

[98] Sill TJ, von Recum H a (2008) Electrospinning: applications in drug delivery and tissue engineering. *Biomaterials* 29(13):1989–2006.

[99] Reneker DH, Kataphinan W, Theron A, Zussman E, Yarin AL (2002) Nanofiber garlands of polycaprolactone by electrospinning. *Polymer (Guildf)* 43(25):6785–6794.

[100] Kameoka J, Craighead HG (2003) Fabrication of oriented polymeric nanofibers on planar surfaces by electrospinning. *Appl Phys Lett* 83(2):371–373.

[101] Teo W-E, Inai R, Ramakrishna S (2011) Technological advances in electrospinning of nanofibers. *Sci Technol Adv Mater* 12(1):13002.

[102] Greiner A, Wendorff JH (2007) Electrospinning: A fascinating method for the preparation of ultrathin fibers. *Angew Chemie - Int Ed* 46(30):5670–5703.
[103] Mitchell GR (2015) *Electrospinning: principles, practice and possibilities* (Royal Society of Chemistry).
[104] Cipitria a., Skelton a., Dargaville TR, Dalton PD, Hutmacher DW (2011) Design, fabrication and characterization of PCL electrospun scaffolds—a review. *J Mater Chem* 21(26):9419.
[105] Nezarati RM, Eifert MB, Cosgriff-Hernandez E (2013) Effects of humidity and solution viscosity on electrospun fiber morphology. *Tissue Eng Part C Methods* 19(10):810–819.
[106] Lee KH, Kim HY, La YM, Lee DR, Sung NH (2002) Influence of a mixing solvent with tetrahydrofuran and N,N-dimethylformamide on electrospun poly(vinyl chloride) nonwoven mats. *J Polym Sci Part B Polym Phys* 40(19):2259–2268.
[107] Mit-uppatham C, Nithitanakul M, Supaphol P (2004) Ultrafine electrospun polyamide-6 fibers: Effect of solution conditions on morphology and average fiber diameter. *Macromol Chem Phys* 205(17):2327–2338.
[108] Bölgen N, et al. (2005) In vitro and in vivo degradation of non-woven materials made of poly(-caprolactone) nanofibers prepared by electrospinning under different conditions. *J Biomater Sci Polym Edn* 16(12):1537–1555.
[109] Yang F, Murugan R, Wang S, Ramakrishna S (2005) Electrospinning of nano/micro scale poly(l-lactic acid) aligned fibers and their potential in neural tissue engineering. *Biomaterials* 26(15):2603–2610.
[110] Duan B, Dong C, Yuan X, Yao K (2004) Electrospinning of chitosan solutions in acetic acid with poly(ethylene oxide). *J Biomater Sci Polym Ed* 15(6):797–811.
[111] Geng X, Kwon O-H, Jang J (2005) Electrospinning of chitosan dissolved in concentrated acetic acid solution. *Biomaterials* 26(27):5427–32.
[112] Tao J, Shivkumar S (2007) Molecular weight dependent structural regimes during the electrospinning of PVA. *Mater Lett* 61(11–12):2325–2328.
[113] Koski A, Yim K, Shivkumar S (2004) Effect of molecular weight on fibrous PVA produced by electrospinning. *Mater Lett* 58(3–4):493–497.
[114] Deitzel J, Kleinmeyer J, Harris D, Tan NB (2001) The effect of processing variables on the morphology of electrospun nanofibers and textiles. *Polymer (Guildf)* 42:261–272.
[115] Shenoy SL, Bates WD, Frisch HL, Wnek GE (2005) Role of chain entanglements on fiber formation during electrospinning of polymer solutions: good solvent, non-specific polymer–polymer interaction limit. *Polymer (Guildf)* 46(10):3372–3384.
[116] Eda G, Shivkumar S (2007) Bead-to-fiber transition in electrospun polystyrene. *J Appl Polym Sci* 106(1):475–487.
[117] Ferry JD (1980) *Viscoelastic properties of polymers* (John Wiley & Sons).
[118] Eda G, Liu J, Shivkumar S (2007) Solvent effects on jet evolution during electrospinning of semi-dilute polystyrene solutions. *Eur Polym J* 43(4):1154–1167.
[119] Castellanos A (1998) A Survey of Conduction Phenomena in Liquid Dielectrics. *Electrohydrodynamics* (Springer), pp 165–173.
[120] You Y, Lee SJ, Min BM, Park WH (2006) Effect of solution properties on nanofibrous structure of electrospun poly(lactic-co-glycolic acid). *J Appl Polym Sci* 99(3):1214–1221.
[121] Wannatong L, Sirivat A, Supaphol P (2004) Effects of solvents on electrospun polymeric fibers: Preliminary study on polystyrene. *Polym Int* 53(11):1851–1859.
[122] Zuo W, et al. (2005) Experimental study on relationship between jet instability and formation of beaded fibers during electrospinning. *Polym Eng Sci* 45(5):704–709.
[123] Fong H, Chun I, Reneker D (1999) Beaded nanofibers formed during electrospinning. *Polymer (Guildf)* 40:4585–4592.
[124] Son WK, Youk JH, Lee TS, Park WH (2004) The effects of solution properties and polyelectrolyte on electrospinning of ultrafine poly(ethylene oxide) fibers. *Polymer (Guildf)* 45(9):2959–2966.
[125] Sun Z, Deitzel JM, Knopf J, Chen X, Gillespie JW (2012) The effect of solvent dielectric properties on the collection of oriented electrospun fibers. *J Appl Polym Sci* 125(4):2585–2594.
[126] Zeng J, et al. (2003) Biodegradable electrospun fibers for drug delivery. *J Control Release* 92(3):227–231.
[127] Lin T, Wang H, Wang H, Wang X (2004) The charge effect of cationic surfactants on the elimination of fibre beads in the electrospinning of polystyrene. *Nanotechnology* 15(9):1375–1381.
[128] Wade RJ, Burdick JA (2014) Advances in nanofibrous scaffolds for biomedical applications: From electrospinning to self-assembly. *Nano Today* 9(6):722–742.
[129] Tripatanasuwan S, Zhong Z, Reneker DH (2007) Effect of evaporation and solidification of the charged jet in electrospinning of poly(ethylene oxide) aqueous solution. *Polymer (Guildf)* 48(19):5742–5746.
[130] Zong X, et al. (2002) Structure and process relationship of electrospun bioabsorbable nanofiber membranes. *Polymer (Guildf)* 43(16):4403–4412.
[131] Demir MM, Yilgor I, Yilgor E, Erman B (2002) Electrospinning of polyurethane fi bers. *Polymer (Guildf)* 43(11):3303–3309.
[132] Wang C, et al. (2009) Correlation between processing parameters and microstructure of electrospun poly(D,l-lactic acid) nanofibers. *Polymer (Guildf)* 50(25):6100–6110.
[133] Nangrejo M, Bragman F, Ahmad Z, Stride E, Edirisinghe M (2012) Hot electrospinning of polyurethane fibres. *Mater Lett* 68:482–485.
[134] Kidoaki S, Kwon IK, Matsuda T (2006) Structural features and mechanical properties of in situ-bonded meshes of segmented polyurethane electrospun from mixed solvents. *J Biomed Mater Res - Part B Appl Biomater* 76(1):219–229.
[135] Matsuda T, et al. (2005) Mechano-active scaffold design of small-diameter artificial graft made of electrospun segmented polyurethane fabrics. *J Biomed Mater Res - Part A* 73(1):125–131.
[136] Koombhongse S, Liu W, Reneker D (2001) Flat Polymer Ribbons and Other Shapes by Electrospinning. *J Polym Sci Part*

B Polym Phys 39(1):2598–2606.

[137] Comyn J (1997) *Handbook of organic solvent properties* (Arnold, London). 1st Ed. doi:10.1016/S0143-7496(97)88687-3.

[138] Hasan A, et al. (2014) Electrospun scaffolds for tissue engineering of vascular grafts. *Acta Biomater* 10(1):11–25.

[139] Hadjizadeh A, et al. (2015) A review of key challenges of electrospun scaffolds for tissue-engineering applications. *J Tissue Eng Regen Med* 4(7):524–531.

[140] Grasl C, Bergmeister H, Stoiber M, Schima H, Weigel G (2010) Electrospun polyurethane vascular grafts: in vitro mechanical behavior and endothelial adhesion molecule expression. *J Biomed Mater Res A* 93(2):716–23.

[141] Naveen N, et al. (2013) Synthesis of nonwoven nanofibers by electrospinning - A promising biomaterial for tissue engineering and drug delivery. *Polym Polym Compos* 12(7):449–456.

[142] Keun Kwon I, Kidoaki S, Matsuda T (2005) Electrospun nano- to microfiber fabrics made of biodegradable copolyesters: Structural characteristics, mechanical properties and cell adhesion potential. *Biomaterials* 26:3929–3939.

[143] You Y, Min BM, Lee SJ, Lee TS, Park WH (2005) In vitro degradation behavior of electrospun polyglycolide, polylactide, and poly(lactide-co-glycolide). *J Appl Polym Sci* 95(2):193–200.

[144] Deshpande P, et al. (2013) Simplifying corneal surface regeneration using a biodegradable synthetic membrane and limbal tissue explants. *Biomaterials* 34(21):5088–5106.

[145] Jeffries EM, Allen RA, Gao J, Pesce M, Wang Y (2015) Acta Biomaterialia Highly elastic and suturable electrospun poly (glycerol sebacate) fibrous scaffolds. 18:30–39.

[146] Yang L, et al. (2008) Mechanical properties of single electrospun collagen type I fibers. *Biomaterials* 29(8):955–962.

[147] Wnek GE, Carr ME, Simpson DG, Bowlin GL (2003) Electrospinning of nanofiber fibrinogen structures. *Nano Lett* 3(2):213–216.

[148] Wang K, et al. (2013) Creation of macropores in electrospun silk fibroin scaffolds using sacrificial PEO-microparticles to enhance cellular infiltration. *J Biomed Mater Res - Part A* 101:3474–3481.

[149] Jung S, et al. (2012) Thickness and Pore Size Control of Chitin Nanofibers by Ultra-sonication and Its Biological Effect in vitro. *Biomater Res* 16(1):11–18.

[150] Martins A, et al. (2009) Surface modification of electrospun polycaprolactone nanofiber meshes by plasma treatment to enhance biological performance. *Small* 5(10):1195–1206.

[151] Pham QP, Sharma U, Mikos AG (2006) Electrospun poly(epsilon-caprolactone) microfiber and multilayer nanofiber/microfiber scaffolds: characterization of scaffolds and measurement of cellular infiltration. *Biomacromolecules* 7(10):2796–805.

[152] Prabhakaran MP, Venugopal J, Chan CK, Ramakrishna S (2008) Surface modified electrospun nanofibrous scaffolds for nerve tissue engineering. *Nanotechnology* 19(45). doi:10.1088/0957-4484/19/45/455102.

[153] Voorneveld J, Oosthuysen A, Franz T, Zilla P, Bezuidenhout D (2016) Dual electrospinning with sacrificial fibers for engineered porosity and enhancement of tissue ingrowth. *J Biomed Mater Res Part B Appl Biomater*:1–14.

[154] Zhang S, et al. (2009) Gelatin nanofibrous membrane fabricated by electrospinning of aqueous gelatin solution for guided tissue regeneration. *J Biomed Mater Res Part A* 90(3):671–679.

[155] Hardick O, Stevens B, Bracewell DG (2011) Nanofibre fabrication in a temperature and humidity controlled environment for improved fibre consistency. *J Mater Sci* 46(11):3890–3898.

[156] İÇOĞLU Hİ, ĞULATA RT (2017) Effect of ambient parameters on morphology of electrospun polyetherimide (PEI) fibers. *J Text Apparel/Tekstil ve Konfeksiyon* 27(3).

[157] Casper CL, Stephens JS, Tassi NG, Chase DB, Rabolt JF (2004) Controlling Surface Morphology of Electrospun Polystyrene Fibers: Effect of Humidity and Molecular Weight in the Electrospinning Process. *Macromolecules* 37(2):573–578.

[158] Huang L, Bui NN, Manickam SS, McCutcheon JR (2011) Controlling electrospun nanofiber morphology and mechanical properties using humidity. *J Polym Sci Part B Polym Phys* 49(24):1734–1744.

[159] Medeiros ES, Mattoso LHC, Offeman RD, Wood DF, Orts WJ (2008) Effect of relative humidity on the morphology of electrospun polymer fibers. *Can J Chem* 86(6):590–599.

[160] Lee JS, et al. (2004) Role of molecular weight of atactic poly(vinyl alcohol) (PVA) in the structure and properties of PVA nanofabric prepared by electrospinning. *J Appl Polym Sci* 93(4):1638–1646.

[161] Megelski S, Stephens J, Chase D, Rabolt J (2002) Micro-and nanostructured surface morphology on electrospun polymer fibers. *Macromolecules* 35:8456–8466.

[162] Yuan XY, Zhang YY, Dong C, Sheng J (2004) Morphology of ultrafine polysulfone fibers prepared by electrospinning. *Polym Int* 53(11):1704–1710.

[163] Ding W, et al. (2010) Manipulated electrospun PVA nanofibers with inexpensive salts. *Macromol Mater Eng* 295(10):958–965.

[164] Bosworth LA, Downes S (2012) Acetone, a Sustainable Solvent for Electrospinning Poly(-Caprolactone) Fibres: Effect of Varying Parameters and Solution Concentrations on Fibre Diameter. *J Polym Environ* 20(3):879–886.

[165] Wang T, Kumar S (2006) Electrospinning of polyacrylonitrile nanofibers. *J Appl Polym Sci* 102(2):1023–1029.

[166] Heikkilä P, Harlin A (2008) Parameter study of electrospinning of polyamide-6. *Eur Polym J* 44(10):3067–3079.

[167] Zhao S, Wu X, Wang L, Huang Y (2004) Electrospinning of ethyl-cyanoethyl cellulose/tetrahydrofuran solutions. *J Appl Polym Sci* 91(1):242–246.

[168] Zeng J, et al. (2003) Ultrafine fibers electrospun from biodegradable polymers. *J Appl Polym Sci* 89(4):1085–1092.

[169] Thompson CJ, Chase GG, Yarin AL, Reneker DH (2007) Effects of parameters on nanofiber diameter determined from electrospinning model. *Polymer (Guildf)* 48(23):6913–6922.

[170] Cui W, Li X, Zhou S, Weng J (2007) Investigation on process parameters of electrospinning system through orthogonal

experimental design. *J Appl Polym Sci* 103(5):3105–3112.

[171] Macossay J, Marruffo A, Rincon R, Eubanks T, Kuang A (2007) Effect of needle diameter on nanofiber diameter and thermal properties of electrospun poly (methyl methacrylate). *Polym Adv Technol* 18(3):180–183.

[172] Katti DS, Robinson KW, Ko FK, Laurencin CT (2004) Bioresorbable nanofiber-based systems for wound healing and drug delivery: Optimization of fabrication parameters. *J Biomed Mater Res* 70B(2):286–296.

[173] Ki CS, et al. (2005) Characterization of gelatin nanofiber prepared from gelatin-formic acid solution. *Polymer (Guildf)* 46(14):5094–5102.

[174] Zeleny J (1935) The role of surface instability in electrical discharges from drops of alcohol and water in air at atmospheric pressure. *J Franklin Inst* 219(6):659–675.

[175] Pillay V, et al. (2013) A review of the effect of processing variables on the fabrication of electrospun nanofibers for drug delivery applications. *J Nanomater* 2013:22.

[176] Beachley V, Wen X (2009) Effect of electrospinning parameters on the nanofiber diameter and length. *Mater Sci Eng C* 29(3):663–668.

[177] Zargham S, Bazgir S, Tavakoli A, Rashidi AS, Damerchely R (2012) The Effect of Flow Rate on Morphology and Deposition Area of Electrospun Nylon 6 Nanofiber. *J Eng Fiber Fabr* 7(4):42–49.

[178] Milleret V, Simona B, Neuenschwander P, Hall H (2011) Tuning electrospinning parameters for production of 3D-fiber-fleeces with increased porosity for soft tissue engineering applications. *Eur Cell Mater* 21(1473–2262):286–303.

[179] Feltz KP, Kalaf EAG, Chen C, Martin RS, Sell SA (2017) A review of electrospinning manipulation techniques to direct fiber deposition and maximize pore size. *Electrospinning* 1:46–61.

[180] Doustgani A, Vasheghani-Farahani E, Soleimani M (2013) Aligned and random nanofibrous nanocomposite scaffolds for bone tissue engineering. *Nanomedicine J* 1(1):20–27.

[181] McClure MJ, Sell S a, Ayres CE, Simpson DG, Bowlin GL (2009) Electrospinning-aligned and random polydioxanone-polycaprolactone-silk fibroin-blended scaffolds: geometry for a vascular matrix. *Biomed Mater* 4(5):55010.

[182] Thomas V, et al. (2006) Mechano-morphological studies of aligned nanofibrous scaffolds of polycaprolactone fabricated by electrospinning. *J Biomater Sci Polym Ed* 17(9):969–984.

[183] Wang HB, et al. (2009) Creation of highly aligned electrospun poly-L-lactic acid fibers for nerve regeneration applications. *J Neural Eng* 6(1):16001.

[184] Chakraborty S, Liao I-C, Adler A, Leong KW (2009) Electrohydrodynamics: A facile technique to fabricate drug delivery systems. *Adv Drug Deliv Rev* 61(12):1043–54.

[185] Hong Y, Li Y, Yin Y, Li D, Zou G (2008) Electrohydrodynamic atomization of quasi-monodisperse drug-loaded spherical/wrinkled microparticles. *J Aerosol Sci* 39(6):525–536.

[186] Hogan CJ, et al. (2007) Controlled size polymer particle production via electrohydrodynamic atomization. *Colloids Surfaces A Physicochem Eng Asp* 311(1–3):67–76.

[187] Xie J, Lim LK, Phua Y, Hua J, Wang CH (2006) Electrohydrodynamic atomization for biodegradable polymeric particle production. *J Colloid Interface Sci* 302(1):103–112.

[188] Gañán-Calvo AM, Dávila J, Barrero A (1997) Current and droplet size in the electrospraying of liquids. Scaling laws. *J Aerosol Sci* 28(2):249–275.

[189] Almería B, Deng W, Fahmy TM, Gomez A (2010) Controlling the morphology of electrospray-generated PLGA microparticles for drug delivery. *J Colloid Interface Sci* 343:125–133.

[190] Yao J, Kuang Lim L, Xie J, Hua J, Wang C-H (2008) Characterization of electrospraying process for polymeric particle fabrication. *J Aerosol Sci* 39(11):987–1002.

[191] Almería B, Gomez A (2014) Electrospray synthesis of monodisperse polymer particles in a broad (60nm-2 m) diameter range: Guiding principles and formulation recipes. *J Colloid Interface Sci* 417:121–130.

[192] Zhang X, Reagan MR, Kaplan DL (2009) Electrospun silk biomaterial scaffolds for regenerative medicine. *Adv Drug Deliv Rev* 61(12):988–1006.

[193] Pham QP, Sharma U, Mikos AG (2006) Electrospinning of polymeric nanofibers for tissue engineering applications: a review. *Tissue Eng* 12(5):1197–211.

[194] Barnes CP, Sell SA, Boland ED, Simpson DG, Bowlin GL (2007) Nanofiber technology: Designing the next generation of tissue engineering scaffolds. *Adv Drug Deliv Rev* 59(14):1413–1433.

[195] Liao S, et al. (2006) Biomimetic electrospun nanofibers for tissue regeneration. *Biomed Mater* 1(3). doi:10.1088/1748-6041/1/3/R01.

[196] Qin Y (2008) Alginate fibers: an overwiew of the production processes and applications in wound management. *Polym Int* 57(April):171–180.

[197] Jafari M, et al. (2015) Polymeric scaffolds in tissue engineering: a literature review. *J Biomed Mater Res Part B Appl Biomater*:n/a-n/a.

[198] Szentivanyi A, Chakradeo T, Zernetsch H, Glasmacher B (2011) Electrospun cellular microenvironments: Understanding controlled release and scaffold structure. *Adv Drug Deliv Rev* 63(4):209–220.

[199] Wu J, Hong Y (2016) Enhancing cell infiltration of electrospun fibrous scaffolds in tissue regeneration. *Bioact Mater* 1(1):56–64.

[200] Zhong S, Zhang Y, Lim CT (2012) Fabrication of Large Pores in Electrospun Nanofibrous Scaffolds for Cellular Infiltration: A Review. *Tissue Eng Part B Rev* 18(2):77–87.

[201] Garg K, Pullen N a., Oskeritzian C a., Ryan JJ, Bowlin GL (2013) Macrophage functional polarization (M1/M2) in response to varying fiber and pore dimensions of electrospun scaffolds. *Biomaterials* 34(18):4439–4451.

[202] Madden LR, et al. (2010) Proangiogenic scaffolds as functional templates for cardiac tissue engineering. *Proc Natl Acad Sci* 107(34):15211–15216.

[203] McClure MJ, Wolfe PS, Simpson DG, Sell SA, Bowlin GL (2012) The use of air-flow impedance to control fiber deposition patterns during electrospinning. *Biomaterials* 33(3):771–779.

[204] Brown BN, Ratner BD, Goodman SB, Amar S, Badylak SF (2012) Macrophage polarization: An opportunity for improved outcomes in biomaterials and regenerative medicine. *Biomaterials* 33(15):3792–3802.

[205] Simonet M, et al. (2014) Tailoring the void space and mechanical properties in electrospun scaffolds towards physiological ranges. *J Mater Chem B* 2(3):305–313.

[206] Chen M, Patra PK, Warner SB, Bhowmick S (2007) Role of Fiber Diameter in Adhesion and Proliferation of NIH 3T3 Fibroblast on Electrospun Polycaprolactone Scaffolds. *Tissue Eng* 13(3):579–587.

[207] Sun B, et al. (2014) Advances in three-dimensional nanofibrous macrostructures via electrospinning. *Prog Polym Sci* 39(5):862–890.

[208] Simonet M, Schneider OD, Neuenschwander P, Stark WJ (2007) Ultraporous 3D Polymer Meshes by Low-Temperature Electrospinning: Use of Ice Crystals as a Removable Void Template. *Polym Degrad Stab* 47(12):2020–2026.

[209] Zander NE, Orlicki J a, Rawlett AM, Beebe TP (2013) Electrospun polycaprolactone scaffolds with tailored porosity using two approaches for enhanced cellular infiltration. *J Mater Sci Mater Med* 24(1):179–87.

[210] Wang Z, et al. (2014) The effect of thick fibers and large pores of electrospun poly(-caprolactone) vascular grafts on macrophage polarization and arterial regeneration. *Biomaterials* 35(22):5700–10.

[211] Tomadakis MM, Robertson TJ (2003) Pore size distribution, survival probability, and relaxation time in random and ordered arrays of fibers. *J Chem Phys* 119(3). doi:10.1063/1.1582431.

[212] Joshi VS, Lei NY, Walthers CM, Wu B, Dunn JCY (2013) Macroporosity enhances vascularization of electrospun scaffolds. *J Surg Res* 183(1):18–26.

[213] Wang Z, et al. (2014) The effect of thick fibers and large pores of electrospun poly(-caprolactone) vascular grafts on macrophage polarization and arterial regeneration. *Biomaterials* 35(22):5700–10.

[214] Ju YM, Choi JS, Atala A, Yoo JJ, Lee SJ (2010) Bilayered scaffold for engineering cellularized blood vessels. *Biomaterials* 31(15):4313–21.

[215] Gu BK, et al. (2013) Fabrication of sonicated chitosan nanofiber mat with enlarged porosity for use as hemostatic materials. *Carbohydr Polym* 97(1):65–73.

[216] Lee JB, et al. (2011) Highly porous electrospun nanofibers enhanced by ultrasonication for improved cellular infiltration. *Tissue Eng Part A* 17(21–22):2695–702.

[217] Ho Y-C, Huang F-M, Chang Y-C (2007) Cytotoxicity of formaldehyde on human osteoblastic cells is related to intracellular glutathione levels. *J Biomed Mater Res B Appl Biomater* 83(2):340–344.

[218] Lee YH, et al. (2005) Electrospun dual-porosity structure and biodegradation morphology of Montmorillonite reinforced PLLA nanocomposite scaffolds. *Biomaterials* 26(16):3165–3172.

[219] Jiang J, et al. (2015) Expanding Two-Dimensional Electrospun Nanofiber Membranes in the Third Dimension by a Modified Gas-Foaming Technique. *ACS Biomater Sci Eng* 1(10):991–1001.

[220] Hwang PTJ, et al. (2016) Poly(-caprolactone)/gelatin composite electrospun scaffolds with porous crater-like structures for tissue engineering. *J Biomed Mater Res - Part A* 104(4):1017–1029.

[221] Choi HW, Johnson JK, Nam J, Farson DF, Lannutti J (2007) Structuring electrospun polycaprolactone nanofiber tissue scaffolds by femtosecond laser ablation. *J Laser Appl* 19(4):225.

[222] Lee BL-P, et al. (2012) Femtosecond Laser Ablation Enhances Cell Infiltration into Three-Dimensional Electrospun Scaffolds. *NIH Public Access* 29(6):997–1003.

[223] Vaquette C, Cooper-White JJ (2011) Increasing electrospun scaffold pore size with tailored collectors for improved cell penetration. *Acta Biomater* 7(6):2544–57.

[224] Zhang K, Wang X, Jing D, Yang Y, Zhu M (2009) Bionic electrospun ultrafine fibrous poly(L-lactic acid) scaffolds with a multi-scale structure. *Biomed Mater* 4(3). doi:10.1088/1748-6041/4/3/035004.

[225] Zhang D, Chang J (2008) Electrospinning of Three-Dimensional Nanofibrous Tubes with Controllable Architectures. *Nano Lett* 8(10):3283–3287.

[226] Maghdouri-White Y, Elmore LW, Bowlin GL, Dréau D (2016) Breast epithelial cell infiltration in enhanced electrospun silk scaffolds. *J Tissue Eng Regen Med* 10(2).

[227] Ki CS, et al. (2008) Development of 3-D nanofibrous fibroin scaffold with high porosity by electrospinning: Implications for bone regeneration. *Biotechnol Lett* 30(3):405–410.

[228] Guo C, Zhou L, Lv J (2013) Effects of expandable graphite and modified ammonium polyphosphate on the flame-retardant and mechanical properties of wood flour-polypropylene composites. *Polym Polym Compos* 21(7):449–456.

[229] Ionescu LC, Lee GC, Sennett BJ, Burdick J a, Mauck RL (2010) An anisotropic nanofiber/microsphere composite with controlled release of biomolecules for fibrous tissue engineering. *Biomaterials* 31(14):4113–20.

[230] Whited BM, Whitney JR, Hofmann MC, Xu Y, Rylander MN (2011) Pre-osteoblast infiltration and differentiation in highly porous apatite-coated PLLA electrospun scaffolds. *Biomaterials* 32(9):2294–304.

[231] Ifkovits JL, Wu K, Mauck RL, Burdick J a (2010) The influence of fibrous elastomer structure and porosity on matrix organization. *PLoS One* 5(12):e15717.

[232] Baker BM, et al. (2008) The potential to improve cell infiltration in composite fiber-aligned electrospun scaffolds by the selective removal of sacrificial fibers. *Biomaterials* 29(15):2348–58.

[233] Wang K, et al. (2014) Improvement of cell infiltration in electrospun polycaprolactone scaffolds for the construction of

vascular grafts. *J Biomed Nanotechnol* 10(8):1588–1598.

[234] Kim TG, Chung HJ, Park TG (2008) Macroporous and nanofibrous hyaluronic acid/collagen hybrid scaffold fabricated by concurrent electrospinning and deposition/leaching of salt particles. *Acta Biomater* 4(6):1611–1619.

[235] Nam J, Huang Y, Agarwal S, Lannutti J (2007) Improved Cellular Infiltration in Electrospun Fiber via Engineered Porosity. *Tissue Eng* 13(9):2249–2257.

[236] Leong MF, Rasheed MZ, Lim TC, Chian KS (2009) In vitro cell infiltration and in vivo cell infiltration and vascularization in a fibrous, highly porous poly(D,L-lactide) scaffold fabricated by cryogenic electrospinning technique. *J Biomed Mater Res - Part A* 91(1):231–240.

[237] Leong MF, Chan WY, Chian KS, Rasheed MZ, Anderson JM (2010) Fabrication and in vitro and in vivo cell infiltration study of a bilayered cryogenic electrospun poly(D,L-lactide) scaffold. *J Biomed Mater Res A* 94(4):1141–9.

[238] Wang K, et al. (2016) Three-Layered PCL Grafts Promoted Vascular Regeneration in a Rabbit Carotid Artery Model. *Macromol Biosci* 16(4):608–918.

[239] Vacanti NM, et al. (2012) Localized delivery of dexamethasone from electrospun fibers reduces the foreign body response. *Biomacromolecules* 13(10):3031–3038.

[240] Chew SY, Wen Y, Dzenis Y, Leong KW (2006) The role of electrospinning in the emerging field of nanomedicine. *Curr Pharm Des* 12(36):4751–4770.

[241] Luu YK, Kim K, Hsiao BS, Chu B, Hadjiargyrou M (2003) Development of a nanostructured DNA delivery scaffold via electrospinning of PLGA and PLA-PEG block copolymers. *J Control Release* 89:341–353.

[242] Sahoo S, Ang LT, Goh JC-H, Toh S-L (2009) Growth factor delivery through electrospun nanofibers in scaffolds for tissue engineering applications. *J Biomed Mater Res Part A* 93(4):1539–1550.

[243] Luong-Van E, et al. (2006) Controlled release of heparin from poly(epsilon-caprolactone) electrospun fibers. *Biomaterials* 27(9):2042–50.

[244] Martins A, et al. (2010) Osteogenic induction of hBMSCs by electrospun scaffolds with dexamethasone release functionality. *Biomaterials* 31(22):5875–5885.

[245] Qi H, Hu P, Xu J, Wang A (2006) Encapsulation of drug reservoirs in fibers by emulsion electrospinning: morphology characterization and preliminary release assessment. *Biomacromolecules* 7(8):2327–30.

[246] Nguyen TTT, Ghosh C, Hwang S-G, Chanunpanich N, Park JS (2012) Porous core/sheath composite nanofibers fabricated by coaxial electrospinning as a potential mat for drug release system. *Int J Pharm* 439(1–2):296–306.

[247] Jiang H, et al. (2005) A facile technique to prepare biodegradable coaxial electrospun nanofibers for controlled release of bioactive agents. *J Control Release* 108:237–243.

[248] Huang Z-M, et al. (2006) Encapsulating drugs in biodegradable ultrafine fibers through co-axial electrospinning. *J Biomed Mater Res A* 77(1):169–79.

[249] Jiang Y-N, Mo H-Y, Yu D-G (2012) Electrospun drug-loaded core-sheath PVP/zein nanofibers for biphasic drug release. *Int J Pharm* 438(1–2):232–9.

[250] Yoo HS, Kim TG, Park TG (2009) Surface-functionalized electrospun nanofibers for tissue engineering and drug delivery. *Adv Drug Deliv Rev* 61(12):1033–1042.

[251] Khan I, Smith N, Jones E, Finch DS, Elizabeth R (2005) Analysis and evaluation of a biomedical polycarbonate urethane tested in an in vitro study and an ovine arthroplasty model . Part I : materials selection and evaluation. *Biomaterials* 26:621–631.

[252] Cooper SL, Guan J (2016) *Advances in Polyurethane Biomaterials* (Woodhead Publishing) doi:10.1017/CBO9781107415324.004.

[253] Reynolds MM, et al. (2006) Nitric oxide releasing polyurethanes with covalently linked diazeniumdiolated secondary amines. *Biomacromolecules* 7(3):987–994.

[254] Pedicini A, Farris RJ (2003) Mechanical behavior of electrospun polyurethane. *Polymer (Guildf)* 44(22):6857–6862.

[255] Theron JP, et al. (2010) Modification, crosslinking and reactive electrospinning of a thermoplastic medical polyurethane for vascular graft applications. *Acta Biomater* 6(7):2434–2447.

[256] Choi WS, et al. (2016) Enhanced Patency and Endothelialization of Small-Caliber Vascular Grafts Fabricated by Coimmobilization of Heparin and Cell-Adhesive Peptides. *ACS Appl Mater Interfaces* 8(7):4336–4346.

[257] Saad B, et al. (1998) Degradable and highly porous polyesterurethane foam as biomaterial: Effects and phagocytosis of degradation products in osteoblasts. *J Biomed Mater Res* 39(4):594–602.

[258] Borkenhagen M, Stoll RC, Neuenschwander P, Suter UW, Aebischer P (1998) In vivo performance of a new biodegradable polyester urethane system used as a nerve guidance channel. *Biomaterials* 19(23):2155–2165.

[259] Lendlein A, Neuenschwander P, Suter UW (1998) Tissue-compatible multiblock copolymers for medical applications, controllable in degradation rate and mechanical properties. *Macromol Chem Phys* 199:2785–2796.

[260] Lendlein A, Colussi M, Neuenschwander P, Suter UW (2001) Hydrolytic Degradation of Phase-Segregated Multiblock Copoly (ester urethane) s Containing Weak Links. *Macromol Chem Phys* 202(13):2702–2711.

[261] A. Henry J, Simonet M, Pandit A, Neuenschwander P (2007) Characterization of a slowly degrading biodegradable polyesterurethane for tissue engineering scaffolds. *J Biomed Mater Res A* 81(3):669–679.

[262] Evrova O, et al. (2016) Bioactive, Elastic, and Biodegradable Emulsion Electrospun DegraPol Tube Delivering PDGF-BB for Tendon Rupture Repair. *Macromol Biosci* DOI: 10.10:1–16.

[263] Riboldi S a., Sampaolesi M, Neuenschwander P, Cossu G, Mantero S (2005) Electrospun degradable polyesterurethane membranes: Potential scaffolds for skeletal muscle tissue engineering. *Biomaterials* 26(22):4606–4615.

[264] Riboldi S a, et al. (2008) Skeletal myogenesis on highly orientated microfibrous polyesterurethane scaffolds. *J Biomed Mater*

Res A 84(4):1094–101.

[265] Brizzola S, et al. (2009) Morphologic features of biocompatibility and neoangiogenesis onto a biodegradable tracheal prosthesis in an animal model. *Interact Cardiovasc Thorac Surg* 8(6):610–614.

[266] Acocella F, Brizzola S (2011) *Electrospinning for Tissue Regeneration* doi:10.1533/9780857092915.2.168.

[267] Milleret V, Simonet M, Bittermann AG, Neuenschwander P, Hall H (2009) Cyto- and hemocompatibility of a biodegradable 3D-scaffold material designed for medical applications. *J Biomed Mater Res - Part B Appl Biomater* 91(1):109–121.

[268] Milleret V, Hefti T, Hall H, Vogel V, Eberli D (2012) Influence of the fiber diameter and surface roughness of electrospun vascular grafts on blood activation. *Acta Biomater* 8(12):4349–56.

[269] Buschmann J, et al. (2013) Cellular response of healing tissue to DegraPol tube implantation in rabbit Achilles tendon rupture repair: An in vivo histomorphometric study. *J Tissue Eng Regen Med* 7(5):413–420.

[270] Meier Bürgisser G, et al. (2014) Prevention of peritendinous adhesions using an electrospun DegraPol polymer tube: a histological, ultrasonographic, and biomechanical study in rabbits. *Biomed Res Int* 2014(656240):11.

[271] Horst M, et al. (2015) Polyesterurethane and acellular matrix based hybrid biomaterial for bladder engineering. *J Biomed Mater Res - Part B Appl Biomater* Early view:1–10.

[272] Buschmann J, et al. (2015) Synthesis, characterization and histomorphometric analysis of cellular response to a new elastic DegraPol® polymer for rabbit Achilles tendon rupture repair. *J Tissue Eng Regen Med* 9(5):584–594.

[273] Limbert G, Omar R, Krynauw H, Bezuidenhout D, Franz T (2016) The anisotropic mechanical behaviour of electro-spun biodegradable polymer scaffolds : Experimental characterisation and constitutive formulation. *J Mech Behav Biomed Mater* 53:21–39.

[274] Lane DA, Ulf L (1989) *Heparin: chemical and biological properties, clinical applications*.

[275] Berry D, et al. (2003) Heparan sulphate glycosaminoglycans derived from endothelial cells and smooth muscle cells differentially modulate fibroblast growth factor-2 biological activity through fibroblast growth factor receptor-1. *BiochemJ* 373:241–249.

[276] Rabenstein DL (2002) Heparin and heparan sulfate: structure and function. *Nat Prod Rep* 19(3):312–331.

[277] Liang Y, Kiick KL (2014) Heparin-functionalized polymeric biomaterials in tissue engineering and drug delivery applications. *Acta Biomater* 10(4):1588–1600.

[278] S S-E (2015) Drug delivery via heparin conjugates. *Comprehensive Biomaterials*, eds Ducheyne P, Healy K, Hutmacher DE, Grainger DW, Kirkpatrick CJ (Newnes).

[279] Petitou M, Casu B, Lindahl U (2003) 1976 – 1983 , a critical period in the history of heparin : the discovery of the antithrombin binding site. *Biochimie* 85:83–89.

[280] Lee J, Yoo JJ, Atala A, Lee SJ (2012) Controlled heparin conjugation on electrospun poly (e-caprolactone)/ gelatin fibers for morphology-dependent protein delivery and enhanced cellular affinity. *Acta Biomater* 8:2549–2558.

[281] Guan R, Sun X, Hou S, Wu P, Chaikof EL (2004) A Glycopolymer Chaperone for Fibroblast Growth Factor-2. *Bioconjugate Chem* 2(15):145–151.

[282] Zou J, Yang Y, Liu Y, Chen F, Li X (2011) Release kinetics and cellular pro fi les for bFGF-loaded electrospun fi bers : Effect of the conjugation density and molecular weight of heparin. *Polymer (Guildf)* 52(15):3357–3367.

[283] Lee J, et al. (2007) Characterization of the surface immobilized synthetic heparin binding domain derived from human fibroblast growth factor-2 and its effect on osteoblast differentiation. *J Biomed Mater Res - Part A*:2–11.

[284] Lyon M, Rushton G, Gallagher JT (1997) The Interaction of the Transforming Growth Factor-bs with Heparin / Heparan Sulfate Is Isoform-specific. *J Biol Chem* 272(29):18000–18006.

[285] Lee J, Yoo JJ, Atala A, Lee SJ (2012) The effect of controlled release of PDGF-BB from heparin-conjugated electrospun PCL/gelatin scaffolds on cellular bioactivity and infiltration. *Biomaterials* 33(28):6709–20.

[286] McLuckie M, et al. (2017) High heparin content surface modified polyurethane discs promote rapid and stable angiogenesis in full thickness skin defects through VEGF immobilization. *J Biomed Mater Res Part A*:1–8.

[287] Chung Y, et al. (2010) Efficient revascularization by VEGF administration via heparin-functionalized nanoparticle – fibrin complex. *J Control Release* 143(3):282–289.

[288] Ceccarelli M, et al. (2009) Anti-inflammatory effects of low molecular weight heparin derivative in a rat model of carrageenan-induced pleurisy. *J Cell Mol Med* 13(8 B):2704–2712.

[289] Young E (2008) The anti-inflammatory effects of heparin and related compounds. *Thromb Res* 122(6):743–752.

[290] Mcluckie M, et al. (2017) High heparin content surface-modified polyurethane discs promote rapid and stable angiogenesis in full thickness skin defects through VEGF immobilization. *J Biomater*:1–8.

[291] Rema RB, Rajendran K, Ragunathan M (2012) Angiogenic efficacy of Heparin on chick chorioallantoic membrane. *Vasc Cell* 4(1):8.

[292] Bezuidenhout D, et al. (2010) Covalent surface heparinization potentiates porous polyurethane scaffold vascularization. *J Biomater Appl* 24(5):401–18.

[293] Fujita M (2000) Heparin and angiogenic therapy. *Eur Heart J* 21(4):270–274.

[294] Chiodelli P, Bugatti A, Urbinati C, Rusnati M (2015) Heparin/heparan sulfate proteoglycans glycomic interactome in angiogenesis: Biological implications and therapeutical use. *Molecules* 20(4):6342–6388.

[295] Sakiyama-Elbert SE (2014) Incorporation of heparin into biomaterials. *Acta Biomater* 10(4):1581–1587.

[296] Hadjizadeh A, Ghasemkhah F, Ghasemzaie N (2017) Polymeric Scaffold Based Gene Delivery Strategies to Improve Angiogenesis in Tissue Engineering: A Review. *Polym Rev* 57(3). doi:10.1080/15583724.2017.1292402.

[297] Carmeliet P, Jain RK (2000) Angiogenesis in cancer and other diseases. *Nature* 407:249–257.

[298] Kim H, et al. (2010) CD31+ cells represent highly angiogenic and vasculogenic cells in bone marrow: Novel role of

nonendothelial CD31+ cells in neovascularization and their therapeutic effects on ischemic vascular disease. *Circ Res* 107(5):602–614.

[299] Hadjizadeh A, Doillon CJ (2010) Directional migration of endothelial cells towards angiogenesis using polymer fibres in a 3D co-culture system. *J Tissue Eng Regen Med* 4(7):524–531.

[300] Papetti M, Herman IM (2002) Mechanisms of normal and tumor-derived angiogenesis. *AJP Cell Physiol* 282(5):947–970.

[301] Cabric S, et al. (2010) Anchoring of vascular endothelial growth factor to surface-immobilized heparin on pancreatic islets: implications for stimulating islet angiogenesis. *Tissue Eng Part A* 16(3):961–970.

[302] Rensburg AJ Van, et al. (2017) Improved vascularization of porous scaffolds through growth factor delivery from heparinized polyethylene glycol hydrogels. *Acta Biomater* 49:89–100.

[303] Webber MJ, et al. (2010) Capturing the stem cell paracrine effect using heparin-presenting nanofibres to treat cardiovascular diseases. *J Tissue Eng Regen Med* 4(8):600–610.

[304] Ghanaati S, et al. (2009) Dynamic in vivo biocompatibility of angiogenic peptide amphiphile nanofibers. *Biomaterials* 30(31):6202–6212.

[305] Rajangam K, et al. (2006) Heparin binding nanostructures to promote growth of blood vessels. *Nano Lett* 6(9):2086–2090.

[306] Webber MJ, Appel EA, Meijer EW, Langer R (2015) Supramolecular biomaterials. *Nat Mater* 15(1):13–26.

[307] Casper CL, Yamaguchi N, Kiick KL, Rabolt JF (2005) Functionalizing electrospun fibers with biologically relevant macromolecules. *Biomacromolecules* 6(4):1998–2007.

[308] Kurpinski KT, Stephenson JT, Janairo RRR, Lee H, Li S (2010) The effect of fiber alignment and heparin coating on cell infiltration into nanofibrous PLLA scaffolds. *Biomaterials* 31(13):3536–42.

[309] Sheikh Z, Brooks PJ, Barzilay O, Fine N, Glogauer M (2015) Macrophages, foreign body giant cells and their response to implantable biomaterials. *Materials (Basel)* 8(9):5671–5701.

[310] Kwon IK, Matsuda T (2005) Co-electrospun nanofiber fabrics of poly(L-lactide-co-epsilon-caprolactone) with type I collagen or heparin. *Biomacromolecules* 6(4):2096–105.

[311] Cheng Q, Komvopoulos K, Li S (2014) Plasma-assisted heparin conjugation on electrospun poly(L-lactide) fibrous scaffolds. *J Biomed Mater Res - Part A* 102(5):1408–1414.

[312] Du F, et al. (2012) Gradient nanofibrous chitosan/poly e{open}-caprolactone scaffolds as extracellular microenvironments for vascular tissue engineering. *Biomaterials* 33(3):762–770.

[313] Centola M, et al. (2010) Combining electrospinning and fused deposition modeling for the fabrication of a hybrid vascular graft. *Biofabrication* 2(1):14102.

[314] Dang TT, et al. (2011) Spatiotemporal effects of a controlled-release anti-inflammatory drug on the cellular dynamics of host response. *Biomaterials* 32(19):4464–4470.

[315] Wu P, Grainger DW (2006) Drug/device combinations for local drug therapies and infection prophylaxis. *Biomaterials* 27(11):2450–2467.

[316] Bhardwaj U, Sura R, Papadimitrakopoulos F, Burgess DJ (2007) Controlling acute inflammation with fast releasing dexamethasone-PLGA microsphere/pva hydrogel composites for implantable devices. *J diabetes Sci Technol* 1(1):8–17.

[317] Hickey T, Kreutzer D, Burgess DJ, Moussy F (2002) Dexamethasone/PLGA microspheres for continuous delivery of an anti-inflammatory drug for implantable medical devices. *Biomaterials* 23(7):1649–1656.

[318] Holmin S, Mathiesen T (1996) Dexamethasone and colchicine reduce inflammation and delayed oedema following experimental brain contusion. *Acta Neurochir (Wien)* 138(4):418–424.

[319] Durmus M, et al. (2003) The effects of single-dose dexamethasone on wound healing in rats. *Anesth Analg* 97(5):1377–1380.

[320] Gahm C, Holmin S, Rudehill S, Mathiesen T (2005) Neuronal degeneration and iNOS expression in experimental brain contusion following treatment with colchicine, dexamethasone, tirilazad mesylate and nimodipine. *Acta Neurochir (Wien)* 147(10):1071–1084.

[321] Zhang Z, Fauser U, Schluesener HJ (2008) Early attenuation of lesional interleukin-16 up-regulation by dexamethasone and FTY720 in experimental traumatic brain injury. *Neuropathol Appl Neurobiol* 34(3):330–9.

[322] Nguyen LTH, Liao S, Chan CK, Ramakrishna S (2011) Electrospun Poly(l-Lactic Acid) Nanofibres Loaded with Dexamethasone to Induce Osteogenic Differentiation of Human Mesenchymal Stem Cells. *J Biomater Sci Polym Ed* (October 2014):1771–1791.

[323] Gaharwar AK, et al. (2014) Amphiphilic beads as depots for sustained drug release integrated into fibrillar scaffolds. *J Control Release* 187:66–73.

[324] Innocente F, et al. (2009) Paclitaxel-eluting biodegradable synthetic vascular prostheses: a step towards reduction of neointima formation? *Circulation* 120(11 Suppl):S37-45.

[325] Zeng J, et al. (2005) Poly(vinyl alcohol) nanofibers by electrospinning as a protein delivery system and the retardation of enzyme release by additional polymer coatings. *Biomacromolecules* 6(3):1484–1488.

[326] Assmann U, et al. (2010) Fiber scaffolds of polysialic acid via electrospinning for peripheral nerve regeneration. *J Mater Sci Mater Med* 21(7):2115–2124.

[327] Costa P, Lobo JMS (2001) Modeling and comparison of dissolution profile. *Eur J Pharm Sci* 13:123–133.

[328] El-Arini SK, Leuenberger H (1995) Modelling of drug release from polymer matrices : Effect of drug loading. *Int J Pharm* 121:141–148.

[329] Korsmeyer RW, Gurny R, Doelker E, Buri P, Peppas NA (1983) Mechanisms of solute release from porous hydrophilic polymers. *Int J Pharm* 15(1):25–35.

[330] Sell SA, McClure MJ, Garg K, Wolfe PS, Bowlin GL (2009) Electrospinning of collagen/biopolymers for regenerative medicine and cardiovascular tissue engineering. *Adv Drug Deliv Rev* 61(12):1007–1019.

[331] Dash S, Murthy PN, Nath L, Chowdhury P (2010) Kinetic modeling on drug release from controlled drug delivery systems. *Acta Pol Pharm* 67(3):217–23.

[332] Berger K, Sauvage LR, Rao a M, Wood SJ (1972) Healing of arterial prostheses in man: its incompleteness. *Ann Surg* 175(1):118–27.

[333] Veith FJ, et al. (1986) Six-year prospective multicenter randomized comparison of autologous saphenous vein and expanded polytetrafluoroethylene grafts in infrainguinal arterial reconstructions. *J Vasc Surg* 3(1):104–14.

[334] Clagett GP (2002) What's new in vascular surgery. *J Am Coll Surg* 194(2):165–201.

[335] Pennel T, Zilla P, Bezuidenhout D (2013) Differentiating transmural from transanastomotic prosthetic graft endothelialization through an isolation loop-graft model. *J Vasc Surg* 58(4):1053–61.

[336] Kim T, Chung H, Park T (2008) Macroporous and nanofibrous hyaluronic acid/collagen hybrid scaffold fabricated by concurrent electrospinning and deposition/leaching of salt particles. *Acta Biomater* 4:1611–1619.

[337] Gao Y, et al. (2016) Pilot Mouse Study of 1 mm Inner Diameter (ID) Vascular Graft Using Electrospun Poly(ester urea) Nanofibers. *Adv Healthc Mater* (November). doi:10.1002/adhm.201600400.

[338] Schmidt C, Bezuidenhout D, Higham L, Zilla P, Davies NH (2011) Induced chronic hypoxia negates the pro-angiogenic effect of surface immobilized heparin in a polyurethane porous scaffold. *J Biomed Mater Res A* 98(4):621–8.

[339] Riesenfeld J, Roden L (1990) Quantitative analysis of N-sulfated, N-acetylated, and unsubstituted glucosamine amino groups in heparin and related polysaccharides. *Anal Biochem* 188(2):383–389.

[340] Bergmeister H, et al. (2013) Healing characteristics of electrospun polyurethane grafts with various porosities. *Acta Biomater* 9(4):6032–40.

[341] Shevach M, Soffer-Tsur N, Fleischer S, Shapira A, Dvir T (2014) Fabrication of omentum-based matrix for engineering vascularized cardiac tissues. *Biofabrication* 6(2):24101.

[342] Guru BS, Hiziroglu HR (2004) *Electromagnetic field theory fundamentals* (Cambridge university press).

[343] Loh QL, Choong C (2013) Three-Dimensional Scaffolds for Tissue Engineering Applications: Role of Porosity and Pore Size. *Tissue Eng Part B Rev* 19(6):485–502.

[344] Braghirolli DI, Steffens D, Pranke P (2014) Electrospinning for regenerative medicine: a review of the main topics. *Drug Discov Today* 19(6):743–753.

[345] Jose AD, Collison D (1970) The normal range and determinants of the intrinsic heart rate in man. *Cardiovasc Res* 4(2):160–167.

[346] Weissler AM, Harris WS, Schoenfeld CD (1968) Systolic time intervals in heart failure in man. *Circulation* 37(2):149–159.

[347] Püspöki Z, Storath M, Sage D, Unser M (2016) Transforms and Operators for Directional Bioimage Analysis: A Survey. *Focus on Bio-Image Informatics*, Advances in Anatomy, Embryology and Cell Biology., eds De Vos WH, Munck S, Timmermans J-P (Springer International Publishing), pp 69–93.

[348] Rezakhaniha R, et al. (2012) Experimental Investigation of Collagen Waviness and Orientation in the Arterial Adventitia Using Confocal Laser Scanning Microscopy. *Biomech Model Mechanobiol* 11(3–4):461–473.

[349] Fonck E, et al. (2009) Effect of Aging on Elastin Functionality in Human Cerebral Arteries. *Stroke* 40(7):2552–2556.

[350] Nock R, Nielsen F (2004) Statistical region merging. *IEEE Trans Pattern Anal Mach Intell* 26(11):1452–1458.

[351] Davies N, et al. (2008) The dosage dependence of VEGF stimulation on scaffold neovascularisation. *Biomaterials* 29(26):3531–8.

[352] Baker BM, et al. (2012) Sacrificial nanofibrous composites provide instruction without impediment and enable functional tissue formation. *Proc Natl Acad Sci U S A* 109(35):14176–81.

[353] Talacua H, et al. (2012) Subcutaneous Testing of E-spun PCL Patches Suitable for in Situ Heart Valve Tissue Engineering. *QScience Proc* 2012(4):34.

[354] Bergmeister H, et al. (2013) Healing characteristics of electrospun polyurethane grafts with various porosities. *Acta Biomater* 9(4):6032–6040.

[355] Ying TH, et al. (2008) Scaffolds from electrospun polyhydroxyalkanoate copolymers: Fabrication, characterization, bioabsorption and tissue response. *Biomaterials* 29(10):1307–1317.

[356] Stankus JJ, Freytes DO, Badylak SF, Wagner WR (2008) Hybrid nanofibrous scaffolds from electrospinning of a synthetic biodegradable elastomer and urinary bladder matrix. *J Biomater Sci Polym Ed* 19(5):635–652.

[357] Phipps MC, Clem WC, Grunda JM, Clines GA, Bellis SL (2012) Increasing the pore sizes of bone-mimetic electrospun scaffolds comprised of polycaprolactone, collagen I and hydroxyapatite to enhance cell infiltration. *Biomaterials* 33(2):524–34.

[358] Cao H, Mchugh K, Chew SY, Anderson JM (2009) The topographical effect of electrospun nanofibrous scaffolds on the *in vivo* and *in vitro* foreign body reaction. *J Biomed Mater Res Part A* 9999A:NA-NA.

[359] Ji W, et al. (2012) Biocompatibility and degradation characteristics of PLGA-based electrospun nanofibrous scaffolds with nanoapatite incorporation. *Biomaterials* 33(28):6604–6614.

[360] Charan J, Kantharia ND (2013) How to calculate sample size in animal studies? *J Pharmacol Pharmacother* 4(4):303.

[361] Festing MFW, Altman DG (2002) Guidelines for the design and statistical analysis of experiments using laboratory animals. *ILAR J* 43(4):244–258.

[362] Shapiro SS, Wilk MB (1965) An analysis of variance test for normality (complete samples). *Biometrika* 52(3/4):591–611.

[363] Saad B, Neuenschwander P, Uhlschmid GK, Suter UW (1999) New versatile, elastomeric, degradable polymeric materials for medicine. *Int J Biol Macromol* 25:293–301.

[364] McCarthy SJ, et al. (1998) Quantitative Analysis of the Degradation In Vitro of Pellethane 2363-80A and Pellethane 2363-55D by Transmission FTIR Microscopy. *Annual Meeting-Society for Biomaterials in Conjunction with the International*

Biomaterials Symposium, p 392.

[365] Theron JP, et al. (2010) Modification, crosslinking and reactive electrospinning of a thermoplastic medical polyurethane for vascular graft applications. *Acta Biomater* 6(7):2434–47.

[366] Szycher M (1988) Biostability of polyurethane elastomers: a critical review. *J Biomater Appl* 3(2):297–402.

[367] Jung JH, Ree M, Kim H (2006) Acid- and base-catalyzed hydrolyses of aliphatic polycarbonates and polyesters. *Catal Today* 115(1–4):283–287.

[368] Sarkar S, Salacinski HJ, Hamilton G, Seifalian a. M (2006) The Mechanical Properties of Infrainguinal Vascular Bypass Grafts: Their Role in Influencing Patency. *Eur J Vasc Endovasc Surg* 31(6):627–636.

[369] Barker RE, Sharbaugh AH (1965) Ionic conduction in polymer films and related systems. *Journal of Polymer Science: Polymer Symposia*, pp 139–152.

[370] Xie J, Marijnissen JCM, Wang C-H (2006) Microparticles developed by electrohydrodynamic atomization for the local delivery of anticancer drug to treat C6 glioma in vitro. *Biomaterials* 27(17):3321–32.

[371] Yu LYu, Shen HM, Xu ZL (2009) PVDF–TiO2 Composite Hollow Fiber Ultrafiltration Membranes Prepared by TiO2 Sol–Gel Method and Blending Method. *J Appl Phys* 113:1763–1772.

[372] Zamani M, Prabhakaran MP, Ramakrishna S (2013) Advances in drug delivery via electrospun and electrosprayed nanomaterials. *Int J Nanomedicine* 8:2997–3017.

[373] Sridhar R, Ramakrishna S (2013) Electrosprayed nanoparticles for drug delivery and pharmaceutical applications. *Biomatter* 3(3). doi:10.4161/biom.24281.

[374] Wu Y, Mackay JA, Mcdaniel JR, Chilkoti A, Clark RL (2009) Fabrication of Elastin-Like Polypeptide Nanoparticles for Drug Delivery by Electrospraying Fabrication of Elastin-Like Polypeptide Nanoparticles for Drug Delivery by Electrospraying. *Biomacromolecules* 10:19–24.

[375] Arya N, Chakraborty S, Dube N, Katti DS (2009) Electrospraying: A facile technique for synthesis of chitosan-based micro/nanospheres for drug delivery applications. *J Biomed Mater Res - Part B Appl Biomater* 88:17–31.

[376] Bock N, Woodruff M a., Hutmacher DW, Dargaville TR (2011) Electrospraying, a Reproducible Method for Production of Polymeric Microspheres for Biomedical Applications. *Polymers (Basel)* 3(4):131–149.

[377] Tang K, Gomez a. (1996) Monodisperse Electrosprays of Low Electric Conductivity Liquids in the Cone-Jet Mode. *J Colloid Interface Sci* 184(2):500–11.

[378] De Gennes P-G (1979) *Scaling concepts in polymer physics* (Cornell university press).

[379] Nomi M, Atala A, De Coppi P, Soker S (2002) Principals of neovascularization for tissue engineering. *Mol Aspects Med* 23(6):463–483.

[380] Savoji H, et al. (2014) Electrospun nanofiber scaffolds and plasma polymerization: A promising combination towards complete, stable endothelial lining for vascular grafts. *Macromol Biosci* 14(8):1084–1095.

[381] Soliman S, et al. (2011) Controlling the porosity of fibrous scaffolds by modulating the fiber diameter and packing density. *J Biomed Mater Res A* 96(3):566–74.

[382] Humphrey JD (2008) Vascular adaptation and mechanical homeostasis at tissue, cellular, and sub-cellular levels. *Cell Biochem Biophys* 50(2):53–78.

[383] Huang AH, Niklason LE (2014) Engineering of arteries in vitro. *Cell Mol Life Sci* 71(11):2103–2118.

[384] Lien SM, Ko LY, Huang TJ (2009) Effect of pore size on ECM secretion and cell growth in gelatin scaffold for articular cartilage tissue engineering. *Acta Biomater* 5(2):670–679.

[385] Beredjiklian PK, et al. (2003) Regenerative versus reparative healing in tendon: A study of biomechanical and histological properties in fetal sheep. *Ann Biomed Eng* 31(10):1143–1152.

[386] Wu W, Allen R a, Wang Y (2012) Fast-degrading elastomer enables rapid remodeling of a cell-free synthetic graft into a neoartery. *Nat Med* 18(7):1148–53.

[387] Sussman EM, Halpin MC, Muster J, Moon RT, Ratner BD (2014) Porous Implants Modulate Healing and Induce Shifts in Local Macrophage Polarization in the Foreign Body Reaction. *Ann Biomed Eng* 42(7):1508–1516.

[388] Xia Z, Triffitt JT (2006) A review on macrophage responses to biomaterials. *Biomed Mater* 1:1–9.

[389] Okazaki T, Ebihara S, Takahashi H, Asada M, Kanda A (2005) Macrophage Colony-Stimulating Factor Induces Vascular Endothelial Growth Factor Production in Skeletal Muscle and Promotes Tumor Angiogenesis. *J Immunol* 147:7531–7538.

[390] Middleton W, Lindsey Jr R (1964) Hydrogen Bonding in Fluoro Alcohols. *J Am Chem Soc* 86(22):4948–4952.

[391] Yong-kyu Lee HTM and YB (1998) Preparation of slightly hydrophobic heparin derivatives which can be used for solvent casting in polymeric formulation. *Thromb Res* 92:149–156.

[392] Rai R, Tallawi M, Grigore A, Boccaccini AR (2012) Synthesis, properties and biomedical applications of poly(glycerol sebacate) (PGS): A review. *Prog Polym Sci* 37(8):1051–1078.

[393] von Burkersroda F, Schedl L, Göpferich A (2002) Why degradable polymers undergo surface erosion or bulk erosion. *Biomaterials* 23(21):4221–31.

[394] Rezaie AR (1998) Calcium Enhances Heparin Catalysis of the Antithrombin-Factor Xa. *J Biol Chem* 273(27):16824–16827.

[395] Whisstock JC, et al. (2000) Conformational changes in serpins: II. The mechanism of activation of antithrombin by heparin. *J Mol Biol* 301(5):1287–305.

[396] Capila I, Linhardt RJ (2002) Heparin-protein interactions. *Angew Chem Int Ed Engl* 41(3):391–412.

[397] Murugan R, Ramakrishna S (2007) Design strategies of tissue engineering scaffolds with controlled fiber orientation. *Tissue Eng* 13(8):1845–66.

[398] Jia L, Prabhakaran MP, Qin X, Ramakrishna S (2014) Guiding the orientation of smooth muscle cells on random and aligned polyurethane/collagen nanofibers. *J Biomater Appl*. doi:10.1177/0885328214529002.

[399] Deitzel J, Kleinmeyer J, Hirvonen J, Tan NB (2001) Controlled deposition of electrospun poly (ethylene oxide) fibers. *Polymer (Guildf)* 42:8163–8170.

[400] Kim GH, Han H, Park JH, Kim WD (2007) An applicable electrospinning process for fabricating a mechanically improved nanofiber mat. *Polym Eng Sci* 47(5):707–712.

[401] Kim G, Cho Y-S, Kim WD (2006) Stability analysis for multi-jets electrospinning process modified with a cylindrical electrode. *Eur Polym J* 42(9):2031–2038.

[402] Stankus JJ, Guan J, Wagner WR (2004) Fabrication of biodegradable elastomeric scaffolds with sub-micron morphologies. *J Biomed Mater Res A* 70(4):603–14.

[403] Sahay R, Thavasi V, Ramakrishna S (2011) Design Modifications in Electrospinning Setup for Advanced Applications. *J Nanomater* 2011:1–17.

[404] Arras MML, Grasl C, Bergmeister H, Schima H (2012) Electrospinning of aligned fibers with adjustable orientation using auxiliary electrodes. *Sci Technol Adv Mater* 13(3):35008.

[405] Qin X, Yang E, Li N, Wang S (2007) Effect of Different Salts on Electrospinning of Polyacrylonitrile (PAN) Polymer Solution. *J Appl Phys* 103(July 2006):3865–3870.

[406] Shin J, et al. (2004) Effect of organosoluble salts on the nanofibrous structure of electrospun poly (3-hydroxybutyrate- co -3-hydroxyvalerate). *Int J Biol Macromol* 34:249–256.

[407] Eichhorn SJ, Sampson WW (2010) Relationships between specific surface area and pore size in electrospun polymer fibre networks. *J R Soc* 7:641–649.

[408] Lv Q, Cao C, Zhu H (2003) A novel solvent system for blending of polyurethane and heparin. *Biomaterials* 24(22):3915–3919.

[409] Zhao W, Liu W, Li J, Lin X, Wang Y (2014) Preparation of animal polysaccharides nanofibers by electrospinning and their potential biomedical applications. *J Biomed Mater Res A*:1–12.

[410] Sun H, Mei L, Song C, Cui X, Wang P (2006) The in vivo degradation, absorption and excretion of PCL-based implant. *Biomaterials* 27(9):1735–1740.

[411] Lam CXF, Hutmacher DW, Schantz J-T, Woodruff MA, Teoh SH (2009) Evaluation of polycaprolactone scaffold degradation for 6 months in vitro and in vivo. *J Biomed Mater Res A* 90(3):906–19.

[412] Talacua H, et al. (2015) In Situ Tissue Engineering of Functional Small-Diameter Blood Vessels by Host Circulating Cells Only. *Tissue Eng Part A* 21(19–20). doi:10.1089/ten.tea.2015.0066.

[413] Roh JD, et al. (2010) Tissue-engineered vascular grafts transform into mature blood vessels via an inflammation-mediated process of vascular remodeling. *Proc Natl Acad Sci* 107(10):4669–4674.

[414] Bratlie KM, et al. (2010) Rapid biocompatibility analysis of materials via in vivo fluorescence imaging of mouse models. *PLoS One* 5(4):1–8.

[415] Nidhi K, Indrajeet S, Khushboo M, Gauri K, Sen DJ (2011) Local Drug Delivery System: Inhibition of Inflammatory Angiogenesis in a Murine Sponge Model by Dexamethasone-Loaded Polyurethane Implants. *J Pharm Sci* 100(7):2886–2895.

[416] Luo JC, et al. (2004) Dexamethasone delays ulcer healing by inhibition of angiogenesis in rat stomachs. *Eur J Pharmacol* 485(1–3):275–281.

[417] Saad B, et al. (1996) Interactions of osteoblasts and macrophages with biodegradable and highly porous polyesterurethane foam and its degradation products. *J Biomed Mater Res* 32:355–366.

[418] Saad B, et al. (1997) Development of degradable polyesterurethanes for medical applications: In vitro and in vivo evaluations. *J Biomed Mater Res* 36(1):65–74.

[419] Saad B, Keiser O, Welti M (1997) Multiblock copolyesters as biomaterials: in vitro biocompatibility testing. *J Mater …* 8:497–505.

[420] Saad B, et al. (1999) Chondrocyte-biocompatibility of DegraPol-foam: in vitro evaluations. *J Biomater Sci Polym Ed* 10(11):1107–19.

[421] Saad B, et al. (2000) DegraPol-Foam: A degradable and highly porous polyesterurethane foam as a new substrate for bone formation. *Artif Organs* 24(12):939–945.

[422] Yang L, et al. (2003) Tissue engineered cartilage generated from human trachea using DegraPol® scaffold. *Eur J Cardiothoracic Surg* 24(2):201–207.

[423] Danielsson C, Ruault S, Simonet M, Neuenschwander P, Frey P (2006) Polyesterurethane foam scaffold for smooth muscle cell tissue engineering. *Biomaterials* 27(8):1410–1415.

[424] Milleret V, Bittermann AG, Mayer D, Hall H (2009) Analysis of effective interconnectivity of degrapol-foams designed for negative pressure wound therapy. *Materials (Basel)* 2:292–306.

7 Appendices

A1: Properties of organic solvents

A selection for experimental electrospinning

Solvent name	ε -	γ [dyn/cm]	σ_e [S/cm]	Vp [mmHg]	P -	μ [cPoise]	T_h [^{0}C]	SG -
Dioxane	2.2	40.0	5.E-15	32.0	16.4	1.30	101	1.03
Anisole*	4.3	36.2	N/a	N/a	N/a	1.05	154	0.99
Chloroform	4.8	27.2	1.E-10	169.0	25.9	0.57	61	1.48
Chlorobenzene	5.6	33.0	7.E-11	9.5	18.8	0.80	132	1.11
Ethyl acetate	6.0	24.0	1.E-09	78.0	23.0	0.43	77	0.90
Tetrahydrofuran (THF)	7.6	28.0	5.E-05	133.0	21.0	0.55	66	0.88
Trifluoroethanol (TFE)*	8.6	16.5	N/a	N/a	N/a	0.90	77	1.38
Dichloromethane (DCM)	9.1	28.1	4.E-11	376.0	30.9	0.44	40	1.33
Dichloroethane (DCE)	10.5	32.2	4.E-11	71.0	32.7	0.90	84	1.25
Hexafluoro isopropanol (HFIP)*	17.8	16.1	N/a	120.0	N/a	1.02	58	1.60
Cyclohexanone	18.2	34.5	5.E-18	3.1	28.0	2.20	156	0.95
Isopropanol	18.3	21.7	6.E-08	35.1	54.6	2.00	82	0.79
Acetone	20.6	23.3	5.E-09	194.0	35.5	0.33	56	0.79
Ethanol	22.4	22.3	1.E-09	45.7	65.4	1.08	78	0.79
Methyl pyrrolidone (NMP)	32.2	40.7	2.E-08	0.3	36.0	1.80	202	1.03
Methanol	32.6	22.6	2.E-09	103.0	46.2	0.60	64	0.79
Dimethylformamide (DMF)	36.7	35.0	6.E-08	3.8	40.4	0.82	153	0.95
Dimethylacetamide (DMAC)	37.2	34.0	N/a	1.0	40.1	0.92	166	0.95
Acetonitrile	37.5	29.1	6.E-10	71.0	46.0	0.38	82	0.78
Trifluoro acetic acid (TFA)*	42.1	22.0	N/a	N/a	N/a	0.74	72	1.53
Dimethyl sulfoxide (DMSO)	46.6	43.7	2.E-09	0.7	44.4	2.00	189	1.10
Water	80.1	72.8	5.E-01	19.0	100.0	0.89	100	1.00
Formamide	109.5	58.9	N/a	30.0	N/a	3.23	210	1.13

Dielectric constant at 20^{0}C (ε), surface tension at 20^{0}C (γ), electrical conductivity (σ_e), vapour pressure (Vp), polarity (P), dipole (D), boiling point (T_b) and specific gravity (SG). References: Handbook of organic solvent properties (Ian Smallwood, 1996) [137] & *http://depts.washington.edu

A2: Additional DegraPol® review summaries

DegraPol® as biomaterial selection for tissue engineering (TE) applications over 20 years (1996-2016)

TE application	Structure/ technique	DegraPol Name	Pore size [µm]	Porosity [%]	E [MPa]	Relevant study/*in vitro* cell culture [conclusion]	Relevant *in vivo* study [conclusion]	Ref
Bone regeneration	Foam/ Freeze-immersion-precipitation	DegraPol/btc®	100-150	1g DP = 7.3 cm^3	n/a	Rat osteoblasts and macrophages [degradation products failed to induce any cytotoxic effects nor did it activate macrophages at low concentrations – 2-20µm PHB-P particles]	n/a	[417]
General	Film/ Heat pressing	DegraPol/btd44 DegraPol/btc44 DegraPol/bld43nc DegraPol/blc44nc	n/a	n/a	190 200 120 150	Fibroblasts and macrophages [did not activate macrophages thus did not induce cytotoxic effects]	Rat subcutaneous implantation [Favourable tissue compatibility, Mw reduced by 50% after 12 months]	[418]
General	Film/ Heat pressing	DegraPol/bsc43 DegraPol/bsd43 DegraPol/bst41	n/a	n/a	n/a	Fibroblasts and macrophages [did not activate macrophages thus did not induce cytotoxic effects]	Rat subcutaneous implantation [Mw reduced by 20 (PEE) or 40% (PE) after 2 months]	[419]
General	Film/ Heat pressing	DegraPol™/btcg	n/a	n/a	50-500	Influence of glycolide content and hard to soft segment ratio on mechanical properties [elastic moduli increased with increasing hard segment ratio; degradation rate can be controlled independent of mechanical properties by controlling glycolide]	n/a	[259]
Nerve regeneration	Tube/ Melt extrusion	DegraPol®/btgc b8 DegraPol®/btgc b27 DegraPol®/btgc b41	n/a	n/a	1.9 8.4 46	n/a	Rat sciatic nerve implantation [mass loss up to 88wt% over 24 weeks: lower b content = higher degradation rate]	[258]
Bone regeneration	Foam/ Freeze-immersion-precipitation	DegraPol b29 DegraPol b44 DegraPol b68	100-400	n/a	50 200 380	Rat chondrocytes, osteoblasts and macrophages [Favourable cell adhesion and proliferation on DP surface; degradation products failed to induce any cytotoxic effects nor did it activate macrophages at low concentrations]	n/a	[363]

TE application	Structure/ technique	DegraPol Name	Pore size [µm]	Porosity [%]	E [MPa]	Relevant study/*in vitro* cell culture [conclusion]	Relevant *in vivo* study [conclusion]	Ref
Cartilage regeneration	Foam/ Freeze-immersion-precipitation	DegraPol	100-300	n/a	n/a	Rat chondrocytes [Compatible substrate for chondrocytes]	n/a	[420]
Bone regeneration	Foam/ Freeze-immersion-precipitation	DegraPol	100-400	n/a	n/a	Rat osteoblasts and human cell line HFO1 [Cells attached and proliferated preferentially on DP surfaces]	Rat subcutaneous implantation [Most areas within the pores were filled with fibrous tissue after 2 weeks]	[421]
General	Film/ Heat pressing	DegraPol™/btcg	n/a	n/a	50-400	Hydrolytic degradation in buffered solutions [Degradation rate is determined by quantity and distribution of glycolyl-glycolate ester bonds; higher glycolate content = higher degradation rate]	n/a	[260]
Cartilage regeneration	Foam/ Freeze-immersion-precipitation	DegraPol	150-200	n/a	n/a	Human tracheal chondrocytes [Cultivated chondrocytes populated DP film and successfully formed cartilage like architecture]	n/a	[422]
Smooth muscle regeneration	Foam/ Freeze-immersion-precipitation	DegraPol	100-300	n/a	n/a	Human primary bladder smooth muscle cells [Cell grown on the DP foam as well as inside the pores; SMC proliferated on DP]	n/a	[423]
Negative pressure wound therapy	Foam/ Freeze-immersion-precipitation	DegraPol	160 ±50	n/a	n/a	n/a	n/a	[424]
Skeletal muscle	Microfibres/ Electrospinning	DegraPol	10	n/a	10	Line cells (C2C12 and L6) and primary human satellite cells (HSCs); mechanical characterisation [DP membranes showed promising cellular response and did not produce toxic residuals; displayed satisfactory mechanical performance; Mw reduced by 45% after 4 weeks]	n/a	[263]
General	Microfibres/ Electrospinning	DegraPol	10-100	n/a	10-25	Fibroblast viability; hydrolytic degradation investigation [DP structures was not cytotoxic; 70-74% Mw reduction over 346days]	n/a	[261]

TE application	Structure/ technique	DegraPol Name	Pore size [µm]	Porosity [%]	E [MPa]	Relevant study/*in vitro* cell culture [conclusion]	Relevant *in vivo* study [conclusion]	Ref
General	Microfibres/ Electrospinning	DegraPol	~60	64-91 (LTE)	0.4-1.0 [km]	n/a	n/a	[208]
Skeletal muscle	Microfibres/ Electrospinning	DegraPol	n/a	n/a	n/a	Myoblast culture [Improved myogenesis can be obtained and directed within highly orientated DP fibres]	n/a	[264]
Cartilage regeneration	Microfibres/ Electrospinning	DegraPol	30-80	n/a	n/a	Chondrocytes (static & dynamic) [DP fibrous scaffold successfully supported cell phenotype]	Rabbits for 8 weeks [DP provided a good substrate for fibrous tissue deposition with an excellent degree of neo-angiogenesis (increasing number of positive CD31 stained cells over 8 weeks) – full resorption was not observed]	[265, 266]
General	Microfibres/ Electrospinning	DegraPol	n/a	n/a	n/a	Fibroblasts & endothelial cells [Cells behaved differently on DP structures; fibroblast adhesion and proliferation was superior compared to endothelial cells. Furthermore, hemocompatibility was found to be similar or better to PLGA or stainless steel]	n/a	[267]
Cardiovascular	Microfibres/ Electrospinning	DegraPol30	n/a	80	1.0	n/a	n/a	[21]
General	Microfibres/ Electrospinning	DegraPol	n/a	75-93 (PEG)	0.5-2.2 (r) 10 (a)	Fibroblasts [Cell proliferation was similar between PLGA and DP; cellular infiltration increased with increasing porosity]	n/a	[178]
Blood vessel	Microfibres/ Electrospinning	DegraPol	7-45* converted	n/a	n/a	Whole human blood [No differences between PLGA and DP. Decreased fibre diameter triggered lower coagulation; larger fibres triggered higher thrombin formation and platelet adhesion]	n/a	[268]
Tendon regeneration	Microfibres/ Electrospinning	DegraPol	n/a	75	n/a	n/a	Rabbit Achilles tendon implantation for 12 weeks [Observable degradation of 50%; DP scaffolds had favourable tissue response and could potentially serve as a carrier for GFs]	[269]

TE application	Structure/ technique	DegraPol Name	Pore size [µm]	Porosity [%]	E [MPa]	Relevant study/*in vitro* cell culture [conclusion]	Relevant *in vivo* study [conclusion]	Ref
Tendon regeneration	Microfibres/ Electrospinning	DegraPol new	n/a	75	n/a	n/a	Rabbit Achilles tendon implantation for 6 weeks [Successfully prevented peritendinous adhesion; DP groups had 20% less adhesion with no additional inflammation]	[270]
Smooth muscle regeneration	Microfibres/ Electrospinning	DegraPol15	n/a	71	n/a	Smooth muscle cells [Cell proliferation and viability of DP was comparable to PLGA]	Rat cystoplasty model for 8 weeks [DP revealed higher smooth muscle regeneration and lower inflammatory response compared to PLGA]	[271]
Tendon regeneration	Microfibres/ Electrospinning	DegraPol classic DegraPol new	n/a	75	45 (f) 6 (f)	n/a	Rabbit Achilles tendon implantation for 12 weeks [No adverse reactions of tendon tissue; no difference of cellular response to new compared to classic DP tube]	[272]
Cardiovascular	Microfibres/ Electrospinning	DegraPol30	n/a	76	5.6	n/a	n/a	[273]
Tendon regeneration	Microfibres/ Emulsion electrospinning	DegraPol classic/new	n/a	60-70	1.5-2.3	Electrospinning parameter study, drug release and rabbit tenocyte culture [Increased cell proliferation confirmed]	n/a	[262]

Chemical composition of DegraPol® over 20 years (1996-2016)

DegraPol (Mw)	Hard segment-diol		Junction unit	Soft segment-diol		Ref
	Crystallisable blocks	Crystallisable block content %(w/w)		Non-crystallisable blocks	Glycolide content (mol%)	
DegraPol/btc® (60-110kDa) PEU	α,ω -dihydroxy-[oligo((R)-3-hydroxybutyrate-co-(R)-3-hydroxyvalerate)-block-ethylene glycol] Mn~2300	n/a (equal amounts were reacted)	2,2,4-trimethylhexamethylene diisocyanate	α,ω-dihydroxy-[poly-ε-caprolactone-block- diethylene glycol-block-poly-ε-caprolactone] Mn~1200	0	[417]
DegraPol/btd44 (75kDa) PEU	α,ω -dihydroxy-[oligo((R)-3-hydroxybutyrate-co-(R)-3-hydroxyvalerate)-block-ethylene glycol] Mn~2300	44	2,2,4-trimethylhexamethylene diisocyanate	α,ω-dihydroxy-poly(adipic acid-alt-(1,2-ethane diol; 1,4-butane diol; 3-oxa-1,5-pentanediol)) Mn~1000	0	[418]
DegraPol/btc44 (66kDa) PEU	α,ω -dihydroxy-[oligo((R)-3-hydroxybutyrate-co-(R)-3-hydroxyvalerate)-block-ethylene glycol] Mn~2300	44	2,2,4-trimethylhexamethylene diisocyanate	α,ω-dihydroxy-[poly-ε-caprolactone-block- diethylene glycol-block-poly-ε-caprolactone] Mn~1200	0	[418]
DegraPol/bld43nc (97kDa) PEU	α,ω -dihydroxy-[oligo((R)-3-hydroxybutyrate-co-(R)-3-hydroxyvalerate)-block-ethylene glycol] Mn~2300	43	lysinmethylester-diisocyanate (S)-2,6- diisocyanate methyl caproate	α,ω-dihydroxy-poly(adipic acid-alt-(1,2-ethane diol; 1,4-butane diol; 3-oxa-1,5-pentanediol)) Mn~1000	0	[418]
DegraPol/blc44nc (77kDa) PEU	α,ω -dihydroxy-[oligo((R)-3-hydroxybutyrate-co-(R)-3-hydroxyvalerate)-block-ethylene glycol] Mn~2300	44	lysinmethylester-diisocyanate (S)-2,6- diisocyanate methyl caproate	α,ω-dihydroxy-[poly-ε-caprolactone-block- diethylene glycol-block-poly-ε-caprolactone] Mn~1200	0	[418]
DegraPol/bsc43 (29kDa) PE	α,ω -dihydroxy-[poly((R)-3-hydroxybutyrate-co-(R)-3-hydroxyvalerate)-block-ethylene glycol] Mn~2400	43	Sebacoylchloride	α,ω-dihydroxy-[poly-ε-caprolactone-block- diethylene glycol-block- poly -ε-caprolactone] Mn~1200	0	[419]
DegraPol/bsd43 (40kDa) PE	α,ω -dihydroxy-[poly((R)-3-hydroxybutyrate-co-(R)-3-hydroxyvalerate)-block-ethylene glycol] Mn~2400	43	Sebacoylchloride	α,ω-dihydroxy-poly(adipic acid-alt-(1,2-ethane diol; 1,4-butane diol; 3-oxa-1,5-pentanediol)) Mn~1000	0	[419]
DegraPol/bst41 (42kDa) PEE	α,ω -dihydroxy-[poly((R)-3-hydroxybutyrate-co-(R)-3-hydroxyvalerate)-block-ethylene glycol] Mn~2400	41	Sebacoylchloride	α,ω-dihydroxy-poly(1-oxa-pentamethylene) Mn~650	0	[419]

DegraPol™/btcg (>100kDa) PEU	α,ω -dihydroxy-[poly((R)-3-hydroxybutyrate-co-(R)-3-hydroxyvalerate)-block-ethylene glycol] Mn<3000	26-61	2,2,4-trimethylhexamethylene diisocyanate	poly[glycolide-co-(ε-caprolactone)]	18-86	[259]
DegraPol®/btgc b8 (178kDa) PEU	α,ω -dihydroxy-[poly((R)-3-hydroxybutyrate-co-(R)-3-hydroxyvalerate)-block-ethylene glycol] Mn<3000	8	2,2,4-trimethylhexamethylene diisocyanate	poly[glycolide-co-(ε-caprolactone)]	27	[258]
DegraPol®/btgc b17 (105kDa) PEU	α,ω -dihydroxy-[poly((R)-3-hydroxybutyrate-co-(R)-3-hydroxyvalerate)-block-ethylene glycol] Mn<3000	17	2,2,4-trimethylhexamethylene diisocyanate	poly[glycolide-co-(ε-caprolactone)]	24	[258]
DegraPol®/btgc b41 (160kDa) PEU	α,ω -dihydroxy-[poly((R)-3-hydroxybutyrate-co-(R)-3-hydroxyvalerate)-block-ethylene glycol] Mn<3000	41	2,2,4-trimethylhexamethylene diisocyanate	poly[glycolide-co-(ε-caprolactone)]	15	[258]
DegraPol (60-110kDa) PEU	α,ω -dihydroxy-[oligo((R)-3-hydroxybutyrate-co-(R)-3-hydroxyvalerate)-block-ethylene glycol] Mn~2300	29, 44, 68	2,2,4-trimethylhexamethylene diisocyanate	α,ω-dihydroxy-[poly-ε-caprolactone-block- diethylene glycol-block-poly-ε-caprolactone] Mn~1200	0	[363]
DegraPol n/a	α,ω -dihydroxy-[oligo((R)-3-hydroxybutyrate-co-(R)-3-hydroxyvalerate)-block-ethylene glycol] Mn~2300	44	2,2,4-trimethylhexamethylene diisocyanate	α,ω-dihydroxy-[poly-ε-caprolactone-block- diethylene glycol-block-poly-ε-caprolactone] Mn~1200	0	[420]
DegraPol n/a	α,ω -dihydroxy-[oligo((R)-3-hydroxybutyrate-co-(R)-3-hydroxyvalerate)-block-ethylene glycol] Mn~2300	44	2,2,4-trimethylhexamethylene diisocyanate	α,ω-dihydroxy-[poly-ε-caprolactone-block- diethylene glycol-block-poly-ε-caprolactone] Mn~1200	0	[421]
DegraPol™/btcg PEU (>100kDa)	poly[(3-(R)-hydroxybutyrate)-co-(3-(R)-hydroxyvalerate)]-diol	31-61	2,2,4-trimethylhexamethylene diisocyanate	poly[(e-caprolactone)-co-glycolide]-diol	18-69	[260]
DegraPol n/a	α,ω -dihydroxy-[oligo((R)-3-hydroxybutyrate-co-(R)-3-hydroxyvalerate)-block-ethylene glycol] Mn~2300	n/a	2,2,4-trimethylhexamethylene diisocyanate	α,ω-dihydroxy-[poly-ε-caprolactone-block- diethylene glycol-block-poly-ε-caprolactone] Mn~1200	0	[422]
DegraPol PEU n/a	α,ω -dihydroxy-[oligo((R)-3-hydroxybutyrate-co-(R)-3-hydroxyvalerate)-block-ethylene glycol] Mn~2300	n/a	2,2,4-trimethylhexamethylene diisocyanate	α,ω-dihydroxy-[poly-ε-caprolactone-block- diethylene glycol-block-poly-ε-caprolactone] Mn~1200	0	[423]

DegraPol PEU (60-110kDa)	poly[3-(R- hydroxy- butyrate)-co-(e-caprolactone)]-diol Mn~2660	40	2,2,4-trimethylhexamethylene diisocyanate	poly[(ε-caprolactone)-co-glycolide]-diol	n/a	[424]
DegraPol® PEU (~50kDa)	poly((R)-3-hydroxybutyric acid)-diol	n/a?	2,2,4-trimethylhexamethylene diisocyanate	poly(ε-caprolactone-co-glycolide)-diol	n/a	[263]
DegraPol TM PEU (60kDa)	poly((R)-3-hydroxybutyric acid)-diol	~67 (1:1.5 hard-to-soft)	2,2,4-trimethylhexamethylene diisocyanate	poly(ε-caprolactone-co-glycolide)-diol	n/a	[261]
DegraPol® PEU (70kDa)	poly[(3-(R)-hydroxybutyrate)-co-(3-(R)-hydroxyvalerate)]-diol	n/a?	2,2,4-trimethylhexamethylene diisocyanate	poly[(e-caprolactone)-co-glycolide]-diol	n/a	[208]
DegraPol® PEU (60-100kDa)	poly{(3-(R)-hydroxybuterate)-co-(ε-caprolactone)}-diol	~50 (equal amounts)	2,2,4-trimethylhexamethylene diisocyanate	poly(ε-caprolactone)-diol	0	[264]
DegraPol® PEU (61kDa)	poly((R)-3-hydroxybutyric acid)-diol	40	2,2,4-trimethylhexamethylene diisocyanate	poly(e- caprolactone-co-glycolide)-diol	n/a	[265, 266]
DegraPol® PEU (60-100kDa)	poly (3-(R)-hydroxybutyrate)-co-(ε-caprolactone)-diol Mn~2660	40	2,2,4-trimethylhexamethylene diisocyanate	poly(ε-caprolactone)-diol	0	[267]
DegraPol® DP30 PEU (70-80kDa)	poly[3-(R- hydroxy- butyrate)-co-(e-caprolactone)]-diol	40	2,2,4-trimethylhexamethylene diisocyanate	poly(ε-caprolactone)-diol-ε co-glycolide	30	[21]
DegraPol® PEU (70kDa)	poly[(3-(R)-hydroxybutyrate)-co-(3-(R)-hydroxyvalerate)]-diol	n/a?	2,2,4-trimethylhexamethylene diisocyanate	poly[(e-caprolactone)-co-glycolide]-diol	n/a	[178]
DegraPol® PEU (70kDa)	poly[(3-(R)-hydroxybutyrate)-co-(3-(R)-hydroxyvalerate)]-diol	n/a?	2,2,4-trimethylhexamethylene diisocyanate	poly[(e-caprolactone)-co-glycolide]-diol	n/a	[268]
DegraPol® PEU (n/a)	poly[3-(R- hydroxy- butyrate)-co-(e-caprolactone)]-diol Mn~2660	40	2,2,4-trimethylhexamethylene diisocyanate	poly[(e-caprolactone)-co-glycolide]-diol	n/a	[269]
DegraPol new PEU (~110kDa)	poly (3-(R)-hydroxybutyrate)-co-(ε-caprolactone)-diol Mn~2824	25	2,2,4-trimethylhexamethylene diisocyanate	poly(ε-caprolactone)-diol-ε co-glycolide Mn~1000	15	[270]
DegraPol® DP15 PEU (60kDa)	poly[3-(R- hydroxy- butyrate)-co-(e-caprolactone)]-diol	40	2,2,4-trimethylhexamethylene diisocyanate	poly(ε-caprolactone)-diol-ε co-glycolide	15	[271]

DegraPol classic PEU (60-110kDa)	poly (3-(R)-hydroxybutyrate)-co-(ε-caprolactone)-diol Mn~2660	40	2,2,4-trimethylhexamethylene diisocyanate	poly(ε-caprolactone)-diol-ε co-glycolide Mn~1250	15	[272]
DegraPol new PEU (60-110kDa)	poly (3-(R)-hydroxybutyrate)-co-(ε-caprolactone)-diol Mn~2824	25	2,2,4-trimethylhexamethylene diisocyanate	poly(ε-caprolactone)-diol-ε co-glycolide Mn~1000	15	[272]
DegraPol® DP30 PEU (77.67±5.7kDa)	poly (3-(R)-hydroxybutyrate)-co-(ε-caprolactone)-diol	40	2,2,4-trimethylhexamethylene diisocyanate	poly(ε-caprolactone)-diol-ε co-glycolide	30	[273]
DegraPol new PEU (100-110kDa)	poly (3-(R)-hydroxybutyrate)-co-(ε-caprolactone)-diol Mn~2824	25	2,2,4-trimethylhexamethylene diisocyanate	poly(ε-caprolactone)-diol-ε co-glycolide Mn~1000	15	[262]

A3: Supporting thromboelastography results

Callibration data for individual TEG channels tested against the Level I biological control fluid

Channel	R[min]	K [min]	Angle [deg]	MA [mm]
A1	1.5	0.8	84	52.5
A2	1.4	0.8	84.4	53.1
B1	1.4	0.8	83.2	50.5
B2	1.4	0.8	84.4	53.1
C1	1.5	0.8	82.4	56.4
C2	1.5	0.8	84	53.7
D1	1.2	0.8	83.9	55.8
D2	1.3	0.8	84.1	54.5
Suggested Level I ranges	0.0-3.0	0.0-2.0	77.0-89.0	44.0-61.0

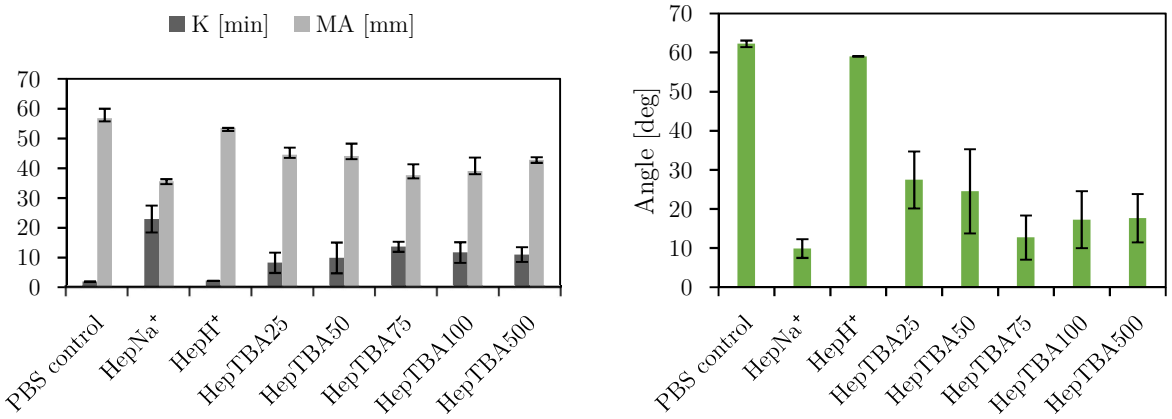

Additional data for TEG performance analysis of HepTBA products

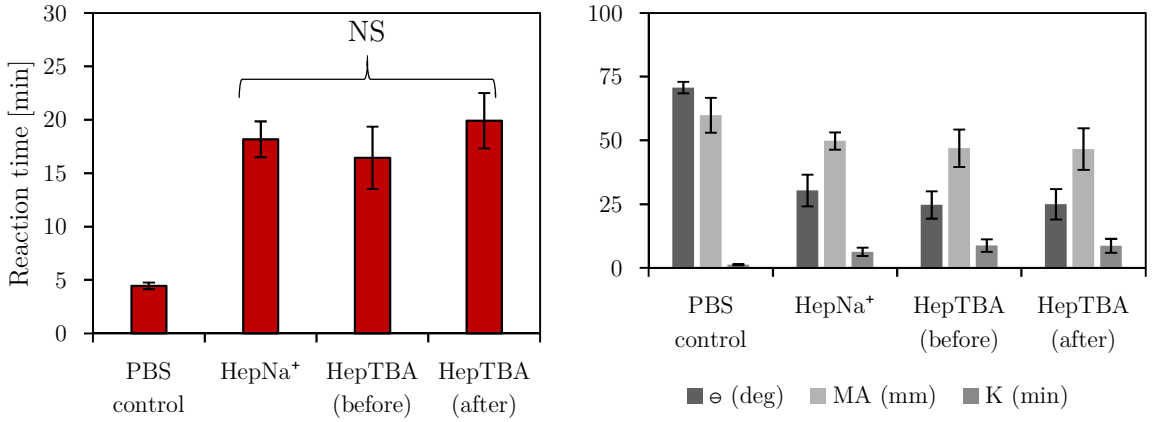

Detailed TEG results for HepTBA500 before and after electrospinning

A4: Output of a typical mechanical tensile testing report

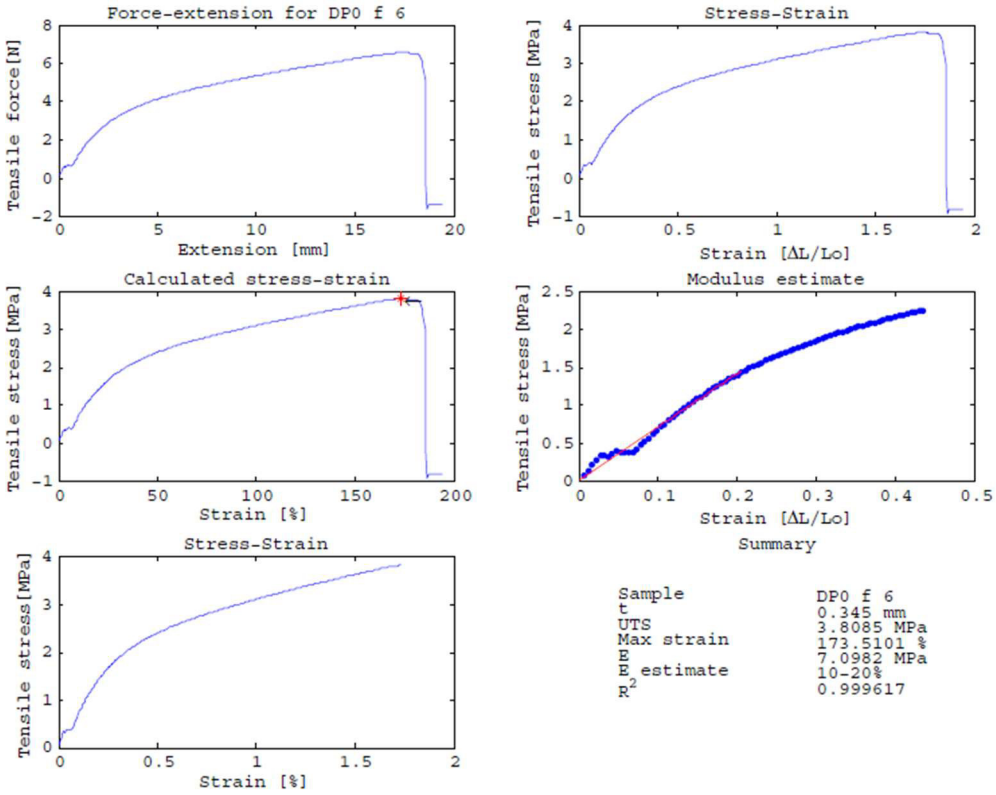

Specimen example: DegraPol® (DP0) film

A5: Output of a typical statistical report

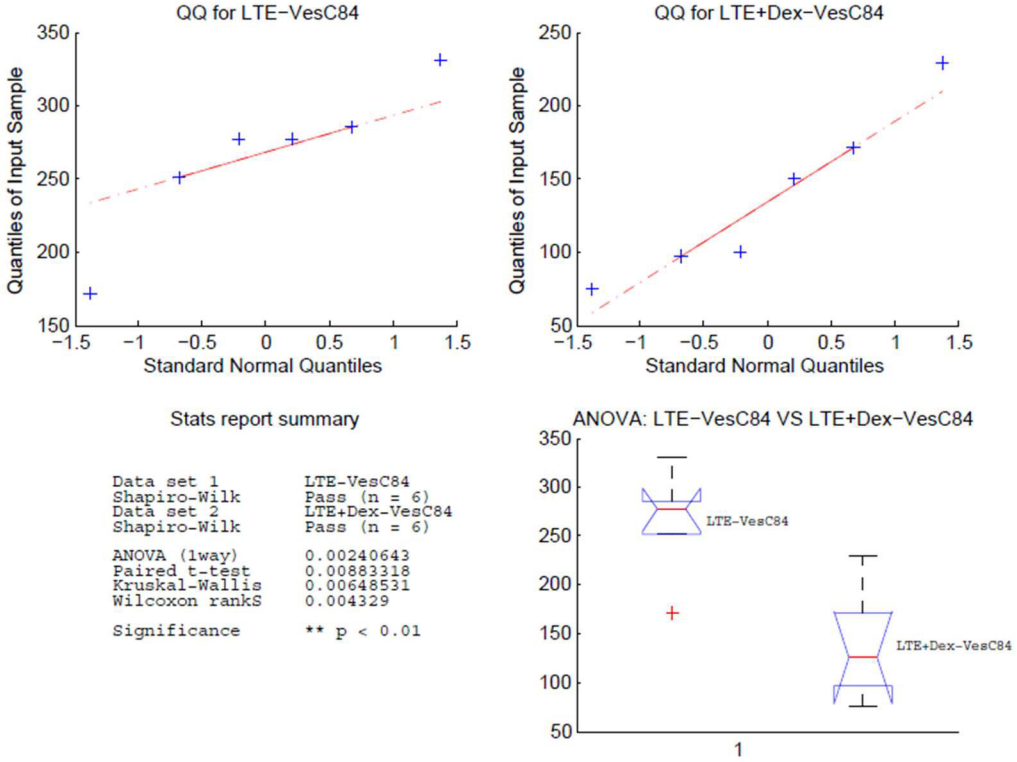

Example: histological results (vascular density at 84days) of explanted electrospun scaffolds (DegraPol®, n = 6).

A6: Comparison of tissue ingrowth from different fixation media

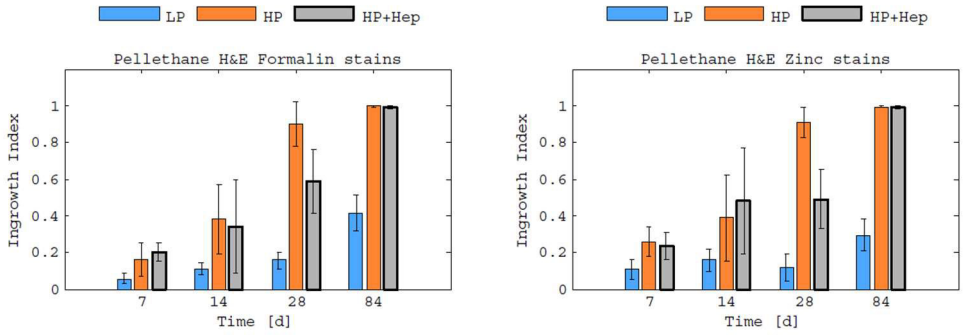

Tissue ingrowth of Pellethane® groups over 3 months

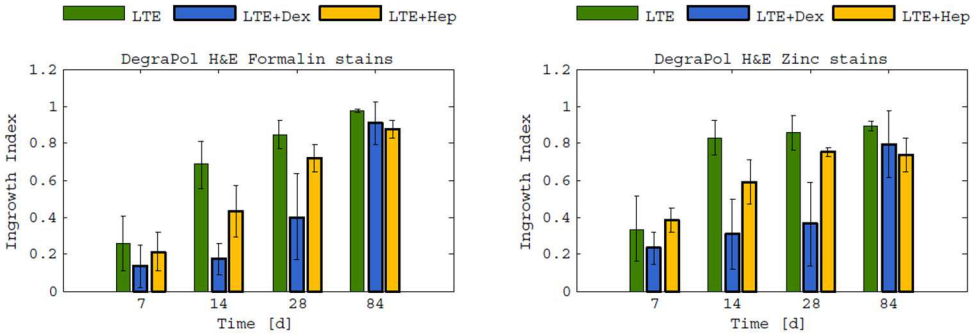

Tissue ingrowth of DegraPol® groups over 3 months

A7: Solvents tested for DegraPol® solubility at room temperature

Solvent	Score	Solvent	Score
Acetone	3	Ethyl acetate	3
Acetonitrile	3	Ethylene glycol	4
Anisole	2	Hexafluoro isopropanol (HFIP)	1
Chlorobenzene	2	Isopropanol	4
Chloroform	1	Methanol	4
Cyclohexanone	2	Methylpyrrolidone (NMP)	2
Dichloromethane (DCM)	1	Tetrahydrofuran (THF)	2
Dichloroethane (DCE)	1	Toluene	2
Dioxane	2	Trifluoro ethanol (TFE)	1
Dimethylacetamide (DMAC)	2	Trifluoro acedic acid	1
Dimethylformamide (DMF)	2		

Scores are allocated as: (1) solvent, (2) good swelling agent, (3) poor swelling agent and (4) non-solvent.

A8: Supporting NMR spectra of heparin ion-exchange process

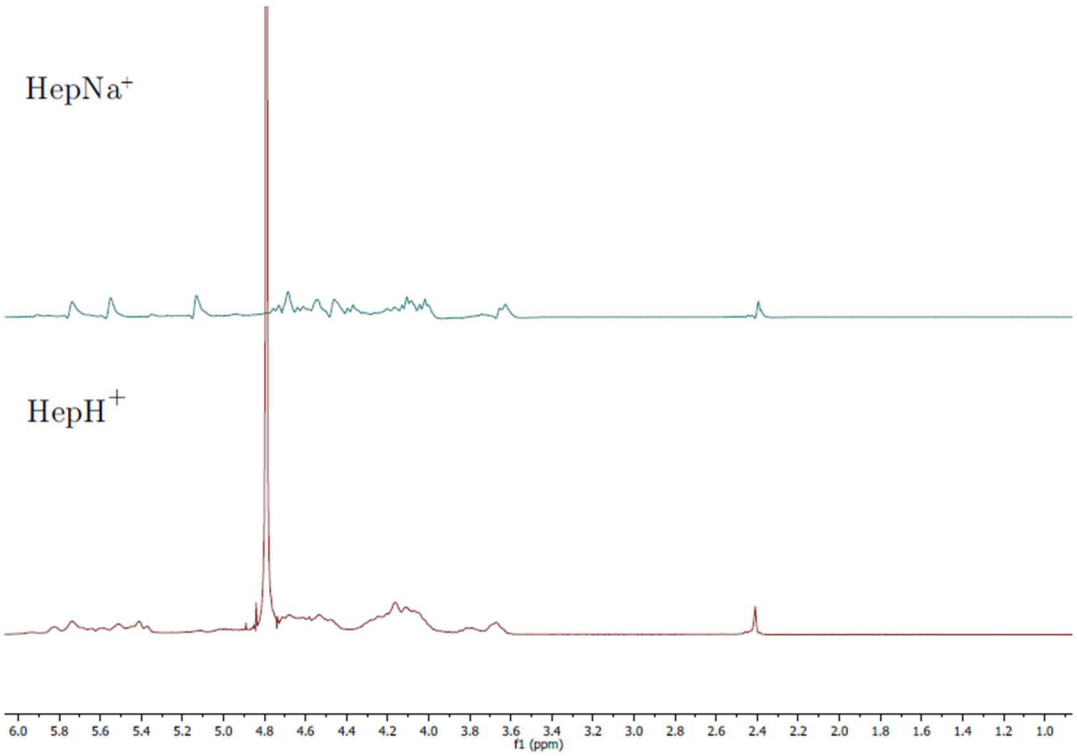

Heparin sodium ($HepNa^+$) and heparin acid ($HepH^+$) before/after removal of Na^+ during the ion-exchange process.

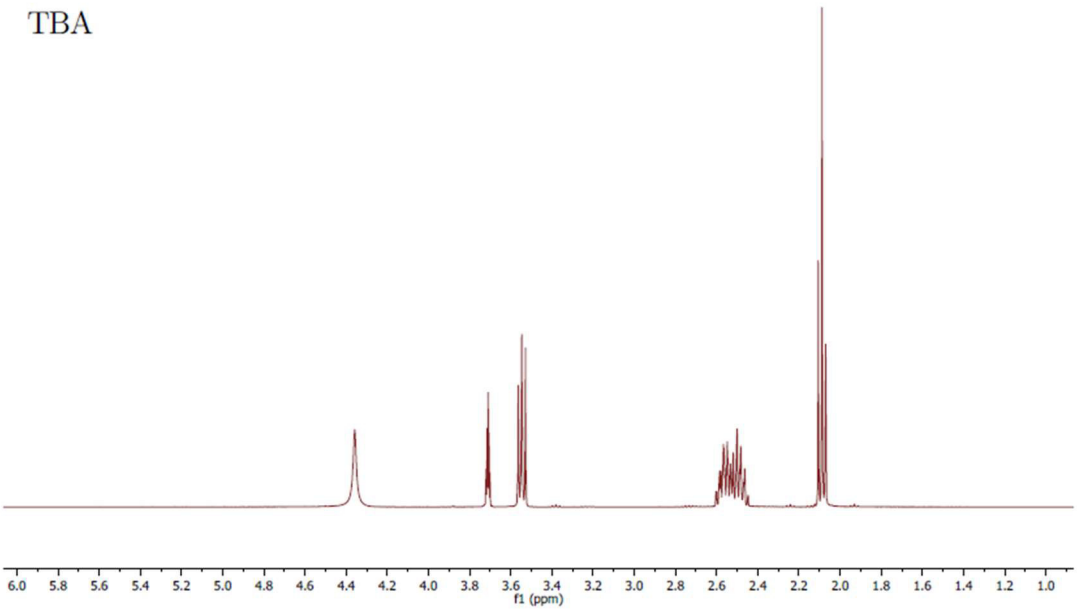

Tributylamine (TBA) before ion-exchange process

A9: Supporting numerical results of electric field simulations

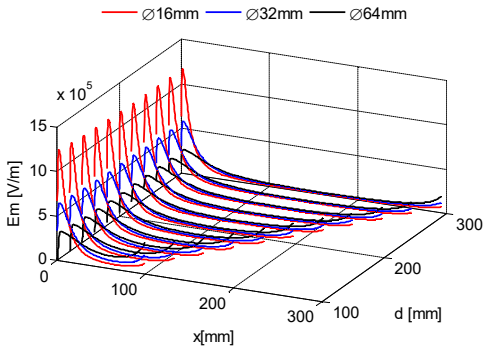

Electric field at various collecting distances

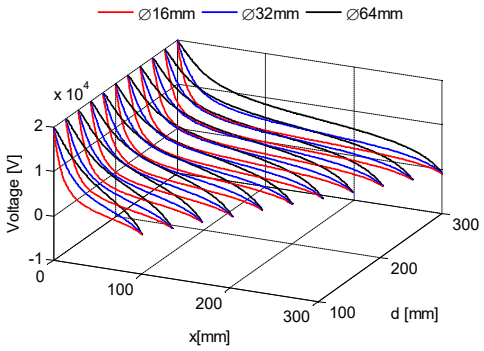

Voltage drop at various collecting distances

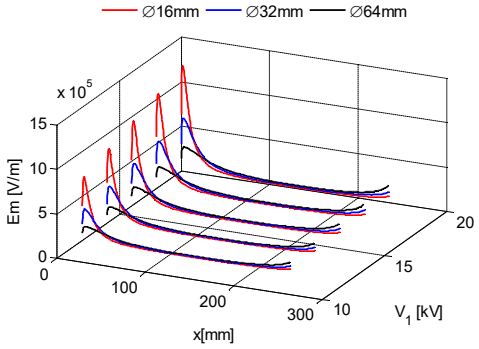

Electric field at different applied voltages

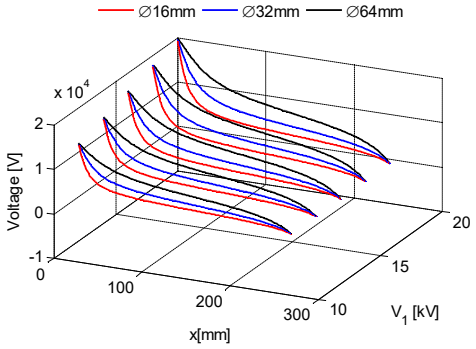

Voltage drop at different applied voltages

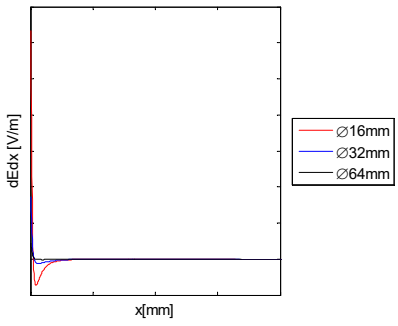

Derivative of the electric field (equation 2-5) created by an annual disc.

A10: Coaxial drug encapsulation attempt

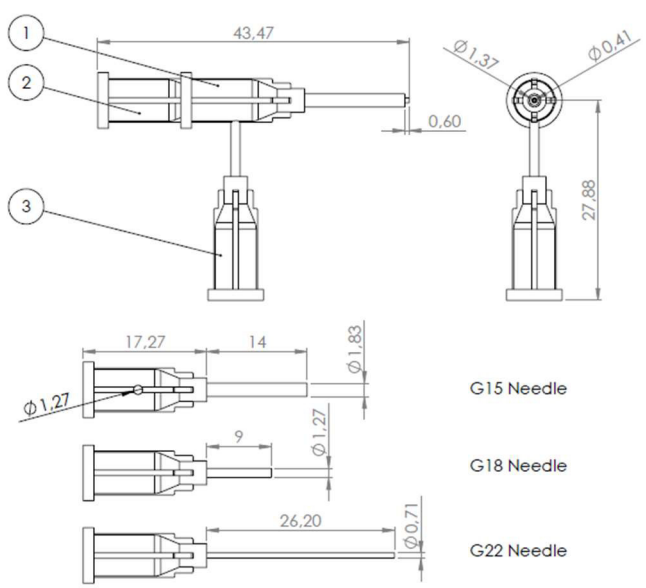

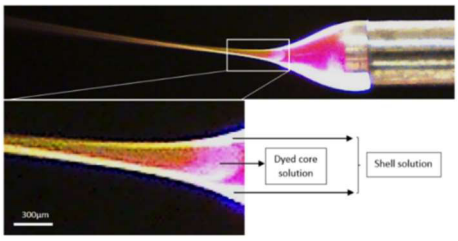

Taylor cone

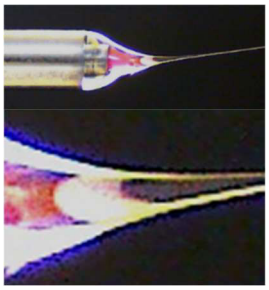

Before PEO removal

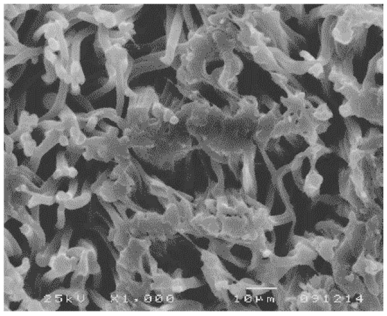

After PEO removal

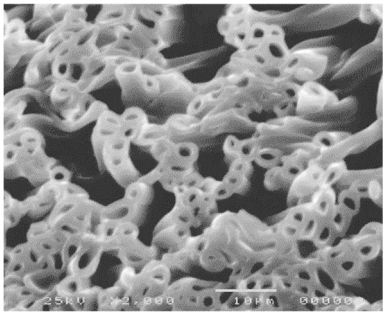

Solid PU fibres (cross)

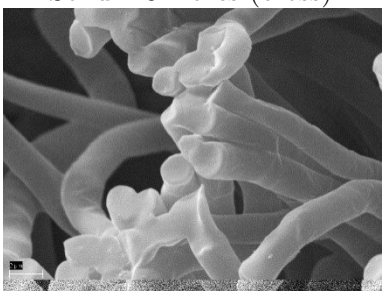

Hollow PU fibres (cross)

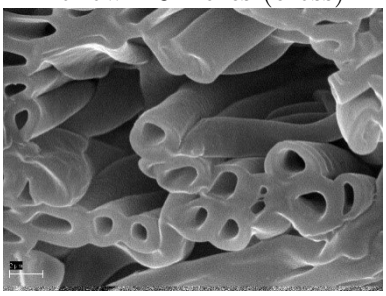

Hollow PU fibres (top)